

MAGNETIC STRATIGRAPHY AND ENVIRONMENTAL MAGNETISM OF OCEANIC  
SEDIMENTS

By

HELEN F. EVANS

A DISSERTATION PRESENTED TO THE GRADUATE SCHOOL  
OF THE UNIVERSITY OF FLORIDA IN PARTIAL FULFILLMENT  
OF THE REQUIREMENTS FOR THE DEGREE OF  
DOCTOR OF PHILOSOPHY

UNIVERSITY OF FLORIDA

2006

Copyright 2006

by

Helen F. Evans

For Jane and Eryl

## ACKNOWLEDGMENTS

I would like to thank my advisor, Jim Channell, for giving me the opportunity to study in Florida and for all his help and support over the last 7 years. I also thank my committee members Ellen Martin, Neil Opdyke, John Jaeger and Bo Gustafson for agreeing to supervise my research over the last five years and for all their help, academic and otherwise. I also had the pleasure of collaborating and interacting with a number of talented individuals without whose help I would not have been able to accomplish this work: Gary Acton, Paul Bown, Yohan Guyodo, Sean Higgins, Claude Hillaire-Marcel, Dave Hodell, Kainian Huang, Mark Leckie, Ulla Rohl, Joseph Stoner, Ray Thomas, Thomas Westerhold and many others. My research was made possible by the technical and financial support of several organizations including the National Science Foundation, the JOIDES U.S. Sciences Support Advisory Committee (USSAC), and the Graduate Student Council. Support was also provided by the Institute for Rock Magnetism, the College of Liberal Arts and Sciences, the Graduate School, the McLaughlin family, and the department of Geological Sciences at the University of Florida.

I thank all those who gave me their moral support during my years of study, which often consisted of many hours of festivities in the numerous bars and restaurants in Gainesville, San Francisco and further afield. I thank in particular Gillian Rosen, Joe Graves, Joann and Jason Hochstein, Howie Scher, George and Katherin Kamenov, Cara Gentry, Jen Mays, Steve Volpe, Phil D'Amo, Brickly Way, Kendall Fountain, Adi Gilli, Simon Nielsen, Dave Hodell, Mike Rosenmeier, William Kenney, Yohan Guyodo and Victoria Meija. Finally I would like to express my gratitude to my family without whose support I would not have been able to complete this work. I thank my late mother Eryl, my father Terry and my brother Michael. I also thank Diane and John Thomas, Judy and Robin Ganz, and Molly and Reg Beynon.



## TABLE OF CONTENTS

	<u>page</u>
ACKNOWLEDGMENTS.....	4
LIST OF TABLES.....	7
LIST OF FIGURES .....	8
ABSTRACT .....	12
 CHAPTER	
1 INTRODUCTION .....	14
2 LATE MIOCENE-HOLOCENE MAGNETIC POLARITY STRATIGRAPHY AND ASTROCHRONOLOGY FROM ODP LEG 198-SHATSKY RISE.....	18
Introduction .....	18
Methods.....	19
Magnetostatigraphic Interpretation.....	20
Astrochronology .....	23
Discussion .....	24
Conclusions .....	27
3 INTEGRATED NEOGENE MAGNETIC, CYCLE AND BIO- STRATIGRAPHY FROM ODP SITE 1208 (SHATSKY RISE, PACIFIC OCEAN).....	48
Introduction .....	48
Site Location and Lithology .....	51
Magnetic Stratigraphy.....	51
Cycle Stratigraphy .....	53
Calcareous Nannofossils .....	54
Planktonic Foraminifera.....	56
Conclusions .....	58
4 PALEOINTENSITY-ASSISTED CHRONOSTRATIGRAPHY OF DETRITAL LAYERS ON THE EIRIK DRIFT (NORTH ATLANTIC) SINCE MARINE ISOTOPE STAGE 11 .....	75
Introduction .....	75
Methods.....	76
NRM and Normalized Remanence Record.....	78
Polarity Excursions .....	79
Relative Paleointensity.....	79
Chronology .....	80
Detrital Layer Stratigraphy.....	81

	Discussion .....	84
	Conclusions .....	87
5	RELATIVE PALEOINTENSITY STACK FOR THE LAST 85 KYR ON A REVISED GISP CHRONOLOGY, AND ENVIRONMENTAL MAGNETISM OF THE GARDAR DRIFT .....	105
	Introduction .....	105
	Site Locations .....	107
	Methods.....	108
	Directional Magnetic Data .....	110
	Normalized Remanence .....	111
	Stable Isotope Data and Age Models.....	112
	Bulk Magnetic and Physical Parameters.....	112
	Relative Paleointensity Stack .....	113
	Environmental Magnetism .....	115
	Conclusions .....	118
6	RELATIVE GEOMAGNETIC PALEOINTENSITY IN THE GAUSS AND GILBERT CHRONS FROM IODP SITE U1313 (NORTH ATLANTIC) .....	136
	Introduction .....	136
	Methods.....	138
	Results .....	139
	Discussion .....	142
7	ODP SITE 1092 REVISED COMPOSITE DEPTH SECTION HAS IMPLICATIONS FOR UPPER MIOCENE "CRYPTOCHRONS" .....	161
	Introduction .....	161
	Revised Composite Depths (rmed).....	162
	Implications for Magnetic Stratigraphy .....	163
8	ASTRONOMICAL AGES FOR MIOCENE POLARITY CHRONS C4AR-C5R (9.3- 11.2 MA), AND FOR THREE EXCURSION CHRONS WITHIN C5N.2N.....	171
	Introduction .....	171
	Methods and Results .....	173
	Comparison with Other Timescales.....	175
	Excursion Chrons.....	178
9	CONCLUSIONS AND FUTURE WORK .....	189
	LIST OF REFERENCES .....	191
	BIOGRAPHICAL SKETCH.....	204

## LIST OF TABLES

<u>Table</u>	<u>page</u>
2-1 Latitude, longitude, water depth .....	28
2-2 Magnetostratigraphic age model .....	29
2-3 Comparison of astrochronological age models .....	30
2-4 Astrochronological ages for Leg 198 .....	31
3-1 Depths of reversal boundaries from ODP Site 1208 .....	59
3-2 Astronomically calibrated ages for reversal boundaries from ODP Site 1208 .....	60
3-3 Nannofossil datums for ODP Site 1208 .....	61
3-4 Plio-Pleistocene foraminifer datums .....	62
3-5 Miocene foraminifer datums .....	63
4-1 Core, latitude, longitude, water depth and base age of the core. ....	89
4-2 DC and LDC layer properties in Core MD99-2227 .....	90
4-3 Detrital Layers from other studies considered to be correlative to detrital layers identified on Eirik drift .....	91
5-1 Summary of the cores used in this study and the eleven cores used in the relative paleointensity stack .....	120
6-1 Depth of polarity chrons from IODP Site U1313 .....	146
6-2 Polarity reversal ages determined at Site U1313 .....	147
7-1 Adjusted depths of core tops from ODP site 1092 .....	166
7-2 Position of the polarity zone boundaries at site 1092 .....	167
8-1 Astronomical ages from recent timescales compared with those inferred at ODP Site 1092 .....	181

## LIST OF FIGURES

<u>Figure</u>	<u>page</u>
2-1 Bathymetric map of Shatsky Rise.....	32
2-2 Representative orthogonal projections of AF demagnetization data. ....	33
2-3 Site 1207 component inclination and declination from discrete samples for 0-80 meters. ....	34
2-4 Site 1207 component inclination and declination from discrete samples for 80-160 meters ....	35
2-5 Interval sedimentation rates and age versus depth.....	36
2-6 Site 1209 component inclination and declination from discrete samples .....	37
2-7 Site 1210 component inclination and declination from discrete samples .....	38
2-8 Site 1211 component inclination and declination from discrete samples .....	39
2-9 Site 1212 component inclination and declination from discrete samples .....	40
2-10 Power spectra .....	41
2-11 The astronomical solution for obliquity compared with tuned L* reflectance data from Site 1207.....	42
2-12 The astronomical solution for obliquity compared with tuned L* reflectance data from Site 1208.....	43
2-13 The astronomical solution for obliquity compared with tuned L* reflectance data from Site 1209.....	44
2-14 The astronomical solution for obliquity compared with tuned L* reflectance data from Site 1210.....	45
2-15 The astronomical solution for obliquity compared with tuned L* reflectance data from Site 1211.....	46
2-16 Cross-spectral analysis .....	47
3-1 Bathymetric map showing the location of Shatsky Rise in the Pacific Ocean.....	64
3-2 Inclination, declination and MAD values plotted against meters below sea floor .....	65
3-3 Inclination, declination and MAD values.....	66

3-4	Inclination, declination and MAD values.....	67
3-5	Orthogonal projections showing AF demagnetization data.....	68
3-6	Interval sedimentation rates.....	69
3-7	Reflectance ( $L^*$ ) data .....	70
3-8	Plio-Pleistocene planktonic foraminifer and calcareous nannofossil datums.....	71
3-9	Miocene planktonic foraminifer and calcareous nannofossil datums .....	72
3-10	Calcareous nannofossil biostratigraphy.....	73
3-11	A proposed biostratigraphy for the mid-latitude North Pacific .....	74
4-1	Location map showing the Labrador Sea .....	92
4-2	Component inclination, corrected component declination and maximum angular deviation .....	93
4-3	Component inclination, declination and maximum angular deviation (MAD) values recording Laschamp and Iceland Basin polarity excursions .....	94
4-4	Anhyseretic susceptibility ( $k_{arm}$ ) plotted against volume susceptibility ( $k$ ) .....	95
4-5	NRM, ARM, IRM and volume susceptibility.....	96
4-6	JPC19: Relative paleointensity record correlated to that from ODP Site 983.....	97
4-7	JPC18: Relative paleointensity data correlated to ODP Site 983 .....	98
4-8	JPC15: Relative paleointensity data correlated to ODP Site 983 .....	99
4-9	MD99-2227: Relative paleointensity data correlated to ODP Site 983 .....	100
4-10	$k_{arm}/k$ and magnetic susceptibility versus age.....	101
4-11	Core MD99-2227: $k_{arm}/k$ , magnetic susceptibility, bulk (GRAPE) density .....	102
4-12	Photographs and X-radiographs of three detrital .....	103
4-13	Hysteresis ratios $M_r/M_s$ plotted versus $H_{cr}/H_c$ .....	104
5-1	Location map for cores analyzed in this study.....	121
5-2	Correlation of the magnetic susceptibility records.....	122
5-3	Orthogonal projections of alternating field demagnetization data.....	123

5-4	Component inclination, declination and maximum angular deviation (MAD) values ...	124
5-5	Plot of anhysteretic susceptibility ( $k_{arm}$ ) versus volume susceptibility ( $k$ ).....	125
5-6	Paleointensity proxies.....	126
5-7	Core JPC13 benthic oxygen isotope record.....	127
5-8	Relative paleointensity records from Cores JPC2, JPC5 correlated to Core JPC13 .....	128
5-9	Interval sedimentation rates for Cores JPC2, JPC5 and JPC13 .....	129
5-10	Core JPC13: GRA bulk density .....	130
5-11	Anhysteretic susceptibility divided by volume magnetic susceptibility .....	131
5-12	Eleven relative paleointensity records from the North Atlantic Ocean.....	132
5-13	The new relative paleointensity stack .....	133
5-14	Comparison of the EHC06 paleointensity stack to $^{36}\text{Cl}$ flux.....	134
5-15	Comparison of the EHC06 paleointensity stack .....	135
6-1	Location map for IODP Site U1313.....	148
6-2	Magnetic polarity stratigraphy from IODP Site U1313 in the 120-200 mcd interval.....	149
6-3	Magnetic polarity stratigraphy from IODP Site U1313 in the 200-280 mcd interval ....	150
6-4	Vector end-point projections of AF demagnetization data.....	151
6-5	Interval sedimentation rates .....	152
6-6	Gauss Chronozone at Site U1313 .....	153
6-7	The magnetic grain size proxy, anhysteretic susceptibility divided by susceptibility ....	154
6-8	Later part of the Gilbert Chronozone at Site U1313 .....	155
6-9	Relative paleointensity records from IODP Site U1313 .....	156
6-10	Volume magnetic susceptibility from u-channel samples.....	157
6-11	Volume magnetic susceptibility from u-channel samples and $L^*$ reflectance data measured shipboard.....	158
6-12	Mean volume magnetic susceptibility .....	159
6-13	Output of a gaussian filter centered on a period of 41 kyr .....	160

7-1	Fe intensity (XRF) data plotted as a five-point moving average .....	168
7-2	Inclination of the characteristic magnetization component.....	169
7-3	Site 1092 .....	170
8-1	Magnetic component inclination for the C4Ar.1n-C5r.1n interval.....	182
8-2	Oxygen isotope records from the C4An-C5r.1n interval at ODP Site 1092 .....	183
8-3	Power spectrum generated from the oxygen isotope stack in the depth domain.....	184
8-4	Upper plot shows the correlation of the filtered (filter centered at $0.0244 \pm 0.0073$ kyr <sup>1</sup> ) oxygen isotope stack to the astronomical solution for obliquity.....	185
8-5	Interval sedimentation rates for the C4Ar.1n-C5r.1n interval.....	186
8-6	Comparison of the age estimates of polarity chrons at ODP Site 1092 .....	187
8-7	The Site 1092 relative paleointensity record for C5n.2n.....	188

Abstract of Dissertation Presented to the Graduate School  
of the University of Florida in Partial Fulfillment of the  
Requirements for the Degree of Doctor of Philosophy

MAGNETIC STRATIGRAPHY AND ENVIRONMENTAL MAGNETISM OF OCEANIC  
SEDIMENTS

By

Helen F. Evans

December 2006

Chair: James E. T. Channell  
Major: Geology

This dissertation presents the results of chronostratigraphic studies on marine sediment cores from three Oceans. Using a combination of magnetic stratigraphy, biostratigraphy and cycle stratigraphy it is possible to produce chronostratigraphies that exceed the resolution of any individual technique.

In the North Atlantic, environmental magnetic records from Eirik Drift, south of Greenland, record detrital signals related to the melting of the Greenland and Laurentide Ice Sheets. The detrital layer stratigraphy has been placed in a paleointensity-assisted chronostratigraphic template, based on paleointensity and stable isotope data, to enhance correlation of detrital layers across the North Atlantic region. In the central Atlantic, on Gardar Drift, correlation of a benthic oxygen isotope record to the Greenland and Vostok Ice cores has placed cores from the drift on a revised GISP chronology. A stack of relative paleointensity records was developed and placed on the revised GISP chronology. In marine isotope stage 3, a benthic isotope record appears to record changes in bottom water temperature that are coeval with magnetic grain size changes.

IODP Site U1313 from the North Atlantic produced a high-resolution polarity stratigraphy and relative paleointensity record between 2.5 and 6.0 Ma. This is one of a handful



of paleointensity records for this interval. Cycles in magnetic susceptibility allowed age-calibration by correlation to a benthic oxygen isotope stack.

Sediment cores from the Pacific Ocean produced excellent magnetic stratigraphies, and cycles in the sediment allowed astronomic calibration of reversal boundaries. Based on the correlation of planktonic foraminifer datums to the magnetic stratigraphy at ODP Site 1208, a new planktonic foraminifer zonation for the northwest Pacific Ocean can be precisely correlated to polarity chrons and astronomically calibrated ages. Numerous paleomagnetic excursions are tentatively identified for the first time in Pacific sediments.

Oxygen isotope records from the Late Miocene (9.3-11.2 Ma) at ODP Site 1092 (South Atlantic) allowed astronomic calibration of ages of reversal boundaries and three polarity excursions within Chron 5. This is the first time astronomically calibrated ages have been assigned to these polarity excursion chrons and indicate a duration for the excursions of 3-4 kyrs.

## CHAPTER 1 INTRODUCTION

Stratigraphy is a fundamental part of Geology. Earth processes unfold over a great range of time scales from millions of years to minutes and seconds. One of the challenges in stratigraphy is to be able to assign dates to events in the geologic record. The geologic timescale is the means by which we can understand the history of the Earth and magnetic reversal stratigraphy provides the central framework for the geologic timescale to which other dating techniques (biostratigraphic, radiometric, orbital) can be tied. This is because magnetic reversals are, on geologic timescales, globally synchronous, environmentally independent events.

The geomagnetic timescale of Heirtzler et al. (1968) was one of the foundations of the plate tectonic revolution. They proposed a geomagnetic polarity timescale for the Late Cretaceous to Recent based on a few long magnetic anomaly profiles. The evolution of the polarity timescale since 1968 has involved two types of revisions: adjustments of the relative spacing of some anomalies and calibration of the polarity sequence in time (Cande and Kent, 1992). Over the past forty years the pattern of normal and reversed polarities has been extensively studied and most of its large-scale features for the past 200 million years are now well understood (Gradstein et al., 2005).

Classic magnetic polarity reversal stratigraphy lacks the resolution necessary for the high-resolution (millennial-scale) climate studies being conducted today. This led to the development of high-resolution cryogenic magnetometers capable of measuring whole-core samples or u-channel samples. This in turn led to the development of "composite sections" for marine sediment cores whereby multiple cores were taken at a single site and spliced together to provide a complete stratigraphic section (Hagelberg et al., 1995).

Changes in the intensity of the Earth's magnetic field occur over much shorter timescales than polarity reversals. These changes can be measured in sedimentary cores to produce records of relative geomagnetic paleointensity. This is done by normalizing the natural remanent magnetization by an artificial remanence to remove intensity changes due to changes in concentration of magnetic material in the core. Records of relative paleointensity have been shown to be globally correlative on millennial timescales for the last glacial cycle (Laj et al. 2004).

In attempting to understand the time-depth relationship in marine sediment cores and therefore understand more about the Earth's climate and evolution my work covers three Oceans, the South Atlantic, the North Atlantic and the Pacific. Below is a summary of the work presented in this dissertation. The nature of this work is collaborative and, as such, data provided by my colleagues is included in this dissertation. Their contribution is acknowledged and clearly detailed in the following summary.

In Chapter 2 magnetostratigraphic and cyclostratigraphic results are presented for the 0-12 Ma interval from sites drilled during ODP Leg 198 to Shatsky Rise. Cyclic alternations in the percentage of calcium carbonate, as shown by color reflectance data and gamma ray attenuation bulk density measured on the sediments, allowed astronomic calibration of the magnetic stratigraphy from six ODP Sites. This chapter was published in the Scientific Results Volume for Ocean Drilling Program (ODP) Leg 198 (Evans et al., 2005). Chapter 3 is a continuation of this work and has produced an integrated magneto- bio- and cyclostratigraphy from ODP Site 1208 for the 1-12 Ma interval. Biostratigraphic data included in this chapter were provided by Nicholas Venti, Mark Leckie (U. Massachusetts, foraminifer) and Paul Bown (University College London, nannofossils).

In Chapters 4 and 5, I used sedimentary relative paleointensity records to correlate between cores collected on drift deposits in the North Atlantic. In Chapter 4, I present a study of sediments from the Eirik drift for the 0-400 ka interval. Detrital layers identified within four cores are placed in a paleointensity assisted chronostratigraphic framework. Environmental magnetic records from climatically sensitive regions such as the North Atlantic can provide information about changes in the strength of bottom currents and ice sheet dynamics both of which are climatically sensitive. Oxygen isotope data used in this chapter were provided by Jim Wright and Lauren Nietzke (Rutgers University) and Claude Hillaire-Marcel (GEOTOP) (Core MD99-2227). This chapter is under review in the journal *Geophysics, Geochemistry and Geosystems*. In Chapter 5 cores from the Gardar Drift provide records of changes in magnetic grain size over glacial/interglacial and stadial/interstadial cycles for the last 130 ka. These changes are interpreted as changes in the speed of bottom currents forming the drift deposits over glacial/interglacial cycles and stadial/interstadial cycles. David Hodell (UF) provided oxygen isotope data in Chapter 5.

In Chapter 6 a paleomagnetic study of IODP Site U1313 from the North Atlantic is presented. The magnetic stratigraphy spans the interval from 2.5-6.3 Ma including the Gauss and Gilbert chronozones. A relative paleointensity record for the Gauss and Gilbert chrons, is one of only a handful of such records for this time interval. Cycles in magnetic susceptibility have allowed astronomic calibration of the ages of reversal boundaries.

In 2001, my MS thesis consisted of a paleomagnetic study of ODP Site 1092 from the South Atlantic. Chapter 7 presents a revision of the composite depth scale from ODP Site 1092. X-Ray fluorescence (XRF) scanning data were provided by Thomas Westerhold (University Bremen). This chapter was published in *Geophysical Journal International* (Evans et al. 2004).

In Chapter 8 we use cyclic alternations in a stack of three oxygen isotope records (Paulsen et al., in press) from ODP Site 1092 in the South Atlantic to astronomically tune the magnetic stratigraphy from 9.3-11.2 Ma. This includes the long normal polarity chron C5n.2n and three short reverse polarity intervals within it identified by Evans and Channell (2003). It also includes a critical age tie-point from the Cande and Kent (1995) Geomagnetic Polarity Timescale (GPTS) at the base of C5n.2n. This chapter is under review at *Earth and Planetary Science Letters*.

## CHAPTER 2

### LATE MIOCENE-HOLOCENE MAGNETIC POLARITY STRATIGRAPHY AND ASTROCHRONOLOGY FROM ODP LEG 198-SHATSKY RISE

#### **Introduction**

Shatsky Rise is a medium-sized large igneous province in the west-Central Pacific Ocean (Figure 2-1) and is possibly the oldest existing oceanic plateau. The rise consists of three prominent topographic highs. Sites 1209, 1210, 1211 and 1212 were cored on the Southern High (Bralower, Premoli Silva, Malone et al., 2002). Eight sites on the Southern High of the rise were drilled during Deep Sea Drilling Project (DSDP) and earlier Ocean Drilling Program (ODP) legs (Sites 47, 48, 49, 50, 305, 306, 577, and 810). Of these, ODP Sites 577 and 810 provided interpretable Neogene magnetic stratigraphies.

Sites 1207 and 1208, from the Northern and Central Highs, provided unexpectedly expanded late Miocene (12.5 Ma) to Holocene sequences. These locations had not been cored during previous DSDP/ODP expeditions. The initial age model for all of the sites was based on correlation of the sequence of polarity zones to the geomagnetic polarity timescale (GPTS) (Cande and Kent, 1992, 1995). Mean sedimentation rates at the five sites vary from 1- to 4 cm/k.y. Latitude and longitude of the sites and basal ages of the Neogene sediments are given in Table 2-1. Neogene sediments at the sites consisted mostly of light gray to pale orange nannofossil oozes with varying amounts of clay, radiolarians, and diatoms. Magnetic susceptibility is low ( $< 2 \times 10^{-5}$  SI) at all the sites and shows a decreasing trend from the Quaternary to the late Miocene. Composite sections were constructed shipboard for four of the sites (1209, 1210, 1211, and 1212) using multi-sensor track (MST) data including magnetic susceptibility, gamma ray attenuation (GRA) bulk density, and reflectance data. Sites 1207 and 1208 were not double-cored, and depths at these sites are in meters below sea floor (mbsf). The

magnetic stratigraphy from the six sites (1207, 1208, 1209, 1210, 1211, and 1212), was based on shipboard pass-through magnetometer measurements and discrete samples measured post-cruise.

Sediments from five of the sites (1207, 1208, 1209, 1210, and 1211) showed a prominent cyclicity in reflectance data for parts of the sections, and this is the basis for the construction of an astronomically tuned age model for the 0- to 8-Ma interval. The astronomically calibrated polarity timescale has been well established for the 0- to 6-Ma interval (Shackleton et al., 1990, 1995; Hilgen 1991a, 1991b). Hilgen (1991a, 1991b) produced his astronomically calibrated polarity timescale for the 2- to 5.23-Ma interval using sapropel occurrences and carbonate content in Mediterranean sections. These polarity chron ages were incorporated into the GPTS of Cande and Kent (1995).

In this study we produced an astronomically calibrated magnetic reversal stratigraphy for the 0- to 8-Ma interval. This is in good agreement with Hilgen (1991a, 1991b) and Shackleton et al., (1995) in the 0- to 6-Ma interval. In the 6-to 8-Ma interval, polarity chron ages are in better agreement with the Shackleton et al. (1995) timescale, differing by up to ~200 k.y. from that of Hilgen et al. (1995) and the ATNTS 2004 of Lourens et al. (2004). This chapter was published in the Scientific Results Volume for ODP Leg 198 (Evans et al., 2005).

## **Methods**

Two types of paleomagnetic measurements were made on sediments collected during ODP Leg 198; pass-through measurements on half-cores and discrete sample measurements. Discrete sample cubes (2cm x 2cm) were collected during Leg 198 to augment measurements using the shipboard pass-through magnetometer. Shipboard measurements on half-cores were made at 5-cm intervals. A total of 747 discrete samples were taken at 50-cm intervals. Discrete samples were collected from the center of the half-cores to avoid deformation at the outer edges of the core. Magnetic measurements on the cubes were performed in the magnetically shielded room at

the University of Florida using a 2G-Enterprises cryogenic magnetometer. The samples were step-wise alternating-field (AF) demagnetized using a D-Tech D2000 AF demagnetizer. Magnetization component directions were determined using the method of Kirschvink (1980), applied to the 20- to 60 mT peak field demagnetization interval.

The astrochronology developed for Sites 1207, 1208, 1209, 1210, and 1211 was based on cycles seen in reflectance data ( $L^*$ ) measured shipboard on a purpose-built track. Reflectance of visible light from soft sediment cores was measured using a spectrophotometer at 2.5-cm intervals and provided a high-resolution record of color variations for visible wavelengths (400-700 nm).  $L^*$  reflectance represents "lightness" of the sediment which is usually controlled by changes in percent carbonate.

The initial age model for each site was based on correlation of the polarity zone sequence to the timescale of Cande and Kent (1995). Power spectra using the Blackman-Tukey method with a Bartlett window from the Analyseries software of Paillard et al. (1996) indicate the presence of obliquity and eccentricity peaks. The reflectance data were then tuned to the astronomic solutions for obliquity from Laskar et al. (1993). This allowed astronomically calibrated ages to be assigned to the polarity reversal boundaries at Sites 1207, 1208, 1209, 1210 and 1211. Site 1212 was not included in the astrochronology, as it contains a hiatus at 4- to 5-Ma.

### **Magnetostratigraphic Interpretation**

Site 1207 is the only site that has been drilled on the Northern High of Shatsky Rise. The sequence of sediment recovered was mostly Neogene in age (0-163.8 mbsf) underlain by Campanian and older oozes and cherts. The sediment consists of nannofossil ooze with diatoms, radiolarians, and clay in varying amounts (Bralower, Premoli Silva, Malone et al., 2002). The samples taken for paleomagnetic analysis were AF demagnetized in 5-mT steps up to either 50,



60, or 70 mT, depending on the intensity of the natural remanent magnetization (NRM). Less than 10% of the NRM remains after demagnetization at these peak fields, indicating a low-coercivity remanence carrier, most likely magnetite. Orthogonal projections of demagnetization data (Figure 2-2) show well-defined components for most of the Neogene section after removal of the steep drilling related overprint at peak AF fields of 20 mT. Maximum angular deviation (MAD) values are low for most of the section ( $< 10^\circ$ ), indicating well-defined characteristic magnetization components; however, some intervals, particularly the interval between 50-60 mbsf (Figure 2-3), have slightly higher MAD values and less well-defined components. The interpretation of the magnetic stratigraphy from shipboard and discrete sample data can be accomplished by polarity zone pattern fit to the GPTS (Cande and Kent, 1992, 1995) (Table 2-2). This pattern fit is satisfactory to the base of Subchron C5An.1n (Figures 2-3, 2-4). Below the polarity zone equivalent to Subchron C5An.1n, recovery was intermittent and biostratigraphy indicates a hiatus with Campanian age sediments below (Bralower, Premoli Silva, Malone et al., 2002). Sedimentation rates average 1-2 cm/k.y. throughout the section with some slightly higher (3-4 cm/k.y.) rates in the late Pliocene and late Miocene (Figure 2-5A). Component declination has been corrected for each core using Tensor orientation data measured shipboard. The mean inclination in normal polarity zones for the Site is  $57.8^\circ$ , close to the expected inclination of  $56^\circ$  for a geocentric axial dipole at this site; however, reversed polarity intervals have a mean inclination of  $-51.1^\circ$ , shallower than expected. This can be attributed to shallowing of reversed polarity directions by the steep downward-directed drilling overprint, shown clearly in the orthogonal projections (Figure 2-2A).

Sites 1209, 1210, 1211, and 1212 are located on the southern high of Shatsky Rise (Figure 2-1). Multiple holes were drilled at each site and composite sections were constructed

using shipboard MST data. Discrete sample cubes were only collected from Holes 1209A, 1210A, 1211A, and 1212A. The shipboard data from the pass-through magnetometer are consistent between the different holes at each site and confirms the interpretation of the magnetic stratigraphy (see Shipboard Scientific Party, 2002).

As for Site 1207, orthogonal projections from discrete sample data show two components:- a steep downward drilling related overprint and well-defined characteristic components (Figure 2-2 B, C, D, E). In most cases the drilling related overprint was easily removed in peak AF fields of 10-20 mT. Little of the natural remanent magnetization remained at peak fields of 60 mT. MAD values are generally  $<5^\circ$  throughout the sections. The expected inclination for the Southern Rise is  $51^\circ$ ; again, all the sites show slightly steeper than expected inclinations in normal polarity zones and shallower than expected inclination in reversed polarity zones. The magnetostratigraphic age models indicate mean sedimentation rates between 1- and 3 cm/k.y. for most of the Neogene (Figure 2-5 B, C, D, E).

The polarity interpretation at Sites 1209, 1210, and 1211 is unambiguous back to Subchron C3Bn (Table 2-2) (Figures 2-6, 2-7, 2-8). Below this level, interpretation becomes difficult due to decreasing sedimentation rates leading to a hiatus recognized at all sites between the upper Miocene, and Oligocene and older sequences. At Site 1212, a hiatus accounts for the interval between 4 and 5 Ma (Chron C3), and the polarity interpretation can be accomplished to Subchron C4n.2n (Figure 2-9). This interpretation of the sequence of polarity zones is confirmed by the shipboard biostratigraphy. The interpretation of the polarity stratigraphy was carried out using data measured shipboard augmented with discrete sample cubes. When the magnetostratigraphic data were placed on the composite depth scale, the reversal boundaries were found to be consistent between holes, indicating that there is very little error in the depths

of polarity zone boundaries or in composite depth calculations. The magnetic measurements made shipboard do include a small amount of error due to the response function of the shipboard magnetometer. The response function of the wide-access magnetometer used to measure half-cores is ~10 cm, resulting in a cm-scale uncertainty in the placement of the reversal boundaries.

Site 1208 is located on the Central High of Shatsky Rise and also provided an expanded late Miocene to Holocene section. The magnetic stratigraphy from Site 1208 will be presented in Chapter 3.

### **Astrochronology**

Cycles were visually identifiable in  $L^*$  reflectance data from all six of the sites in this study. For Sites 1209, 1210, and 1211, we worked with spliced composite records rather than data from a single hole. Reflectance data were initially placed on the magnetostratigraphic age model based on the polarity timescale of Cande and Kent (1995). Power spectra for untuned sections of reflectance data placed on this age model consistently show a concentration of power at orbital frequencies, particularly around the 41 k.y. obliquity cycle (Figure 2-10).

The reflectance records were then tuned to the astronomical solution for obliquity from Laskar et al. (1993), as this was the most visually identifiable cycle in the reflectance data and the power spectra for different time intervals in all the sites showed a concentration of power at the obliquity frequency (Figure 2-10). In constructing the astrochronological age model, we assume that there was no phase lag between the orbital forcing and the response. For convenience, the reflectance data were broken up into 1 Myr intervals when compared to the astronomical solution and each site was tuned independently. Cycles were readily apparent in the reflectance data for all sites, and tuning of the record required a minimum of adjustment of peaks in the reflectance data to the astronomical solution (Figures 2-11, 2-12, 2-13, 2-14).

Astronomically tuned ages were calculated for polarity reversals in the 1 to 8-Ma interval at Site

1207 (Table 2-3). At Site 1209, tuning was performed in the 1 to 7-Ma interval and at Sites 1210 and 1211 in the 1 to 5-Ma interval. Site 1208 has also provided an astrochronological age model for the 1 to 6-Ma interval (Figure 2-12) and is included in Table 3. The tuned age models are compared to each other (Table 2-3) and are compared with other recently published astrochronologies for this time period (Table 2-4). The output of a band-pass filter centered on 41 k.y. is shown below the astronomical solution for obliquity and the raw reflectance data in Figures 2-11, 2-12, 2-13, 2-14, and 2-15.

To test the validity of the timescale we used cross-spectral analysis performed using the Blackman-Tukey method and Analyseries software (Paillard et al., 1996). Coherence between the reflectance data and the astronomical solution for obliquity was significant at all the sites, although the coherence values depend on which time interval is being examined. At Site 1207 coherence was  $\sim 0.8$  for the 1.2 to 1.8-Ma and 6.2 to 6.8-Ma intervals (Figure 2-16A). The coherence values at Site 1208 were  $> 0.8$  for the entire 1 to 6-Ma interval. Sites 1209, 1210, and 1211 also showed coherence values between 0.8 and 1 (Figure 2-16C, 2-16D, 2-16E).

## **Discussion**

Comparison of the tuned ages for polarity reversal boundaries at the five sites in the 1.5 to 2-Ma interval showed that polarity chron ages are in good agreement. For other time intervals there are some significant differences (more than an obliquity cycle) between sites (Table 2-3). Intervals with enhanced 41 k.y. power in reflectance data are considered more reliable (*italics in Table 2-3*). Site 1208 showed the strongest cyclicity, with Site 1207 also showing a clear signal in some intervals particularly the 2.1 to 2.7-Ma and 4.5 to 5-Ma intervals.

During ODP Leg 138 to the eastern equatorial Pacific, 11 sites were drilled and most of them showed a prominent cyclicity in GRA density. Shackleton et al. (1995) used these cycles in GRA bulk density records to produce an orbitally-tuned age model for the 0 to 12.5-Ma interval.

They worked entirely in the time domain comparing smoothed GRA bulk density records with the target record of summer insolation at 65°N. In their tuning they assumed that no phase lag existed between insolation and GRA bulk density controlled by proportion of SiO<sub>2</sub> and CaCO<sub>3</sub> (high density), high carbonate content being associated with high Northern Hemisphere insolation. Age control points were added to the data to align prominent groups of density maxima. The records were broken into 0.8-m.y. intervals for convenient viewing. Each site was tuned independently over the chosen time interval. Shackleton et al. (1995) found that some intervals in these records were more easily tuned than others, similar to results from Leg 198. Shackleton et al. (1995) noted that it was difficult to tune the 0- to 1-Ma interval, which was also the case at four of the Leg 198 Sites (1208, 1209, 1210, and 1211). The 1- to 2-Ma interval for the Leg 138 sites carries a clear 41 k.y. obliquity cycle. For Leg 198 sites, the 1.2- to 1.6-Ma interval also carries a very clear obliquity cycle (Figures 2-11, 2-12, 2-13, 2-14, 2-15). In the 2.4- to 2.6-Ma interval, a very strong obliquity cycle was observed at Site 846 (Leg 138), and this same interval also carries a strong 41 k.y. signal at Sites 1209, 1210, and 1211. Comparison between the Site 1207 age model and ages from Shackleton et al. (1995) indicate consistency for the 1-to 8-Ma time interval (Table 2-4).

Hilgen et al. (1995) developed an astronomical timescale for the interval from 3- to 9.7-Ma using lithologic cyclicity seen in sedimentary sections in the Mediterranean. These sections comprise open marine sediments that alternate between carbonate-rich and carbonate-poor marls or homogeneous marls and sapropels. The individual sapropels were related to precession minima, and the clusters of sapropels to the 400-k.y. eccentricity cycles. In tuning the section, the target curve used was the 65°N summer insolation curve. To obtain an astronomical age for the youngest polarity reversal in the sequence, Hilgen et al. (1995) took the Shackleton et al.

(1995) age for the onset of Subchron C3An.2n of 6.576 Ma. They then matched the lithologic cycles in the section to the astronomical solution using the correlation of sapropel clusters to eccentricity. The age of the calibration point (6.576 Ma) had to be adjusted to 100 k.y. older to establish a consistent correlation between sapropel clusters and eccentricity maxima. The ages from Hilgen et al. (1995) differ significantly with those from Leg 198 in the 6-to 8-Ma interval (Table 4). At the top of Subchron C3Bn the difference is more than 200 k.y. In the interval from 7.2- to 8.1-Ma, the difference is ~ 100 k.y. which is the amount of adjustment of the 6.576-Ma tie point used by Hilgen et al. (1995) for the age of the youngest polarity reversal in their section.

ODP Site 926 on the Ceara Rise also produced an orbitally tuned timescale from 5- to 14-Ma (Shackleton and Crowhurst, 1997). This timescale cannot be directly compared with the Leg 198 timescale because of a lack of polarity reversals at Site 926. Backman and Raffi (1997) used the cyclostratigraphic age model from Site 926 to calibrate ages of the calcareous nannofossil datums for the late Miocene. These ages were then compared with the biomagnetochronology from Site 853 (ODP Leg 138). The center of the peak in abundance of transitional morphotypes of *Triquetrorhabdulus rugosus* at Site 853 occurred 120-130 k.y. after the corresponding peak at Site 926. The age estimates of Hilgen et al. (1995) were then applied to the Site 853 data and the peak center was found to coincide at Sites 853 and 926. Therefore, Backman and Raffi (1997) considered that the Hilgen et al. (1995) ages are more reliable in this interval than the ages of Shackleton et al. (1995).

Lourens et al. (2004) have recalibrated the Miocene astronomic timescales of Shackleton and Crowhurst (1997) and Hilgen et al. (1995) using the astronomic solution of Laskar et al. (2004). For the last 13 Ma the retuning resulted in almost negligible changes in the ages of reversal boundaries (Lourens et al., 2004). For the 6- to 8- Ma interval the ATNTS2004 is in

close agreement with that of Hilgen et al (1995) and therefore differs significantly with the results of this study.

### **Conclusions**

Five sites from Shatsky Rise have produced high-quality magnetic stratigraphies from the late Miocene to Holocene. Cycles identified in reflectance data from Sites 1207, 1208, 1209, 1210, and 1211 have allowed astronomic calibration of the polarity reversal sequence from ~8 Ma to present. The assumption that there is no phase lag between sedimentary cyclicity and the astronomical parameters allowed the cycles to be tuned to the astronomical solution for obliquity. Cross-spectral analysis on the tuned age model indicated high coherence between the astronomic solution and the reflectance data and confirms the reliability of the tuning. The age model has been compared with other published astrochronologies and is found to be in good agreement with Hilgen (1991a, 1991b) (and, therefore, Cande and Kent [1995]) in the 1-to 6-Ma interval. In the 6-to 8-Ma interval the age model differs significantly from that of Lourens et al. (in press) and Hilgen et al. (1995) from the Mediterranean. It is in better agreement with the ODP Leg 138 timescale of Shackleton et al. (1995) from the Pacific Ocean.

Table 2-1. Latitude, longitude, water depth, the oldest Neogene magnetic polarity chron identified, and the basal age of the Neogene section.

Site	Latitude	Longitude	Water depth	Basal Chron	Basal Age (Ma)
1207	37°47.4287' N	162°45.0530'E	3100m	C5An2n	12.184
1209	32° 39.1001'N	158°30.3560'E	2387m	C3Bn	7.091
1210	32° 13.4123'N	158°15.5618'E	2573m	C3Bn	7.091
1211	32° 0.1300'N	157°50.9999'E	2907m	C3Bn	7.091
1212	32° 26.9000'N	157°42.7016'E	2682m	C4n.2n	8.072



Table 2-2. Magnetostratigraphic age model for Sites 1207, 1209, 1210, 1211 and 1212. Polarity chron labels are according to Cande and Kent (1992, 1995). Ages of chrons are from Cande and Kent (1995). Depths are in meters below sea floor (mbsf) for Site 1207 and meters composite depth (mcd) for Site 1209, 1210, 1211 and 1212.

Chron	Ma (CK95)	1207 (mbsf)	1209 (mcd)	1210 (mcd)	1211 (mcd)	1212 (mcd)
C1n	0.00	0.00	0.00	0.00	0.00	0.00
base	0.780	12.35	11.28	14.89	8.00	11.95
C1r.1n	0.990	16.26	13.32	18.07	9.550	14.12
base	1.070	16.77	14.22	19.71	10.27	14.98
C2n	1.770	24.38	25.28	32.03	16.74	23.62
base	1.950	28.40	28.21	34.70	18.38	25.78
C2r.1n	2.197	29.73		37.68	23.70	26.95
base	2.229	30.25		38.09	30.08	27.78
C2An.1n	2.581	43.13	37.69	46.51	30.90	32.61
base	3.040	51.77	49.43	56.88	32.34	39.00
C2An.2n	3.110	53.25		58.52	33.98	39.81
base	3.220	56.79		60.37	37.37	41.67
C2An.3n	3.330	58.77	52.34	61.81	41.17	43.00
base	3.580	66.91	58.03	67.35	42.51	48.68
C3n.1n	4.180	80.23	66.22	75.36	43.94	
base	4.290	83.34	68.23	77.62	44.66	
C3n.2n	4.480	87.19		80.90	46.92	
base	4.620	90.46		82.34	49.28	
C3n.3n	4.800	92.39	73.24	83.78	50.72	
base	4.890	94.32	74.08	85.42	51.70	
C3n.4n	4.980	96.84	75.59	86.45	52.69	
base	5.230	99.95	78.76	91.17	53.80	
C3An.1n	5.894	105.73	82.94	94.05	54.29	54.44
base	6.137	106.77	84.95	95.69	55.15	56.17
C3An.2n	6.269	109.29	86.12	97.02		58.31
base	6.567	114.18	90.13	99.12		59.14
C3Bn	6.935	116.56	93.81	100.35		59.88
base	7.091	120.41	96.15	101.46		61.03
C3Br.1n	7.135					61.60
base	7.170					63.58
C3Br.2n	7.341	123.08				64.57
base	7.375	123.53				65.14
C4n.1n	7.432	125.16				65.39
base	7.562	126.05				66.95
C4n.2n	7.650	126.34				67.37
base	8.072	129.01				70.00
C4r.1n	8.225	130.79				
base	8.257	132.27				
C4An	8.699	134.50				
base	9.025	136.72				
C4Ar.1n	9.23	137.76				
base	9.308	138.35				
C4Ar.2n	9.580	140.28				
base	9.642	140.72				
C5n.1n	9.740	141.32				
base	9.880	142.36				
C5n.2n	9.920	142.65				
base	10.949	151.40				
C5r.1n	11.052	153.62				
base	11.099	154.07				
C5r.2n	11.476	155.11				
base	11.531	155.40				
C5An.1n	11.935	157.81				
base	12.078	160.77				
C5An.2n	12.184	161.76				
base	12.401					

Table 2-3. Comparison of astrochronological age models for sites 1207, 1208, 1209, 1210 and 1211. Italics indicate the most reliable ages in intervals where the cyclicity in reflectance is best defined. In italics and brackets are the differences between tuned ages and those of Cande and Kent (1995).

Chron	Ka (CK95) (Hilgen 1991a,b)	Site 1207 Ka (difference)	Site 1208 Ka (difference)	Site 1209 Ka (difference)	Site 1210 Ka (difference)	Site 1211 Ka (difference)
C1n	0	0				
C1r.1r	780	776.7 (-3.3)				
C1r.1n	990	992.8 (2.8)				
C1r.2r	1070	1089.4 (19.4)	1073.9 (3.9)	1069.4 (-0.6)		
C2n	1770	1786.4 (16.4)	1776.2 (6.2)	1770.0 (0)	1777.8 (7.8)	1777.8 (7.8)
C2r.1r	1950	1954.2 (4.2)	1948.7 (-1.3)	1975.4 (25.4)	1972.2 (22.2)	1972.2 (22.2)
C2r.1n	2140	2095.7 (-44.3)	2133.5 (-6.5)			
C2r.2r	2150	2112.0 (-38)	2170.4 (20.4)			
C2An.1n	2581	2620.5 (39.5)	2564.7 (-16.3)	2550.3 (-30.7)	2642.7 (61.7)	2536.1 (-44.9)
C2An.1r	3040	3042.5 (2.5)	3045.2 (5.2)	3032.0 (-8)	3032.9 (-7.1)	3022.2 (-17.8)
C2An.2n	3110	3118.0 (8)	3105.8 (-4.2)		3114.9 (4.9)	3110.9 (0.9)
C2An.2r	3220	3236.5 (16.5)	3229.8 (9.8)		3248.5 (28.5)	3242.3 (22.3)
C2An.3n	3330	3354.5 (24.5)	3340.9 (10.9)	3361.4 (31.4)	3340.5 (10.5)	3352.8 (22.8)
C2Ar	3580	3593.3 (13.3)	3599.6 (19.6)	3648.8 (68.8)	3597.5 (17.5)	3644.4 (64.4)
C3n.1n	4180	4154.0 (-26)	4190.9 (10.9)	4172.5 (-7.5)	4182.8 (2.8)	4169.4 (-10.6)
C3n.1r	4290	4262.5 (-27.5)	4351.9 (61.9)	4305.9 (43.4)	4305.9 (15.9)	4305.6 (15.6)
C3n.2n	4480	4489.8 (9.8)	4523.6 (43.6)		4501.0 (21)	4457.9 (-22.1)
C3n.2r	4620	4637.0 (17)	4683.8 (63.8)		4665.3 (45.3)	4589.3 (-30.7)
C3n.3n	4800	4760.5 (-39.5)	4806.9 (6.9)	4809.0 (9)	4798.8 (-1.2)	
C3n.3r	4890	4857.3 (-32.7)	4880.9 (-9.1)	4880.9 (-9.1)	4891.2 (1.2)	
C3n.4n	4980	4972.5 (-7.5)	4991.8 (11.8)	4981.5 (1.5)	4973.3 (-6.7)	4950.7 (-29.3)
C3r	5230	5245.4 (15.4)	5201.2 (-28.8)	5240.2 (10.2)		
C3An.1n	5894	5886.0 (8)	5952.7 (58.7)	5915.8 (21.8)		
C3An.1r	6137	6143.0 (6)		6073.9 (36.9)		
C3An.2n	6269	6241.5 (-27.5)		6318.3 (49.3)		
C3Ar	6567	6526.2 (-40.8)		6548.3 (-18.7)		
C3Bn	6935	6878.0 (-57)		6971.3 (35.3)		
C3Br.1r	7091	7095.8 (4.8)		7027.7 (-63.3)		
C3Br.1n	7135					
C3Br.2r	7170					
C3Br.2n	7341	7348.2 (8.2)				
C3Br.3r	7375	7388.3 (13.3)				
C4n.1n	7432	7453.5 (3.5)				
C4n.1r	7562	7540.9 (-21.1)				
C4n.2n	7650	7634.1 (15.9)				
C4r.1r	8072	8038.0 (-34)				

Table 2-4. Astrochronological ages for Leg 198 compared to ages Hilgen (1991a, 1991b), Hilgen et al. (1995) and Shackleton et al. (1995). In italics and brackets are the differences between Leg 198 tuned ages and Hilgen et al. (1995) and Shackleton et al. (1995).

Chron	Ka (CK95) Hilgen (1991a,b)	Leg 198	Shackleton et al. (1995) (difference to 198)	Hilgen et al. (1995a) (difference to 198)
C1n	0			
base	780	776.7		
C1r.1n	990	992.8		
base	1070	1089.4		
C2n	1770	1786.4		
base	1950	1954.2		
C2r.1n	2140	2133.5		
base	2150	2170.4		
C2An.1n	2581	2564.7		
base	3040	3042.5	3046 (3.5)	
C2An.2n	3110	3118.0	3131 (13)	
base	3220	3236.5	3233 (-3.5)	
C2An.3n	3330	3354.5	3331 (-23.5)	
base	3580	3593.3	3594 (0.7)	
C3n.1n	4180	4190.9	4199 (8.1)	
base	4290	4351.9	4316 (-35.9)	
C3n.2n	4480	4523.6	4479 (-44.6)	
base	4620	4683.8	4623 (-60.8)	
C3n.3n	4800	4806.9	4781 (-25.9)	
base	4890	4880.9	4878 (-2.9)	
C3n.4n	4980	4972.5	4977 (4.5)	
base	5230	5201.2	5232 (30.8)	
C3An.1n	5894	5952.7	5875 (-77.7)	
base	6137	6143.0	6122 (-21)	
C3An.2n	6269	6241.5	6256 (14.5)	
base	6567	6526.2	6555 (28.8)	6677 (150.8)
C3Bn	6935	6878.0	6919 (41)	7101 (223)
base	7091	7095.8	7072 (-23.8)	7210 (114.2)
C3Br.1n	7135			7256
base	7170			7301
C3Br.2n	7341	7348.2		7455 (106.8)
base	7375	7388.3		7492 (103.7)
C4n.1n	7432	7453.5	7406 (-47.5)	7532 (78.5)
base	7562	7540.9	7533 (-7.9)	7644 (103.1)
C4n.2n	7650	7634.1	7618 (-16.1)	7697 (62.9)
base	8072	8038.0	8027 (-11)	8109 (71)

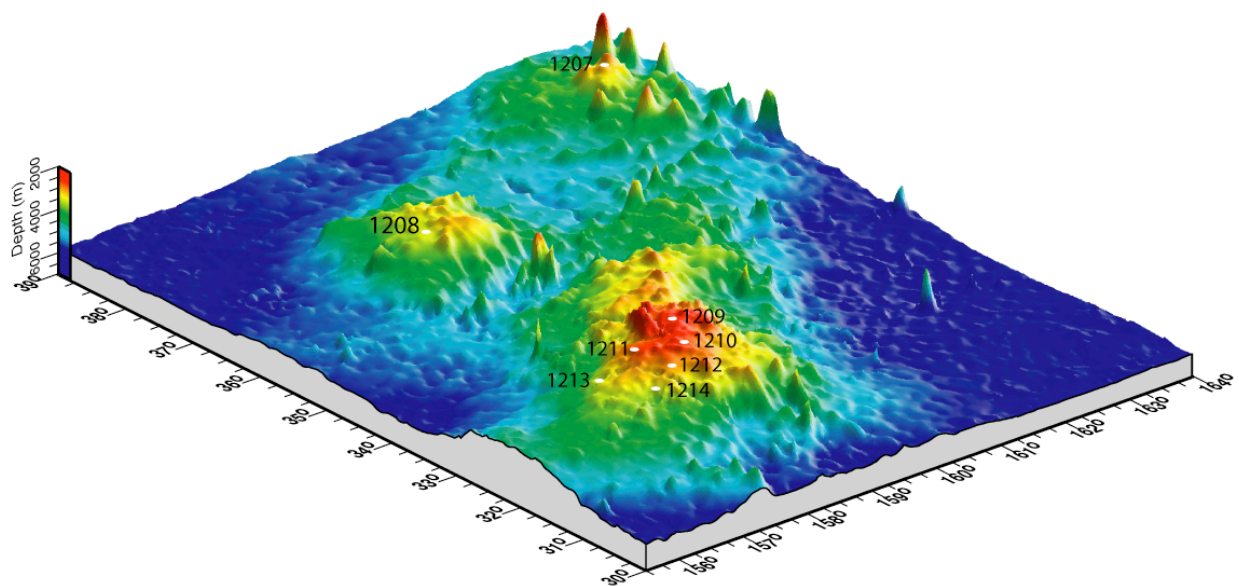


Figure 2-1. Bathymetric map of Shatsky Rise showing the location of sites drilled during ODP Leg 198.

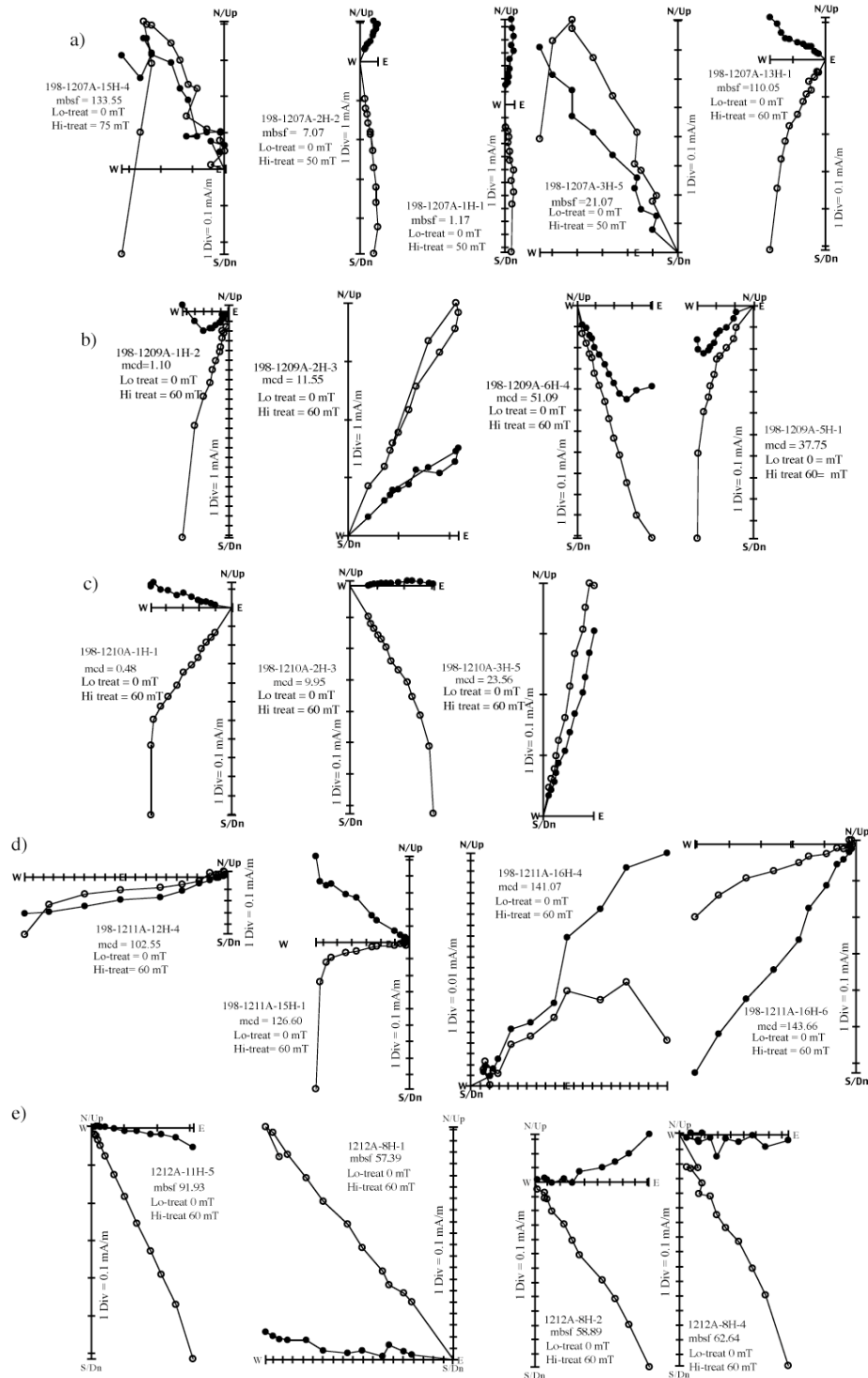


Figure 2-2. Representative orthogonal projections of AF demagnetization data from (A) Site 1207, (B) Site 1209, (C) Site 1210, (D) Site 1211 and (E) Site 1212. Low AF demagnetization treatment and the high treatment are given, as is mbsf or mcd of the sample. Open circles represent the vector end-point projection on the vertical plane, while closed circles represent the vector endpoint projection on the horizontal plane.

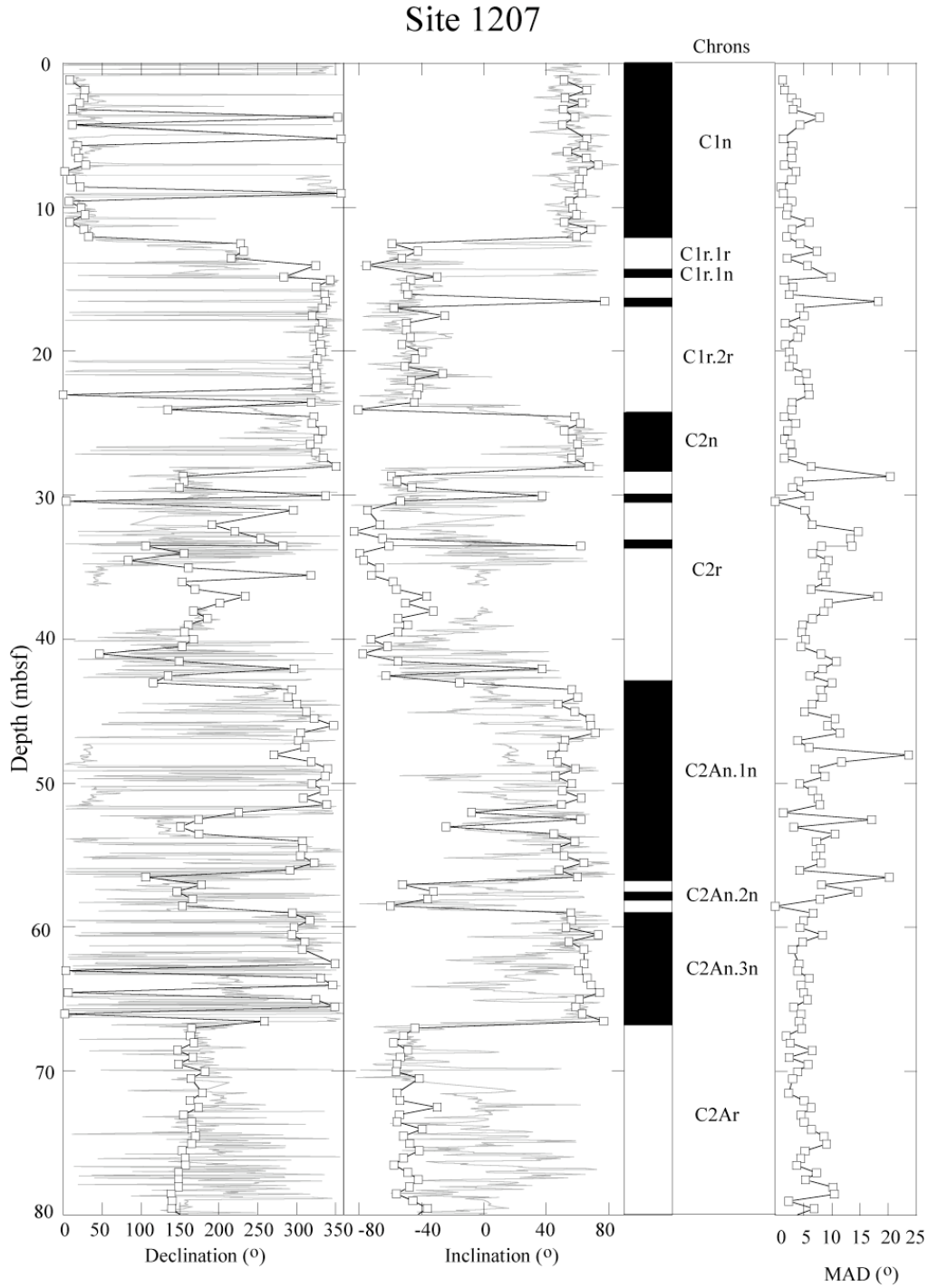


Figure 2-3. Site 1207 component inclination and declination from discrete samples (open squares) for 0-80 meters. Inclination and rotated declination from the shipboard pass-through magnetometer after AF demagnetization at peak fields of 20 mT (gray line). Chrons are labeled according to Cande and Kent (1992). Black indicates normal polarity, white reversed polarity. Also shown are the MAD values calculated for discrete sample data (after Kirschvink, 1980).

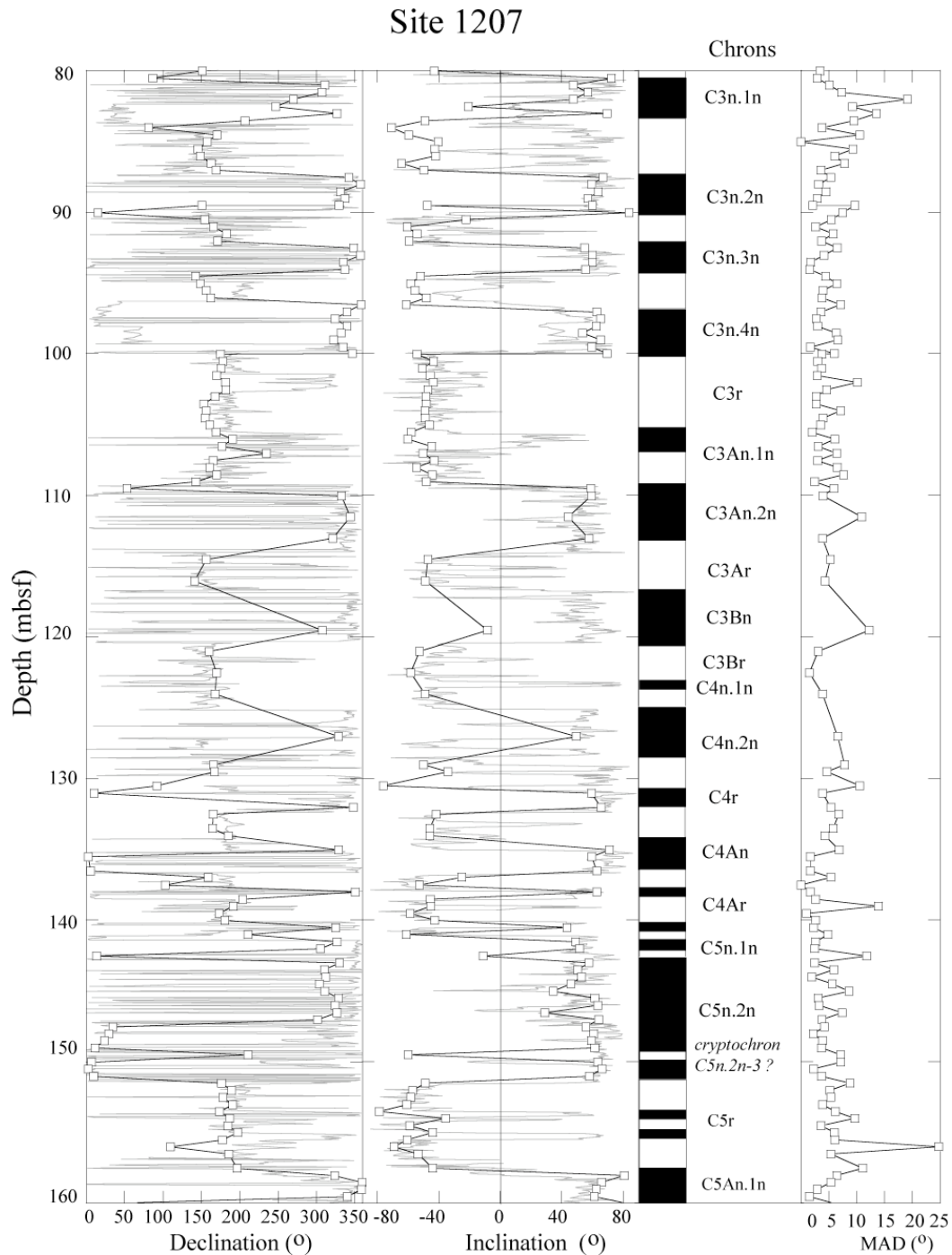


Figure 2-4. Site 1207 component inclination and declination from discrete samples (open squares) for 80-160 meters. Inclination and rotated declination from the shipboard pass-through magnetometer after AF demagnetization at peak fields of 20 mT (gray line). Chrons are labeled according to Cande and Kent (1992). Black indicates normal polarity, white reversed polarity. Also shown are the MAD values calculated for discrete sample data (after Kirschvink, 1980).

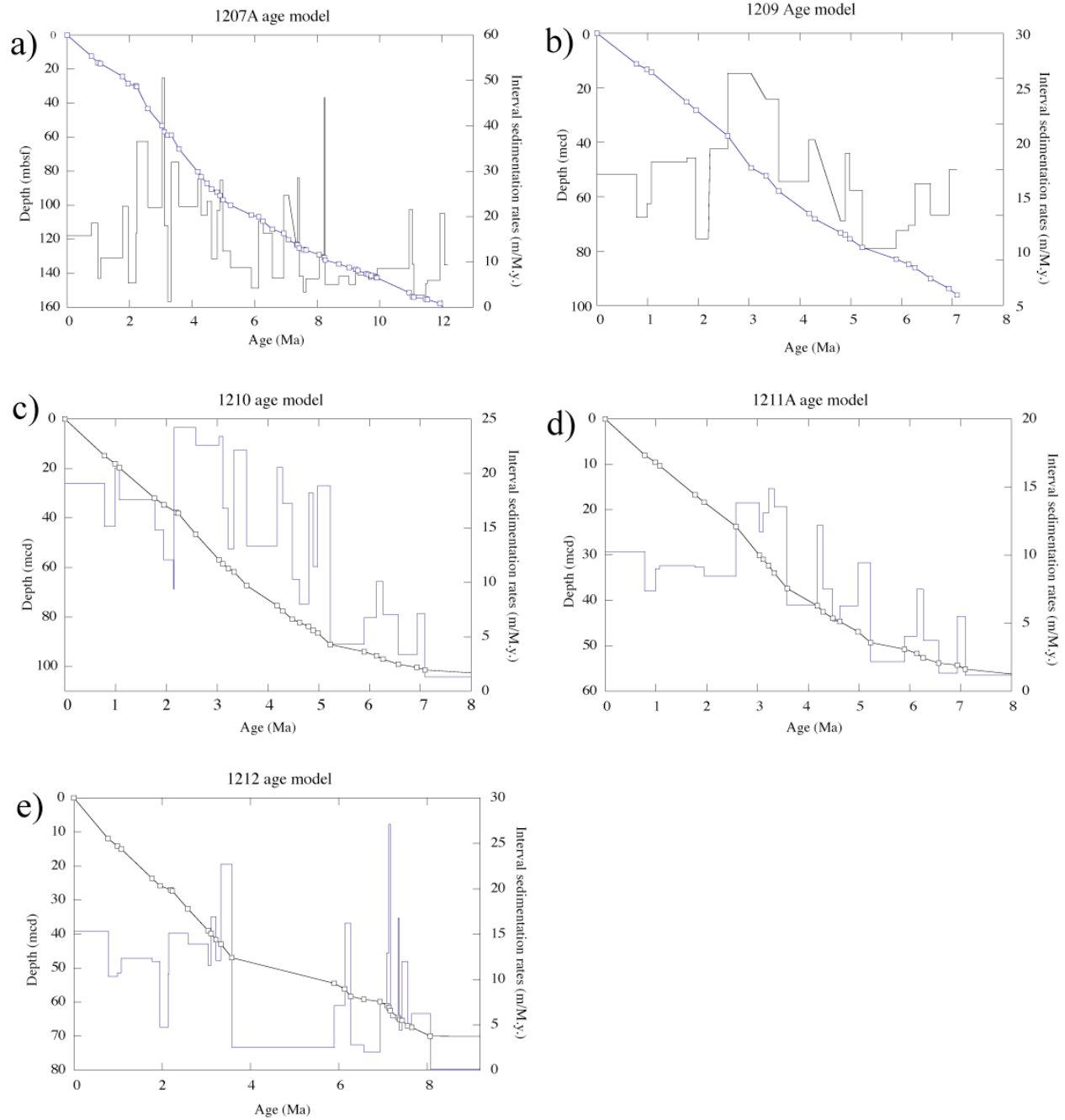


Figure 2-5. Interval sedimentation rates and age versus depth for the initial age model at a) Site 1207, b) Site 1209, c) Site 1210, d) Site 1211 and e) Site 1212.



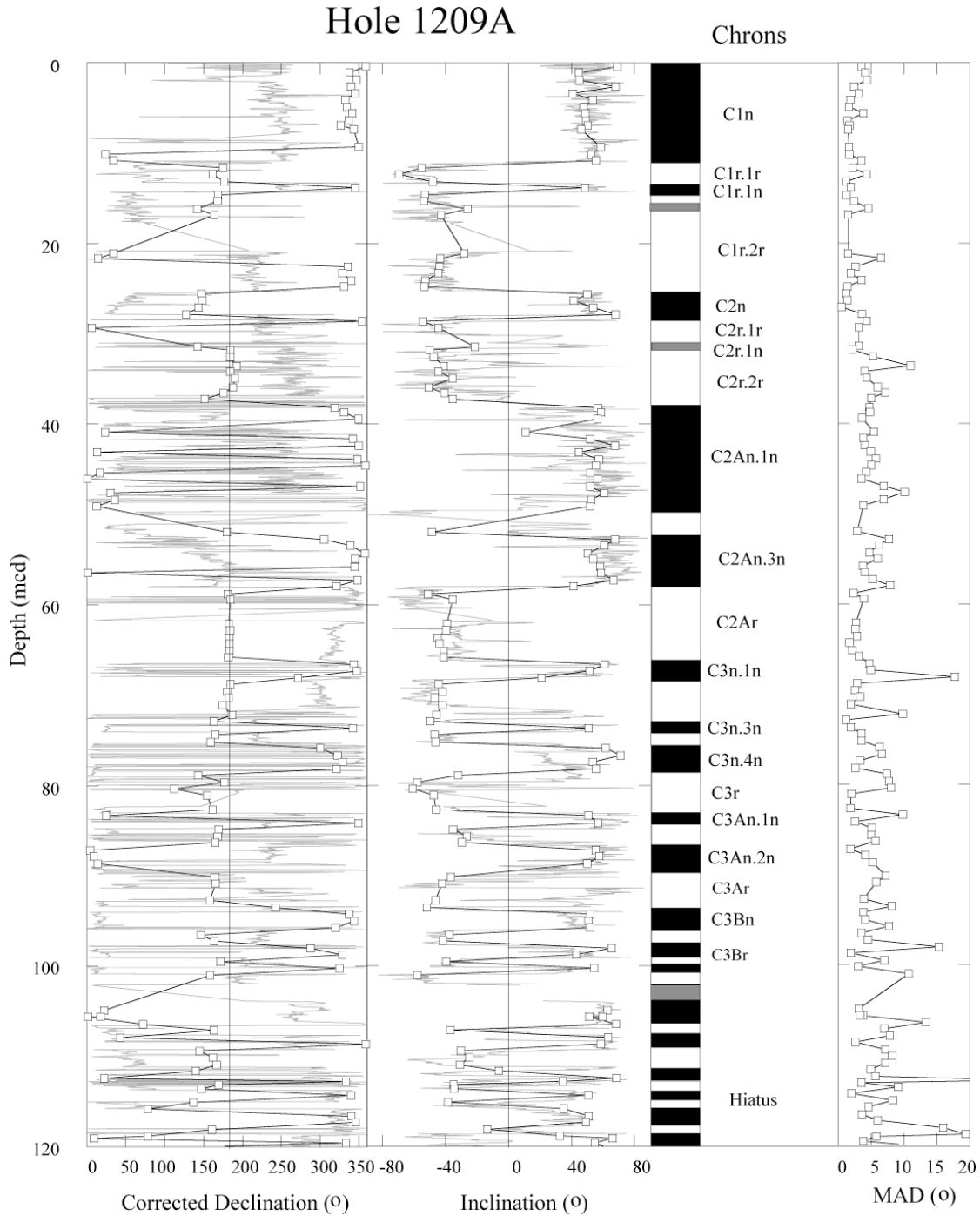


Figure 2-6. Site 1209 component inclination and declination from discrete samples (open squares). Inclination and rotated declination from the shipboard pass-through magnetometer after AF demagnetization at peak fields of 20 mT (gray line). Chrons are labeled according to Cande and Kent (1992). Black indicates normal polarity, white reverse polarity. Also shown are the MAD values calculated for discrete sample data (after Kirschvink, 1980).

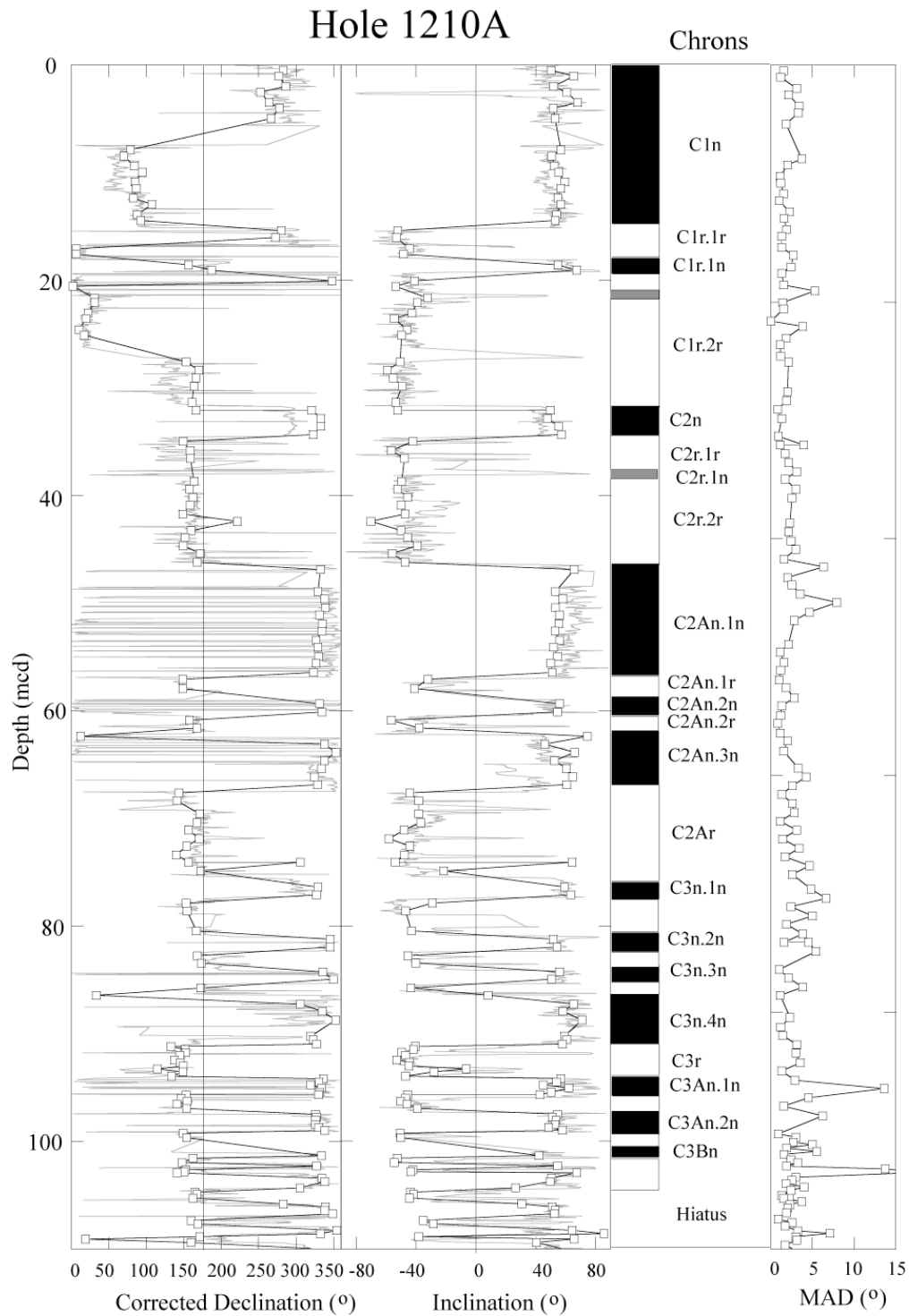


Figure 2-7. Site 1210 component inclination and declination from discrete samples (open squares). Inclination and rotated declination from the shipboard pass-through magnetometer after AF demagnetization at peak fields of 20 mT (gray line). Chrons are labeled according to Cande and Kent (1992). Black indicates normal polarity, white reverse polarity. Also shown are the MAD values calculated for discrete sample data (after Kirschvink, 1980).

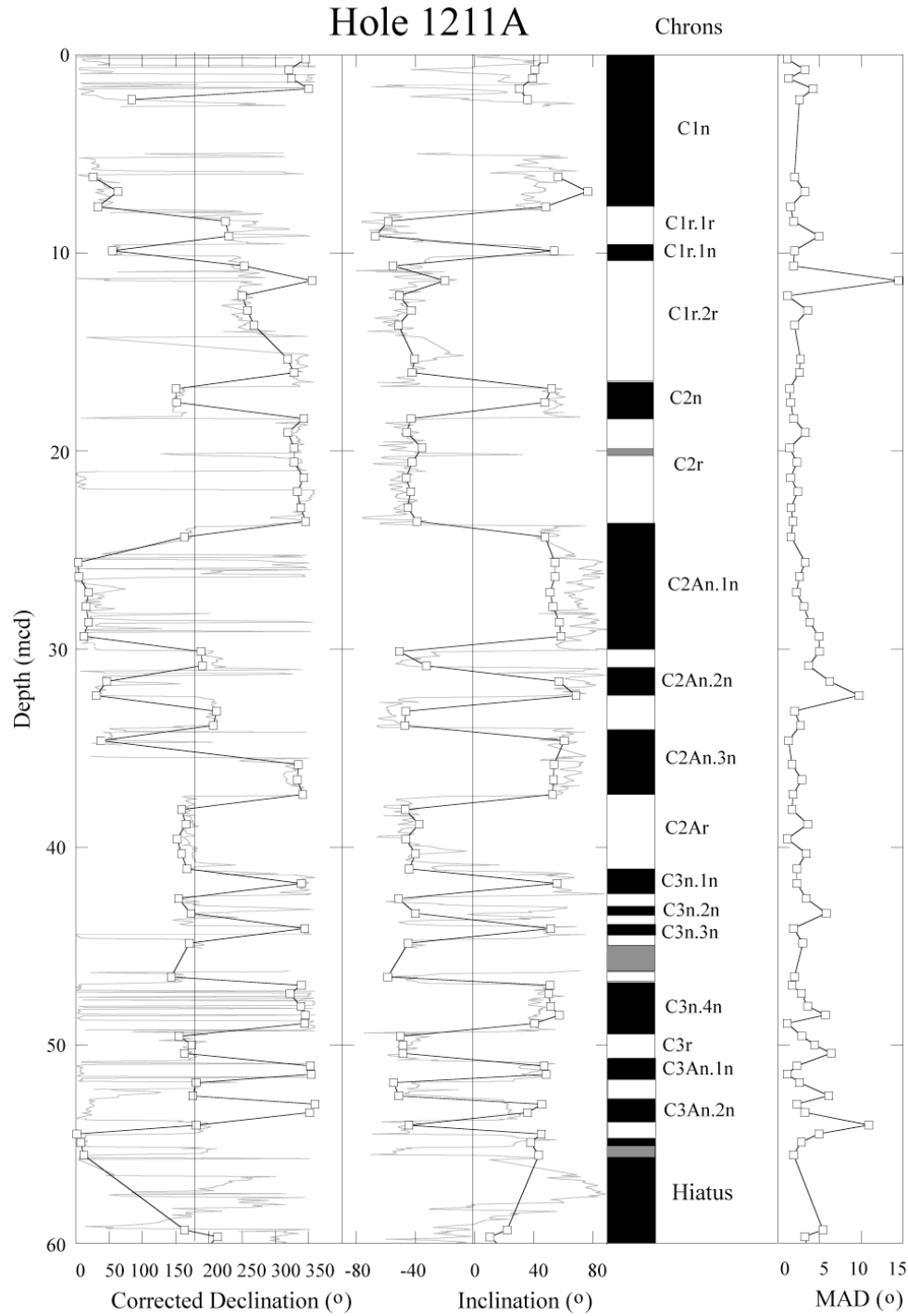


Figure 2-8. Site 1211 component inclination and declination from discrete samples (open squares). Inclination and rotated declination from the shipboard pass-through magnetometer after AF demagnetization at peak fields of 20 mT (gray line). Chrons are labeled according to Cande and Kent (1992). Black indicates normal polarity, white reverse polarity. Also shown are the MAD values calculated for discrete sample data (after Kirschvink, 1980).

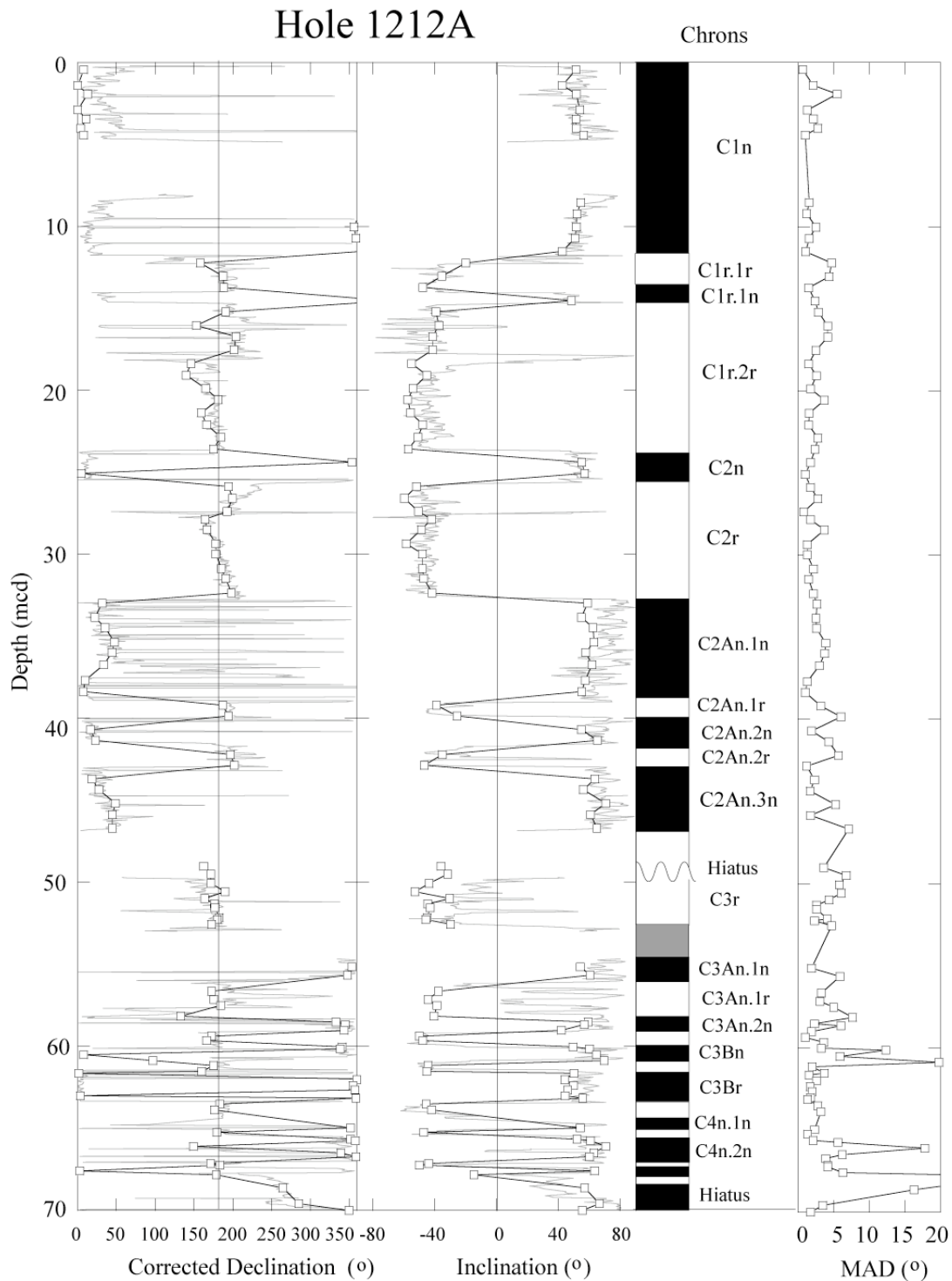


Figure 2-9. Site 1212 component inclination and declination from discrete samples (open squares). Inclination and rotated declination from the shipboard pass-through magnetometer after AF demagnetization at peak fields of 20 mT (gray line). Chrons are labeled according to Cande and Kent (1992). Black indicates normal polarity, white reverse polarity. Also shown are the MAD values calculated for discrete sample data (after Kirschvink, 1980).

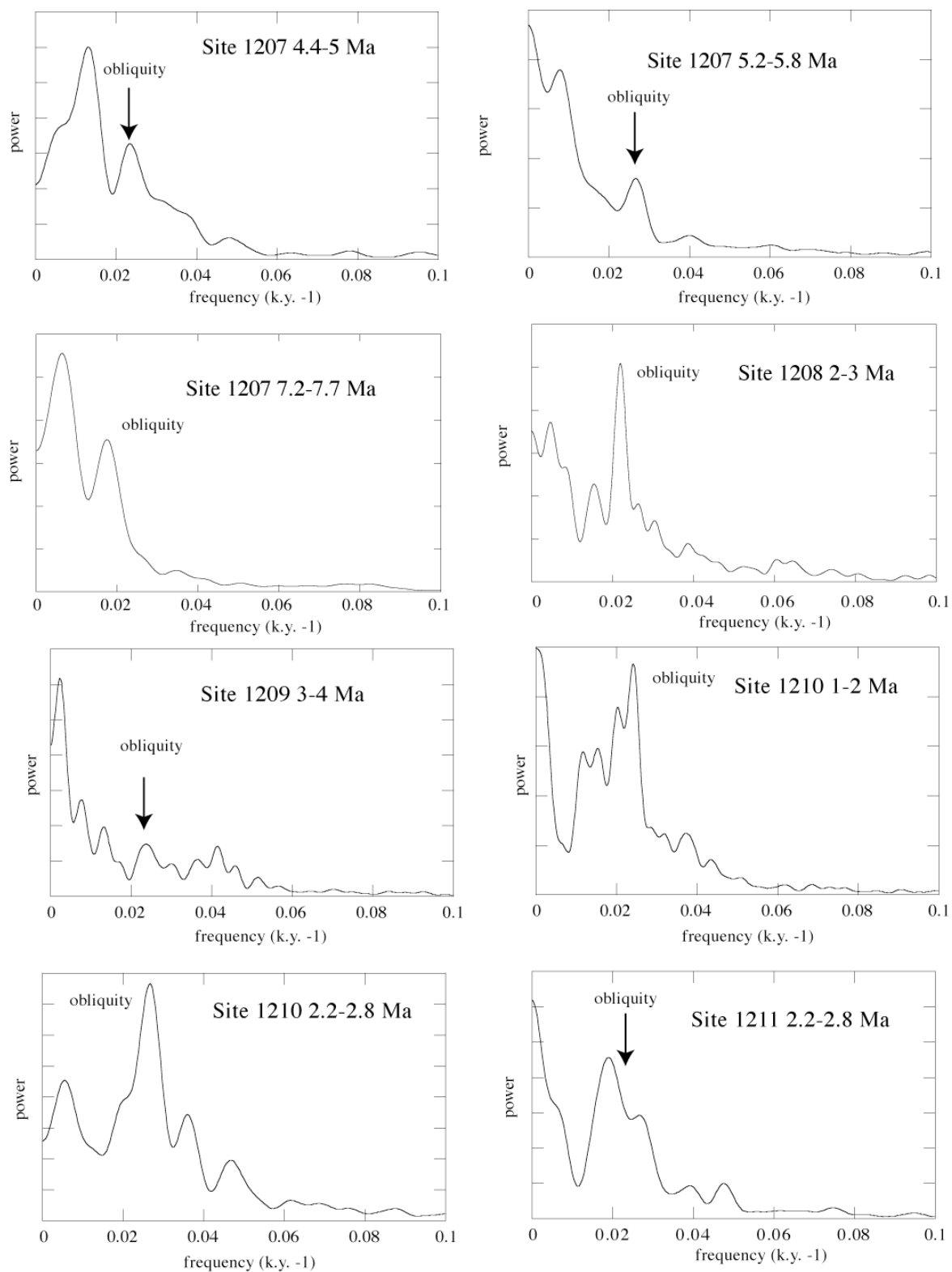


Figure 2-10. Power spectra from a) Site 1207, b) Site 1208 c) Site 1209, d) Site 1210, and e) Site 1211 for reflectance data placed on a Cande and Kent (1995) age model.

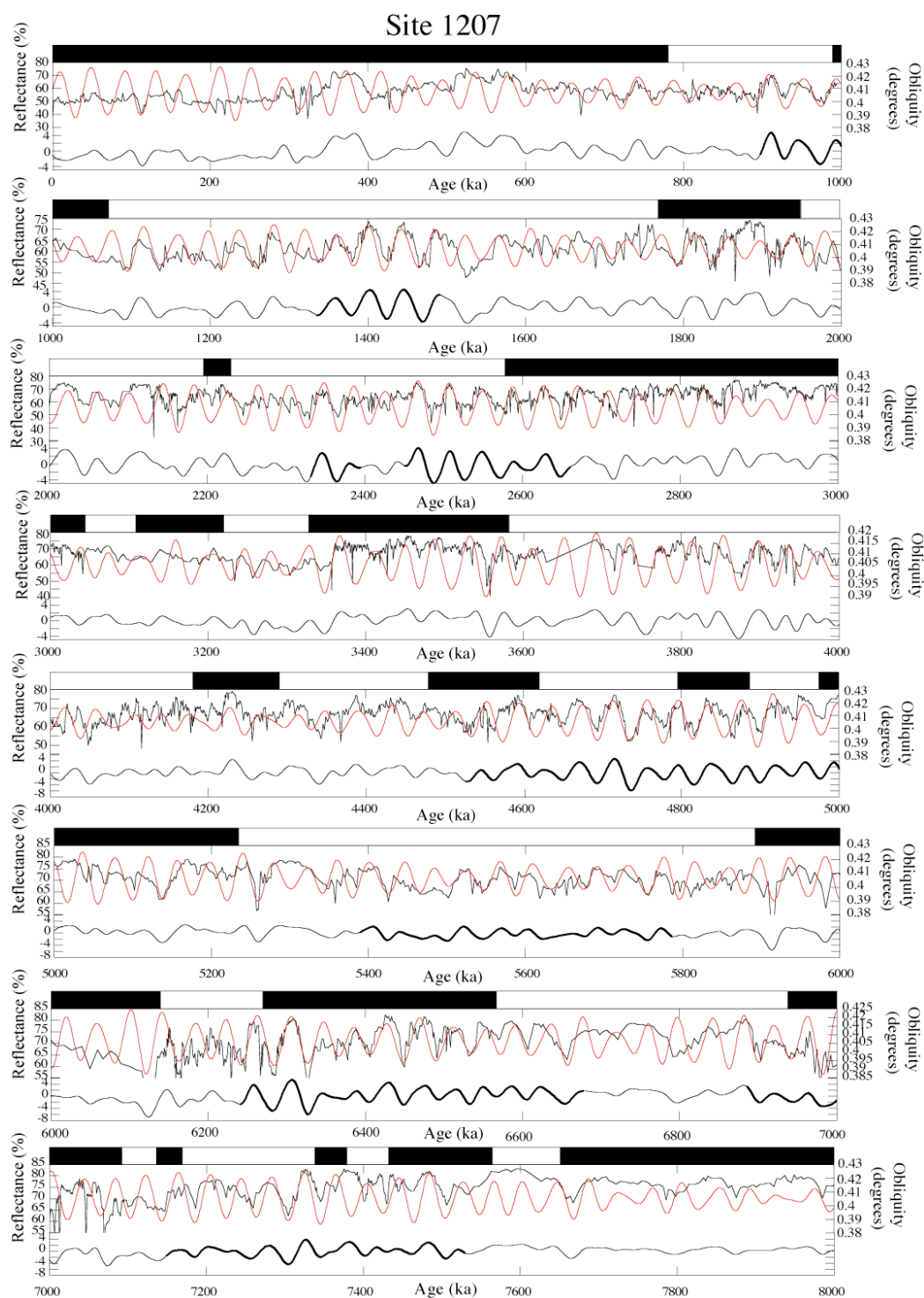


Figure 2-11. The astronomical solution for obliquity (Laskar et al., 1993) compared with tuned  $L^*$  reflectance data from Site 1207 for the 0-8 Ma interval. The reflectance data filtered using a band-pass filter centered on 41kys is shown in the lower part of each frame. Black indicates normal polarity and white reverse polarity. Heavy line on  $L^*$  reflectance data indicates intervals where the cyclicity is best developed.

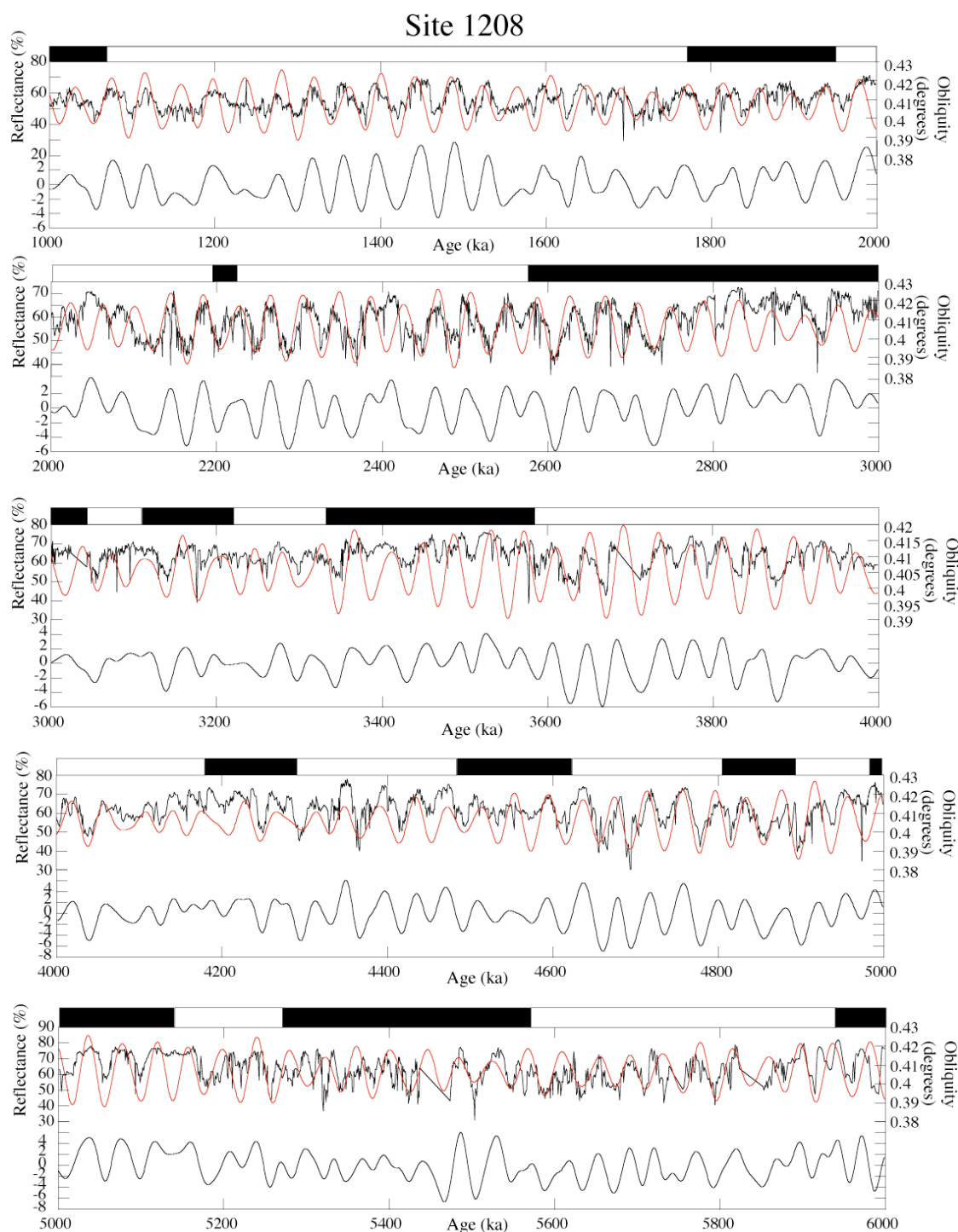


Figure 2-12. The astronomical solution for obliquity (Laskar et al., 1993) compared with tuned L\* reflectance data from Site 1208 for the 1-6 Ma interval. The reflectance data filtered using a band-pass filter centered on 41kyrs is shown in the lower part of each frame. Black indicates normal polarity and white reverse polarity. Heavy line on L\* reflectance data indicates intervals where the cyclicity is best developed.



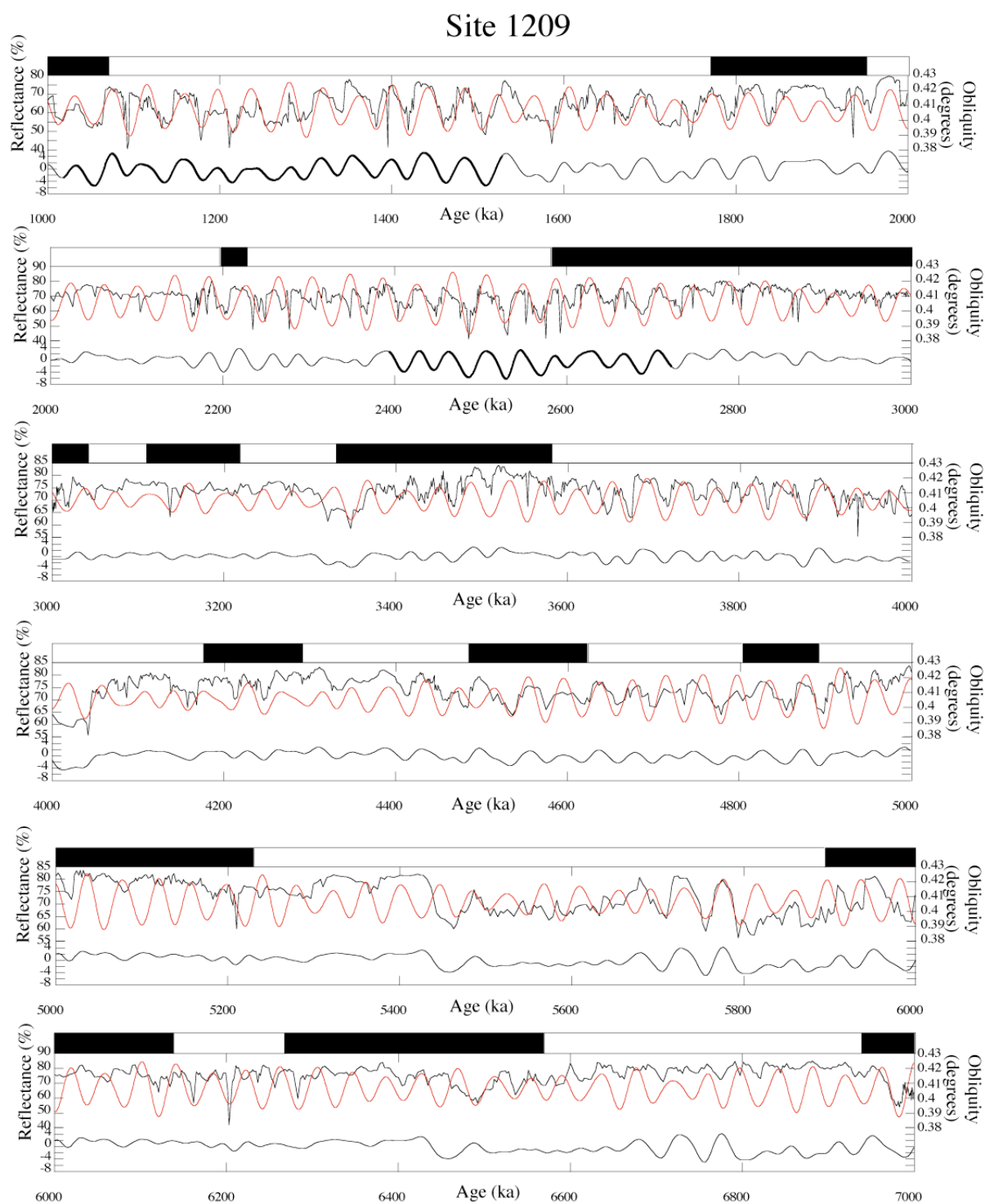


Figure 2-13. The astronomical solution for obliquity (Laskar et al., 1993) compared with tuned L\* reflectance data from Site 1209 for the 1-7 Ma interval. The reflectance data filtered using a band-pass filter centered on 41kyrs is shown in the lower part of each frame. Black indicates normal polarity and white reverse polarity. Heavy line on L\* reflectance data indicates intervals where the cyclicity is best developed.



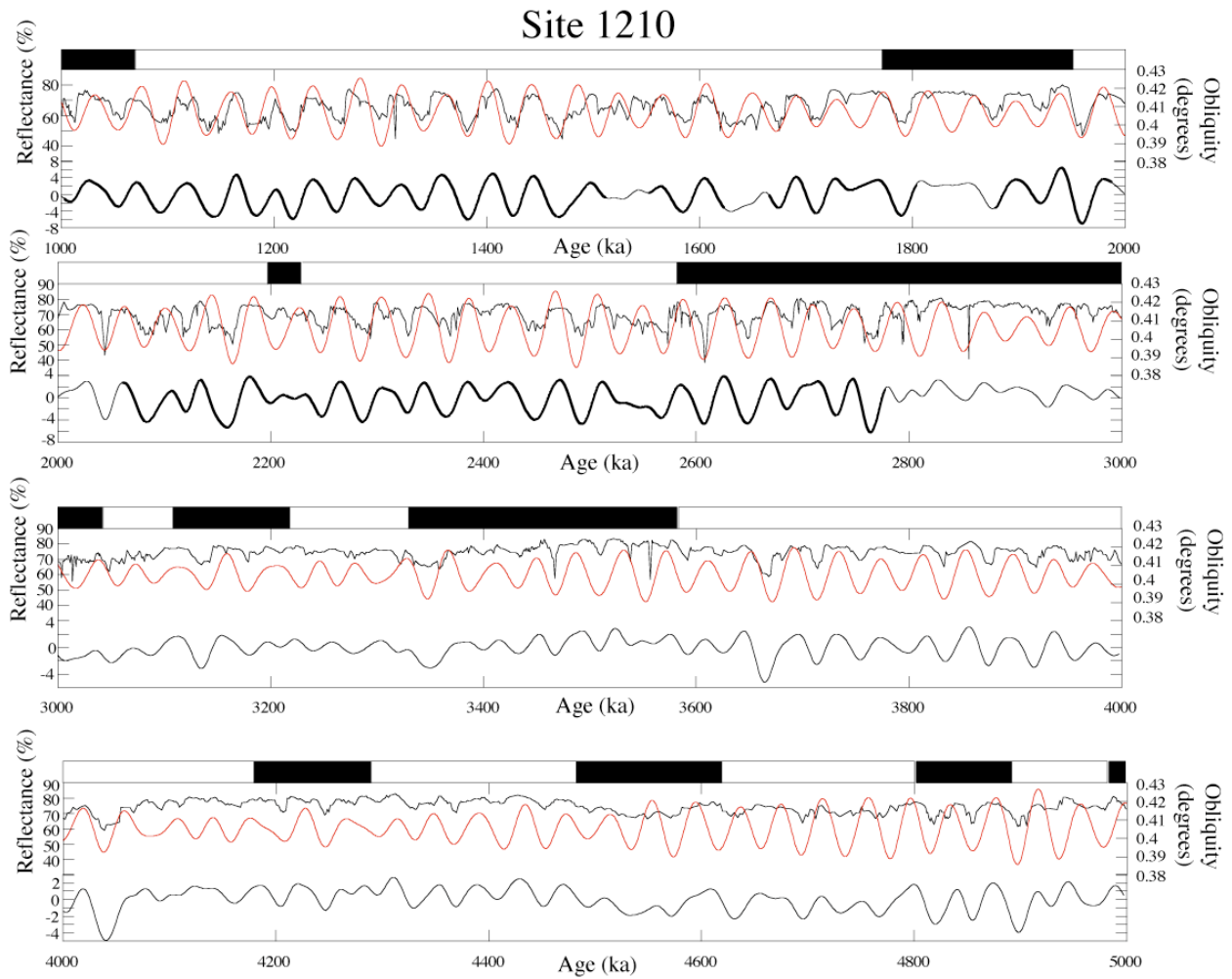


Figure 2-14. The astronomical solution for obliquity (Laskar et al., 1993) compared with tuned L\* reflectance data from Site 1210 for the 1-5 Ma interval. The reflectance data filtered using a band-pass filter centered on 41kyrs is shown in the lower part of each frame. Black indicates normal polarity and white reverse polarity. Heavy line on L\* reflectance data indicates intervals where the cyclicity is best developed.

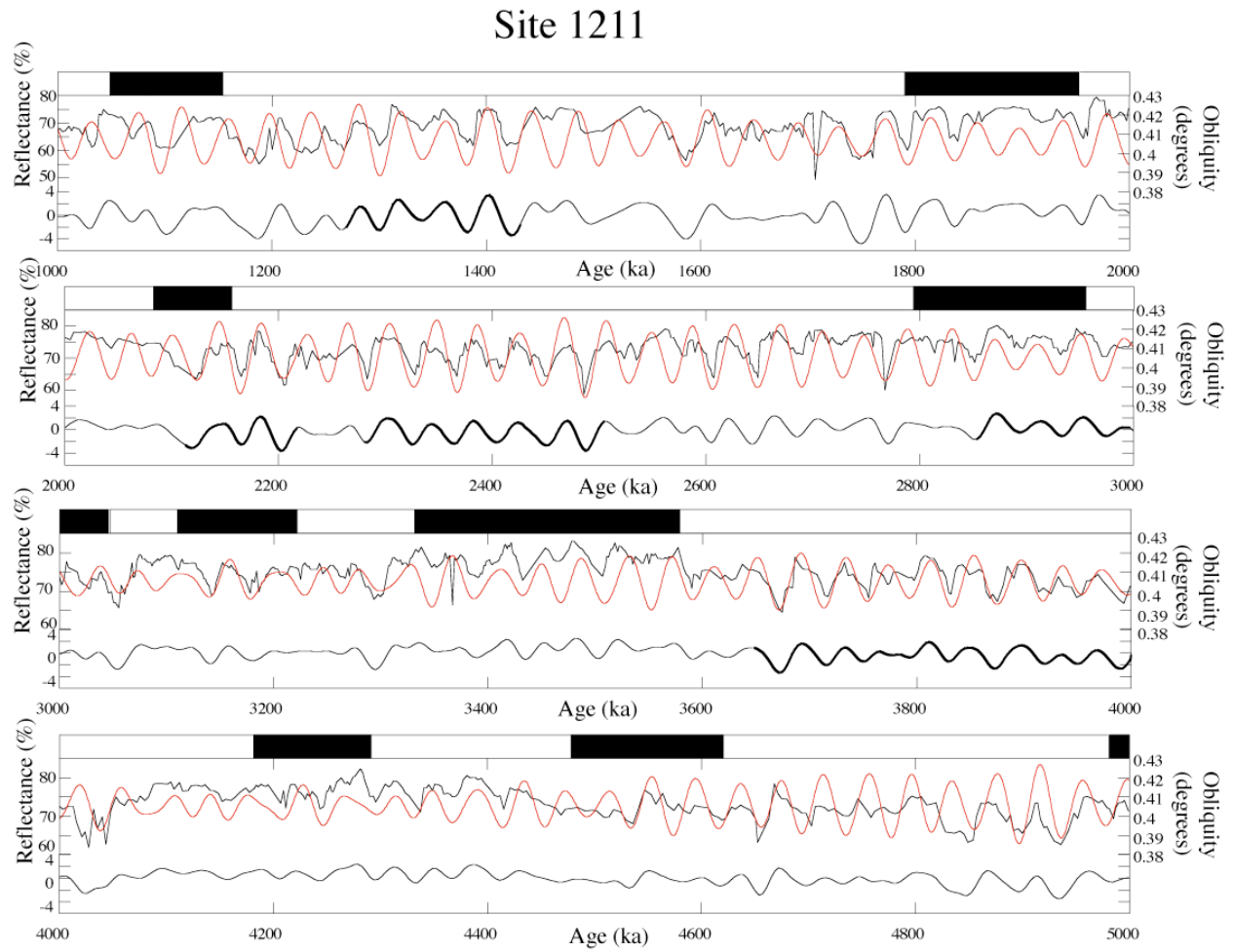


Figure 2-15. The astronomical solution for obliquity (Laskar et al., 1993) compared with tuned L\* reflectance data from Site 1211 for the 1-5 Ma interval. The reflectance data filtered using a band-pass filter centered on 41 kyrs is shown in the lower part of each frame. Black indicates normal polarity and white reverse polarity. Heavy line on L\* reflectance data indicates intervals where the cyclicity is best developed.

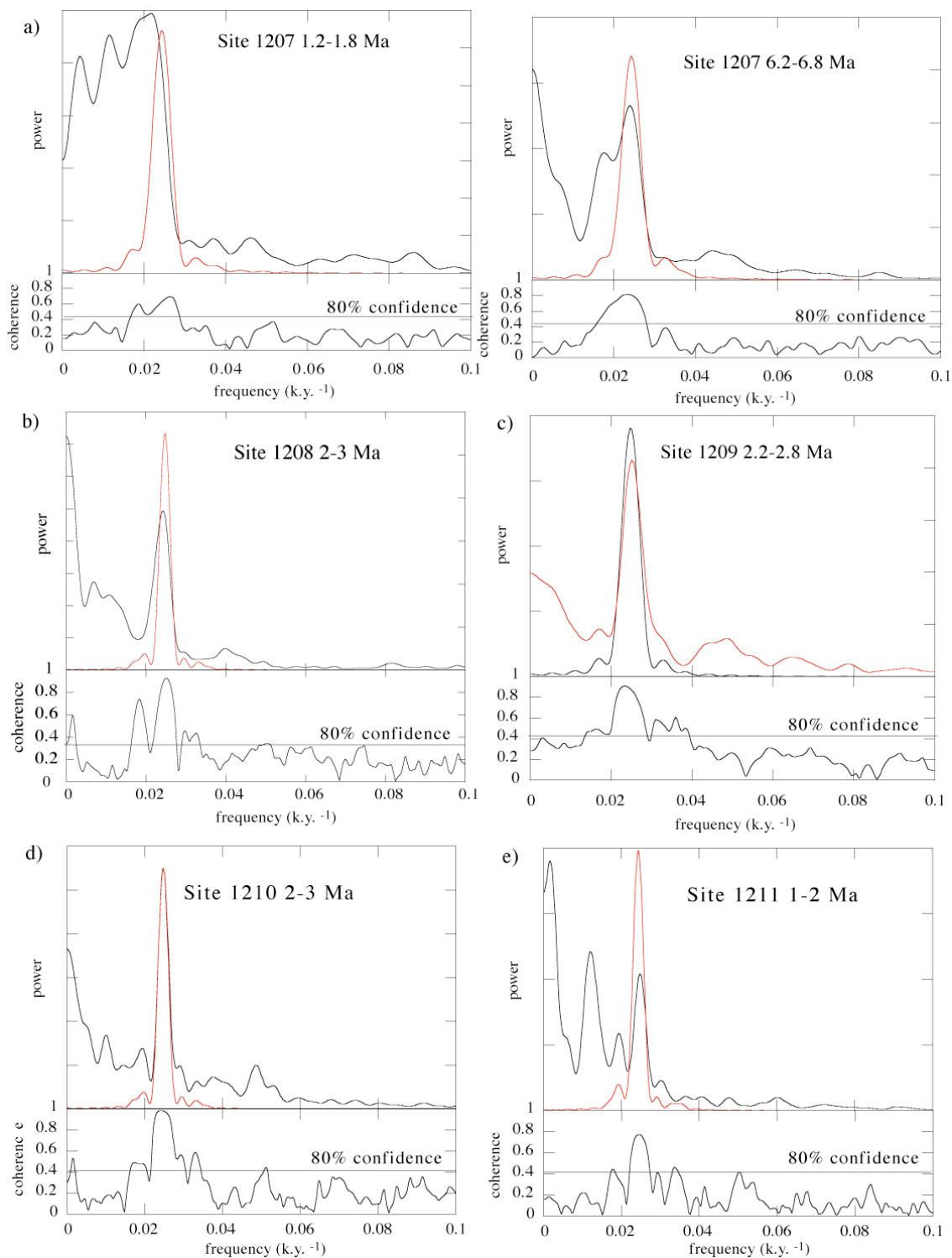


Figure 2-16. Cross-spectral analysis from a) Site 1207, b) Site 1208 c) Site 1209 d) Site 1210 and e) Site 1211. Power spectra for the tuned reflectance data (black) and for the astronomical solution for eccentricity and obliquity (red). Coherence values between the astronomical solutions and reflectance data are shown below.

# CHAPTER 3

## INTEGRATED NEOGENE MAGNETIC, CYCLE AND BIO- STRATIGRAPHY FROM ODP SITE 1208 (SHATSKY RISE, PACIFIC OCEAN)

### **Introduction**

ODP Site 1208 was drilled in 2001 on Shatsky Rise, a large igneous province in the NW Pacific Ocean. A single hole drilled at the site has produced a magnetic polarity stratigraphy for the 0-12 Ma interval. Sedimentation rates decrease from 4-5 cm/kyr in the Brunhes and Matuyama chrons to less than 1 cm/kyr at the base of the studied section. A revised planktonic foraminifer biostratigraphic zonation has been developed for the NW Pacific Ocean using the seventeen most isochronous foraminifer datums. This scheme has been integrated with nannofossil events, and with the magnetic stratigraphy. Cycles in the reflectance ( $L^*$ ) can be matched to astronomic solution for obliquity allowing astronomic calibration of polarity chron boundaries, and planktonic foraminifer and calcareous nannofossil datums. Astronomic ages for polarity chron boundaries are consistent with the ATNTS2004 timescale (Lourens et al., 2004) in the 1-5.2 Ma interval, however, between 5.2 and 6.2 Ma, astronomic ages from Site 1208 differ significantly (by  $\sim 300$  kyr) from the ATNTS2004 timescale.

As polarity reversals can be considered globally synchronous, the integration of polarity chron boundaries and biostratigraphies has become a powerful means of calibrating biostratigraphic zonations, and determining synchronicity of biostratigraphic events (see Berggren et al., 1995a,b). Early work on Neogene foraminifer biostratigraphy in the North Pacific Ocean on Deep Sea Drilling Project (DSDP) Sites 173, 296 and 310 (Keller, 1979a,b,c) was augmented by foraminifer and nannofossil work on ODP Leg 138 in the eastern equatorial Pacific (Raffi and Flores, 1995; Shackleton et al., 1995a). ODP Leg 138 biostratigraphies were integrated into well-defined magnetic stratigraphies (Schneider, 1995) and cyclostratigraphies based on gamma ray attenuation (GRA) bulk density data. Correlation of GRA bulk density

cycles to astronomical calculations for solar insolation provided robust age models for Late Miocene to Recent sediments (Shackleton et al., 1995b). The ODP Leg 138 age models were among the first astrochronologies developed for the Late Miocene to Quaternary, and hence the biostratigraphies generated from ODP Leg 138 sites were rather precisely calibrated. Berggren et al. (1995a,b) incorporated ages and bio-magnetostratigraphic data from ODP Leg 138 into their review of bio-magnetostratigraphic correlations for the Cenozoic and Quaternary.

ODP Site 1208 offers the opportunity to refine biomagnetostratigraphic correlations for the late Neogene. The attributes of ODP Site 1208 include: good preservation of foraminifers and calcareous nannofossils, relatively high sedimentation rates compared to ODP Leg 138 sites, and a robust age model based on magnetic polarity stratigraphy and correlation of reflectance data to astronomical solutions.

The study of ODP Site 1208 is a continuation of the work presented in Chapter 2, which deals largely with ODP Leg 198 sites other than Site 1208. An initial astrochronology for ODP Site 1208 (Chapter 2, Evans et al., 2005) was based on correlation of the shipboard reflectance ( $L^*$ ) data (Shipboard Scientific Party, 2002a) to the astronomical solution for obliquity of Laskar et al. (1993). Here, we update the Site 1208 astrochronology using the new astronomic solutions of Laskar et al. (2004), present the Site 1208 magnetostratigraphy, foraminiferal and nannofossil biostratigraphy, and link these stratigraphies to the new astrochronology. The recalibration of the Site 1208 age model makes little difference to the chronology presented in the previous chapter (and in Evans et al., 2005) because the astronomic solutions in the 0-12 Ma interval do not change significantly in Laskar's two calculations (Laskar et al., 1993; 2004).

Today, Shatsky Rise (Figure 3-1) lies in a subtropical water mass toward the north end of a warm-water mass known as the Kuroshio Extension Current (Shipboard Scientific Party, 2002b).

North of the Northern High of Shatsky Rise (Figure 3-1) lies a significant front, a transition region between subtropical and subarctic water masses. The transition zone waters are derived from off the coast of northern Japan, where the cold, nutrient-rich Oyashio Current mixes with the warm, nutrient-poor Kuroshio Extension Current. Middle Miocene calcareous plankton assemblages are rather uniform and diverse across Shatsky Rise and display warm, subtropical affinities. Since the Late Miocene, however, a faunal and floral gradient has been established across Shatsky Rise (Shipboard Scientific Party, 2002b). Calcareous plankton assemblages progressively lose their warm-water taxa along a traverse from south to north across the Shatsky Rise. At Sites 1207 and 1208 (Figure 3-1), there is a marked decrease in diversity in assemblages that assume temperate (occasionally cold-temperate) affinities, relative to sites further south. The changes in calcareous plankton assemblages are paralleled by a progressive decrease in calcareous preservation from north to south (Shipboard Scientific Party, 2002b).

One of the most noticeable features of the upper Miocene through Pleistocene sections recovered at Shatsky Rise is the decimeter- to meter-scale cycles between darker and lighter lithologies. The darker-colored intervals, in general, contain larger amounts of well-preserved biosiliceous material, and contain calcareous plankton assemblages that have cold-water affinities and have undergone relatively enhanced dissolution. Calcareous plankton preservation is enhanced in the light-colored layers that are poorer in diatoms and represent warmer-water intervals when Site 1208 was located in a subtropical water mass, similar to the situation at Site 1208 today and for the Southern High through most of the Neogene (Shipboard Scientific Party, 2002b).

### **Site Location and Lithology**

ODP Site 1208 is located in 3346m of water on the Central High of Shatsky Rise (Figure 3-1). The Central High of the Rise had not been drilled prior to ODP Leg 198, and the sedimentary sequence at the site revealed ~260 m of Upper Miocene to Recent sediments with ~60m of more condensed Lower and Middle Miocene below. A total of 314.17 m of Neogene age sediment was recovered at the site with an average recovery of 95%. The Upper Miocene to Recent section is composed of nannofossil ooze and nannofossil clay with diatoms and radiolarians, and an average carbonate content of 53% (Shipboard Scientific Party, 2002b). Since 3 Ma, the average sedimentation rates were 4.2 cm/kyr. Prior to 3 Ma, sedimentation rates decrease progressively reaching 1 cm/kyr at ~8 Ma. The character of the seismic reflection record at the site, along with the relatively high sedimentation rate that prevailed during the Pliocene-Pleistocene, suggests that the stratified lens of sediment at the site constitutes a drift deposit formed by current redistribution of sediment that settled on the Central High (Shipboard Scientific Party, 2002b). The sediment drift deposits at Site 1208 are somewhat similar to those drilled along the Meiji Seamount during ODP Leg 145 in that both sections comprise fine-grained sediment devoid of sedimentary structures other than bioturbation (Rea et al., 1993).

### **Magnetic Stratigraphy**

Magnetic measurements on half cores from Site 1208, using the shipboard pass-through magnetometer, revealed an unambiguous magnetic stratigraphy, ranging in age from Recent to Upper Miocene (Figures 3-2, 3-3 and 3-4). The shipboard data are based on a single demagnetization step (20 mT). This abbreviated treatment was necessary to preserve the sediment magnetization for later shore-based study, and to maintain core-flow through the shipboard core laboratory during the cruise. These shipboard data are supported using discrete sample cubes (7cm<sup>3</sup>) collected from the working halves of cores, which were measured at the

University of Florida. The discrete sample cubes were AF demagnetized in 5mT increments up to peak fields of 80 mT. A steep drilling related overprint was removed by 20 mT peak field (Figure 3-5), and the primary magnetization was defined using the standard least squares method (Kirschvink, 1980), giving low maximum angular deviation (MAD) values indicating well defined component magnetizations (Figures 3-2, 3-3 and 3-4).

An initial age model and initial estimate of interval sedimentation rates were calculated using the magnetostratigraphy and the geomagnetic polarity timescale (GPTS) of Cande and Kent (1995) (Figure 3-6a). Sedimentation rates decrease down section averaging 4-5 cm/kyr in the Pleistocene, 3.5-4 cm/kyr in the Pliocene and 1-2 cm/kyr in the Miocene. The duration of the Reunion subchron given in the Cande and Kent (1995) GPTS (10 kyr) causes a large increase in the sedimentation rates in the polarity zone correlative to the Reunion subchron (Figure 3-2). Using a revised age and duration for the Réunion subchron (Channell et al., 2003), sedimentation rates in the polarity zone correlative to the Reunion subchron are reduced to ~4 cm/kyr in keeping with surrounding sedimentation rates.

Numerous excursions can be identified in the shipboard magnetic stratigraphy particularly in the Matuyama Chron, one of which (at 103 mbsf) is confirmed by a single discrete sample corresponding to an age of 2.283 Ma. Channell et al., (2002) identified seven excursions in the Matuyama chron at ODP Site 983 in the North Atlantic that have been labeled: Santa Rosa (932 ka), C1r.1n.1r (1048 ka), Punaruu (1115 ka), Bjorn (1255 ka), Gardar (1472-1480 ka), Gilsa (1567-1575 ka), and C2r.1r.1n (1977 ka).

At ODP Site 1208, shallow inclinations are seen in shipboard data that appear to be correlative to Santa Rosa (950 ka), Punaruu (1123 ka), Gardar (1450 ka), Gilsa (1522 ka), and C2r.1r.1n (1976 ka) (Figure 3-2). An interval of shallow inclination at 896 ka at Site 1208 may



correspond to the Kamikatsura excursion that originates from the work of Maenaka (1983).

Three intervals of shallow inclination are also noted in the Brunhes chron with ages of 134, 193 and 262 ka close to the published ages for the Blake excursion (120 ka), Iceland Basin excursion (189 ka) and 8 $\alpha$  (260 ka) of Lund et al. (2001) (Figure 3-2). One potential excursion is noted in the Gauss chron (Figure 3-3) and three potential excursions in the Gilbert chron (Figure 3-5).

The ages for the Santa Rosa, Blake, Iceland Basin and 8 $\alpha$  are calculated by assuming constant sedimentation rates within the Brunhes and subchron C1r.1r. Ages for other excursions are at Site 1208 are calculated from the astronomic age model described below. All the postulated excursions in the Site 1208 record should be regarded with some caution as they are based on a single demagnetization step (20 mT peak field) from shipboard data.

### **Cycle Stratigraphy**

Shipboard gamma ray attenuation bulk density data and L\* reflectance data (Shipboard Scientific Party, 2002), show a prominent cyclicity in the 1-6 Ma interval, that, based on the initial age model has a period close to 41 kyr (see Chapter 2, Evans et al., 2005). Using the astronomical solutions of the Laskar et al. (2004), the L\* reflectance data was tuned to obliquity by matching the L\* output of a filter centered on 41 kyr to the orbital solution for obliquity (Figure 3-7). The resulting interval sedimentation rates for the 1-6 Ma interval are given in Figure 3-6b. The tuned ages for reversal boundaries, based on this match, are given in Table 3-2. The astronomical calibration of Site 1208 presented here is a recalibration of the astronomical timescale of Evans et al., (2005) using the updated astronomical solutions of Laskar et al. (2004). The recalibration to the new astronomic solutions resulted in little change to the astronomic ages for Site 1208 relative to those given by Evans et al. (2005). Comparison of polarity reversal ages with other timescales, and with results from IODP Site U1313 (Chapter 6), indicates close

agreement with differences < ~60 kyrs between 2.6 Ma and 5 Ma (Table 3-2). Beyond 5.2 Ma, the differences with respect to other timescales increase to over 100 kyr. In the 5.5-6 Ma interval, the polarity reversal ages from Site 1208 are closest to those of Shackleton et al. (1995b) from ODP Leg 138 (equatorial Pacific). The largest discrepancy beyond 5.2 Ma is with ATNTS2004 timescale (Lourens et al., 2004) where the difference in ages is ~ 300 kyrs. The ATNTS2004 timescale uses the work of Hilgen et al. (1995) from the Mediterranean in this interval.

### **Calcareous Nannofossils**

Calcareous nannofossils were semi-quantitatively analyzed using smear slides and standard light microscope techniques (Bown and Young, 1998). The following abundance and preservation categories were used: *Species abundance*: abundant: >10 specimens per field of view (FOV), common: 1–10 specimens per FOV, few: 1 specimen per 2–10 FOV, rare: 1 specimen per 11–100 FOV. *Total nannofossil abundance*: abundant: >10%, common: 1%–10%, few: 0.1%–1%, rare: <0.1%, barren and questionable occurrence. *Nannofossil preservation*: good, moderate, poor (See range chart of Bown, 2005). All core catcher samples were examined and ~60 other samples collected through the Late Miocene to Recent section. Biostratigraphy is described with reference to the zonal scheme of Bukry (1973, 1975; zonal code numbers CN and CP added and modified by Okada and Bukry, 1980) for Cenozoic calcareous nannofossil biostratigraphy.

The middle Miocene–Holocene section yielded a beautiful succession of rich and abundant nannofossil assemblages. Preservation improved up-section but was also dependent upon which part of the light/dark sedimentary cycle was sampled. The darker, diatom-rich intervals yielded more poorly preserved nannofossil assemblages (Shipboard Scientific Party, 2002). The Neogene nannofossil biostratigraphy indicates a relatively complete stratigraphy for the Pliocene–Pleistocene (Figure 3-8) and Miocene (Figure 3-9), with all nannofossil zones from CN5 through

CN15 identified by their primary zonal fossils (Figure 3-10). Calcareous nannofossil range charts are shown in Bown (2005). Zones CN1–CN5 could not be easily distinguished because of the absence of the marker species *Sphenolithus belemnoides*, *Helicosphaera ampliaperta*, and *Discoaster kugleri*. In addition, a number of CN subzones could not be recognized due to the absence of *D. kugleri* (Subzone CN5b), *Discoaster loeblichii*, *Discoaster neorectus* (Subzone CN8b), and *Amaurolithus amplifolius* (subdivisions within Zone CN9) and an anomalously low last occurrence (LO) of *Triquetrorhabdulus rugosus* (Subzone CN10b) (Bown, 2005).

The astronomically calibrated ages of Pliocene to Quaternary calcareous nannofossil datums from Site 1208 (Table 3-3) are generally consistent with ages from Berggren et al. (1995b), that are based largely on work from the Mediterranean (Rio et al., 1990). The LO of *Discoaster brouweri*, however, differs significantly from Berggren et al. (1995b) in both age and correlative polarity chron (Table 3-3). The age of 1.95 Ma given by Berggren et al. (1995b), correlative to the onset of the Olduvai subchron, is based on correlation to Deep Sea Drilling Project (DSDP) Site 606 in the North Atlantic (Backman and Pestiaux, 1987).

At Site 1208, the FO of *Discoaster berggrenii* in the Late Miocene is ~ 0.5 Myrs younger than the age reported in Berggren et al. (1995a). This age is based on correlation to polarity chron C4r.2r from ODP Leg 138. The age is more consistent with that seen at DSDP Site 608 where the datum is correlated to polarity chron C4n (Ruddiman et al., 1987). The FO of *Discoaster hamatus* is a controversial datum (Berggren et al., 1995a) that has very inconsistent correlation to polarity chrons regardless of latitude. In ODP Leg 138 sites, it is correlative to subchron C5n.2n, as at Site 1208. The FO of *Catinaster coalitus* is another controversial datum that, at ODP Site 1208, is correlated to subchron C5n.2n similar to the correlation at ODP Leg 138 sites. Berggren et al. (1995a) give an age of 10.8 Ma for the FO of *Coccolithus*

*miopelagicus*, 200 kyrs younger than the age from Site 1208 (Table 3-3), however the correlation of this datum to polarity subchron C5r.1r at Site 1208 is consistent with the correlation at DSDP Site 608.

### **Planktonic Foraminifera**

158 samples were analyzed for planktonic foraminifers at ~1.5 m intervals, together with core-catcher samples (from the base of each core) collected shipboard from the 320-m-thick upper Neogene section at ODP Site 1208. The samples were soaked in a slightly basic solution, shaken, washed over a 63  $\mu\text{m}$  sieve and dried at 60°C. Specimens of planktic and benthic foraminifers were picked from the >125  $\mu\text{m}$  fraction. Specimens of all recognizable planktic species were identified following the classic taxonomies of Kennett and Srinivasan (1983), Bolli and Saunders (1985), Jenkins (1985), and Iaccarino (1985). Shipboard and shore-based occurrence tables were combined to determine a planktic foraminifer biostratigraphy. Occurrence estimates were based on the following percentages: Rare=1%, rare to few=3%, few=5%, few to common=8%, common=10%, common to abundant=15%, abundant =>20%,

Planktonic foraminiferal abundance varies from abundant to common through the Pleistocene and upper Pliocene but declines in the Miocene to few to rare relative to siliceous microfossils and clay. Temperate-water species dominate many of the Neogene planktonic foraminiferal assemblages at Site 1208 (Shipboard Scientific Party, 2002b).

The magnetostratigraphically-interpolated ages for many foraminiferal datums on Shatsky Rise differed significantly from those reported from the southwest Pacific, due to regional migration patterns. Application of zonal schemes proposed for the southwest Pacific (Jenkins, 1985) and the mid-latitudes were complicated by unexpected changes in the sequence of foraminiferal datums observed at Shatsky Rise. A revised temperate foraminifer biostratigraphy

for the late Neogene uses seventeen of the most isochronous foraminiferal datums at Shatsky Rise as zonal markers (shown in Figure 3-11).

Discrepancies between published ages for planktonic foraminifer datums (Berggren et al., 1995a,b; Lourens et al., 2004) and those identified at Site 1208 are large in some cases. (Tables 3-4 and 3-5). The majority of the magneto-biostratigraphic correlations used in Berggren et al., (1995a,b) and Lourens et al. (2004) are from the Mediterranean (Hilgen, 1990), South Atlantic (Hodell and Kennett, 1987) or South Pacific (Srinivasan and Sinha, 1993). The comparison of the ages of the planktic foraminifer datums is affected by regional differences and varying zonal schemes (Tables 3-4 and 3-5).

The LO of *Gr. tosaensis* at ODP Site 1208 is at 0.292 Ma, significantly younger than the age of 0.65 Ma given by Berggren (1995b). This datum is taken from the work of Berggren et al. (1985) and Srinivasan and Sinha (1993) from the southern Pacific and Indian Oceans. The LO datum of *Gr. puncticulata* has an age of 1.882 Ma at Site 1208, however, an age of 2.41 Ma was obtained at DSDP Site 607 (North Atlantic) where it is correlative to polarity subchron C2An.2n.

The FO of *Gr. truncatulinoides* occurs at the same stratigraphic level as the FO of *Gr. toseanis* at ODP Site 1208. Following Berggren et al. (1995b), the FO of *Gr. toseanis* has an age of 3.35 Ma. At Site 1208, the astronomically calibrated age of the event is 2.015 Ma. The Site 1208 age for this datum is more consistent with the astronomically calibrated age for the FO of *Gr. truncatulinoides* of 2.39 Ma from ODP Leg 138 in the eastern equatorial Pacific (Shackleton et al., 1995a). The LO of *Gr. margaritae* was assigned an age of 3.85 Ma in the ATNTS2004 (Lourens et al., 2004) from ODP Sites 925 and 926 from Ceara Rise. The astronomic age for the datum at Site 1208 is 3.761 Ma.

## Conclusions

ODP Site 1208 has produced a clear magnetic stratigraphy for the 0-12 Ma interval with sedimentation rates in the Brunhes and Matuyama chrons varying in the 4-5 cm/kyr range. These sedimentation rates are some of the highest sedimentation rates seen in this interval in pelagic sediments from the mid- and low latitude Pacific Ocean. This anomalously high sedimentation rate appears to be due to formation of a drift-type deposit on the Central High of Shatsky Rise. The relatively high sedimentation rates have allowed identification of polarity excursions in the Matuyama Chron that have not been previously identified in sediments from the Pacific Ocean. It is important to stress that these excursions are identified in shipboard pass-through magnetic data, and are not based on identification of magnetization components. For this reason, the ratification of these excursions must await further (u-channel) studies of these sediments.

Reflectance ( $L^*$ ) cycles identified in the sediments have allowed astronomic calibration of reversal boundaries and biostratigraphic datums, by correlation of  $L^*$  reflectance data to the astronomic solution for obliquity (Laskar et al., 2004). Calcareous nannofossil biostratigraphy is largely consistent with the most recent review of bio-magnetostratigraphic correlations for this time interval (Berggren et al., 1995a, b). Based on the correlation of planktonic foraminifer datums to the magnetic stratigraphy at Site 1208, a new planktonic foraminifer zonation for the northwest Pacific Ocean has been developed that can be precisely correlated to polarity chrons and astronomically calibrated ages.

Table 3-1. Depths of reversal boundaries from ODP Site 1208. Chrons are labeled according to Cande and Kent (1992). Ages for polarity chrons are from Cande and Kent (1995) and Channell et al., (2003).

Chron	Ma (CK95)	mbsf	Chron	Ma (CK95)	mbsf
C1n	0	0	C3Br.1n	6.946	
base	0.78	42.92	base	6.981	
C1r.1n	0.99	52.57	C3Br.2n	7.153	
base	1.07	55.85	base	7.187	240.33
C1r.2r.1n	1.201	61.18	C4n.1n	7.245	241.08
base	1.211	61.67	base	7.376	241.83
C2n	1.77	85.01	C4n.2n	7.464	242.95
base	1.95	92.81	base	7.892	250.78
C2r.1n*	2.115	99.86	C4r.1n	8.047	251.71
base*	2.153	101.01	base	8.079	252.46
C2An.1n	2.581	119.45	C4An	8.529	256
base	3.04	137.8	base	8.861	260.66
C2An.2n	3.11	140.64	C4Ar.1n	9.069	262.53
base	3.22	144.58	base	9.146	264.02
C2An.3n	3.33	147.76	C4Ar.2n	9.428	265.69
base	3.58	156.88	base	9.491	268.12
C3n.1n	4.18	172.4	C5n.1n	9.592	269.05
base	4.29	176.47	base	9.735	271.85
C3n.2n	4.48	182.51	C5n.2n	9.777	
base	4.62	185.46	base	10.834	282.1
C3n.3n	4.8	189.28	C5r.1n	10.94	287.14
base	4.89	191.01	base	10.989	287.69
C3n.4n	4.98	194.09	C5r.2n	11.378	290.49
base	5.23	200.04	base	11.434	291.42
C3An.1n	5.894	216.47	C5An.1n	11.852	292.17
base	6.137	221.51	base	12	294.03
C3An.2n	6.269	222.25	C5An.2n	12.108	298.69
base	6.567	231.39	base	12.333	299.63
C3Bn	6.935	235.31			
base	7.091	240.34			

\* age from Channell et al. (2003)

Table 3-2. Astronomically calibrated ages for reversal boundaries from ODP Site 1208 compared to ATNTS2004 (Lourens et al., 2004), Cande and Kent (1995), IODP Site U1313 (Evans et al., in preparation, Chapter 6), Hilgen et al., (1995) and ODP Leg 138 (Shackleton et al., 1995b). Differences between Site 1208 ages and published ages are given in parentheses.

Chron	1208 tuned age (Ma)	CK95 (Ma)	Hilgen et al. (1995) (Ma)	ATNTS 2004 (Ma)	ODP Leg 138	IODP Site U1313 Chapter 6
C1n						
base		0.780				
C1r.1n		0.990				
base	1.062	1.070 (-0.008)		1.072 (0.01)		
C1r.2r.1n	1.158	1.201 (0.043)		1.173 (0.015)		
base	1.167	1.211 (0.044)		1.185 (0.018)		
C2n	1.763	1.770 (-0.007)	1.785 (0.022)	1.778 (0.015)		
base	1.944	1.950 (-0.006)	1.942 (-0.002)	1.945 (0.001)		
C2r.1n	2.204	2.140 (0.064)	2.129 (-0.075)	2.128 (-0.076)		
base	2.214	2.150 (0.064)	2.149 (-0.065)	2.148 (-0.066)		
C2An.1n	2.616	2.581 (0.035)	2.582 (-0.34)	2.581 (-0.035)	2.600 (-0.016)	2.616 (0)
base	3.048	3.040 (0.008)	3.032 (0.016)	3.032 (-0.016)	3.046 (-0.002)	3.074 (0.026)
C2An.2n	3.091	3.110 (-0.019)	3.116 (0.025)	3.116 (0.025)	3.131 (0.04)	3.153 (0.062)
base	3.207	3.220 (-0.013)	3.207 (0)	3.207 (0)	3.233 (0.026)	3.268 (0.061)
C2An.3n	3.350	3.330 (0.020)	3.330 (-0.02)	3.330 (-0.02)	3.331 (-0.019)	3.346 (-0.004)
base	3.584	3.580 (0.004)	3.569 (-0.015)	3.596 (0.012)	3.594 (0.01)	3.549 (-0.035)
C3n.1n	4.164	4.180 (-0.016)	4.188 (0.024)	4.187 (0.023)	4.199 (0.035)	4.144 (-0.02)
base	4.307	4.290 (0.017)	4.300 (-0.010)	4.300 (-0.007)	4.316 (0.009)	4.277 (-0.03)
C3n.2n	4.484	4.480 (0.004)	4.493 (+0.009)	4.493 (0.009)	4.479 (-0.005)	4.500 (0.016)
base	4.601	4.620 (-0.019)	4.632 (0.031)	4.631 (0.03)	4.623 (0.022)	4.631 (0.03)
C3n.3n	4.785	4.800 (-0.015)	4.799 (0.014)	4.799 (0.051)	4.781 (-0.004)	4.760 (-0.025)
base	4.897	4.890 (0.007)	4.879 (-0.018)	4.896 (-0.001)	4.878 (-0.019)	4.889 (-0.008)
C3n.4n	4.987	4.980 (0.007)	4.998 (0.011)	4.997 (0.01)	4.977 (-0.01)	5.009 (0.022)
base	5.182	5.230 (-0.048)	5.236 (0.054)	5.235 (0.053)	5.232 (0.05)	5.273 (0.091)
C3An.1n	5.735	5.894 (0.159)	5.952 (0.217)	6.033 (0.298)	5.875 (0.14)	
base	5.955	6.137 (0.182)	6.214 (0.259)	6.252 (0.297)	6.122 (0.167)	



Table 3-3. Nannofossil datums for ODP Site 1208 (Bown, 2005). Ages for the datums are interpolated from the magnetic stratigraphy (this work) and the correlative polarity chron is given. The datums are compared to ages given by Berggren et al. (1995a, b). Tuned ages for the datums are compared to ATNTS2004 (Lourens et al., 2004) and ODP Leg 138 ages for nannofossil datums only (Raffi and Flores, 1995; Shackleton et al., 1995a).

Datum	Depth (mbsf)	1208 Mag. strat. Age (Ma)	Chron Site 1208	Berggren et al.1995a b (Ma) chron	ODP Leg 138	1208 Tuned age (Ma)	ATNTS age (Ma)
FO <i>Emiliana huxleyi</i>	14.24	0.258	C1n	0.26	0.26		0.29
LO <i>P. lacunosa</i>	30.30	0.551	C1n	0.46	0.46		0.44
FO <i>G. omega</i>	43.11	0.784	C1r.1r				
FO <i>G. caribbeanica</i>	87.90	1.837	C2n			1.841	
LO <i>D. brouweri</i>	100.16	2.143	C2r.1n	1.95 Olduvai	1.96	2.146	2.06
LO <i>D. pentaradiatus</i>	116.40	2.510	C2r.2r	2.46-2.56 M/G boundary	2.52	2.499	2.39
LO <i>D. surculus</i>	119.08	2.572	C2r.2r	2.55-2.59 M/G boundary	2.63	2.556	2.52
LO <i>D. tamalis</i>	128.70	2.812	C2An.1n	2.78 top Gauss	2.78	2.802	2.80
LO Large <i>Reticulofenestra</i>	163.90	3.851	C2Ar			3.833	
FO <i>D. tamalis</i>	166.66	3.65	C2Ar			3.95	
LO <i>Sphenolithus</i>	166.66	3.65	C2Ar	3.6 base Gauss	3.66	3.95	
LO <i>Amaurolithus</i>	168.88	4.56	C2Ar			4.03	
FO <i>D. asymmetricus</i>	168.88	4.56	C2Ar	4.2 top Cochiti	4.13	4.03	
FO <i>C. cristatus</i>	187.90	4.735	C3n.2r			4.750	
LO <i>D. quinqueringus</i>	207.00	5.551	C3r	5.6 C3r	5.55	5.472	5.59
FO <i>Amaurolithus</i>	235.52	6.941	C3Bn				
FO <i>D. quinqueringus</i>	250.80	8.075	C4r.1r				
FO <i>D. berggrenii</i>	250.80	8.075	C4r.1r	8.6 C4r.2r	8.45		
FO <i>D. hamatus</i>	265.94	9.586	C4Ar.2n	9.4 C4Ar.2r			
FO <i>C. calyculus</i>	270.10	9.792	C5n.1n				10.79
FO <i>D. hamatus</i>	274.20	10.125	C5n.2n	10.7	10.38		10.55
FO <i>C. coalitus</i>	279.70	10.699	C5n.2n	10.9			10.89
LO <i>C. miopelagicus</i>	285.06	11.009	C5r.1r	10.8			11.02
LO <i>C. premacintyreii</i>	295.41	13.19	C5An.1r		12.65		11.21
LO <i>C. floridanus</i>	295.41	13.19	C5An.1r		13.19		13.33

Table 3-4. Plio-Pleistocene foraminifer datums, with depths, correlative polarity chron, tuned age and compared to Berggren et al. (1995a, b) and ATNTS 2004 (Lourens et al., 2004) from ODP Legs 138 and 111.

Event	Depth mbsf	1208 mag strat age	Chron Site 1208	Berggren et al 95ab age (Ma)	1208 tuned age	ATNTS Age
LO <i>Gr. crassula</i>	0.4	0.007	C1n			
LO <i>Gr. tosaensis</i>	16.1	0.292	C1n	0.65 C1n		0.61
LO <i>Gs. bulloideus</i>	38.2	0.694	C1n			
LO <i>B. praedigitata</i>	43.7	0.797	C1r.1r			
LO <i>Gt. woodi</i>	53.2	1.005	C1r.1n		1.004	2.3
LO <i>Gs. bollii</i>	60.5	1.182	C1r.2r		1.197	
LO <i>Gs. obliquus</i>	66.7	1.331	C1r.2r		1.34	1.3
LO <i>N. acostaensis</i>	76.2	1.559	C1r.2r		1.562	1.58
LO <i>N. humerosa</i>	79.6	1.640	C1r.2r		1.653	
LO <i>Gt. decoraperta</i>	83.6	1.736	C1r.2r		1.742	2.75
LO <i>Gr. puncticulata</i> , FO <i>Gs. tenellus</i> , FO <i>Gs. elongatus</i>	89.7	1.878	C2n	2.41	1.882	2.41
FO <i>Gr. hirsuta</i>	92.3	1.938	C2n		1.930	
FO <i>Gr. toseansis</i> , LO <i>Gr. cibaoensis</i> , FO <i>Gr.</i> <i>truncatulinoides</i>	95.2	2.014	C2r.1r	3.35C2An.2n	2.015	1.93
LO <i>Pu. primalis</i> , LO <i>Gr. limbata</i> FO <i>Ga. parkerae</i>	98.5	2.103	C2r.1r		2.116	
FO <i>Pu. obliquiloculata</i> , FO <i>B. digitata</i>	101.9	2.171	C2r.2r		2.164	
LO <i>Gq. venezuelana</i>	108.1	2.316	C2r.2r		2.282	
LO <i>Ss. paenedehiscens</i> , LO <i>Gt. apertura</i>	111.4	2.393	C2r.2r		2.382	
LO <i>N. "dupac"</i> , FO <i>Ge. siphonifera</i>	121.5	2.632	C2An.1n		2.621	
LO <i>Gr. pseudomiocenica</i>	123.0	2.670	C2An.1n		2.654	
LO <i>Gr. juanai</i> , FO <i>Gr. bermudezi</i>	125.8	2.740	C2An.1n		2.714	
LO <i>Gr. plesiotumida</i> , LO <i>Gs. extremus</i> , LO <i>Gs. triloba</i>	132.5	2.907	C2An.1n		2.902	
FO <i>Gr. limbata</i>	135.3	2.978	C2An.1n		2.966	
LO <i>Gq. conglomerata</i> , LO <i>Gr. sphericomiozea</i>	137.2	3.250	C2An.1n		3.024	
FO <i>Pu. primalis</i>	142.2	3.154	C2An.2n		3.147	
LO <i>Gr. inflata</i>	146.2	3.276	C2An.2r		3.301	
FO <i>Gt. rubescens</i>	147.4	3.318	C2An.2r		3.338	
FO <i>Gr. puncticulata</i> , LO <i>Gr. conoidea</i>	150.0	3.391	C2An.3n	4.5 Nunivak	3.427	
FO <i>Sa. dehiscens</i>	151.5	3.433	C2An.3n	5.2 E.Gilbert	3.457	
LO <i>Ge. pseudobesa</i>	158.2	3.631	C2Ar		3.637	
FO <i>Ge. calida</i> , FO <i>Gr. crassula</i> , LO <i>D. altispira</i> , LO <i>Ss.</i> <i>seminulina</i>	159.6	3.740	C2Ar		3.682	
LO <i>Ss. kochi</i>	161.0	3.739	C2Ar		3.708	4.53
LO <i>Gr. margaritae</i>	162.4	3.793	C2Ar	3.58 G/G boundary	3.761	3.85
FO <i>Gs. bulloideus</i>	165.0	3.894	C2Ar		3.871	
FO <i>Gq. conglomerata</i> , FO <i>Gr. crassiformis</i>	172.0	4.165	C2Ar		4.187	
FO <i>Ga. uvula</i> , FO <i>Gs. extremus</i> , LO <i>Gr. conomiozea</i>	178.7	4.360	C3n.1r		4.413	
FO <i>Gg. umbilicata</i> , FO <i>Ge. aequilateralis</i>	182.9	4.499	C3n.2n		4.54	
FO <i>Gr. sphericomiozea</i>	186.5	4.669	C3n.2r	5.6 C3r	4.696	
FO <i>Gr. conomiozea</i> , LO <i>Gt. nepenthes</i> , FO <i>Gr. pseudomiocenica</i>	190.8	4.879	C3n.3n	4.2 Cochiti	4.873	4.37

Table 3-5. Miocene foraminifer datums, with depths, correlative polarity chron, tuned age and compared to Berggren et al. (1995a, b) and ATNTS 2004 (Lourens et al., 2004) from ODP Legs 138 and 111.

Datum	Depth (mbsf)	1208 mag strat age (Ma)	Chron Site 1208	Berggren et al. (1995b)	1208 tuned age	ATNTS 2004
FO <i>Gr. tumida</i> , LO <i>Gs. kennetti</i>	203.1	5.354	C3r	5.6 C3r	5.327	5.57
FO <i>Gs. bollii</i>	209.4	5.608	C3r		5.591	
FO <i>Gs. kennetti</i>	211.3	5.685	C3r		5.675	
FO <i>Gd. hexagona</i>	214.3	5.806	C3r		5.816	
FO <i>N. dutertrei</i> , FO <i>Gs. conglobatus</i>	217.3	5.934	C3An.1n		5.961	6.2
FO <i>Ss. paenedehiscens</i> , LO <i>Gr. merotumida</i>	224.5	6.342	C3An.2n			
FO <i>Ge. pseudobesa</i> , FO <i>Gr. margaritae</i> , FO <i>Ss. kochi</i> , FO <i>Gr. plesiotumida</i> , FO <i>N. humerosa</i> , FO <i>Gr. scitula</i>	227.3	6.434	C3An.2n	6.0 C3An		
LO <i>Gr. miotumida</i> c.f.	233.6	7.0	C3Ar			
FO <i>Gr. cibaoensis</i> , FO <i>N. acostaensis</i> , FO <i>Gr. miotumida</i> c.f.	240.2	7.4	C3Bn	7.8 C4n.2n		
LO <i>Gq. baroemoensis</i>	245.9	7.9	C4n.2n			
FO <i>Gr. juanai</i>	251.1	8.1	C4r.1r			
FO <i>B. praedigitata</i> , FO <i>Gs. obliquus</i> , FO <i>N. pachyderma</i> (dextral), (sinistral)	255.6	8.7	C4r.1r			
FO <i>Gs. ruber</i> , FO <i>Gt. apertura</i> , LO <i>Gq. dehiscens</i>	263.1	9.4	C4Ar.1n			
FO <i>Gr. merotumida</i>	270.5	9.9	C5n.1n			
LO <i>Gr. praemenardii</i>	272.6	10.0	C5n.2n			
FO <i>N. "dupac"</i>	276.8	10.2	C5n.2n			
LO <i>Gt. druryi</i>	282.3	11.0	C5r.1r			
LO <i>Ss. disjuncta</i>	284.3	11.1	C5r.1r			11.49
FO <i>Gt. decoraperta</i>	285.0	11.1	C5r.1r			
FO <i>Gr. miozea</i>	291.9	11.8	C5r.3r			
LO <i>Gr. mayeri</i>	294.1	12.1	C5An.1r			
LO <i>N. continuosa</i>	295.2	12.1	C5An.1r			
LO <i>Cs. parvulus</i> , LO <i>Gr. panda</i>	296.8	12.2	C5An.1r	11.8 C5r.3r		
FO <i>Gt. nepenthes</i> , FO <i>Gr. mayeri</i> , FO <i>Gr. menardii</i>	298.9	12.3	C5An.2n	11.8 C5r.3r		11.63
FO <i>Gt. druryi</i>	299.7	12.3				

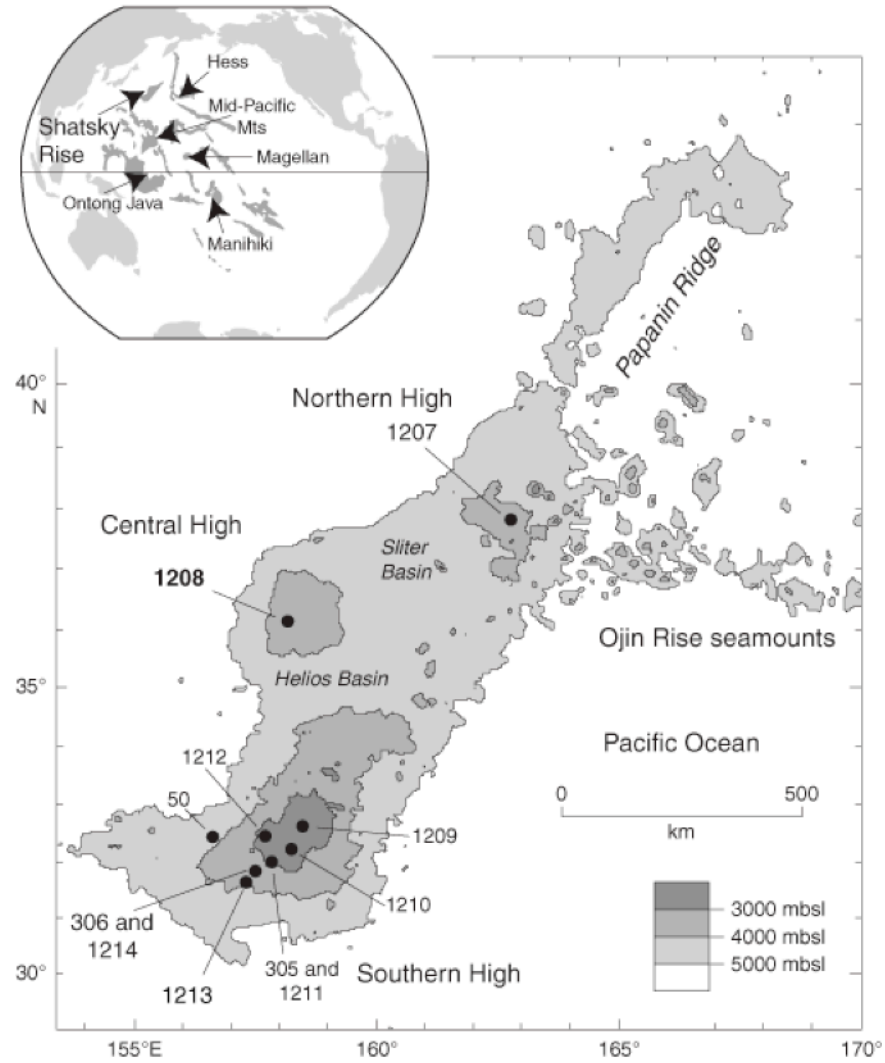


Figure 3-1. Bathymetric map showing the location of Shatsky Rise in the Pacific Ocean and a larger map of Shatsky Rise showing the Sites drilled on ODP Leg 198 including Site 1208 on the Central High of the Rise (after Bown, 2005).

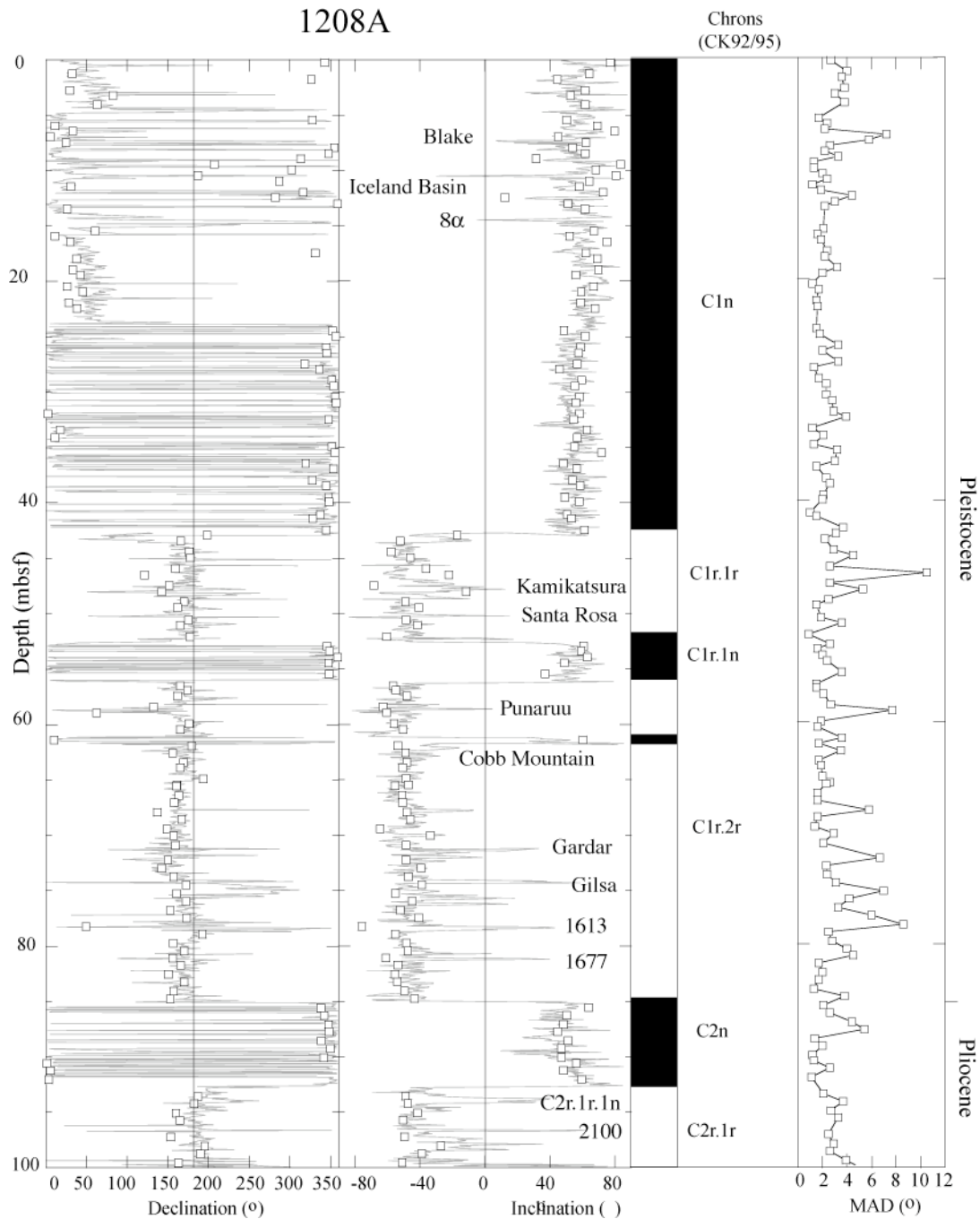


Figure 3-2. Inclination, declination and MAD values plotted against meters below sea floor. Gray line indicates the AF demagnetization data from the shipboard pass-through magnetometer at the 20 mT demagnetization step. Open squares indicate data from discrete samples. The polarity interpretation is shown in black (normal polarity) and white (reverse polarity) and chrons are labeled according to Cande and Kent (1992, 1995). Excursions are labeled according to Channell et al. (2002) and Singer et al. (1999). Ages for excursions are calculated from the astronomic age model for Site 1208.

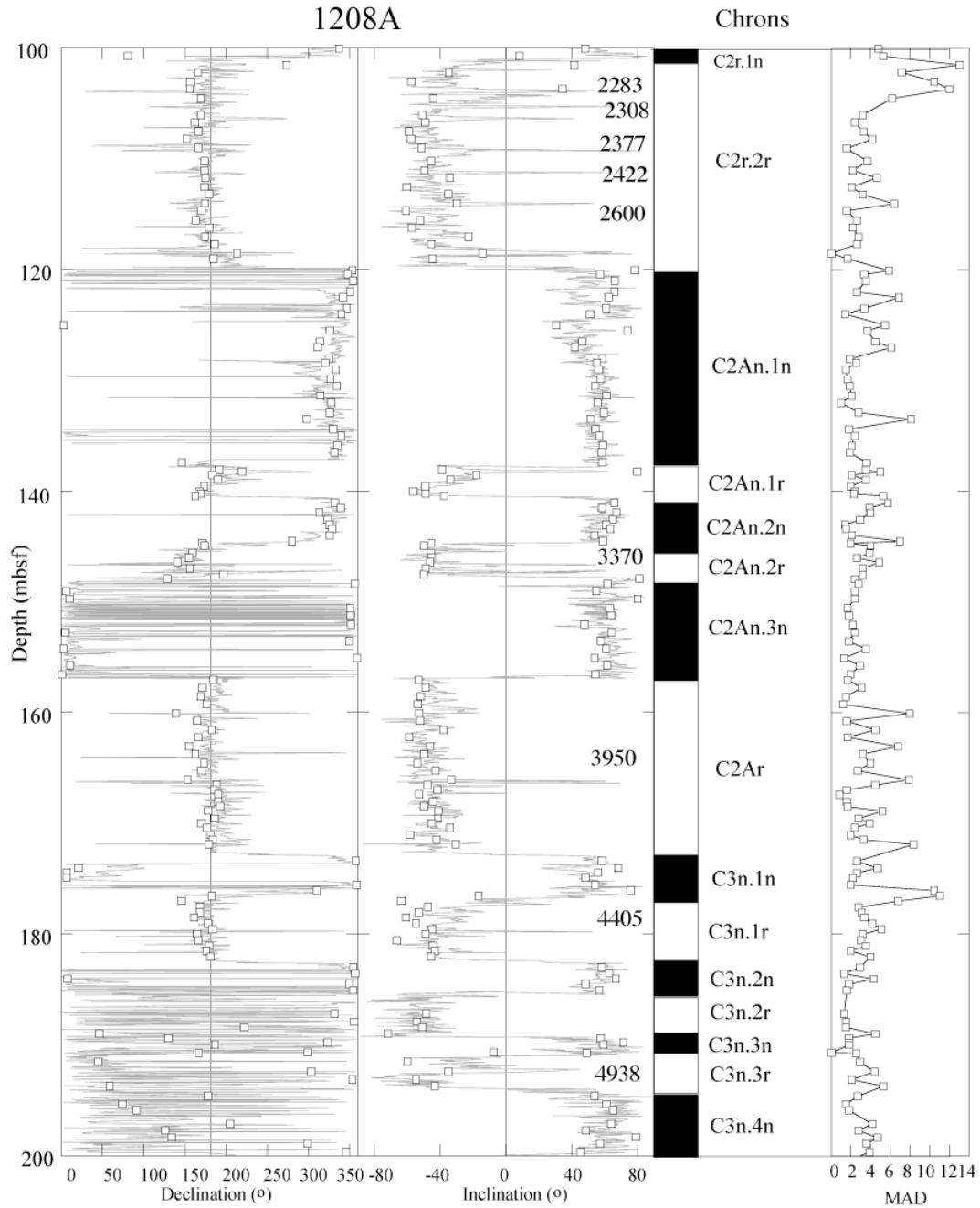


Figure 3-3. Inclination, declination and MAD values plotted against meters below sea floor. Gray line indicates data from the shipboard pass-through magnetometer at the 20 mT demagnetization step. Open squares indicate data from discrete samples. The polarity interpretation is shown in black (normal polarity) and white (reverse polarity) and chronos are labeled according to Cande and Kent (1992, 1995). Excursions are labeled according to Channell et al. (2002) and Singer et al. (1999). Ages for excursions are calculated from the astronomic age model for Site 1208.

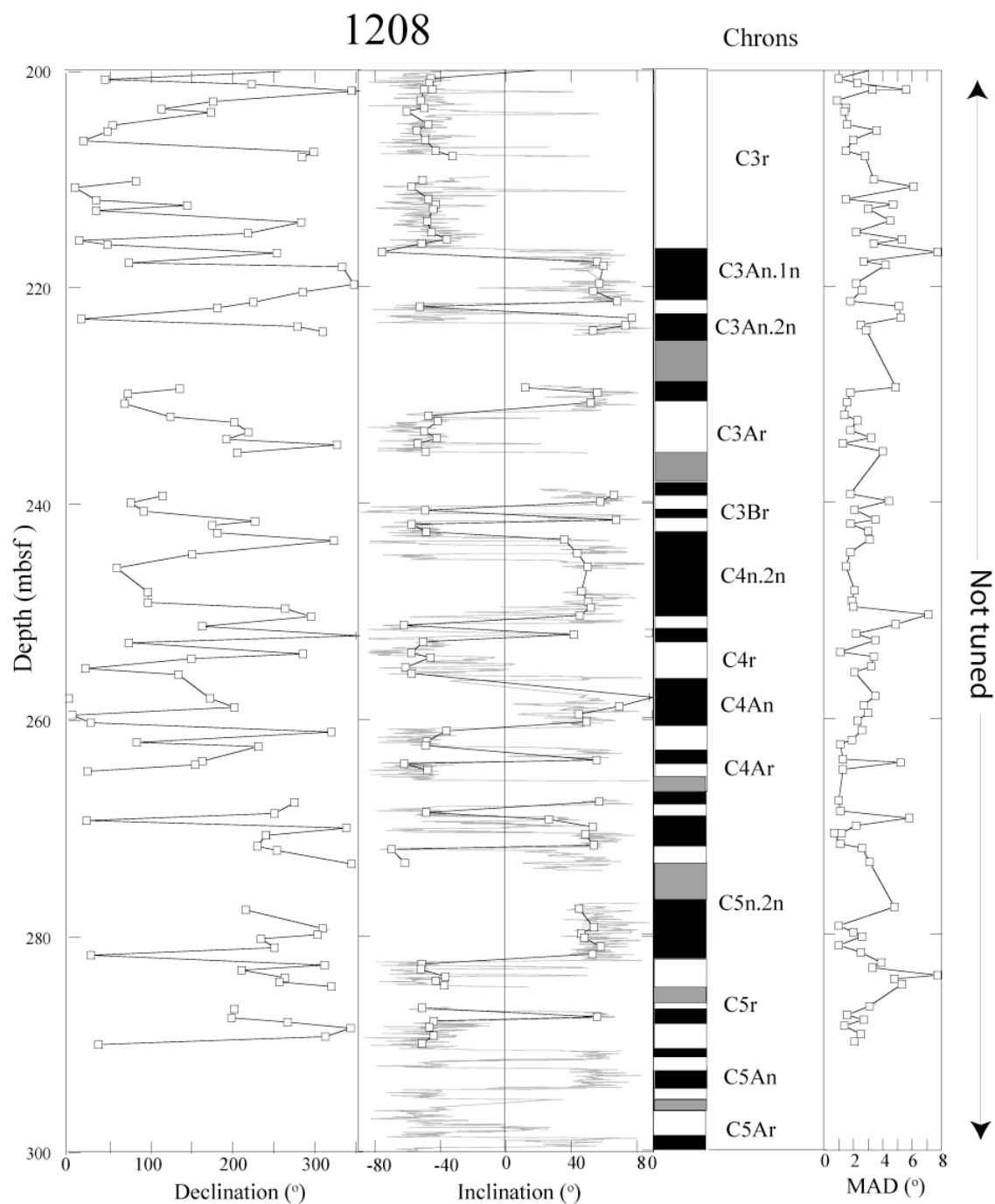


Figure 3-4. Inclination, declination and MAD values plotted against meters below sea floor. Gray line indicates data from the shipboard pass-through magnetometer. Open squares indicate data from discrete samples. The polarity interpretation is shown in black (normal polarity) and white (reverse polarity) and chrons are labeled according to Cande and Kent (1992, 1995). Gray bar indicates indeterminate polarity.

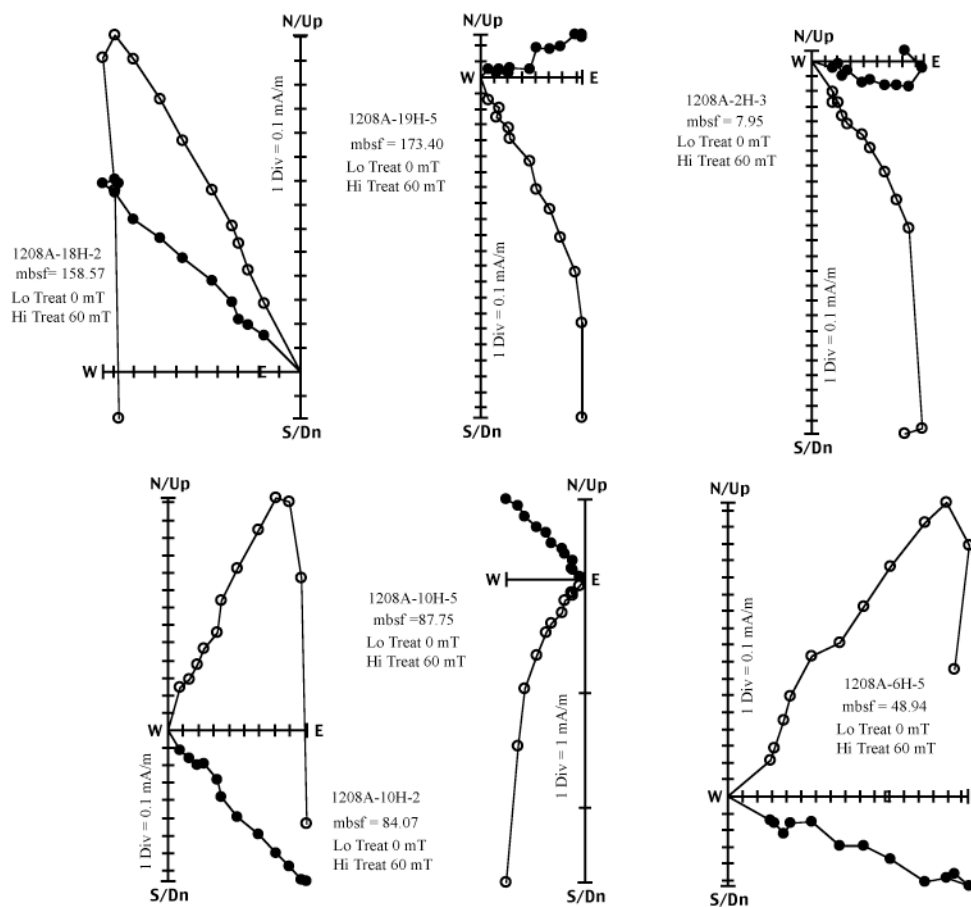


Figure 3-5. Orthogonal projections showing AF demagnetization data from discrete samples. Open circles represent the vector end point projections on the vertical plane and closed circles represent vector end point projections on the horizontal plane.



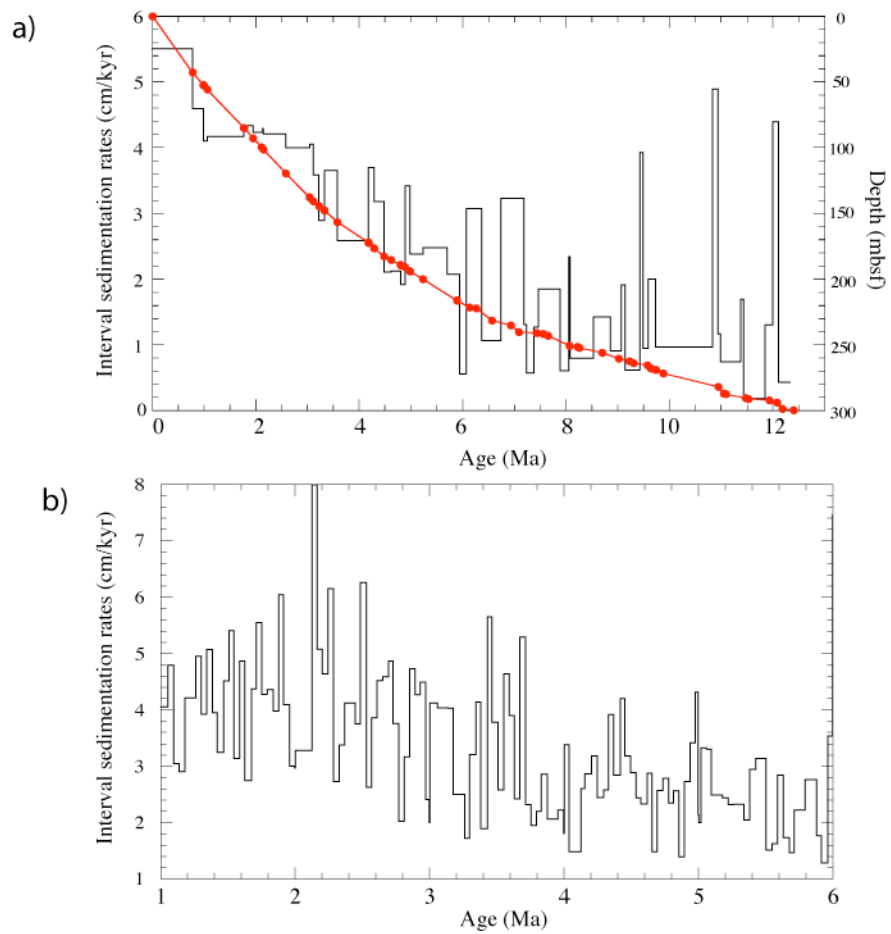


Figure 3-6. a) Interval sedimentation rates (black line) and age versus depth (red line) calculated from the magnetostratigraphic data. b) interval sedimentation rates calculated for the tuned age model for the 1-6 Ma interval.

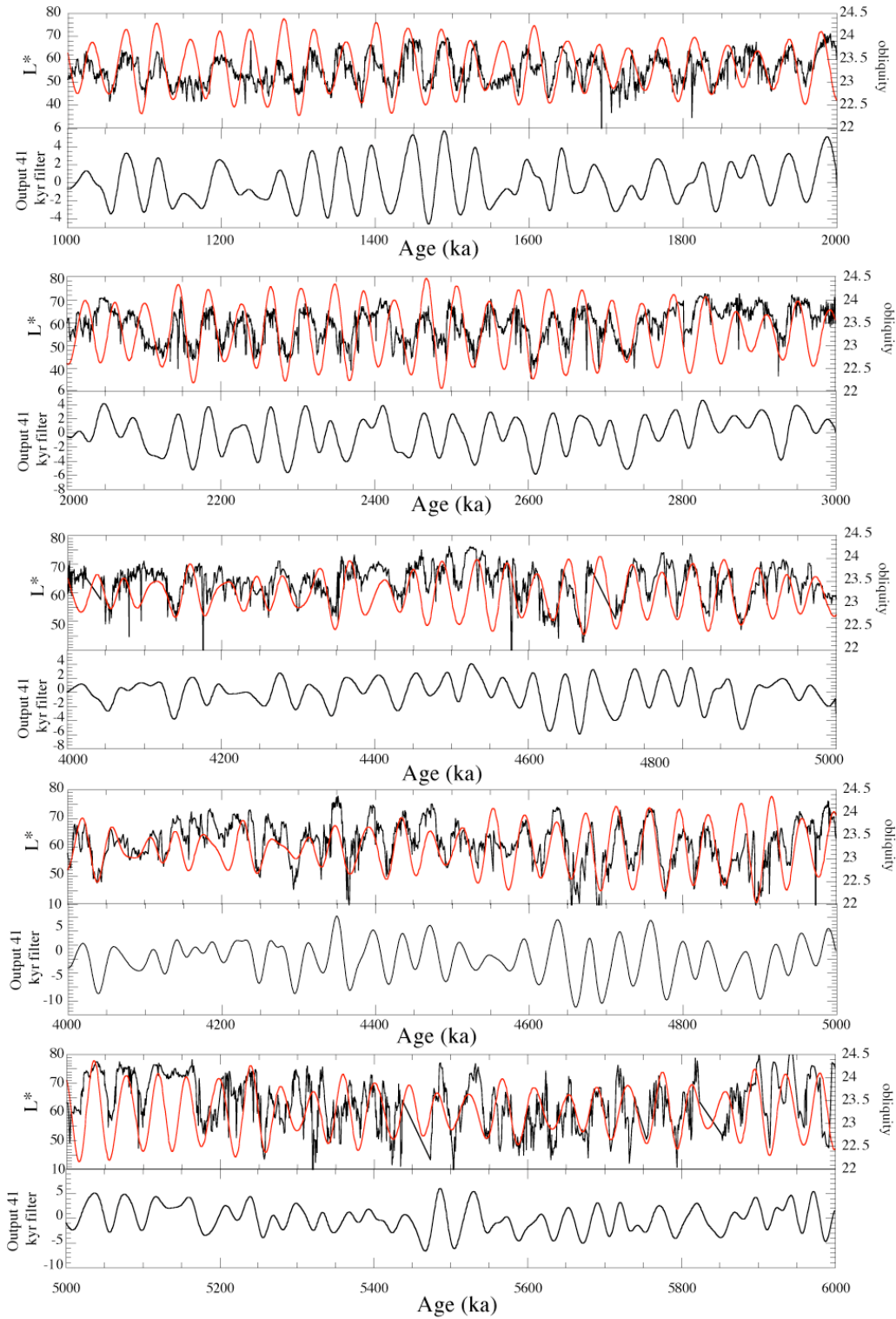


Figure 3-7. Reflectance ( $L^*$ ) data (black line) tuned to the astronomic solution for obliquity from Laskar et al. (2004). Lower plots shows the output of a gaussian filter centered on the obliquity frequency (0.024), applied to the reflectance ( $L^*$ ) data.

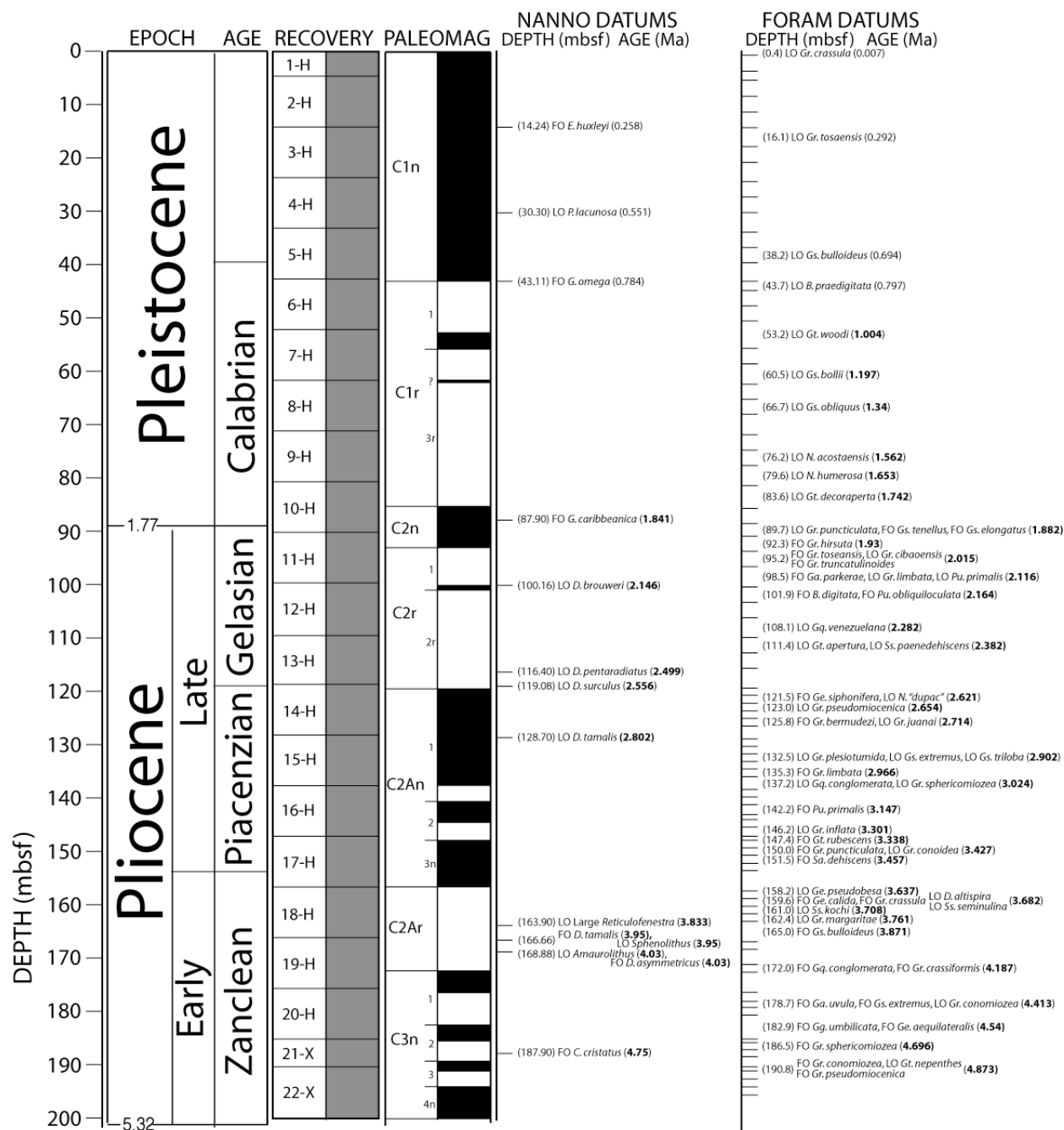


Figure 3-8. Plio-Pleistocene planktonic foraminifer and calcareous nannofossil datums, core recovery, and magnetostratigraphy, plotted against meters below the sea floor. Ages in bold are astronomically calibrated ages from this study. Ticks indicate position of samples taken for foraminifer analysis. Depths in mbsf of datums are given in parentheses before the datum.

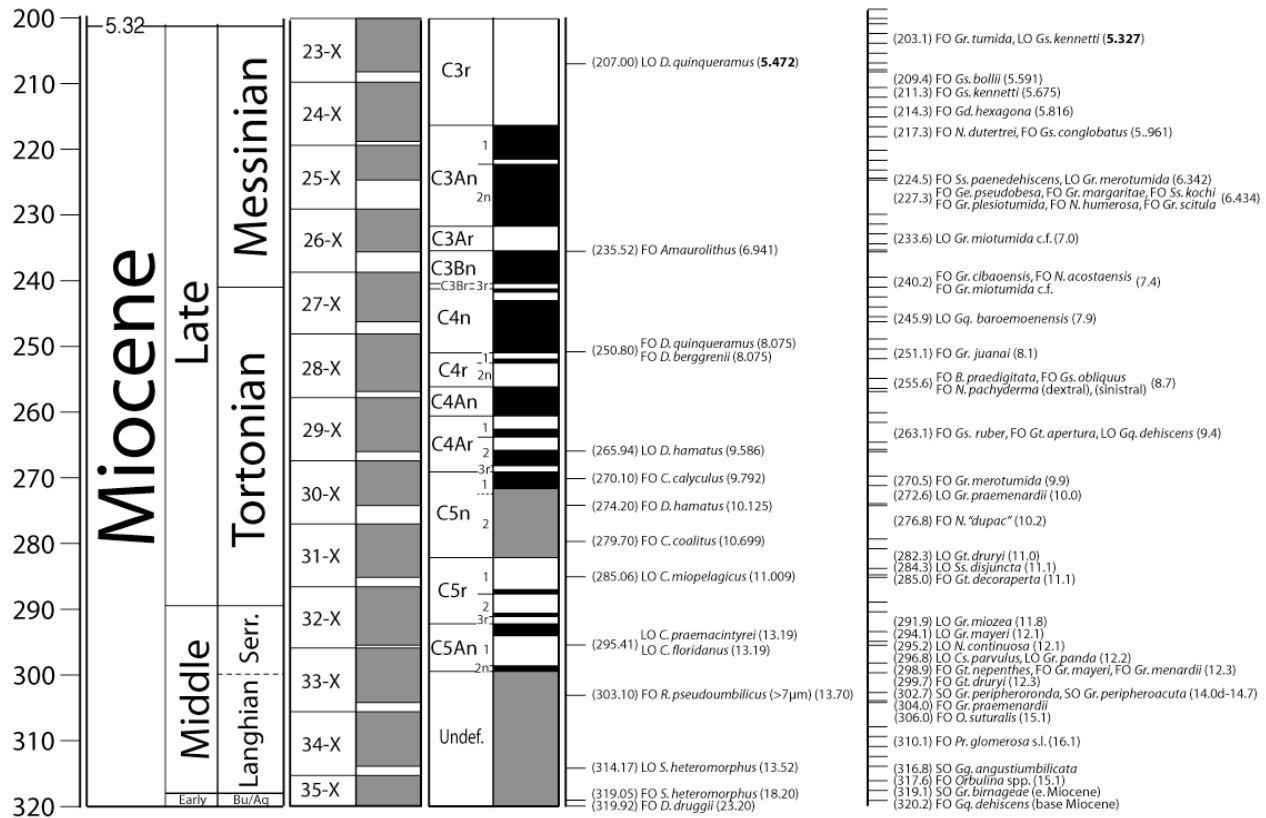


Figure 3-9. Miocene planktonic foraminifer and calcareous nannofossil datums core recovery, and magnetostratigraphy, plotted against meters below the sea floor (after Venti, 2006). Ages in bold are astronomically calibrated ages from this study. Ticks indicate position of samples taken for foraminifer analysis. Depths in mbsf of datums are given in parentheses before the datum.

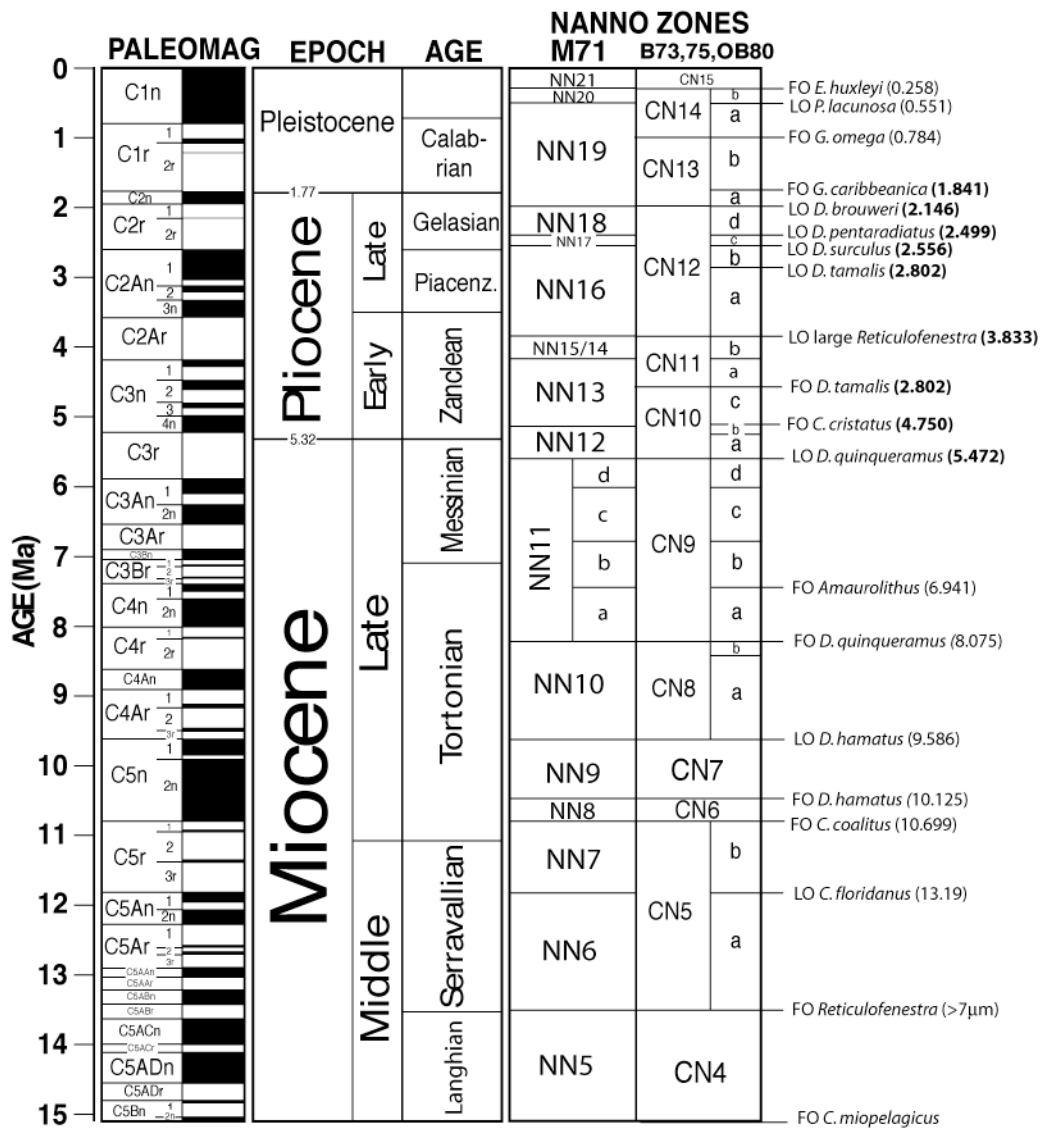


Figure 3-10. Calcareous nannofossil biostratigraphy including the zonations of Martini (1971) and Okada and Bukry (1980) modified from Bukry (1973, 1975). Ages in bold are astronomically calibrated ages from this study.

Figure 3-11. A proposed biostratigraphy for the mid-latitude North Pacific uses 16 planktic foraminifer datums to divide the late Neogene into 15 biozones. The new stratigraphy is integrated into the Geomagnetic Polarity Timescale and compared to pre-existing planktic foraminifer zonal schemes for temperate and tropical region, as well as to tropical calcareous nannofossil zonations (after Venti, 2006). Abbreviations for zonations are as follows: B69: Blow (1969) modified by Kennett and Srinivasan (1981a, 1981b) BKSA95: Berggren et al. (1995b) J85: Jenkins (1985) SK81: Srinivasan and Kennett (1981a) M71: Martini (1971) B73,75: Bukry (1973, 1975), OB80 Okada and Bukry, (1980): Ages in bold are astronomically calibrated ages from this study.

## CHAPTER 4

### PALEOINTENSITY-ASSISTED CHRONOSTRATIGRAPHY OF DETRITAL LAYERS ON THE EIRIK DRIFT (NORTH ATLANTIC) SINCE MARINE ISOTOPE STAGE 11

#### **Introduction**

The Eirik Drift drapes the top of the underlying Eirik Ridge located off the southern tip of Greenland (McCave and Tucholke, 1986). Magnetic anomalies have not been identified directly beneath the Eirik Ridge, although the adjacent oceanic crust in both the Irminger Basin and Labrador Sea is associated with marine magnetic anomaly 24 of Paleocene-Eocene boundary age (Srivastava and Tapscott, 1986). The Eirik drift is 800 km long and has been constructed by the interaction of the southwestward flowing Western Boundary Undercurrent (WBUC) and basement topography (Chough and Hesse, 1985). The WBUC carries water masses originating from the Norwegian and Greenland Seas that enter the North Atlantic over the Iceland-Scotland Ridge and Denmark Strait (McCave and Tucholke, 1986; Lucotte and Hillaire-Marcel, 1994). The WBUC moves over, and constructs the Eirik Drift and then follows bathymetric contours around the Labrador Basin (McCave and Tucholke, 1986).

Drilling on the Eirik Drift includes Site 646 (ODP Leg 105), and piston and gravity cores collected during cruises by the *CSS Hudson* in 1990, the *Marion Dufresne* in 1999 and the *R/V Knorr* in 2002. Seismic records used to extrapolate the sequence recovered at Site 646 indicate that the drift has been constructed since the middle to early Pliocene (Arthur et al., 1989). Although sedimentation on the drift sequence was more or less continuous during the Late Pliocene and Pleistocene, sedimentation rates vary considerably with glacial/interglacial conditions and with location on the drift.

Piston cores HU90-013-012 (water depth: 2830 m) and HU90-013-013 (water depth: 3380 m) (Figure 4-1, Table 4-1), collected in 1990 during a cruise of the *CSS Hudson*, record the last glacial cycle at differing water depths on the Eirik Drift (Hillaire-Marcel et al., 1994). Core

HU90-013-013 shows high sedimentation rates in the Holocene while Core HU90-013-012 has very low Holocene sedimentation rates due to winnowing by the WBUC (Stoner et al., 1995a, 1996). Increases in magnetic concentration and grain size during the early Holocene and at the MIS 6/5e transition in HU90-013-013, were attributed to detrital influx associated with retreat of the Greenland Ice sheet (Stoner et al., 1995b). In core HU90-013-013, four discrete detrital layers were identified within MIS 2 and 3 based on their magnetic properties (coarse magnetic grain size) and relatively high percent carbonate values. Stoner et al. (1996) correlated three of these detrital layers with Heinrich events 1, 2 and 4. Stoner et al., (1998) revised the chronology for core HU90-013-013 by correlation to SPECMAP (Martinson et al., 1987) and refined the ages and correlation of the detrital layers to North Atlantic detrital layers.

We present data from three jumbo piston cores (JPC15, JPC18, JPC19) collected on the Eirik Drift in the summer of 2002 during Cruise KN166-14 of the *RV Knorr*, and from Core MD99-2227 collected during the 1999 *Images* campaign (Figure 4-1). JPC15 was taken on the upper slope of the ridge at a water depth of 2230 m. Core JPC19 was collected from the crest of the ridge at a water depth of 3184 m, and Core JPC18 from the southern flank of the ridge at a water depth of 3435 m. Core MD99-2227 was collected from the western toe of the drift at 3460 m water depth. The recovered sediments are mostly dark gray bioturbated silty clays, with clayey silt and sandy mud, and occasional gray nannofossil/foraminifer rich clayey silt layers (see Turon, Hillaire-Marcel et al., 1999, for a lithologic description of MD99-2227).

### **Methods**

U-channel samples (2x2 cm square cross-section and 150 cm in length) were collected from the center of the split face of piston core sections. These samples were measured on a 2G-Enterprises pass-through cryogenic magnetometer at the University of Florida. Natural remanent magnetization (NRM) was demagnetized step-wise using alternating fields (AF) in 5 mT



increments for 0-60 mT peak fields, and in 10 mT increments for 60 mT-100 mT peak fields. Volume susceptibility was then measured using a susceptibility track specifically designed for u-channels (Thomas et al., 2003) that has a measurement resolution of a few centimeters. Anhysteretic remanent magnetization (ARM) was applied using an AF field of 100 mT and a bias DC field of 50  $\mu$ T. Isothermal remanent magnetization (IRM) was imparted using a 0.5 T DC field. Both artificial remanences were demagnetized with the same AF steps used to demagnetize NRM. Principal components were calculated from the NRM data using the method of Kirschvink (1980) applied to the 20-80 mT interval. Relative paleointensity proxies were generated by normalizing the NRM data by both ARM or IRM, demagnetized at a common peak field. A mean of nine normalized remanence values, in the 20-60 mT peak field range, was used to generate the relative paleointensity proxies. ARM and susceptibility data were also used to ascertain magnetic grain size changes that help define detrital layers. The parameter  $k_{arm}$  (anhysteretic susceptibility), obtained by normalizing ARM intensity by the strength of the dc field used to acquire the ARM, was divided by volume susceptibility, to determine  $k_{arm}/k$ , a proxy for magnetite grain size.

On completion of the magnetic measurements on the u-channel samples, X-radiographs were taken across detrital layers, identified by u-channel magnetic measurements and carbonate analyses, to provide a picture of the internal structure of these layers and identify the presence or absence of traction structures. Discrete toothpick-sized samples, collected at 1-cm intervals across detrital layers, were used for smear slide observation (Table 4-2) and for measurement of magnetic hysteresis parameters using a Princeton Measurements Corp. vibrating sample magnetometer (VSM). Magnetic hysteresis parameters provide a means of estimating magnetite grain size, and therefore of recognizing grading in detrital layers.

Cores were sub-sampled for oxygen isotope analysis at 5-cm spacing. Samples from Core MD99-2227 were analyzed at GEOTOP (Montreal) while samples from the KN166-14 cores were analyzed in the stable isotope laboratory at Rutgers University. For all the cores, foraminifer shells of the planktonic species *Neogloboquadrina pachyderma* (left coiling) were picked in the 150-250  $\mu\text{m}$  fraction for the isotopic analyses. Planktonic foraminifer species were used for the isotopic analyses due to the small amount of benthos present in the cores. For Core MD99-2227, samples were collected at 5 cm intervals for carbonate analyses using an elemental analyzer.

Age models for the piston cores were constructed by matching relative geomagnetic paleointensity records and planktic  $\delta^{18}\text{O}$  records to target curves, with the location of magnetic excursions (Laschamp and Iceland Basin) providing additional age constraints. The combination of paleointensity records and oxygen isotope data provide enhanced temporal resolution compared to using either dataset independently.

### **NRM and Normalized Remanence Record**

The natural remanent magnetization (NRM) data for all four cores are shown as component inclination, corrected component declination, and maximum angular deviation (MAD) values (Figure 4-2). Cores were not oriented during collection, and therefore declination data were corrected by aligning the mean declination of each core to North. Twisting within cores during the coring process is indicated by anomalous declination changes in Core JPC18 (114.5-189 cm) (Figure 4-2). Core MD99-2227 is affected by stretching in the upper 7 meters that has significantly affected the magnetization directions (Figure 4-2).

## **Polarity Excursions**

Brief polarity excursions are a characteristic of the geomagnetic field, at least during the last ~2 Myr, and excursions of known age provide useful stratigraphic markers. Component magnetizations from u-channels indicate directional excursions at 9.3 meters below seafloor (mbsf) in Core JPC15, at 13.4 mbsf in Core JPC18, and at 18.7 mbsf in Core JPC19 (Figures 4-2 and 4-3). For Core JPC15, the observed excursion is correlated to the Laschamp excursion (~41 ka). For Cores JPC18 and JPC19, the observed excursion is correlated to the Iceland Basin excursion (~185 ka). Orthogonal projections of alternating field demagnetization data from intervals recording the Iceland Basin excursion in Cores JPC18 and JPC19 (Figure 4-3) indicate that the excursions are unambiguously recorded by u-channel samples and by discrete samples collected alongside the u-channel trough.

## **Relative Paleointensity**

It is generally accepted that the generation of useful paleointensity proxies requires that the sediments contain magnetite as the only NRM carrier. Also the sediment should have a narrow range of magnetite concentration, as indicated by magnetic concentration parameters varying by less than an order of magnitude, and have restricted magnetite grain-size in the few micron grain-size range, corresponding to pseudo-single domain grains (Tauxe, 1993). There is no evidence from demagnetization characteristics of NRM, or from hysteresis parameters, for high-coercivity magnetic minerals such as hematite or pyrrhotite. Using plots of anhysteretic susceptibility against susceptibility, and the calibration of King et al. (1983), we estimate that these sediments generally have magnetite grain sizes in the 1-10  $\mu\text{m}$  range (Figure 4-4). Records of ARM, IRM and susceptibility (Figure 4-5) show that the concentration parameters generally vary within an order of magnitude, the limit deemed suitable for determination of relative paleointensity proxies

(Tauxe, 1993). The exception is within the coarser-grained intervals in the early part of interglacials, where the concentration parameters vary by more than an order of magnitude.

NRM measured on u-channel samples was normalized using both ARM and IRM, demagnetized at the same peak fields as the NRM. To generate the paleointensity proxies, a mean of nine demagnetization steps in the 20-60 mT interval were used to calculate mean NRM/ARM and mean NRM/IRM. Although the two proxies are generally consistent with each other, mean NRM/ARM has the lower standard deviations and was therefore chosen as the preferred paleointensity proxy.

### **Chronology**

To construct age models for the four cores in this study, we correlate the planktonic oxygen isotope records to the benthic oxygen isotope stack (Lisiecki and Raymo, 2004). We then adjust this correlation to optimize the fit of the relative paleointensity records to the paleointensity record from ODP Site 983 (Channell et al., 1997; Channell, 1999). Following Stoner et al. (2003), the paleointensity and oxygen isotope data from ODP Site 1089 were used to improve the age model for ODP Site 983 particularly in the MIS 3-4 interval. For the Eirik Drift cores, a combination of oxygen isotope data and relative paleointensity data can produce a higher-resolution age model than would be possible using either data set independently.

The magnetic excursion recorded at 18.7 mbsf in JPC19 (Figures 4-2 and 4-3) is interpreted as the Iceland Basin excursion (Channell et al., 1997; Channell, 1999). It lies in a prominent paleointensity low at 185 ka in JPC19 (Figure 4-6), consistent with the expected age of this excursion. According to the age model, Core JPC19, from the crest of the drift at a water depth of 3184 m, has an age at its base of 300 kyrs with a mean sedimentation rate of 10.5 cm/kyr.

In Core JPC18, from southern flank of the Eirik ridge at a water depth of 3435 m, sediments coeval with interglacial periods are apparently missing, as shown by the lack of Holocene oxygen isotope values (Figure 4-7). MIS 5e is also absent in the record, because oxygen isotope values in this interval are too high for full interglacial values. The polarity excursion observed at 13.45 mbsf (Figures 4-2 and 4-3) is identified as the Iceland Basin excursion and it occupies a distinct paleointensity low at 185 ka (Figure 4-7), an age consistent with the observation of this excursion elsewhere. The overall mean sedimentation rate in Core JPC18 is 9 cm/kyr.

Core JPC15 was taken on the upper slope of Eirik ridge at a water depth of 2230 m. The polarity excursion observed at 9.3 mbsf in Core JPC15 (Figures 4-2 and 4-3) occurs within a prominent paleointensity low at ~ 40 ka (Figure 4-8) and is therefore interpreted as the Laschamp excursion. The base of JPC15 has an age of 160 ka and the mean sedimentation rate is 15 cm/kyr (Figure 4-8).

Core MD99-2227 shows significant stretching in the upper part of the core, however, the correlation to the calibrated ODP Site 983 paleointensity record is possible in the lower part (Figure 4-9). The paleointensity correlation is consistent with the correlation of the planktic oxygen isotope record to the benthic oxygen isotope stack of Lisiecki and Raymo (2005). These correlations give a basal age for Core MD99-2227 of 430 ka, and mean sedimentation rates of 10 cm/kyr (Figure 4-9).

### **Detrital Layer Stratigraphy**

The ratio of anhysteretic susceptibility to susceptibility ( $k_{arm}/k$ ) has been shown to be a useful magnetite grain size proxy (e.g. King et al., 1983; Tauxe, 1993). Although the plots of  $k_{arm}$  versus  $k$  of each core (Figure 4-4) indicate magnetic grain sizes within a restricted (few micron) range, the  $k_{arm}/k$  data plotted versus age (Figure 4-10) indicate distinct broad intervals of low

values of  $k_{\text{arm}}/k$  that coincide with the early Holocene (when recorded), with MIS 5e, and with the early parts of MIS 7, 9 and 11 (shaded in Figure 4-10). Low values of  $k_{\text{arm}}/k$  indicate relatively coarse magnetite grain sizes in these intervals. Although Core JPC18 is missing part of the Holocene, and almost the entire MIS 5e, the intervals of low values of  $k_{\text{arm}}/k$  appear to be partially recorded.

Volume magnetic susceptibility data measured on u-channel samples from Cores JPC19 and MD99-2227 show an increase in magnetic concentration in the early Holocene, MIS 5e, and in the early parts of MIS 7, 9 and 11 (Figure 4-10). These intervals of high magnetic concentration coincide with the intervals of low values of  $k_{\text{arm}}/k$  (Figure 4-10) that indicate relatively coarse magnetite grain sizes.

In Core JPC15, high sedimentation rates between 20-60 ka (500-1200 cm) allow the identification of millennial-scale cycles in volume magnetic susceptibility (Figure 4-5). These appear to mimic the D/O cycles the Greenland Ice Core (GISP) oxygen isotope record, and are reminiscent of susceptibility cycles identified by Kissel et al. (1999) in cores along the path of North Atlantic Deep Water (NADW), and attributed to changes in the strength of bottom currents. The depth of the WBUC, that varies in response to the relative outflows of water masses from the Greenland and Norwegian Seas, could also be account for the variations.

In addition to these broad decimeter-scale intervals defined by  $k_{\text{arm}}/k$  and  $k$  values, a total of seventeen cm-scale layers with magnetic properties and percent carbonate values significantly different from the surrounding sediments have been identified in MD99-2227 (Figure 4-11). These layers have been labeled according to marine isotope stage and their detrital carbonate (DC) content. For example, 6LDC indicates a low detrital carbonate (LDC) layer within MIS 6 (Table 4-2).

Eight of the seventeen cm-scale layers are designated detrital carbonate layers (DC) on the basis of their high detrital carbonate contents. Four of these layers (3DC, 7DCa, 8DC, 11DC) are recognized by coarser grained magnetic material (compared to the background sediment), as indicated by low  $k_{arm}/k$  values (Figure 4-11). One of these DC layers (7DCa) shows a peak in magnetic susceptibility while the other seven DC layers do not. Two DC layers (5DC, 9DC) show finer-grained magnetic material (compared to background sediment), and two DC layers (7DCb, 2DC) are not differentiated by magnetic grain size from the background sediment but all DC layers coincide with highs in percent carbonate and six show peaks in GRA bulk density (Figure 4-11). All DC layers are light in color, do not show a sharp base, and appear to show some bioturbation. The X-radiographs of these layers confirm a high concentration of IRD, but no laminae or evidence for traction (Figure 4-12). Smear slides indicate a high percentage of coarse detrital carbonate material in these layers (Table 4-2).

Nine of the seventeen cm-scale detrital layers are designated low detrital carbonate (LDC) layers (Figure 4-11). These do not feature an increase in percent carbonate, but show a peak in magnetic susceptibility, a low in  $k_{arm}/k$ , and an increase in GRA bulk density. These LDC layers occur within MIS 1, 2, 5, 6, 7, 9 and 11 and show sharp bases, bioturbated tops and are 4-18 cm thick (Figure 4-11, Table 4-2). The X-radiographs indicate a sharp base and laminae within the layers (Figure 4-12), some of the laminae are inclined and indicative of traction, implying rapid deposition from turbidity currents or contourites.

Toothpick-sized samples collected at 1-cm intervals through detrital layers were used to determine magnetic hysteresis parameters that can be used as a means of assessing the grain size of magnetite (Day et al., 1977). All but one of the detrital layers exhibit hysteresis parameters that fall within the pseudo-single domain (PSD) grain size range (Figure 4-13). The detrital

carbonate layer identified in MIS2 (2DC) shows coarse multi-domain magnetite that is anomalous compared to all other detrital layers (Figure 4-13). For five of the nine LDC layers, we see evidence for progressive change in hysteresis parameters through the detrital layer indicative of grading, fining upward from the base of the layer. Bioturbation of the detrital layer into the overlying sediment could also cause the layer to appear graded. However, the presence of distinct laminae within the LDC layers shows that no bioturbation of the layer has occurred. None of the DC layers show this “grading” in hysteresis parameters. The presence of grading in the LDC layers indicates a turbiditic rather than a contourite origin for these layers.

Smear slides indicate that LDC layers contain little clay and significant amounts of silt-sized opaque grains, green hornblende and quartz. Trace amounts of detrital carbonate are present in LDC layers and throughout the rest of the core, whereas the percentage of detrital carbonate in the DC layers exceeds 10% (Table 4-2).

### **Discussion**

Sedimentation rates on the Eirik Drift have been shown to be greatly affected by changes in the strength and bathymetry of the Western Boundary Undercurrent (WBUC) that is thought to be switched off during glacials and active during interglacials (Hillaire-Marcel et al., 1994; Hillaire-Marcel and Bilodeau, 2000). The core of this current is thought to occupy water depths between 2500 and 3000 meters (Hillaire-Marcel et al., 1994), resulting in winnowing and almost complete removal of Holocene and MIS 5e sediment from these depths. Cores from outside the influence of the flow would be expected to have interglacial sedimentation rates comparable to, or higher than, glacial sedimentation rates.

When combined with previous studies carried out on the drift, the new results indicate that both water depth and position on the drift influence interval sedimentation rates. Although the site of Core JPC18 is located ~450 meters below the supposed core of the WBUC, sediment of



Holocene and MIS 5e age is missing at this site. This implies that the WBUC is active at deeper water depths than previously supposed on the southern side of the Eirik ridge (Figure 4-1). This may be consistent with a deep branch of the WBUC, with a gyre in the outer Labrador Sea that feeds the Gloria Drift (Figure 4-1).

Cores HU90-013-013 (water depth 3471 m), JPC19 (water depth 3184 m) and MD99-2227 have relatively high Holocene sedimentation rates of 35 cm/kyr, ~13 cm/kyr, and 10 cm/kyr respectively. Sedimentation rates in cores MD99-2227 and JPC19 appear to be low at the onset of deglaciation and then increase. This may be due to increased winnowing by the WBUC at the onset of the deglaciation, offset by increased detrital input as the deglaciation proceeds.

Core HU90-013-012 at 2830 meters water depth lies within the influence of the WBUC and has very low sedimentation rates in the Holocene (Stoner et al., 1995a, 1996). Higher up the slope, Core JPC15 at a water depth of 2230 meters has low sedimentation rates in the Holocene and MIS 5e, although the site supposedly lies outside the main influence of the WBUC. Hillaire-Marcel et al. (1994) noted that, in core HU90-013-06 at even shallower water depths (1105 m) on the Eirik ridge, active bottom currents also resulted in very low Holocene sedimentation rates.

Hillaire-Marcel et al. (1994) interpreted DC and LDC layers deposited during the last glacial cycle at Orphan Knoll, on the western side of the Northwest Atlantic Mid-Ocean Channel (NAMOC), as being related to ice advances of the Laurentide Ice Sheet that triggered turbiditic flows down the NAMOC (Figure 4-1). Sediment suspended by these flows is thought to have deposited cm-scale sandy mud beds rich in detrital carbonate (DC layers) at Orphan Knoll. Not all the detrital layers observed at Orphan Knoll are recognized on Eirik Drift, although two LDC layers and one DC layer in Core HU90-0130-013 (Figure 4-1) were considered coeval with Orphan Knoll detrital layers (Stoner et al., 1996).

The cm-scale detrital layers identified in core MD99-2227 extend the record of detrital layers beyond the last glacial cycle. Detrital layers on Eirik Drift occur during both glacial and interglacial conditions. However, the layers occurring in the interglacials are close to the Terminations in the Holocene, MIS 5, 7 and 11. It is only in MIS 9 that the DC layer appears to occur in the later part of the interglacial implying that the Laurentide Ice Sheet was present throughout MIS 9.

Detrital layer 1LDC with an age of 13 ka in MD99-2227 (Table 4-3) is tentatively correlated to DC0 of Stoner et al. (1998). Layer 2LDC has an age of 18 ka and is correlated to DC1 (16 ka) from Orphan Knoll (Stoner et al., 1998) and with H1 of Bond et al., (1999) from the central Atlantic. The DC layer 2DC correlates with DC2 of Stoner et al. (1998) and with H2 (Bond et al., 1999). The detrital layer labeled 3DC (39 ka) is correlated to DC4 from Orphan Knoll and to H4 (38 ka). As discussed above, the characteristics of LDC layers implies deposition by turbidity currents (derived from the Greenland Slope). If so, this turbiditic activity is sometimes coeval with Heinrich layers of the central Atlantic and with detrital events at Orphan Knoll.

The ages of layers designated 2LDC, 2DC and 3DC in this study are consistent with ages for Heinrich events H1, H2, and H4 (Table 4-3). No identifiable events that coeval with Heinrich events H3, H5 or H6 are found. Hiscott et al. (2001) identified Heinrich-like detrital layers in core MD95-2025 from near Orphan Knoll back to MIS 9. Two detrital carbonate layers within early MIS 5 at Orphan Knoll (H8 and H9 of Hiscott et al., 2001) appear to be coeval with DC events identified on Eirik Drift, implying that instabilities of the Laurentide Ice Sheet are recorded at both sites. Detrital carbonate layers within MIS 7 and MIS 9 at Orphan Knoll (H10 and H13 of Hiscott et al., 2001) are coeval with a LDC layers (7LDC and 10 LDC) identified on

Eirik Drift (Table 4-3), implying that the LIS instabilities that triggered the detrital carbonate layers at Orphan Knoll were coeval with instabilities on the Greenland slope that triggered the LDC layers on Eirik Drift. Such conclusions are highly dependent on the resolution of stratigraphic correlation. While stratigraphic correlation of detrital layers from the Orphan Knoll to the central Atlantic for the last glacial cycle is rather well constrained (Bond et al., 1999; Stoner et al., 1996, 2000), the correlations beyond the last glacial cycle are considerably more speculative (e.g. Hiscott et al., 2001; van Kreveld et al., 1996) due to lack of stratigraphic resolution that inhibits unequivocal correlation of detrital layers.

### **Conclusions**

Piston cores collected from Eirik Drift have produced records of relative paleointensity and of the Laschamp and Iceland Basin polarity excursions that augment oxygen isotope data for generating age models. Magnetic data from cores JPC19 and MD99-2227 show broad intervals of increased magnetic grain size and concentration during MIS 5e and at the MIS 2/1 transition, consistent with observations from Core HU90-013-013 (Stoner et al., 1995b). Core MD99-2227 also shows a similar increase in magnetic grain size and concentration at the onset of interglacial MIS 7, 9 and 11, implying that retreat of the Greenland Ice Sheet produced a characteristic detrital signal at the onset of all interglacial stages over the last 400 kyr.

Seventeen cm-scale detrital carbonate and low detrital carbonate layers are identified in MD99-2227 (Figure 4-11, Table 4-2). They occur in both glacial and interglacial stages. The detrital layers can be subdivided into two classes. Detrital carbonate (DC) layers are composed of carbonate-rich IRD. They usually, but not always, carry a magnetic signal indicating high magnetic concentration and increased magnetic grain size relative to background sediment. Low detrital carbonate (LDC) layers have <10% detrital carbonate, usually show evidence (from magnetic hysteresis ratios) for fining-upward grading, and X-radiograph evidence for traction.

These layers are also usually marked by high magnetic concentration and increased magnetic grain size relative to background sediment.

Based on the differences between DC and LDC layers, we interpret the former as Hudson Strait derived detrital layers, and the latter as layers dominated by material from turbidites derived from the Greenland slope. 1LDC, 2LDC, 2DC and 3DC are correlative with detrital layers observed at Orphan Knoll (Stoner et al., 1996) (Table 4-3). Three of them (1LDC, 2DC and 3DC) are coeval with central Atlantic Heinrich layers H1, H2 and H4 (Bond et al., 1999). Beyond the last glacial cycle, the correlation of detrital layers from Eirik Drift (this paper) to Orphan Knoll (Hiscott et al., 2001) and to the central Atlantic (van Kreveld et al., 1996) is limited by the imprecision of stratigraphic correlation (Table 4-3). Nonetheless, as illustrated here, the use of paleointensity-assisted chronostratigraphy, the combination of relative paleointensity with standard oxygen isotope stratigraphy, improves stratigraphic correlations across the northern North Atlantic Ocean (and beyond), and thereby facilitates the interpretation of detrital layers in terms of their correlation, aerial extent and provenance.

Table 4-1. Core, latitude, longitude, water depth and base age of the core.

Core	Latitude	Longitude	Water depth	Base age (kyr)
JPC15	-45.57	58.20	2230	150
JPC18	-47.13	57.19	3435	300
JPC19	-47.60	57.58	3184	250
MD99-2227	-48.22	58.12	3460	430

Table 4-2. DC and LDC layer properties in Core MD99-2227.

event	Thick- ness (cm)	depth (cm)	Age (ka)	MIS	Name	k peak	k <sub>arm</sub> /k	% carb	GRAPE density	% detr. carb.	X-Ray	Sharp base	Grading
1	5	440.22	13.04	1/2	1LDC	yes	coarse	low	peak	10	traction	yes	yes
2	14	616.85	18.2	2	2LDC	yes	coarse	low	peak	trace	traction	yes	yes
3	15	663	21.4	2	2DC	no		high	peak	15		no	no
4	21	858.7	39.1	3	3DC	no	coarse	high	peak	40		no	no
5	6	1872.3	111.68	5	5LDC	yes	coarse	low	peak	trace		yes	no
6	16	2019.4	129.34	5	5DC	no	fine	high	peak	70		no	no
7	14	2192.9	152.17	6	6LDC	yes	coarse	low	peak	trace	traction	yes	yes
8	16	2505.4	191.58	7	7DCa	yes	coarse	high		20		no	no
9	12	2700	214.98	7	7DCb	no		high	peak	25		no	no
10	6	2872.3	233.42	7	7LDC	yes	coarse	low	peak	trace	traction	yes	no
11	11	3083.7	266.57	8	8DC	no	coarse	high	peak	20		no	no
12	17	3229.2	289.89	9	9DC	no	fine	high	peak	30		no	no
13	5	3536.4	335.6	9/10	9LDC	yes	coarse	low	peak	trace	traction	yes	no
14	18	4008.2	391.03	11	11LDCa	yes	coarse	low	peak	trace	traction	yes	no
15	4	4084.2	403.48	11	11LDCb	yes	coarse	low	peak	5	traction	yes	yes
16	7	4133.7	409.57	11	11LDCc	yes	coarse	low	peak	10	traction	yes	yes
17	7	4240	421.43	11	11DC	no	coarse	high	peak	50	IRD rich	no	no

Table 4-3. Detrital Layers from other studies considered to be correlative to detrital layers identified on Eirik drift.

Event	Name	depth (cm)	MD99-2227 Age (ka)	Stoner et al. (1998) (age ka)	H-layers Bond et al. (1999) (age ka)	Hiscott et al (2001) (age ka)	Van Kreveld et al (1996) (age ka)
1	1LDC	440.22	13.04	DC0 (12)		H1(11-12)	h1 (15)
2	2LDC	616.85	18.2	LDC1 (18)	H1 (16.8)		
3	2DC	663	21.4	LDC3 (21)	H2 (24)	H2 (18-22)	h2 (21)
4	3DC	858.7	39.1	DC4 (36)	H4 (38)	H4 (39-42)	h4 (40-43)
5	5LDC	1872.3	111.68			H8(92-108)	
6	5DC	2019.4	129.34			H9(121-126)	h7 (128-131)
7	6LDC	2192.9	152.17				
8	7DCa	2505.4	191.58				h12 (189)
9	7DCb	2700	214.98				
10	7LDC	2872.3	233.42			H10(231-240)	
11	8DC	3083.7	266.57				
12	9DC	3229.2	289.89				
13	9LDC	3536.4	335.6			H13(335-340)	
14	11LDCa	4008.2	391.03				
15	11LDCb	4084.2	403.48				
16	11LDCc	4133.7	409.57				
17	11DC	4240	421.43				

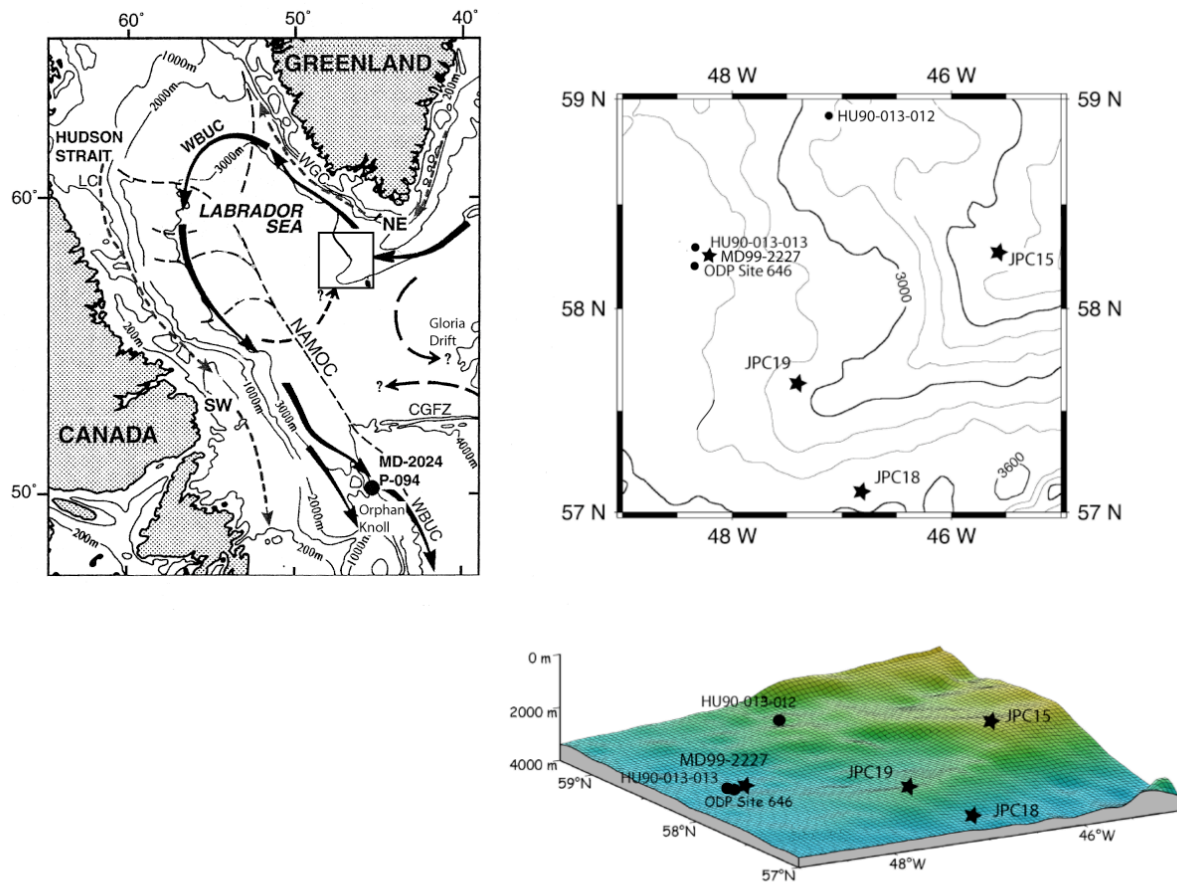


Figure 4-1. Location map showing the Labrador Sea from Hillaire-Marcel and Bilodeau (2000) and the location of piston cores JPC15, JPC18, JPC19, and MD99-2227. Black arrows indicate the path of the Western Boundary Undercurrent. NAMOC: Northwest Atlantic Mid-Ocean Channel.



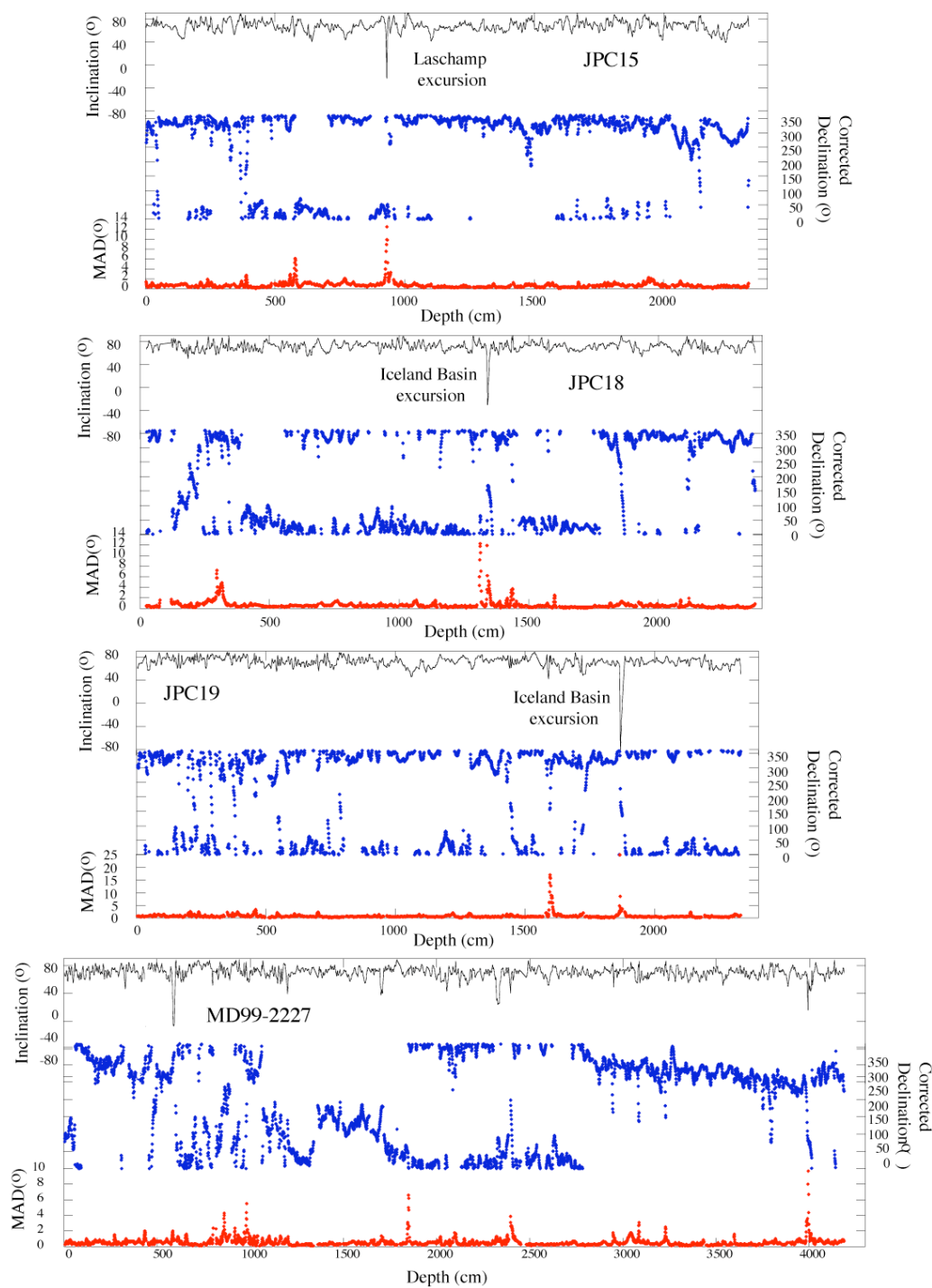


Figure 4-2. Component inclination, corrected component declination and maximum angular deviation (MAD) values for cores JPC15, JPC19, JPC18 and MD99-2227.

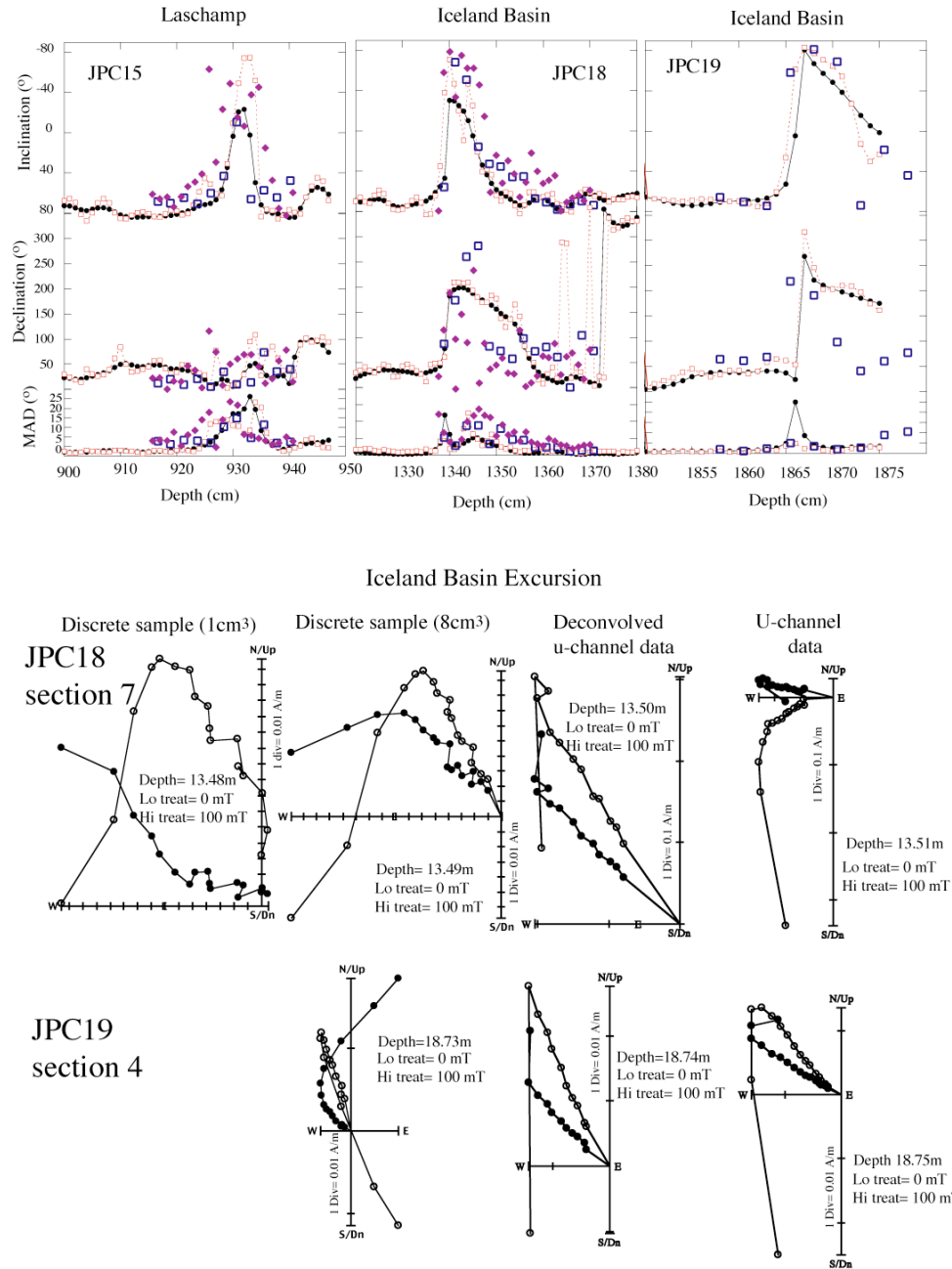


Figure 4-3. a). Component inclination, declination and maximum angular deviation (MAD) values recording Laschamp and Iceland Basin polarity excursions from piston cores JPC15, JPC18 and JPC19. Key: U-channel data (closed circles), deconvolved u-channel data (open squares-dashed line) using the method of Guyodo et al. (2003), 8-cm<sup>3</sup> discrete sample cubes (open squares) and 1-cm<sup>3</sup> cubes (diamonds).3b). Orthogonal projections from the Iceland Basin excursion from cores JPC19 and JPC18, from u-channel data, deconvolved u-channel data, and discrete samples. Open circles represent the vector end point projection on the vertical plane. Closed circles represent the vector end point projection on the horizontal plane.

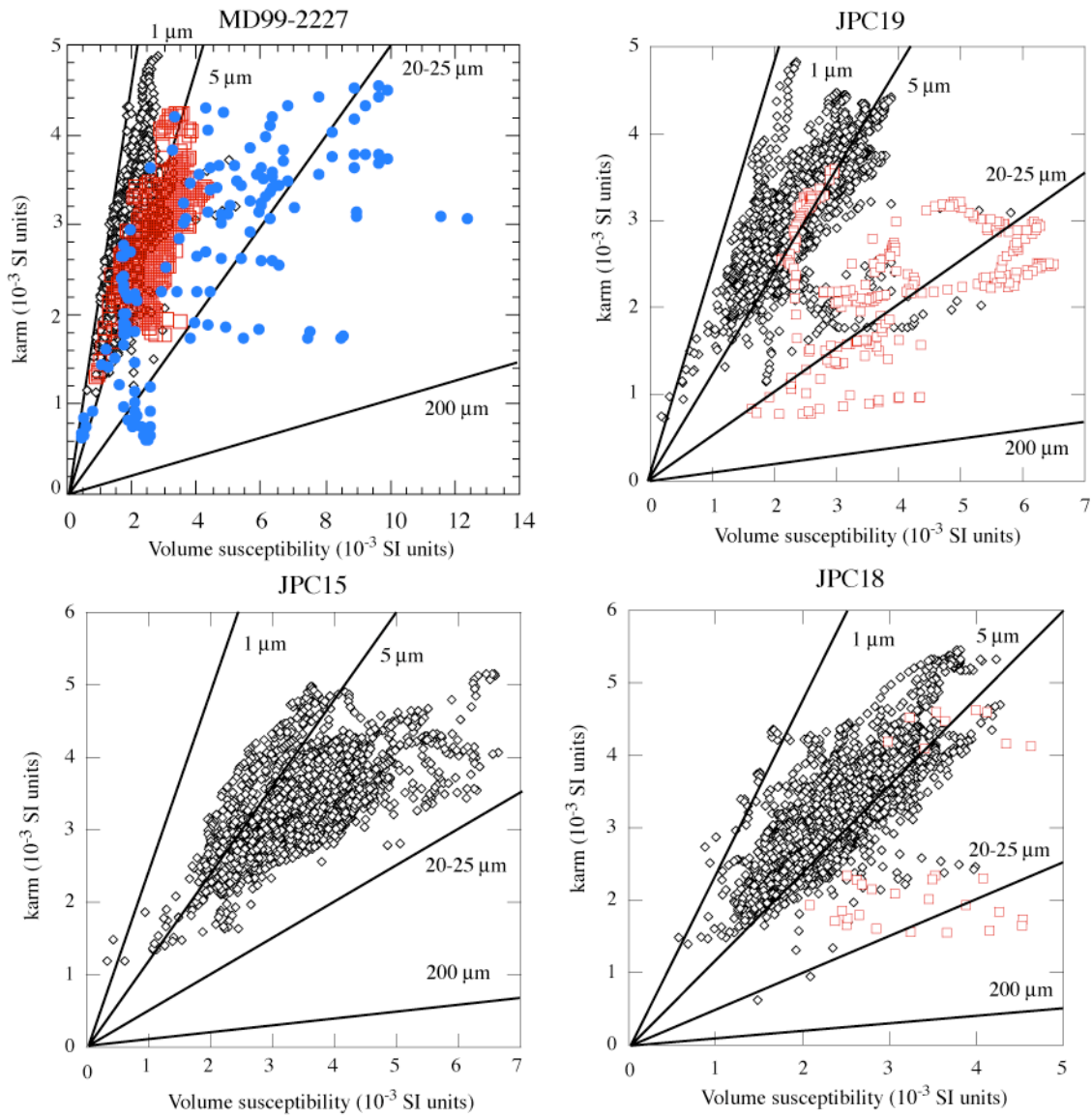


Figure 4-4. Anhyseretic susceptibility ( $k_{arm}$ ) plotted against volume susceptibility ( $k$ ) for JPC18, JPC19, JPC15 and MD99-2227. Diamonds indicate 'background' sediment, red squares indicate coarse decimeter-scale interglacial intervals, and blue circles indicate cm-scale detrital layers. Black lines indicate magnetic grain-size boundaries placed using the calibration of King et al. (1983).

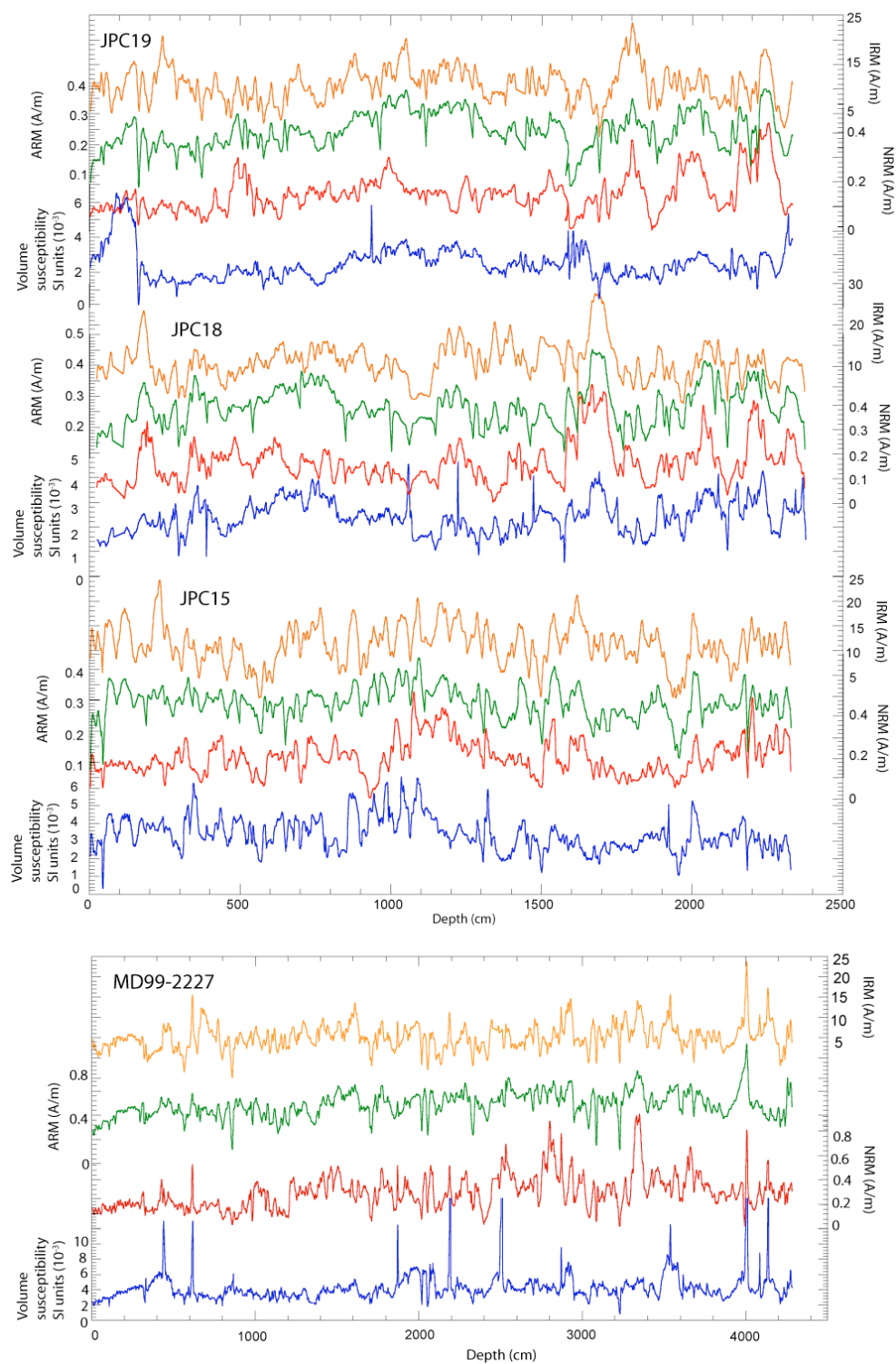


Figure 4-5. NRM, ARM, IRM and volume susceptibility for MD99-2227, JPC15, JPC18 and JPC19. Orange-IRM, green-ARM, red-NRM, blue-volume susceptibility.

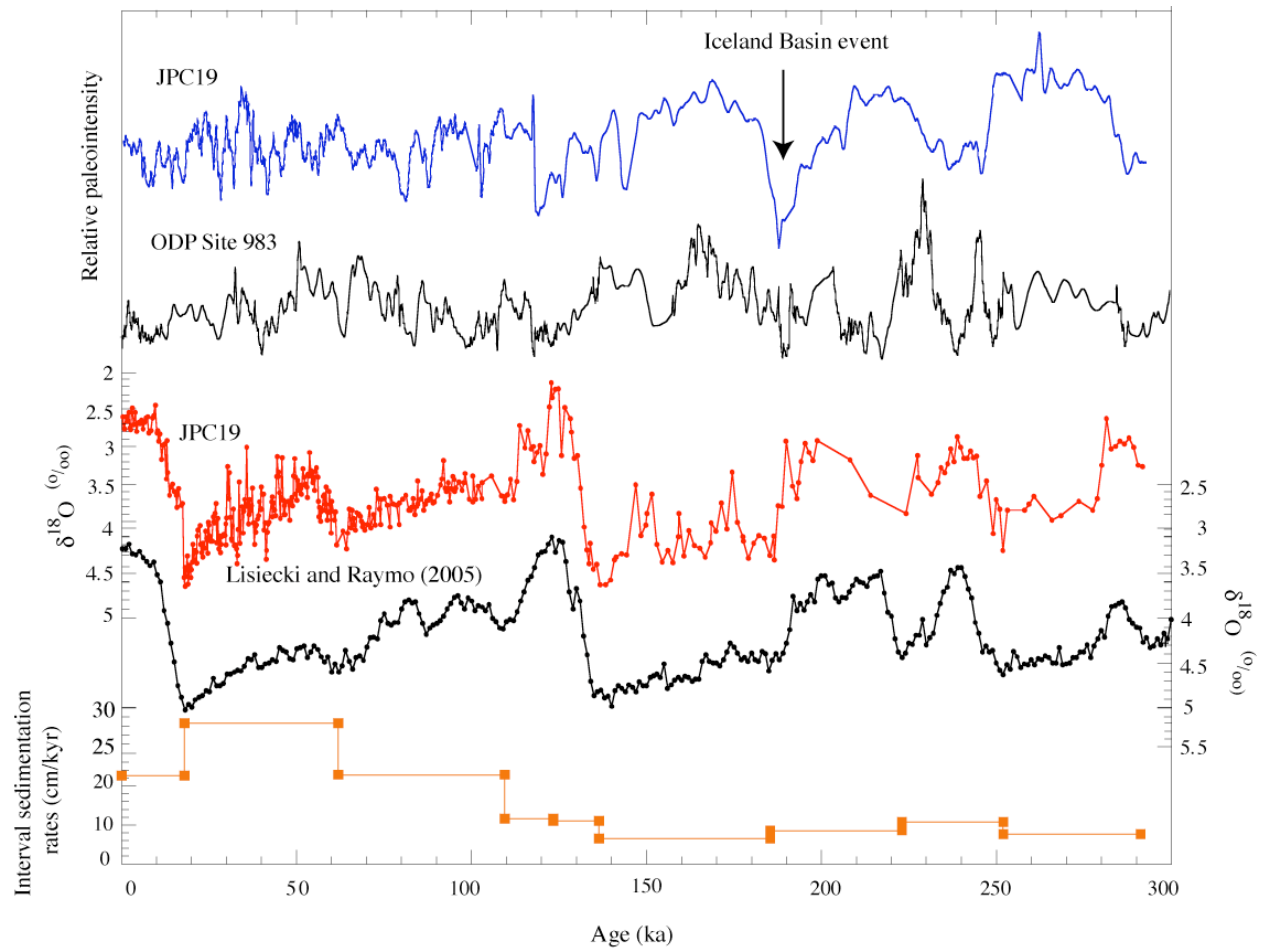


Figure 4-6. JPC19: Relative paleointensity record correlated to that from ODP Site 983 (Channell et al., 1997; Channell, 1999). Lower plot: planktic  $\delta^{18}\text{O}$  data from JPC19 correlated to the benthic  $\delta^{18}\text{O}$  stack of Lisiecki and Raymo (2005). Interval sedimentation rates are shown in orange.

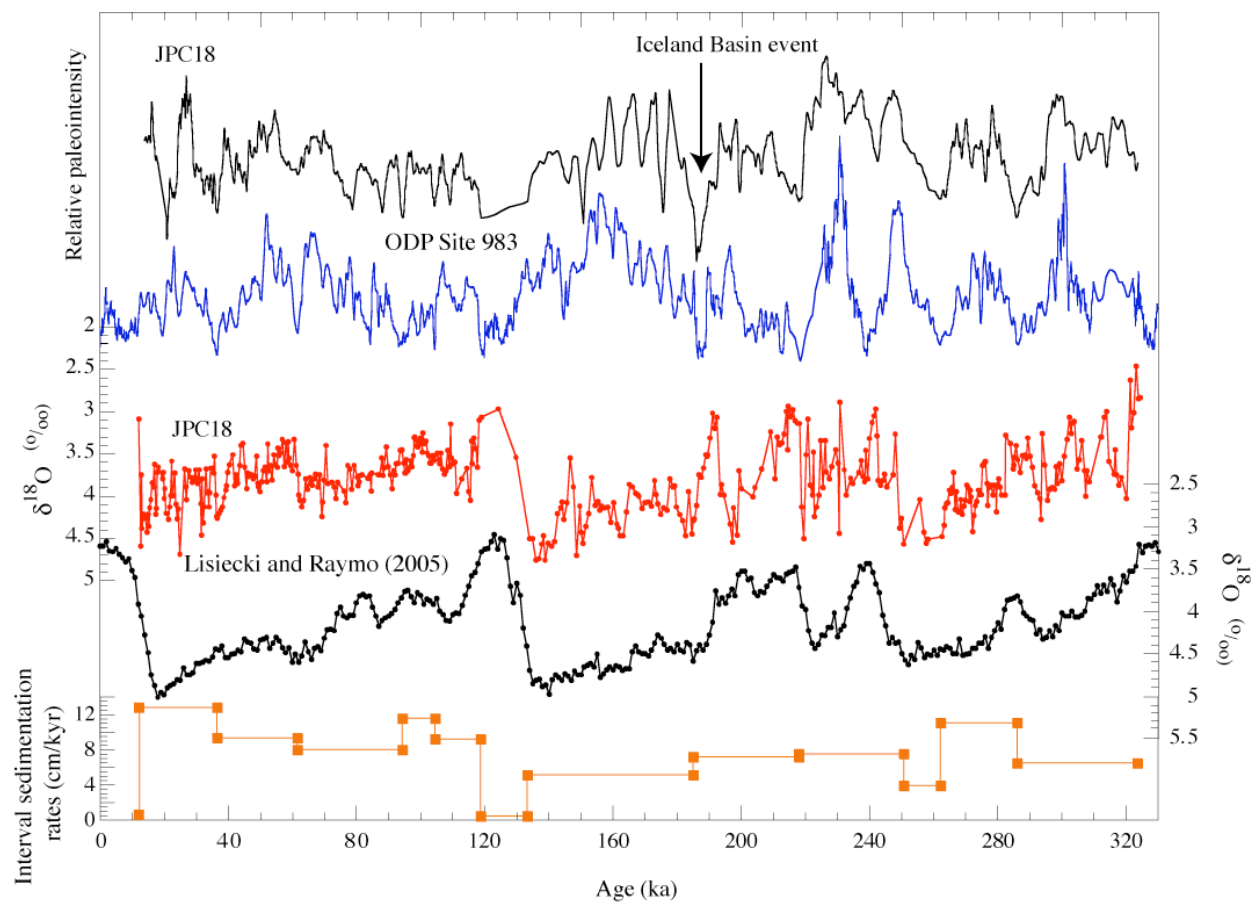


Figure 4-7. JPC18: Relative paleointensity data correlated to ODP Site 983 (Channell et al., 1997; Channell, 1999). Lower plot shows planktic  $\delta^{18}\text{O}$  data correlated to the benthic  $\delta^{18}\text{O}$  stack of Lisiecki and Raymo (2005). Interval sedimentation rates are shown in orange.

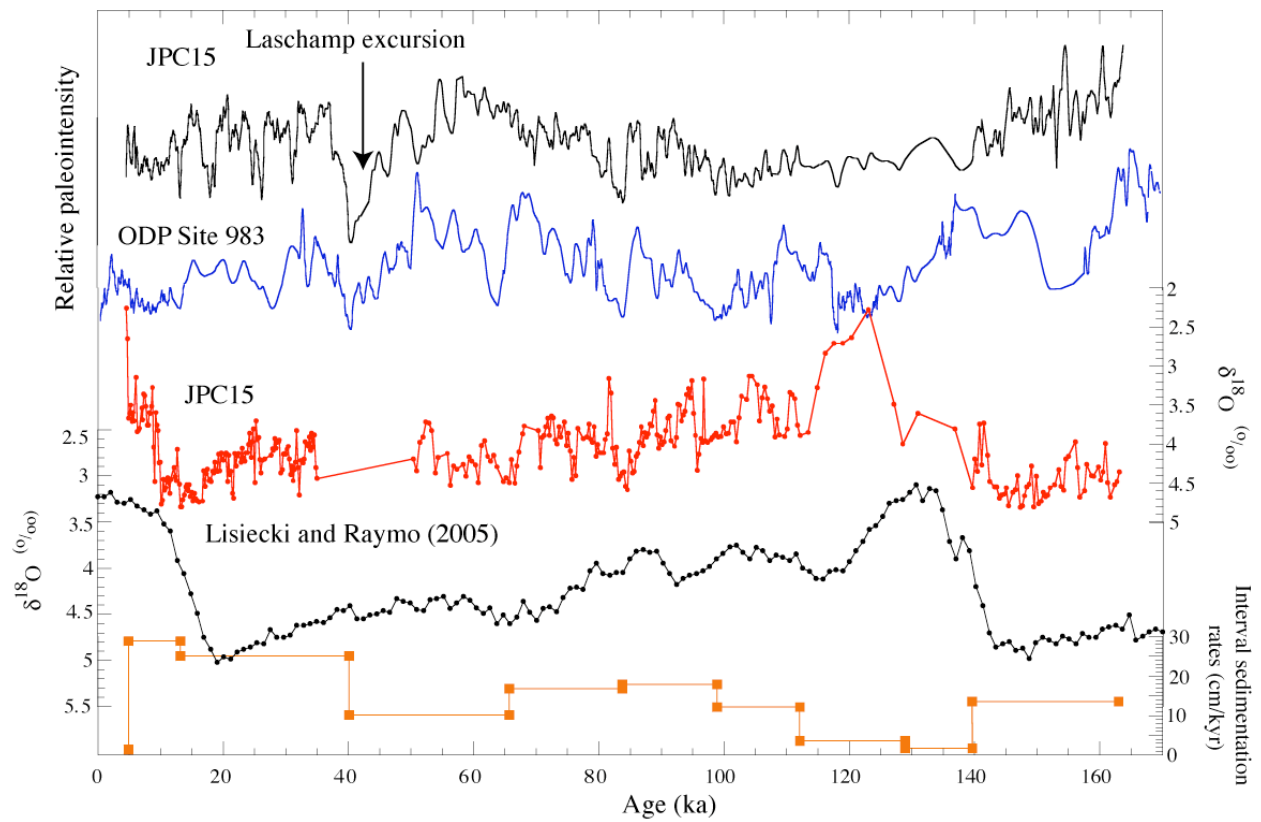


Figure 4-8. JPC15: Relative paleointensity data correlated to ODP Site 983 (Channell et al., 1997; Channell, 1999). Lower plot shows planktic  $\delta^{18}\text{O}$  data correlated to the benthic  $\delta^{18}\text{O}$  stack of Lisiecki and Raymo, (2005). Interval sedimentation rates are shown in orange.

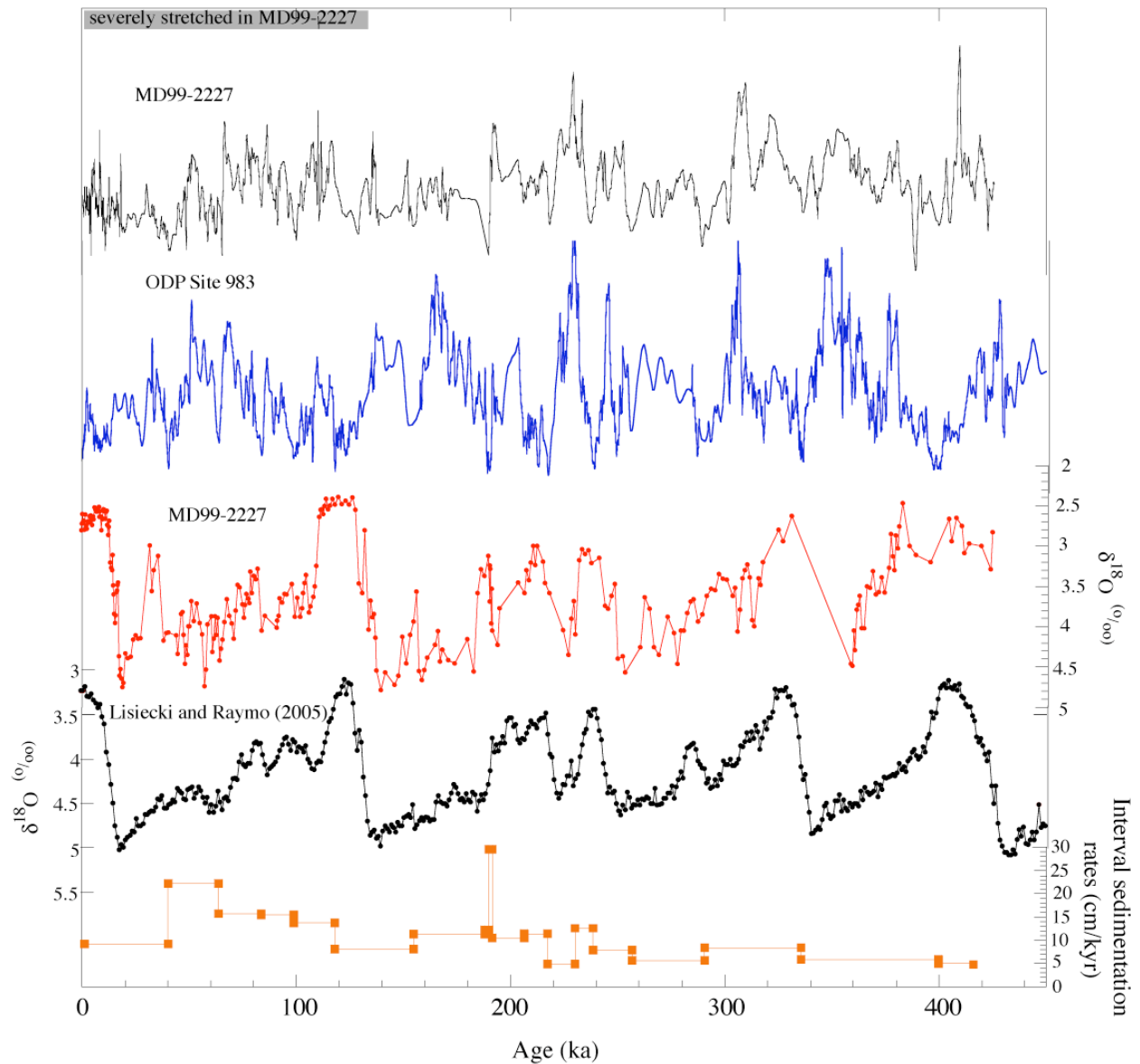


Figure 4-9. MD99-2227: Relative paleointensity data correlated to ODP Site 983 (Channell et al., 1997; Channell, 1999). Lower plot shows planktic  $\delta^{18}\text{O}$  data correlated to the benthic  $\delta^{18}\text{O}$  stack of Lisiecki and Raymo (2005). Black bar indicates stretched interval due to coring. Interval sedimentation rates are shown in orange.



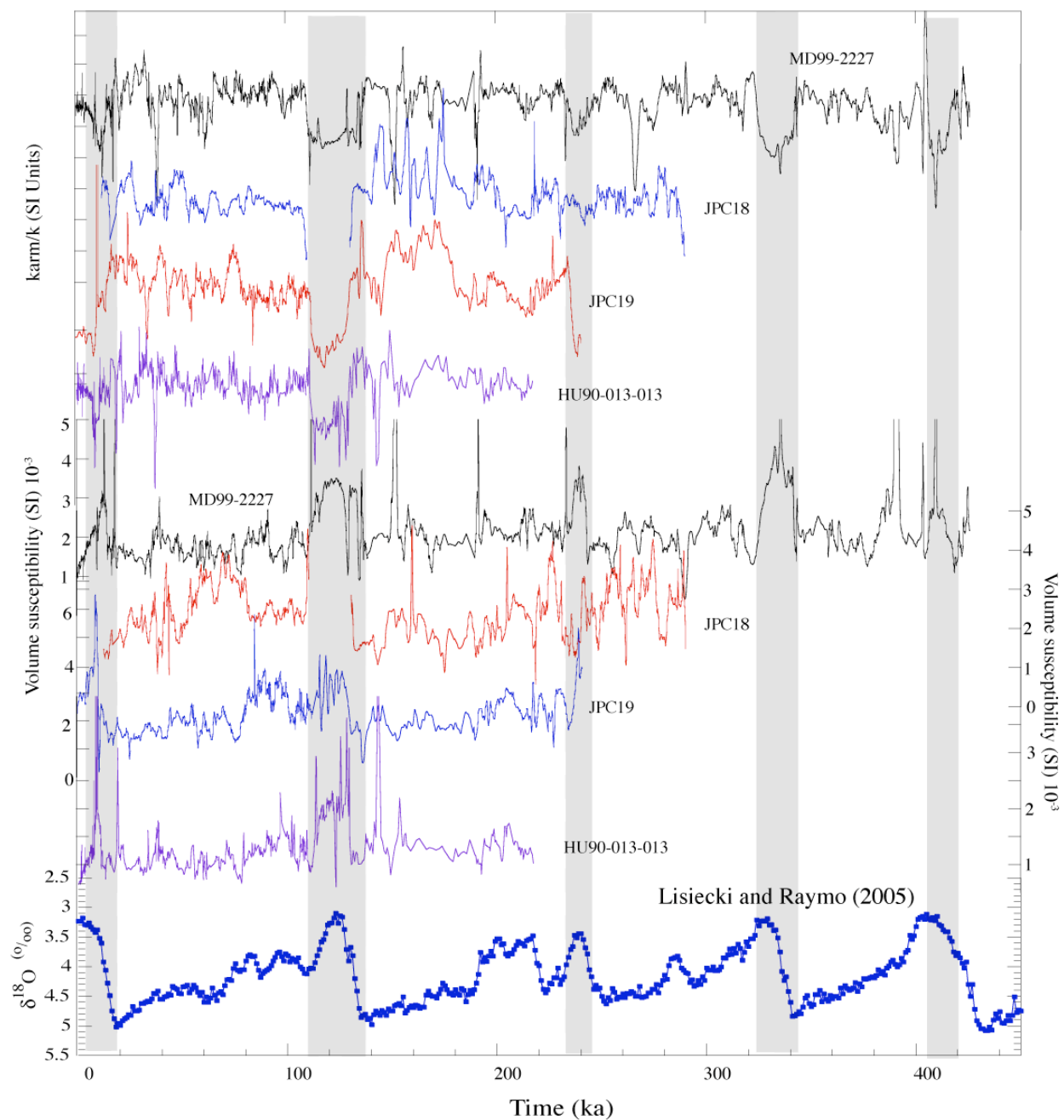


Figure 4-10.  $k_{arm}/k$  and magnetic susceptibility versus age for cores, JPC19, JPC18 and MD99-2227 compared to Core HU90-013-013 (Stoner et al., 1995a). The benthic oxygen isotope stack of Lisiecki and Raymo (2005) is shown at the bottom of the figure. Shaded areas indicate magnetic coarse grain-size intervals (from  $k_{arm}/k$ ) and magnetic concentration intervals (from susceptibility) in early and peak interglacial intervals.

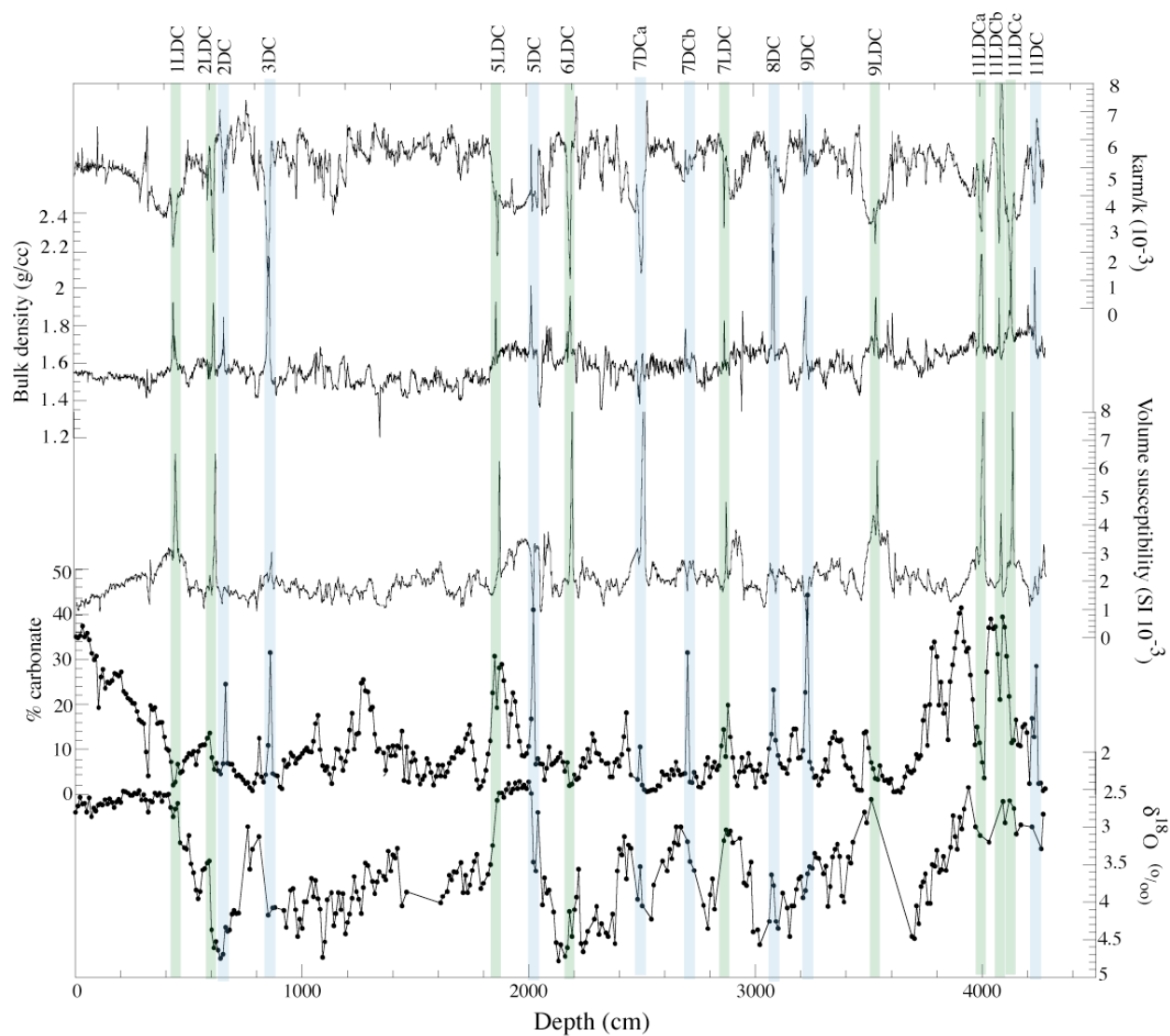


Figure 4-11. Core MD99-2227:  $k_{arm}/k$ , magnetic susceptibility, bulk (GRAPE) density, percent carbonate, and planktic oxygen isotope data. Blue shading indicates detrital carbonate (DC) layers and green shading indicates low detrital carbonate (LDC) layers.

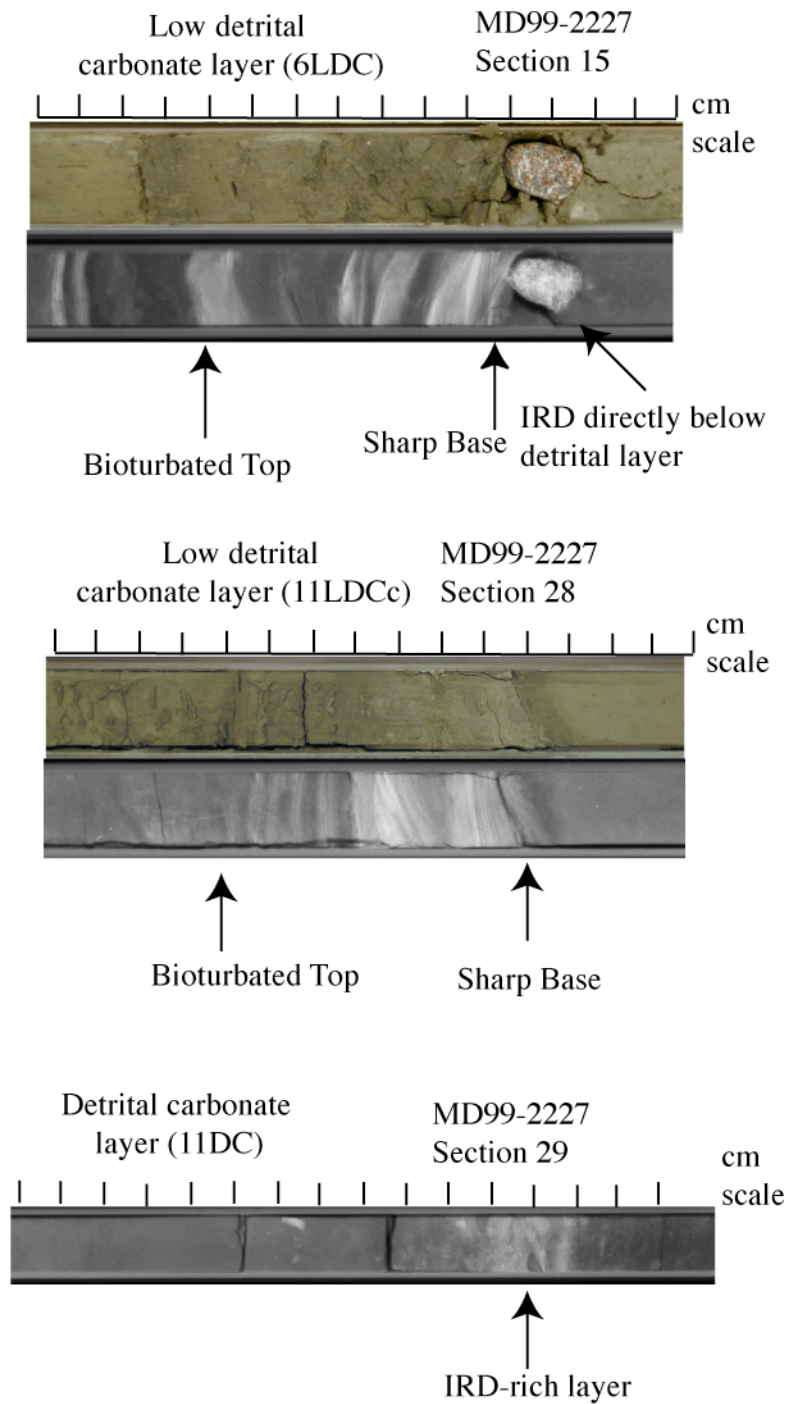


Figure 4-12. Photographs and X-radiographs of three detrital layers identified in MD99-2227. Upper: MD99-2227 section 15 (6LDC), middle: MD99-2227 section 28 (11LDCc), and lower: MD99-2227 section 29 (11DC). In X-radiographs, light color indicates higher density, dark color indicates lower density.

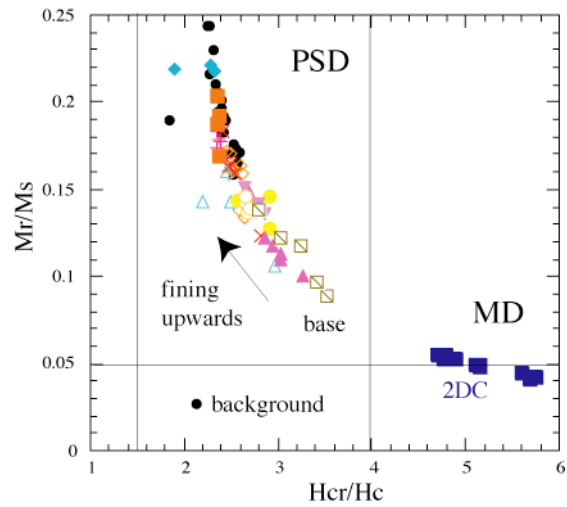


Figure 4-13. Hysteresis ratios  $M_r/M_s$  plotted versus  $H_{cr}/H_c$  (after Day et al., 1977): individual detrital layers from MD99-2227 are shown by colored symbols, with direction of upward fining indicated by arrow. Black circles indicate background sediment.

CHAPTER 5  
RELATIVE PALEOINTENSITY STACK FOR THE LAST 85 KYR ON A REVISED GISP  
CHRONOLOGY, AND ENVIRONMENTAL MAGNETISM OF THE GARDAR DRIFT

**Introduction**

Four cores were collected in the summer of 2002 along a NE-SW transect along the Gardar Drift, at water depths from 1880 m to 3082 m. Chronologies for the cores were developed using relative paleointensity proxies and a benthic oxygen isotope record from the southernmost piston core (JPC13). The magnetic grain size proxy  $k_{\text{arm}}/k$  mimics benthic  $\delta^{18}\text{O}$ , particularly in the northern and southern sites, indicating a link between magnetic grain size and bottom water activity. The benthic  $\delta^{18}\text{O}$  record from Core JPC13 can be correlated to a similar record from core MD95-2042 from the Portuguese Margin, which has been correlated to both the Greenland Ice Core (GISP) and Vostok ice core records. As a result of this correlation, the relative paleointensity records can be placed on the Shackleton-revised GISP chronology. A stack of 11 relative paleointensity records from the North Atlantic region for the 0-85 ka interval has been developed and placed on the revised GISP chronology. This stack (EHC06) shows some significant differences particularly in the 0-30 ka interval when compared to the Global Paleointensity Stack (GLOPIS). At 60 ka, when compared to both GLOPIS and the North Atlantic Paleointensity Stack (NAPIS), there is a difference in the age models of ~2400 years. The EHC06 stack is in better agreement with the independently dated South Atlantic Paleointensity Stack (SAPIS).

Sedimentary relative paleointensity (RPI) records can provide important constraints on mechanisms in the geodynamo, can shed light on proposed geomagnetic-climate linkages, and may provide a means of high-resolution global stratigraphic correlation. High-resolution chronological control is critical for the study of millennial-scale climate change and RPI records provide a potential means of global high-resolution correlation. When oxygen isotope

stratigraphy is combined with RPI records, the combination provides more robust, higher resolution age control than either data set alone. Stacks of RPI records allow the recognition of regionally characteristic RPI features although the stacking process undoubtedly filters out the higher frequency components. The North Atlantic Paleointensity Stack (NAPIS) was constructed from six relative paleointensity records from the North Atlantic (Laj et al., 2000). Chronological control for the NAPIS stack was based on correlation of the oxygen isotope stratigraphy from Core PS2644-5 to the GISP2  $\delta^{18}\text{O}$  record, allowing the stack to be placed on a GISP2 timescale. The NAPIS stack was augmented by addition of records from the North Atlantic, South Atlantic, Indian Ocean and Mediterranean to generate the Global Paleointensity Stack (GLOPIS) of Laj et al. (2004). This stack was synchronized with NAPIS, and therefore placed on the same GISP2 chronology.

Changes over glacial to interglacial cycles in deep and intermediate water circulation may have caused changes in the speed of bottom currents that may be detected in magnetic mineral concentrations and grain size. Magnetic susceptibility and other magnetic concentration parameters from around the North Atlantic Basin, along the path of NADW, have been shown to record changes during MIS 3 that can be correlated to Dansgaard-Oeschger (D/O) events in the Greenland ice cores (Kissel et al., 1999). Lower North Atlantic Deep Water (NADW) production is believed to have increased during interglacials and decreased during glacial periods (Broecker and Denton, 1989). At the present time, a major contributor to NADW is Iceland-Scotland Overflow Water (ISOW) that flows across the Gardar Drift from NE to SW at depths of ~1800-3000 meters (Bianchi and McCave, 2000). At deeper water depths (>3000 meters) in the southern section of the drift, Lower Deep Water (LDW) of southern hemisphere origin has been identified at the sea floor (Bianchi and McCave, 2000) by its high Si content (McCartney, 1992).

Upper NADW is found at water depths shallower than 2000 m in the North Atlantic and is defined by a silicate minimum and salinity maximum (Kawase and Sarmiento, 1986).

In this study we present records of relative paleointensity and benthic oxygen isotopes from a transect across the Gardar Drift, roughly along the path of NADW that forms a loop around the drift (Figure 5-1). A new relative paleointensity stack has been developed using three new relative paleointensity records from this work and eight published records (Table 5-1). Magnetic property data show significant changes across the drift that can be related to changing water masses and bottom current speed.

### **Site Locations**

The Gardar Drift rests on a basement high on the east side of the mid-ocean ridge and stretches for about 1100 km from its northeastern end south of Iceland (<1500 m water depth) to the southwestern end, just north of the Charlie Gibbs fracture zone (>3000 m water depth) (Bianchi and McCave, 2000) (Figure 5-1). The Gardar Drift is being formed by deposition from deep currents transporting detritus from Iceland and the nearby European landmass, thereby creating a smooth, thick, eastward-dipping sediment cover (Bianchi and McCave, 2000). The main flow of Iceland-Scotland Overflow (ISOW) water travels south of Iceland between water depths of 1300 and 2200 meters along the eastern flank of the Reykjanes Ridge and over Gardar Drift (McCave and Tucholke, 1986). The Gardar Drift may have been initiated in the late Early Miocene between 20 and 17 Ma by a prolonged interval of production of northern component water (Miller and Tucholke, 1983). Previous drilling on the Gardar Drift was carried out in 1995 during Ocean Drilling Program (ODP) Leg 162, in 1983 during Deep Sea Drilling Project (DSDP) Leg 94, and by a cruise of the RV Hudson in 1991 that collected Core HU91-045-080, close to the coring site of one of the cores discussed here (JPC13).

The three cores discussed here were collected on the Gardar Drift in the summer of 2002 during a cruise KN166-14 of R/V Knorr that provided site survey data for IODP Expedition 303. The cores were taken in a northeast to southwest transect across the drift (Figure 5-1). Jumbo piston Core JPC13 and accompanying gravity Core GGC12 were taken in a depression at the southernmost tip of the Gardar Drift in 3082 m water depth (Table 1). Core JPC2 was taken at the northern end of the drift close to ODP Sites 984 and 983 in a water depth of 1880 m. Core JPC5 was taken near the center of the drift in 2841 m water depth (Figure 5-1, Table 5-1). In 2004, IODP Expedition 303 revisited the location of Core JPC13 and recovered a sedimentary section down to 244 meters below seafloor (mbsf) that reached the Olduvai Subchronozone with a mean sedimentation rate of 15 cm/kyr (Channell et al., 2006).

Cores JPC2 and JPC5 are typical of sediments deposited on the Gardar Drift during the last glacial cycle and are dominated by fine silts and silty clays with subsidiary amounts of nannofossil ooze. Core JPC13, from the southern part of the drift (Figure 5-1), is atypical and composed of nannofossil ooze and silty clay interspersed with numerous cm- to dm-scale intervals of diatom-rich sediments. Bodén and Backman (1996) identified diatom rich layers in Core EW93-03-17 (57.0°N, 37.0°W) from the west side of the Reykjanes Ridge, about 550 km NW of Core JPC13. They described the laminated diatom ooze as being monospecific and made up of *Thalassiothrix longissima*. The same species of diatom was identified at IODP Site U1304 (Expedition 303 Scientists, 2006) at the same location as Core JPC13.

### **Methods**

U-channel samples were collected from the center of the split face of the jumbo piston cores and gravity cores. The u-channel samples were measured on a 2-G Enterprises narrow-access long-core magnetometer in a magnetically shielded room at the University of Florida. Volume magnetic susceptibility was measured using a track designed for u-channel samples



(Thomas et al., 2002). The natural remanent magnetization (NRM) of u-channel samples was stepwise demagnetized using peak alternating fields from 10 mT to 50 mT in increments of 5 mT, and from 50 mT to 100 mT in increments of 10 mT. Magnetization components were calculated using the method of Kirschvink (1980) for the 20-80 mT demagnetization interval. Anhysteretic remanent magnetization (ARM) was acquired using a 100 mT alternating field and a 50  $\mu$ T DC bias field. Isothermal remanent magnetization (IRM) was acquired using a 0.5 T field. Both artificial remanences (ARM and IRM) were AF demagnetized at the same peak fields as the NRM. Normalized remanence was calculated by dividing the NRM by either ARM or IRM at each peak demagnetization field and calculating a mean of 9 steps in 20-60 mT interval. The normalized remanence data provide relative paleointensity proxy records that can be correlated to other cores from the Gardar Drift and the North Atlantic Ocean.

Comparison of the volume magnetic susceptibility records from Core GGC12 and Core JPC13 indicate that the upper part of Core JPC13 is stretched relative to Core GGC12. To account for the stretching, the magnetic susceptibility record from the upper part of Core JPC13 was correlated to the susceptibility record from Core GGC12 (Figure 5-2). This correlation generated a “corrected” depth scale for the upper part (0-955 cm) of Core JPC13. For the part section of Core JPC13 (955-2357 cm), 404 cm was subtracted from the original depth scale, which is the amount by which the upper part of the core had to be shortened to account for observed stretching.

Samples for stable isotope analysis were collected by dissecting the Core JPC13 and Core GGC12 u-channels into 5-cm intervals after completion of the magnetic measurements. The samples were washed and sieved to retain the (>63  $\mu$ m) sand fraction. Isotope analyses were carried out on the benthic foraminifers *Cibicidoides wuellerstorfi* and, in the Holocene where *C.*

*wuellerstorfi* is scarce, *Hoeglundina elegans*. Benthic foraminiferal tests were cleaned in an ultrasonic bath to remove fine-grained particles and soaked in 15% H<sub>2</sub>O<sub>2</sub> to remove organic matter. Carbon dioxide gas was produced using a Thermo Finnigan Kiel III carbonate preparation device by reacting foraminiferal calcite with 3 drops of H<sub>3</sub>PO<sub>4</sub> at 90°C. Oxygen isotope ratios were measured on-line using a Thermo Finnigan MAT252 mass spectrometer. All isotope results are reported in standard delta notation relative to Vienna Pee Dee Belemnite (VPDB). Analytical precision was estimated by repeated measurements of NBS-19 and was  $\pm 0.06$  ‰ for  $\delta^{18}\text{O}$ . Both *C. wuellerstorfi* and *H. elegans* were corrected to isotopic equilibrium using the corrections of +0.64 and -0.4 respectively (Shackleton et al., 1984). A composite section using data from both cores was produced by splicing the isotope record from Core GGC12 to Core JPC13 at a depth of 274 cm.

Gamma ray attenuation bulk density (GRA bulk density) for Core JPC13 was measured on a GEOTEK multi-sensor core logger using u-channel samples. The calibration standard for GRA bulk density measurements was specially constructed for u-channel samples.

### **Directional Magnetic Data**

Orthogonal projections of NRM data from all four cores show well-defined magnetization components on vector end-point projections (Figure 5-3), with less than 5% of the NRM remaining after demagnetization at peak fields of 100 mT. Maximum angular deviation (MAD) values for component magnetization directions resolved in the 20-80 mT demagnetization interval are generally below 5° (Figure 5-4). Diatom mats in Core JPC13 (shaded intervals in Figure 5-4) occasionally show a high coercivity component that is not demagnetized at peak fields of 100 mT (sample JPC13, section 4 in Figure 5-3). We attribute this to an ARM acquired during the NRM demagnetization procedure possibly due to the presence of ultra-fine magnetite susceptible to the acquisition of ARM. Two intervals between 300-315 cm

and 1600-1920 cm in Core JPC13 show shallower than expected inclination values. These intervals coincide with thick layers of diatom mats, and magnetization directions may be influenced by spurious ARM acquisition during the NRM demagnetization, as mentioned above.

### **Normalized Remanence**

In the absence of secondary remanence acquisition, NRM intensity of sediments depends on the intensity of the geomagnetic field at time of deposition, magnetic mineralogy, grain size and concentration of the magnetic remanence carriers. To produce a proxy for geomagnetic field intensity, the effects of down-core changes in magnetic concentration must be removed.

Assuming that the magnetization is carried by single domain or pseudo single domain magnetite, we can use artificial remanences such as ARM and/or IRM to normalize for the changes in the concentration of magnetic carriers. Tauxe (1993) stipulated that for sediments to be considered suitable for paleointensity studies, they must be relatively homogeneous. Magnetic susceptibility in these cores does not change by more than an order of magnitude. Anhysteretic susceptibility ( $k_{arm}$ ) plotted versus susceptibility ( $k$ ) indicates uniform magnetite grain sizes in the 1-5  $\mu m$  range for all three cores fining southward with Core JPC13 having the finest grain sizes (Figure 5-5).

Two relative paleointensity proxies (NRM/ARM and NRM/IRM) were calculated for each of the cores from a mean of nine demagnetization steps in the 20-60 mT demagnetization interval. The two proxies for each of the four piston cores were normalized to 1 and compared (Figure 5-6). NRM/IRM shows departures from the NRM/ARM proxy in some intervals such as the 1300-1450 cm interval of Core JPC5, although the shape of the curve is similar for both paleointensity proxies. We attribute these departures to finer magnetic grain sizes in these intervals, as indicated by  $k_{arm}/k$  values.

### **Stable Isotope Data and Age Models**

The age model for Core JPC13 was derived from the oxygen isotope stratigraphy by correlation to Core MD95-2042 (Shackleton et al., 2004). Core MD95-2042 was collected on the Portuguese margin at 37°48'N, 10°10'W in a water depth of 3146 m during the 1995 IMAGES cruise (Bassinot et al., 1996). A useful feature of this core is that the planktic  $\delta^{18}\text{O}$  record is remarkably similar to the GISP ice-core  $\delta^{18}\text{O}$  record (Figure 5-7). Shackleton et al. (2004) employed this correlation to obtain a revised GISP chronology by utilizing AMS $^{14}\text{C}$  ages of foraminifera in Core MD95-2042 calibrated using paired  $^{14}\text{C}$  and  $^{230}\text{Th}$  measurements on pristine corals for the younger part of the record, and speleothems at the older end of MIS 3. Hereafter, we refer to this chronology as the Shackleton-revised GISP chronology.

As the benthic oxygen isotope record from Core JPC13 can be satisfactorily correlated to the benthic oxygen isotope record from Core MD95-2042 (Figure 5-7), the Shackleton -revised GISP chronology can be applied to Core JPC13. This chronology can then be extended to Cores JPC2 and JPC5 using relative paleointensity correlations (Figure 5-8). Interval sedimentation rates (Figure 5-9), consistent with the Shackleton-revised GISP chronology, were calculated for Core JPC13 by correlation to Core MD95-2042 (through benthic  $\delta^{18}\text{O}$ ), and for Cores JPC2 and JPC5 by correlation to Core JPC13 (through relative paleointensity, Figure 5-8).

### **Bulk Magnetic and Physical Parameters**

Anhyseretic susceptibility was calculated every cm down-core by normalizing the ARM by the DC bias field used to apply the ARM. ARM was then divided by the volume susceptibility to calculate the magnetite grain size proxy  $k_{\text{arm}}/k$  for Core JPC13 (Figure 5-10). When  $k_{\text{arm}}$  is plotted versus  $k$ , using the calibration of King et al. (1983), the mean grain-sizes from all three cores can be seen to fall within a restricted range, usually less than 5  $\mu\text{m}$  (Figure 5-5).

Diatom-rich sediments in Core JPC13 (shaded in Figure 5-10) are associated with MIS 5, with thin diatom-rich layers distributed within MIS 1-3. Diatom-rich intervals correspond to reduced values of susceptibility, lower and more variable density values, and relatively fine-grained magnetite as indicated by trends in  $k_{\text{arm}}/k$  (Figure 5-10). Volume magnetic susceptibility shows decreasing values southward along the drift that can be attributed to biogenic dilution (Figure 5-11d).

In Core JPC2,  $k_{\text{arm}}/k$  data can be correlated to the benthic oxygen isotope record from ODP Site 983 (Figure 5-11a), indicating that magnetite grain size at this site is varying with isotopic stage and changing abruptly at Termination I and II. Coarser magnetite grain sizes characterize the interglacial intervals and finer grain sizes characterize the glacial intervals. Core JPC13, on the other hand, shows a different pattern (Figure 5-11c) in which  $k_{\text{arm}}/k$  is positively correlated to the benthic oxygen isotope record from the same core during MIS 3. Finer magnetite grain sizes occur in the interglacials and interstadials, and coarser grain sizes in the glacials and stadials (Figure 5-11c). In Core JPC5, a similar positive correlation is only observed the later part of MIS 5 (Figure 5-11b).

### **Relative Paleointensity Stack**

A stack of eleven North Atlantic relative paleointensity records has been developed using the records from Cores JPC2 and JPC5, as well as Core JPC13 to place the stack on the revised GISP age model (Shackleton et al., 2004). The seven published records used to augment the stack (Figure 5-12 and Table 5-2) were chosen based on the presence of an isotopic age model for each record, and a correlation coefficient for each record to JPC13 of  $> 0.5$ . Although Cores JPC2 and JPC5 do not have independent isotopic age models, their relative paleointensity records correlate to that from Core JPC13 with a correlation coefficient exceeding 0.6 (Figure 5-8). The records were then normalized to 1 by dividing by the mean of the paleointensity proxy.

Each record was then optimally correlated to the relative paleointensity proxy from Core JPC13 to place them on the Shackleton-revised GISP chronology. The resulting correlation was then checked for any violations of the individual isotopic age models. The records were then re-sampled at an even spacing of 500 years. An arithmetic mean of the eleven records was calculated along with the standard deviation. A jack-knife test was used to assess errors on the stack in which each record was, in turn, excluded from trial stacks. The departure of the trial stacks from the mean value of the stack yields the estimate of standard deviation for the final stack (Figure 5-13). Only seven of the sites used in the stack have Holocene relative paleointensity records.

The EHC06 stack, on the Shackleton-revised GISP age model generated through Core MD95-2042, was then compared with the 30-100 ka  $^{36}\text{Cl}$  record from the GRIP ice core (Baumgartner et al., 1998) and with the 0-60 ka  $^{10}\text{Be}$ -derived paleointensity estimate (Muscheler et al., 2005), both placed on the GISP2 chronology (Figure 5-14). The stack shows minor offsets with respect to the  $^{10}\text{Be}$ -derived paleointensity estimate in the 0-50 ka interval, and larger offsets (to older ages) with respect to the  $^{36}\text{Cl}$  record beyond 50 ka. These offsets are broadly consistent with, and in the same sense as, the offsets between the revised GISP chronology and the standard GISP2 chronology (Shackleton et al., 2004). When the EHC06 stack is compared to the NAPIS stack (Laj et al., 2000), similar offsets are observed (Figure 5-15). The NAPIS stack was placed on the GISP2 chronology using the marine to ice-core oxygen isotope correlation proposed by Voelker et al. (1998) from Core PS2644. The age of the paleointensity low associated with the Laschamp excursion differs by ~300 years in the two stacks, and the difference in age of paleointensity features increases to 1870 years at the ~ 60 ka paleointensity low (Figure 5-15). These age differences are very consistent with offsets between the Shackleton-revised GISP

chronology and the GISP2 chronology of Meese et al. (1997) (see Table 2 of Shackleton et al., 2004). Major differences between EHC06 and NAPIS occur in the 10-20 ka interval where the NAPIS stack shows a peak while the EHC06 stack shows a low, and between 42-50 ka where a peak in the NAPIS stack is not seen in the EHC06 record.

The global GLOPIS stack (Laj et al., 2004) covers the 0-75 ka interval (Figure 5-15). EHC06 shows a good match to GLOPIS apart from the 0-12 ka interval where GLOPIS utilizes the archeomagnetic data of Yang et al. (2000). GLOPIS shows an upward trend from 20 ka to present that is not seen in EHC06, however, both records show a double peak in the Holocene (Figure 5-15). Comparison to the South Atlantic SAPIS stack (Stoner et al., 2002) indicates a good match in the 30-70 ka. However, in the 20-30 ka interval, the new stack shows a peak where SAPIS shows a significant paleointensity low (Figure 5-15). SAPIS is on a chronology independent of GISP and fits better with EHC06 than with either NAPIS or GLOPIS between 45 ka and 70 ka. The SAPIS chronology was based on the age model for ODP Site 1089 (Hodell et al., 2001) that was constructed by correlating planktic and benthic isotope records to those from Core RC11-83 which has 14 calibrated radiocarbon ages in the 11-41 ka interval (Charles et al., 1996).

### **Environmental Magnetism**

Sediment sorting takes place through differing rates of sediment transport so that an originally unsorted mixture is converted downstream into narrower grain size distributions (McCave et al., 1995). Sediments from the transect along the Gardar Drift show magnetic grain sizes in a restricted range indicative of sorting and deposition by bottom currents, with a tendency for fining to the south accompanied by reduction in magnetic concentration (Figures 5-5 and 5-11d). Current sorting of sediment is thought to take place largely in the 10-63  $\mu\text{m}$  range or sortable silt grain-size fraction (McCave et al., 1995). Below this grain-size range, sediments

are dominantly cohesive as clay minerals (with their charge imbalances) enter the sediment's compositional spectrum, and van der Waals forces play an important role in particle adhesion (McCave et al., 1995). Although the magnetic grain sizes estimated from  $k_{\text{arm}}/k$  values are largely in the 1-5  $\mu\text{m}$  range, the  $k_{\text{arm}}/k$  ratio may be influenced by the coarsest magnetic grains in the grain size population and these grains may lie in the sortable silt fraction.

In Core JPC2, from the northern end of the Gardar Drift, coarser magnetic grain sizes occur during interglacials whereas the finer magnetite is present in the glacials (Figure 5-11a). The magnetic grain size at this site shows a progressive coarsening down-core through MIS 3, fining in MIS 4 and coarsening in MIS 5. The location of Core JPC2, at 1880 m water depth, is presently under the influence of ISOW (Bianchi and McCave, 2000). We interpret the  $k_{\text{arm}}/k$  data to indicate stronger ISOW bottom currents during interglacials that winnow finer sediment leaving coarser material. In the glacials, slower ISOW current strength allows deposition of finer particles. ISOW is an important precursor of NADW, therefore, the grain size data from Core JPC2 implies increased NADW production during interglacials relative to glacial stages.

Bianchi and McCave (2000) divided the Iceland Basin into two areas, north and south of  $58^{\circ} 30' \text{ N}$ , based on studies of surface sediments. North of this boundary, the Gardar Drift is draped by sediments with high (terrigenous) silt/clay ratio, containing abundant current-sorted silt with a strong coarse-grained modal peak. They ascribed this coarser grain-size to the strength of the near-bottom current flow, and the proximity of Iceland, consistent with the coarser grain sizes identified in the Holocene sediments in Core JPC2.

In sediments from the Reykjanes Ridge, Snowball and Moros (2003) identified a saw-toothed pattern in magnetic grain size in MIS 3 during Dansgaard-Oeschger (D/O) cycles with magnetic grain-sizes coarser during interstadials compared to stadials. The changes in magnetite



grain size were interpreted as a proxy for the speed of near-bottom currents, with a gradual intensification in current velocity followed by a sharp decrease. While these short-term changes are not identified in sediments from Core JPC2, the changes in current speed (faster currents in warm periods and slower current in cold periods) are consistent with the changes seen in Core JPC2. The short-term saw-toothed pattern in magnetic grain size identified by Snowball and Moros (2003) is superimposed upon a long-term trend of reduced current speed (finer grain sizes) leading up to the Last Glacial Maximum (LGM), similar to the trend seen in Core JPC2.

In Core JPC5, magnetic grain size does not show a correlation to the benthic oxygen isotope record of either ODP Site 983 or Core JPC13 (Figure 5-11b), but the magnetic fraction is finer-grained than Core JPC2 and coarser grained than Core JPC13 (Figure 5-11). This is indicative of transport by deep currents from a single source manifest by the decrease in concentration and grain size as the currents move southward from the principal detrital source. A similar trend was noted by Ballini et al. (2006) along the path of NADW from just north of the Faeroe Shetland channel, to near the Reykjanes Ridge and into the Irminger Basin. The  $k_{arm}/k$  magnetic grain size in Core JPC5, which is at a water depth of 2841 m, does not show a correlation to the benthic isotope records, other than in the later part of MIS 5, and this may indicate that the site is seeing a mixture of both LDW and ISOW.

Core JPC13 was collected at deeper water depths (3082 m) than either Cores JPC2 or JPC5 and shows the finest magnetic grain sizes of any of the sites (Figure 5-5 and 5-11). In MIS 3, the magnetic grain size proxy can be correlated to the benthic isotope record from the same core (Figure 5-11c). The oxygen isotope record from Core JPC13 can, in turn, be correlated to the  $\delta D$  record of the Vostok ice core (Jouzel et al., 1987), which reflects temperature variations over Antarctica (Figure 5-7). This implies that during the last glacial period the benthic oxygen

isotopes are recording water temperatures that reflect the Antarctic temperature record. The Antarctic climate events A1, A2, A3 and A4 (Figure 5-7) are clearly recorded in the benthic isotope record from Core JPC13, suggesting that a water mass of southern hemisphere origin was bathing the site during MIS 3 precluding the hypothesis that changes sediment source could account for the grain size changes identified in the  $k_{arm}/k$  record. Magnetic grain size as indicated by  $k_{arm}/k$  is coarser during Antarctic Interstadials A1-A4 indicating faster bottom currents (and possibly increased flux of lower deep water (LDW) of Southern Hemisphere origin into the North Atlantic) during Antarctic warm events. During interglacials, the correlation of the benthic  $\delta^{18}O$  record to the magnetic grain size record breaks down and the record shows some similarity to the Greenland Ice core record indicating changes in the bottom-water mass over the site (Figure 5-7).

### **Conclusions**

The new EHC06 relative paleointensity stack of eleven records from the North Atlantic region has been placed on the revised GISP chronology of Shackleton et al. (2004). This stack shows a good correlation with other paleointensity stacks (such as GLOPIS) indicating that the new stack is providing a consistent representation of relative geomagnetic field intensity. It should be noted that three records utilized by EHC06 are also used in NAPIS and seven of the records were used in GLOPIS, although the age model for EHC06 is not the same as for the other stacks. The previous North Atlantic stacks (NAPIS and GLOPIS) are placed on GISP age models by correlation of magnetic concentration parameters to Core PS-2644 (Kissel et al., 1999), and the  $\delta^{18}O$  correlation from this core to GISP (Voelker et al., 1998). The age offsets between EHC06 and NAPIS/GLOPIS are consistent with the age offsets between the GISP chronology and the Shackleton-revised GISP chronology (see Table 2 in Shackleton et al., 2004),

indicating consistency in age models. In the 45-70 ka interval, the Shackleton-revised GISP chronology applied to the EHC06 stack is more consistent with the age model for the SAPIS stack, which is independent of GISP (Stoner et al., 2002), than with the NAPIS/GLOPIS age models that are tied to GISP chronologies. For the Holocene, EHC06 shows a double peak in the Holocene (0-12 ka), which compares well with the archeomagnetic stack of Yang et al. (2000) and with available lake sediment records for this interval (e.g. Snowball and Sandgren, 2004), although the scaling in this interval differs from that adopted in GLOPIS (Figure 5-15).

Magnetite grain size, based on the parameter  $k_{arm}/k$ , shows a correlation to the benthic oxygen isotope records for Cores JPC13 and JPC2. Core JPC2 lies at 1880 m water depth and is bathed in ISOW. The  $k_{arm}/k$  values at Core JPC2 show coarser magnetic grain sizes in the interglacials (faster bottom currents) and finer magnetic grain sizes in the glacials (slower bottom currents) with a trend from coarse to fine through MIS 3 indicating decreasing bottom water current strength. Core JPC5 (2841 m water depth) does not exhibit a clear correlation between the oxygen isotope record and the magnetic grain size implying the site is seeing some mixture of ISOW and LDW. Core JPC13 is the deepest of the sites on the drift, and shows the finest magnetic grain sizes. In MIS 3, the magnetic grain size record can be correlated with the benthic isotope record that in turn can be correlated to the Vostok ice core air-temperature record. The benthic isotope record in Core JPC13 appears to be recording bottom water temperatures that are linked to Vostok air temperature, implying LDW of southern ocean origin. The link to  $k_{arm}/k$  indicates that magnetic grain size (and hence bottom current strength) also changes in concert with bottom-water temperatures.

Table 5-1. Summary of the cores used in this study and the eleven cores used in the relative paleointensity stack, including latitude, longitude, water depth, mean sedimentation rates and references.

Core	Latitude	Longitude	Sedimentation rates (cm/kyr)	Water Depth (meters)	Reference
JPC2	61.04° N	22.92° W	8	1880	This work
JPC5	56.35° N	27.86° W	17	2841	This work
JPC13	53.05° N	33.53° W	15	3082	This work
HU90-013-012	58.92° N	47.12° W	8	2830	Stoner et al., 1995
HU90-013-013	58.20° N	48.37° W	12	3380	Stoner et al., 1995
MD95-2024	50.20° N	45.68° W	24	3448	Stoner et al., 2003
MD95-2009	62.73° N	03.98° W	21.5	1027	Laj et al., 2000
ODP Site 984	61.40° N	24.10° W	18.7	1995	Channell 1999
ODP Site 983	60.40° N	23.63° W	10.8	1660	Channell et al., 1997
ODP Site 919	62.67° N	37.47° W	15	2088	Channell, 2006
PS2644-5	67.87° N	21.77° W	12.4	777	Laj et al., 2000

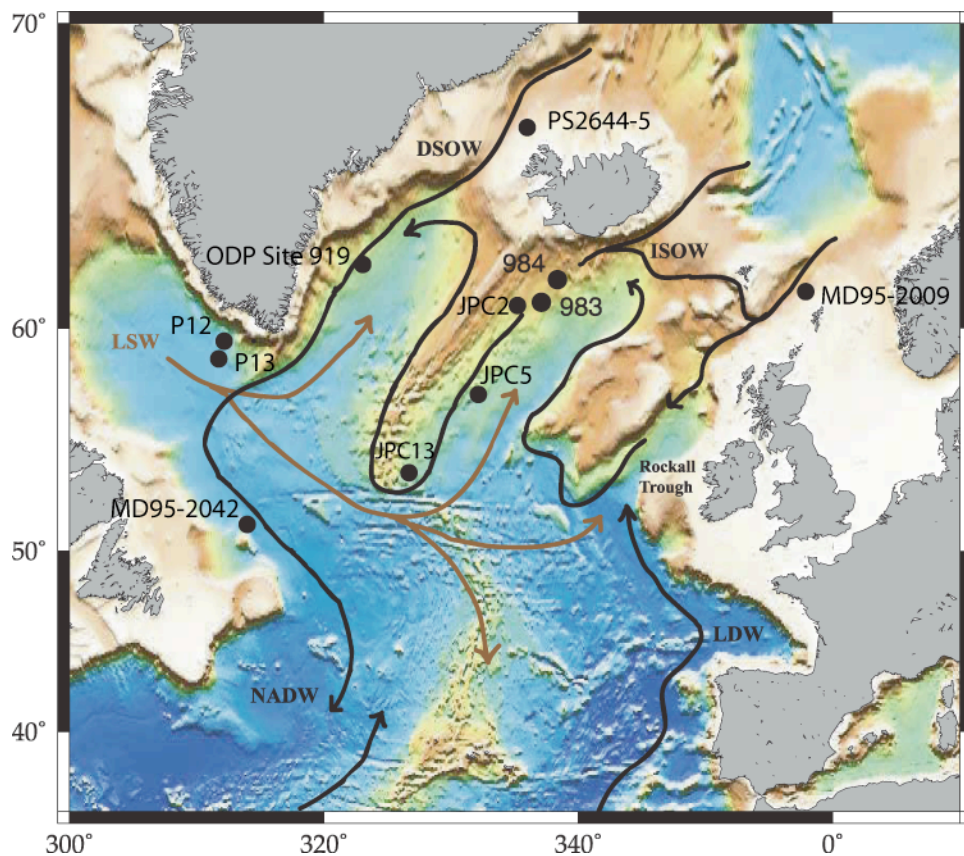


Figure 5-1. Location map for cores analyzed in this study (JPC2, JPC5 and JPC13) and the location of cores used in the paleointensity stack (modified after Raymo et al., 2004). Paths of major deep-water flows are indicated by arrows. Key: NADW-North Atlantic Deep Water, ISOW, Iceland Scotland Overflow Water, DSOW-Denmark Strait Overflow Water, LSW-Labrador Sea Water, LDW-Lower Deep Water. P13-Core HU90-013-013, P12-Core HU90-013-012.

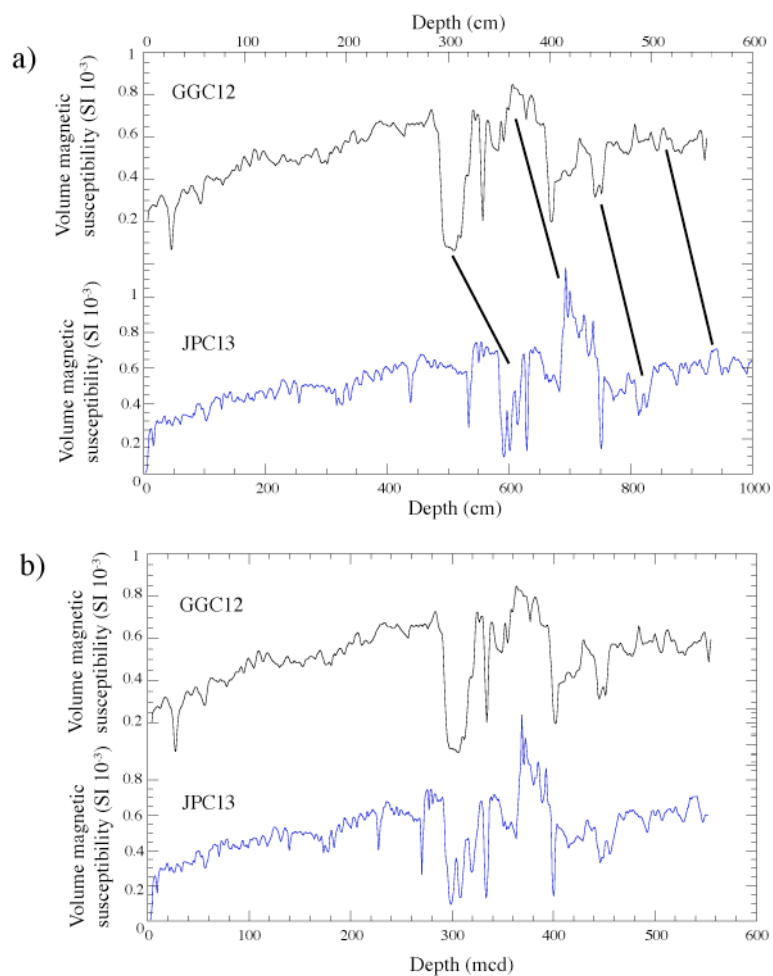


Figure 5-2. a) Correlation of the magnetic susceptibility records from Core GGC12 and Core JPC13 with tie-lines to show the correlation between the two cores. b) Magnetic susceptibility records from Core GGC12 and Core JPC13 after adjustment to account for the stretching in Core JPC13.

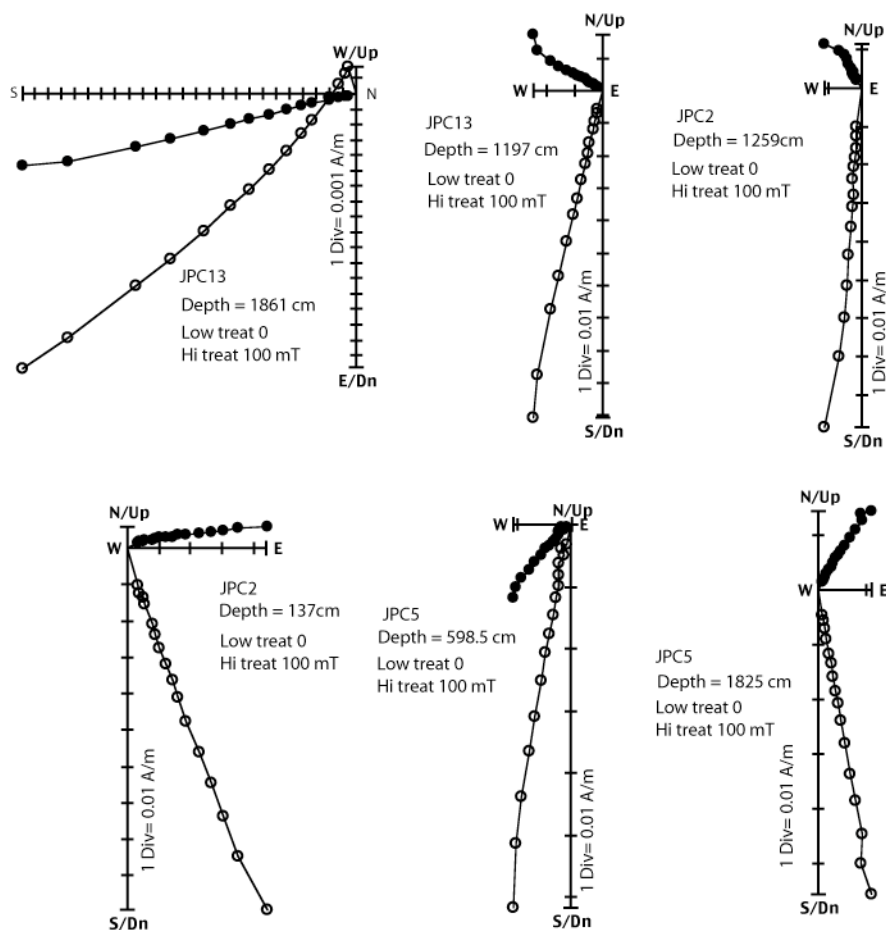


Figure 5-3. Orthogonal projections of alternating field demagnetization data from Cores JPC2, JPC5 and JPC13. Open circles indicate the vector end-point projections on the vertical plane, closed circles indicate the vector end-point projection on the horizontal plane.

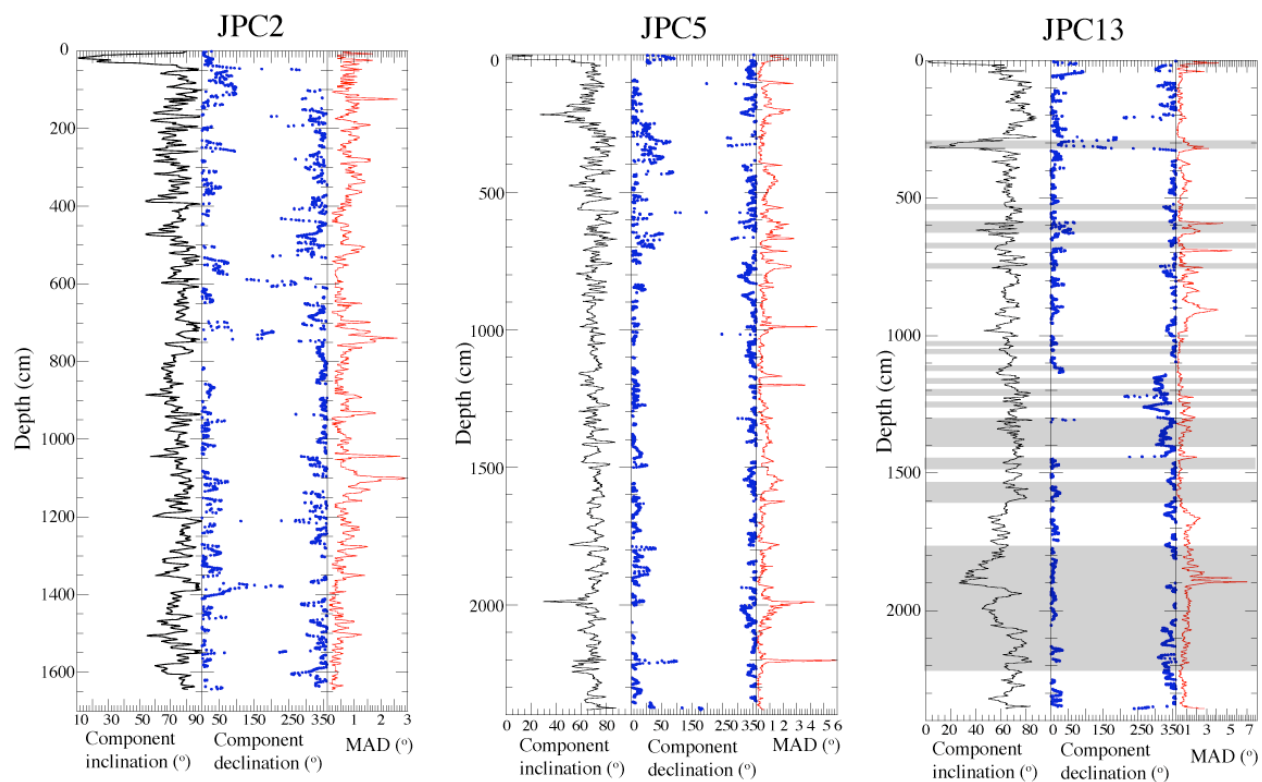


Figure 5-4. Component inclination, declination and maximum angular deviation (MAD) values for Cores JPC2, JPC5, and JPC13. Shading for Core JPC13 indicates the position of diatom-rich intervals. Inclination is shown by a black line, declination by blue dots, and MAD values by a red line.



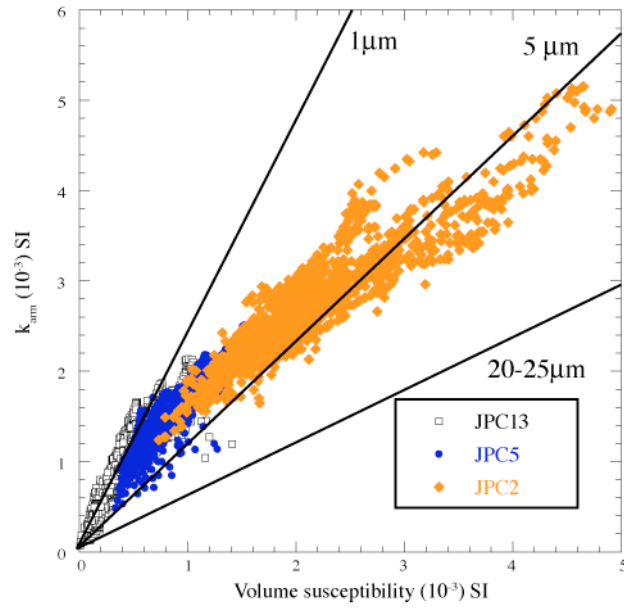


Figure 5-5. Plot of anhysteretic susceptibility ( $k_{arm}$ ) versus volume susceptibility ( $k$ ), open squares represent Core JPC13, closed diamonds Core JPC5 and crosses Core JPC2.

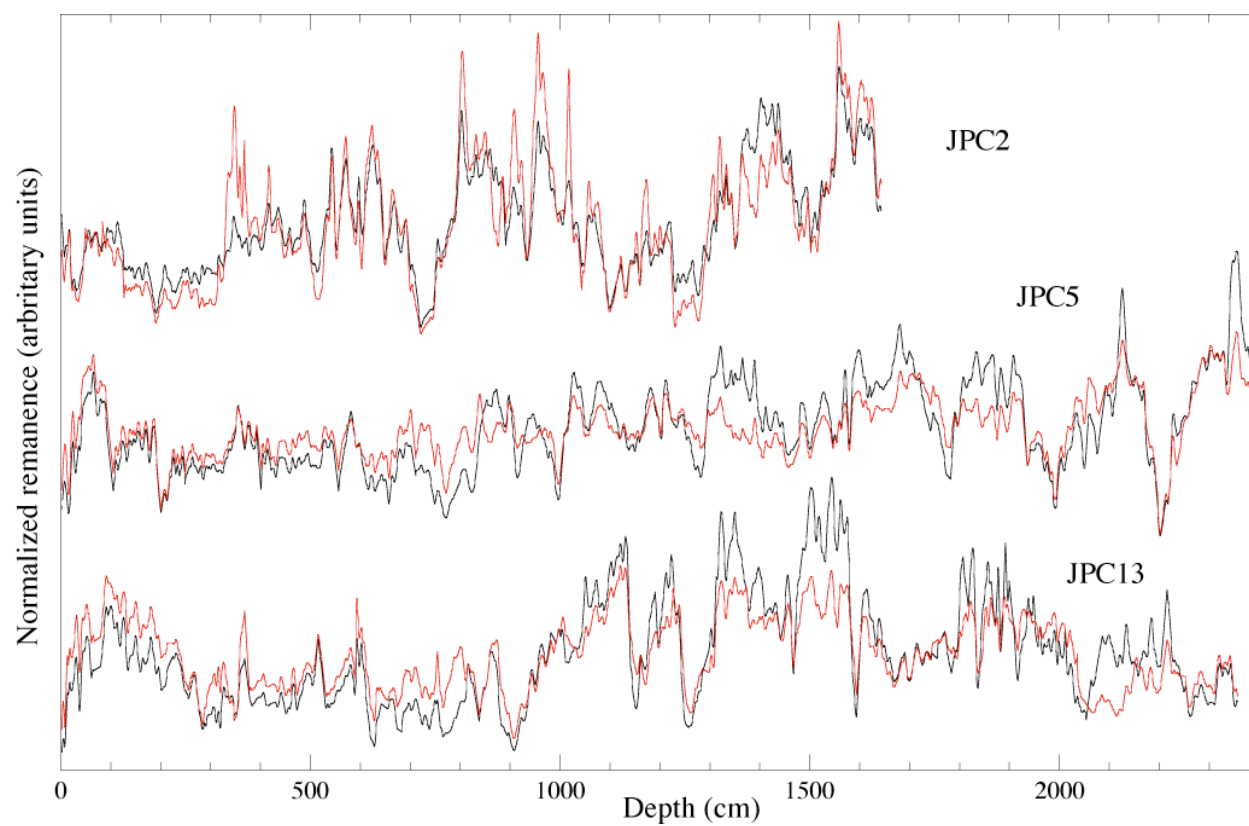


Figure 5-6. Paleointensity proxies: Mean NRM/ARM (red line) and mean NRM/IRM (black line) versus depth compared for Cores JPC2, JPC5 and JPC13.

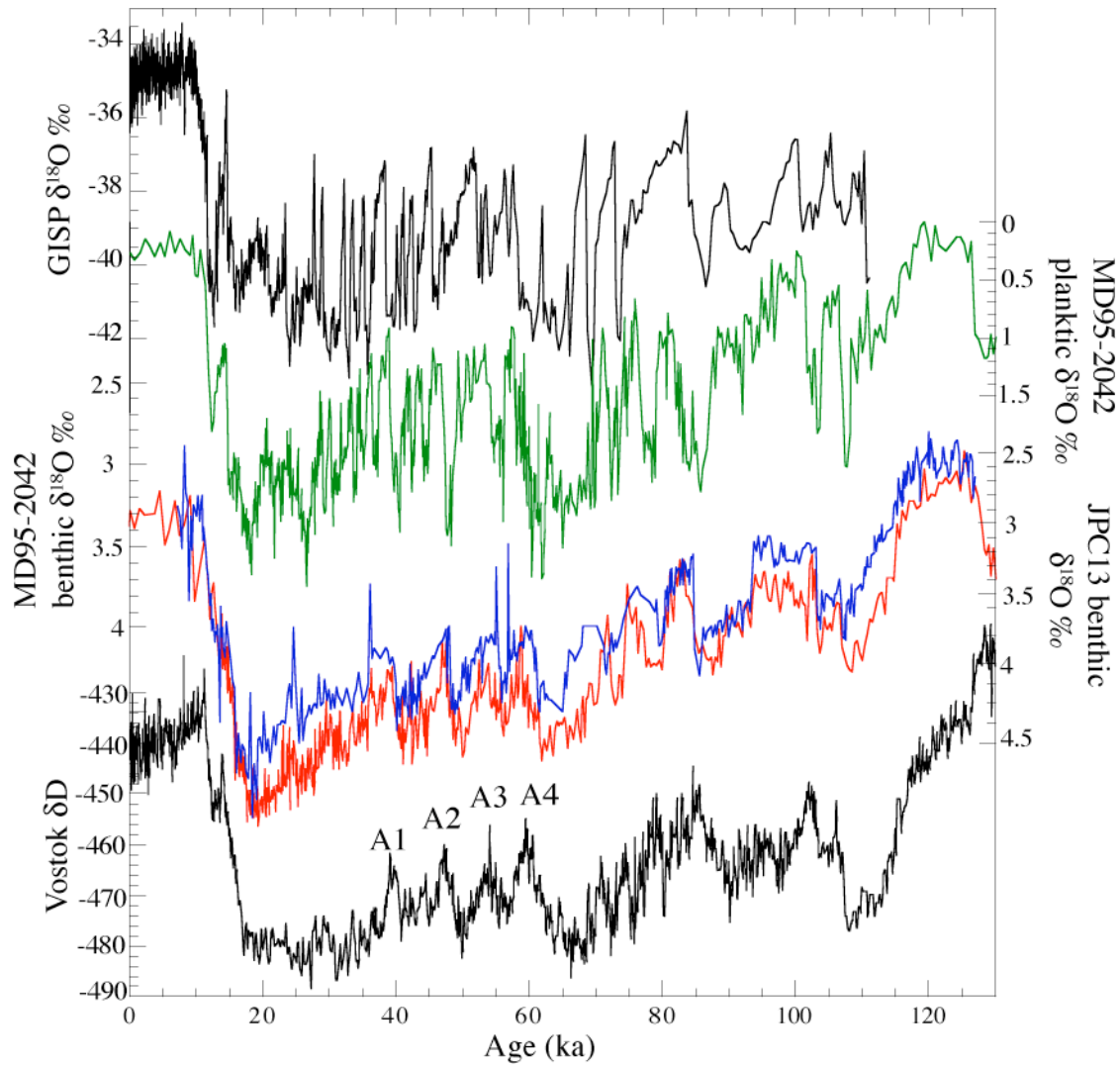


Figure 5-7. Core JPC13 benthic oxygen isotope record (blue line), open circles indicate data from Core GGC12, correlated to the MD95-2042 benthic oxygen isotope record (red line) of Shackleton et al. (2004), and the Vostok ice core  $\delta\text{D}$  record (Jouzel et al., 1987), (on the revised GISP age model of Shackleton et al., 2004) (black line). Also shown is, the MD95-2042 planktic isotope record (green line) of Shackleton et al. (2004) and the GISP  $\delta^{18}\text{O}$  ice core record (Grootes et al., 1997) (on the GISP2 age model of Meese et al., 1997).

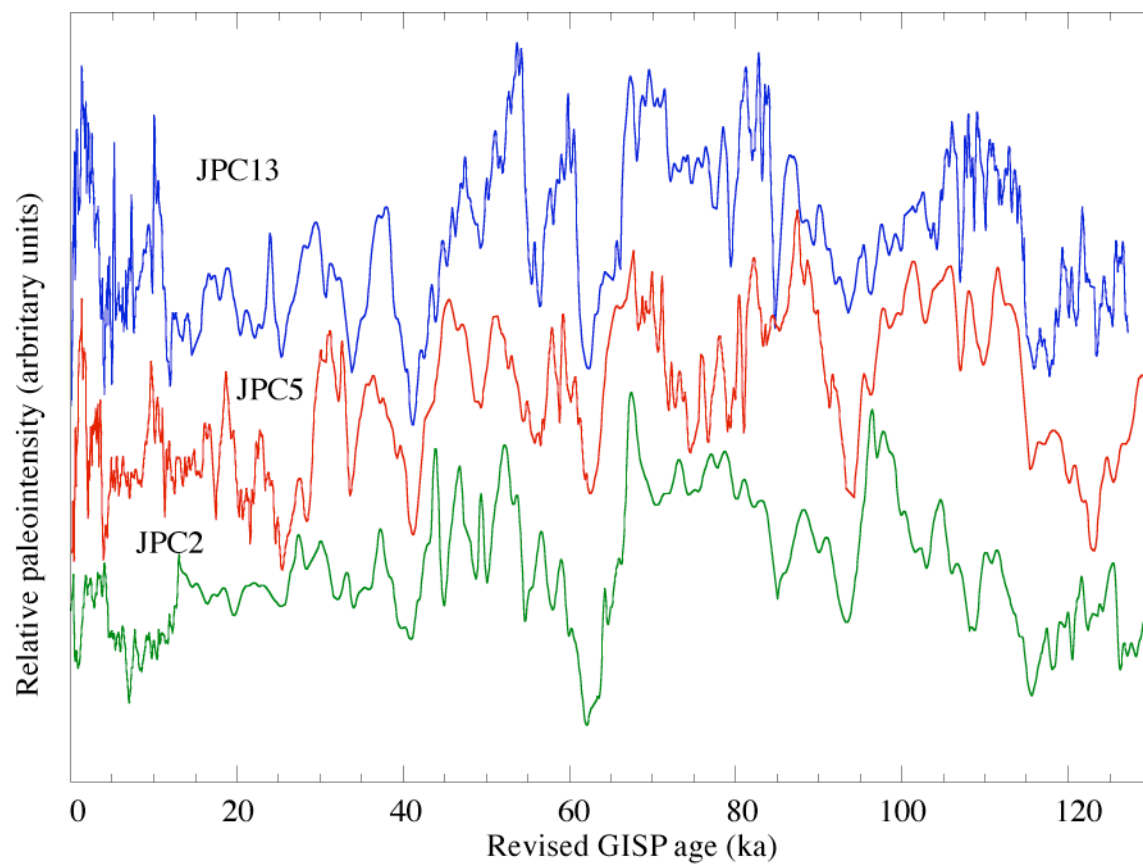


Figure 5-8. Relative paleointensity records from Cores JPC2, JPC5 correlated to Core JPC13 on the revised GISP chronology (Shackleton et al., 2004) for the last 85 ka. The Core JPC13 record is shown in blue, the Core JPC5 record in red and the Core JPC2 record in green.

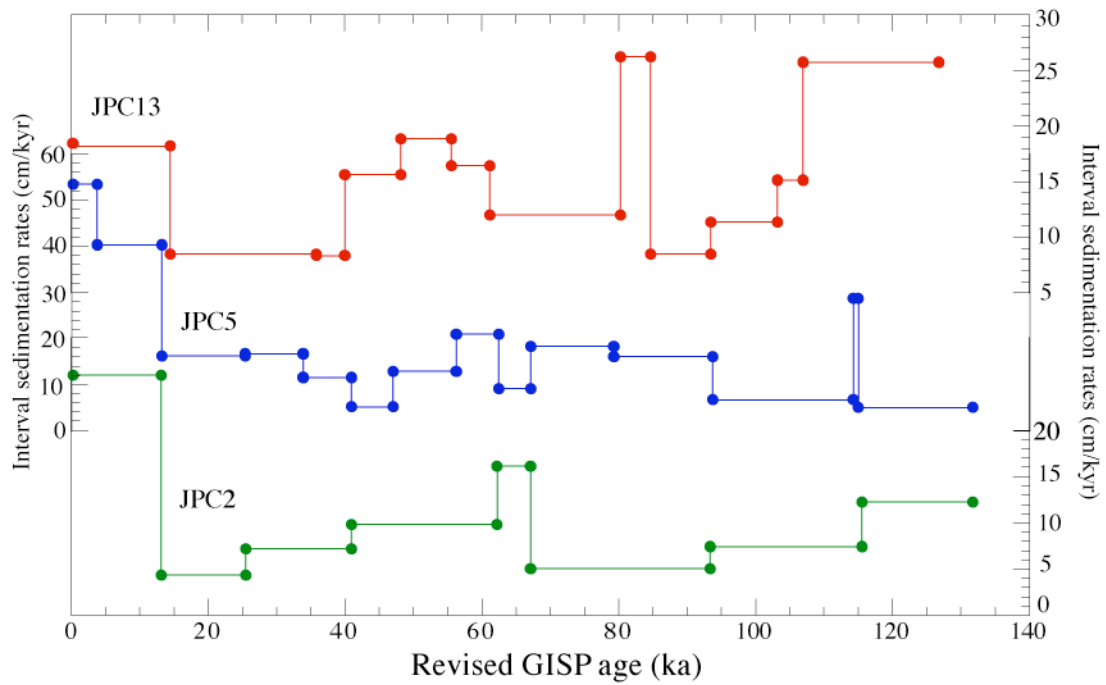


Figure 5-9. Interval sedimentation rates for Cores JPC2, JPC5 and JPC13. The sedimentation rates for Core JPC13 were calculated using the correlation between the benthic isotope records, and the sedimentation rates for Cores JPC5 and JPC2 were calculated based on the correlation of the relative paleointensity records.

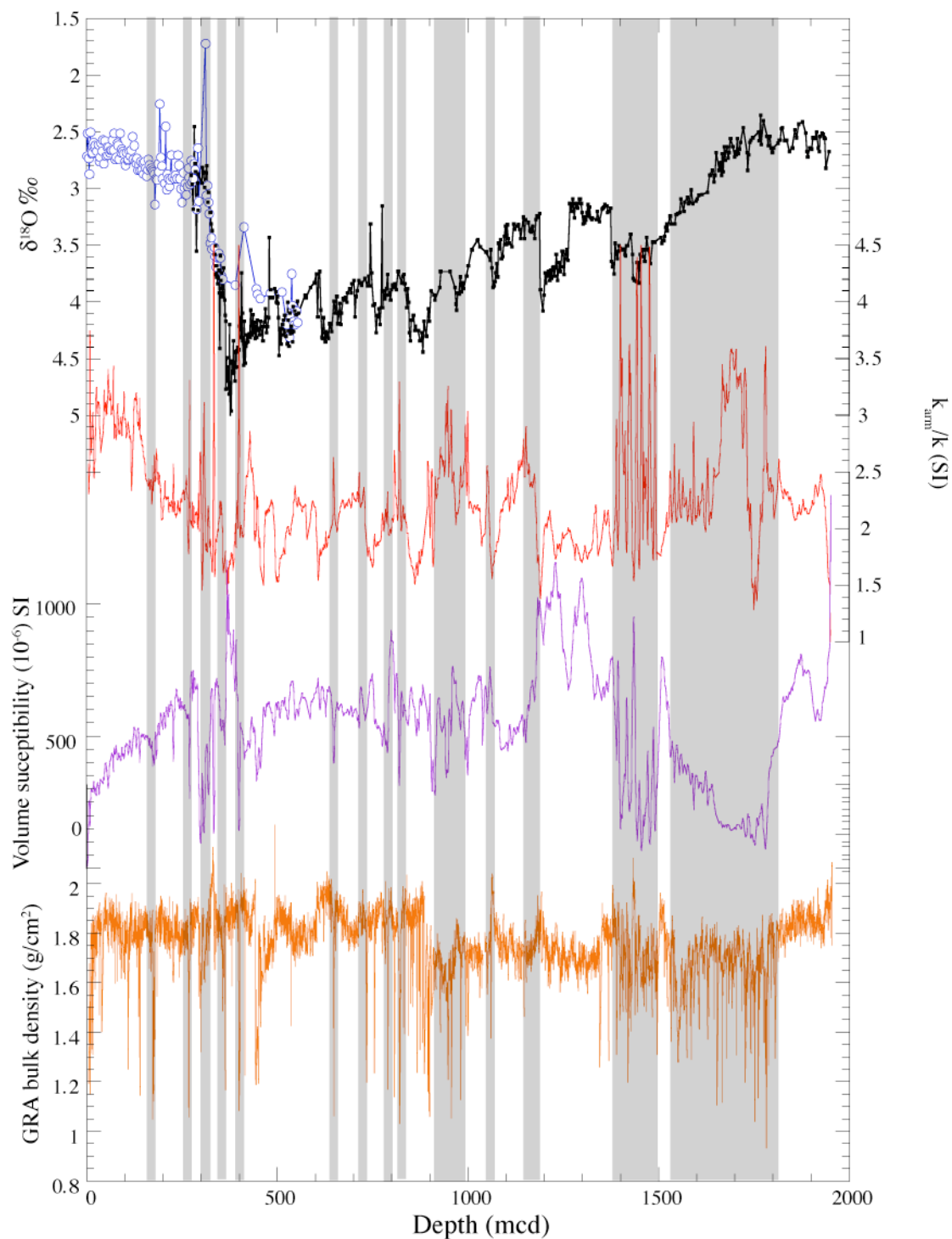


Figure 5-10. Core JPC13: GRA bulk density (orange), anhyseretic susceptibility divided by volume magnetic susceptibility ( $k_{arm}/k$ ) (red), magnetic susceptibility ( $k$ ) (purple), and benthic oxygen isotope data from Core JPC13 (black closed symbols) and GGC12 (open squares). Shaded intervals indicate diatom-rich sediment.

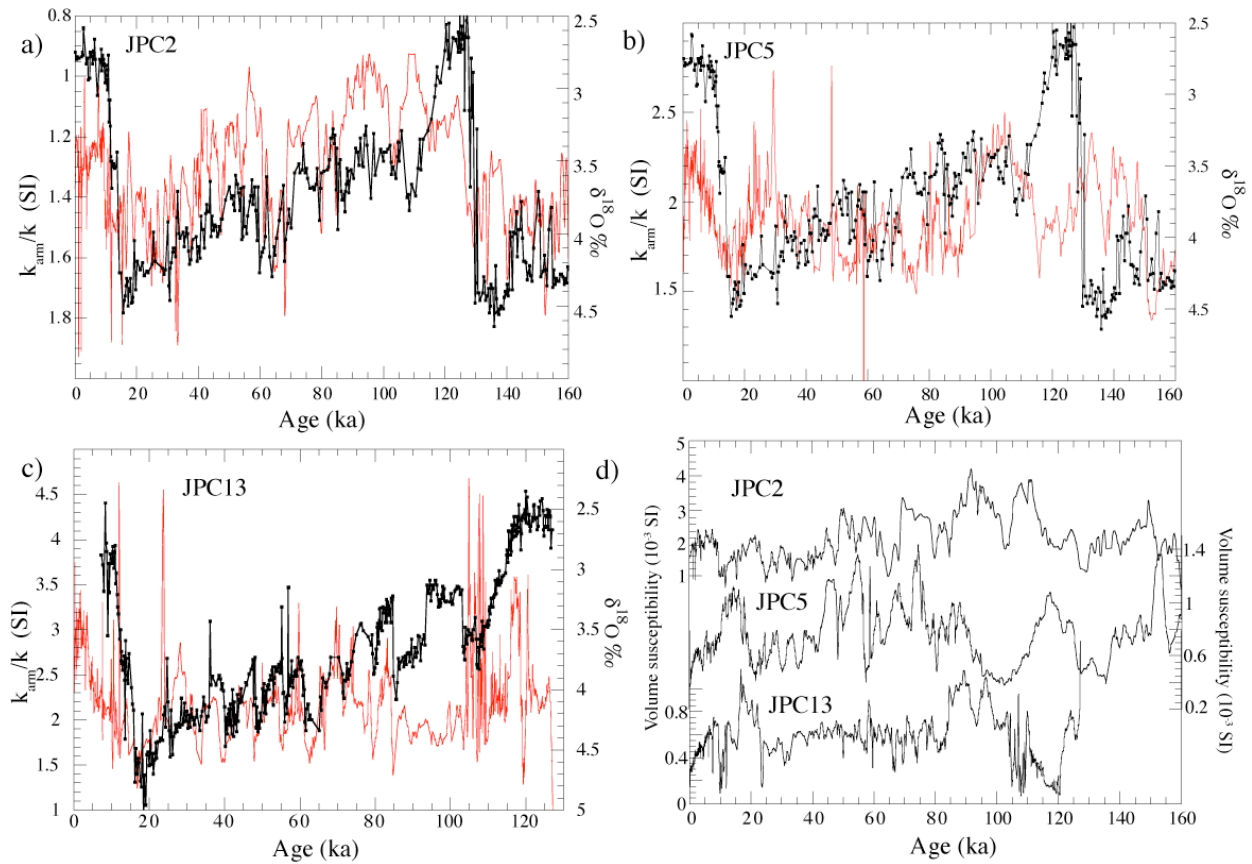


Figure 5-11. a) Anhysteretic susceptibility divided by volume magnetic susceptibility ( $k_{\text{arm}}/k$ ) from Core JPC2 (red line) plotted against the benthic  $\delta^{18}\text{O}$  record (black line) from ODP site 983 (Channell et al., 1997). b) Anhysteretic susceptibility divided by volume magnetic susceptibility ( $k_{\text{arm}}/k$ ) from Core JPC5 (red line), with inverted scale relative to (a), plotted against the benthic  $\delta^{18}\text{O}$  record (black line) from ODP Site 983 (Channell et al., 1997). c) Anhysteretic susceptibility divided by volume magnetic susceptibility ( $k_{\text{arm}}/k$ ), with inverted scale relative to (a), plotted against the benthic  $\delta^{18}\text{O}$  record for Core JPC13. d) Magnetic susceptibility for Core JPC2 (top), Core JPC5 (middle) and Core JPC13 (bottom) showing the decrease in susceptibility from NE to SW along the drift.

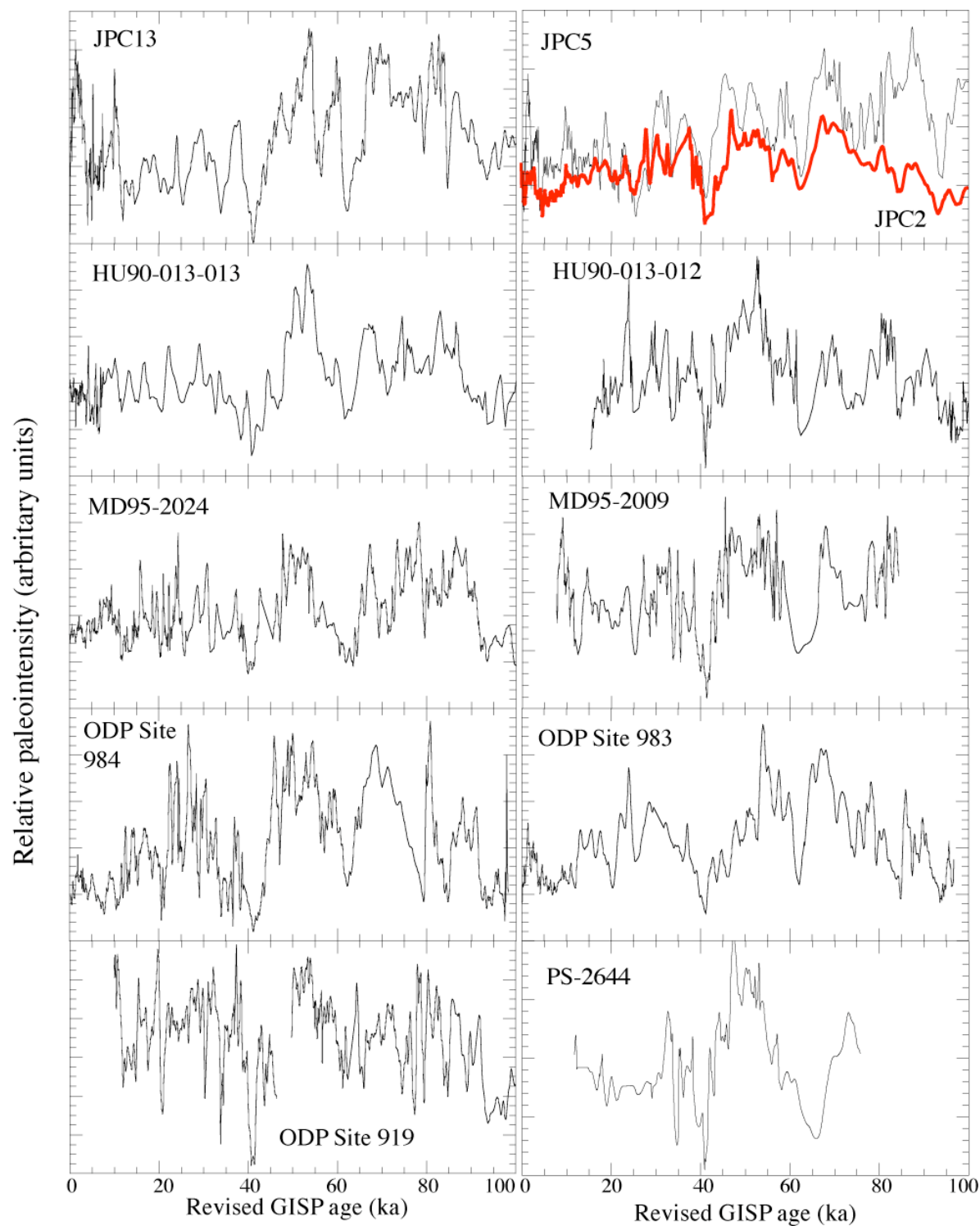


Figure 5-12. Eleven relative paleointensity records from the North Atlantic Ocean used in the new EHC06 stack (see Table 2 for references). The records have been correlated to Core JPC13 to place them on the revised GISP chronology (Shackleton et al., 2004) and then re-sampled at a 500-year interval.



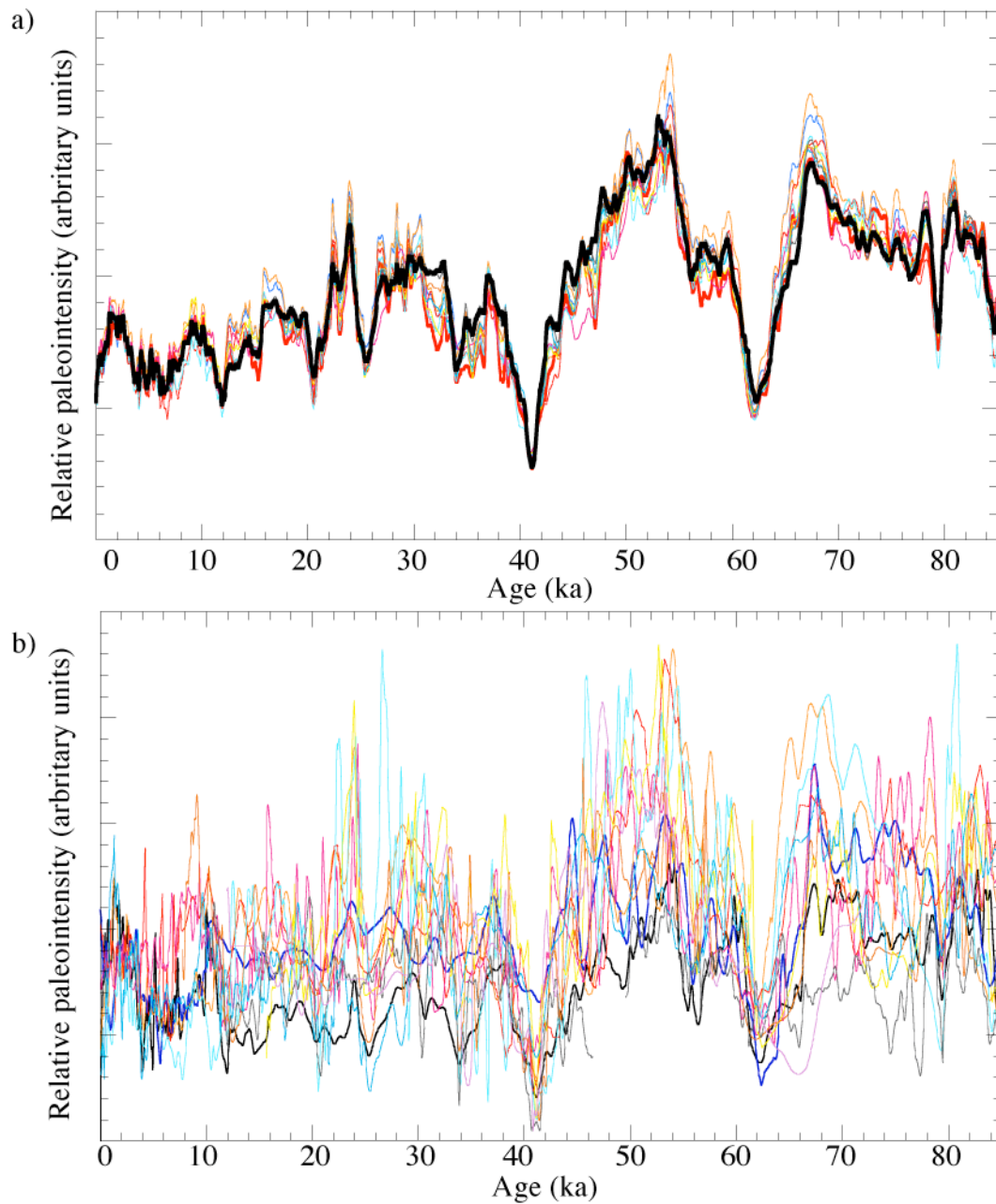


Figure 5-13. a) The new relative paleointensity stack (heavy black line) with the results of the jack-knife sampling. b) The eleven records used in the relative paleointensity stack plotted together on the revised GISP chronology (Shackleton et al., 2004).

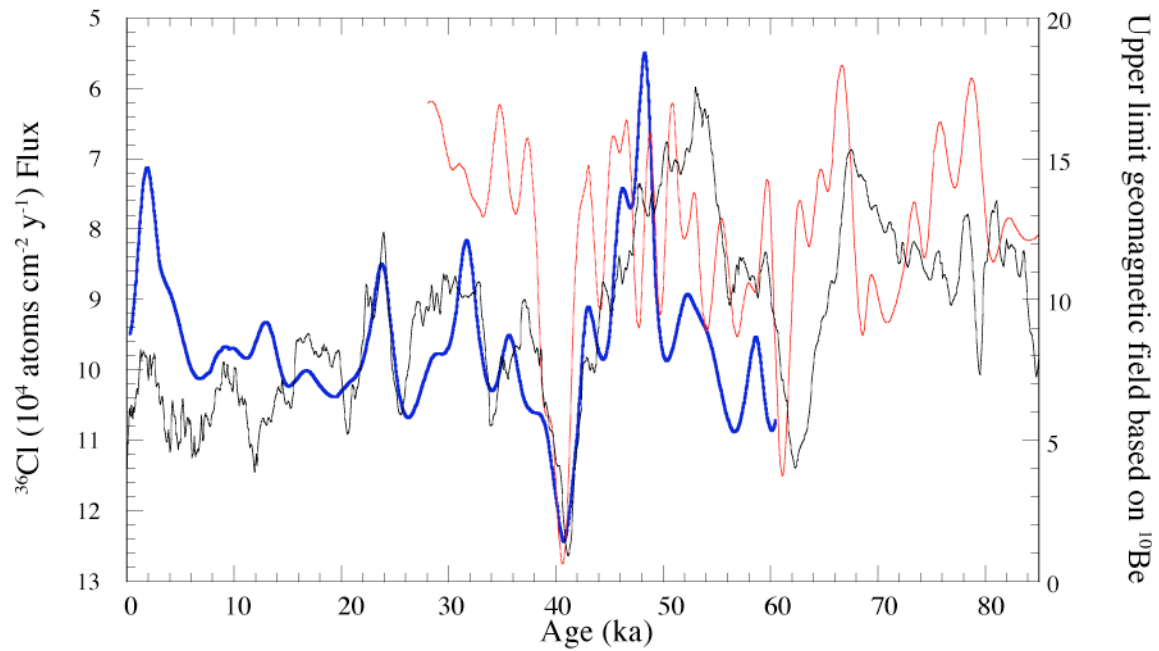


Figure 5-14. Comparison of the EHC06 paleointensity stack to  $^{36}\text{Cl}$  flux (red line) (Baumgartner et al., 1997) and the paleointensity estimate based on the  $^{10}\text{Be}$  flux (blue line) (Muscheler et al., 2005), from the GRIP and GISP Greenland ice cores, respectively.

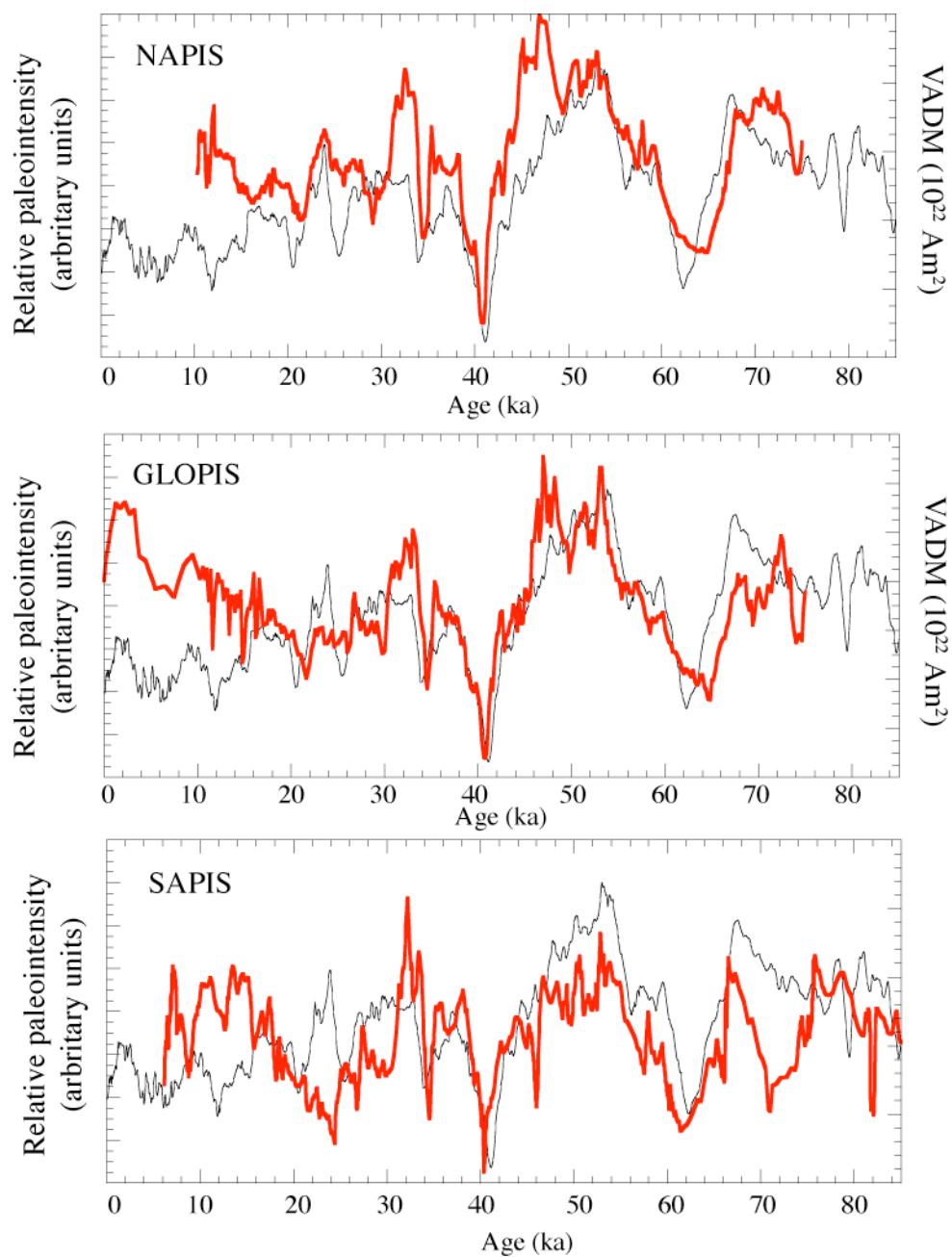


Figure 5-15. Comparison of the EHC06 paleointensity stack (black line) on the revised GISP age (Shackleton et al., 2004) to other paleointensity stacks: a) NAPIS (Laj et al., 2000), b) GLOPIS (Laj et al., 2004) and c) SAPIS (Stoner et al., 2002) (red lines).

## CHAPTER 6

### RELATIVE GEOMAGNETIC PALEOINTENSITY IN THE GAUSS AND GILBERT CHONS FROM IODP SITE U1313 (NORTH ATLANTIC)

#### **Introduction**

Integrated Ocean Drilling Program (IODP) Site U1313 (41°0.068' N, 32°57.44' W) constitutes a reoccupation of Deep Sea Drilling Project (DSDP) Site 607 located at the base of the upper western flank of the Mid-Atlantic Ridge, ~240 miles northwest of the Azores Islands, in a water depth of 3426 m (Figure 6-1). DSDP Site 607 utilized the hydraulic piston corer (VLHPC) and the Extended Core Barrel (XCB) to penetrate to a total depth of 311.3 meters below seafloor (mbsf) (Ruddiman, Kidd, Thomas, et al., 1987). DSDP Sites 607 and 609 (both drilled during DSDP Leg 94) constitute benchmark sites for the long-term (Myr) surface and deep ocean environmental records from the sub-polar North Atlantic (Ruddiman et al., 1986; Raymo et al., 1989). Drilling of DSDP Leg 94 sites preceded the shipboard capability for construction of composite sections and continuous measurement of magnetic parameters with pass-through magnetometers. The magnetostratigraphy from Site 607 was based on discrete samples (Clement and Robinson, 1987), and indicated a clear sequence of reversals to the base of the Matuyama Chronozone, with poor definition of polarity zones in the Gauss and Gilbert Chons.

Four holes (Holes U1313A-D) were cored with the Advanced Piston Corer (APC) using non-magnetic core barrels to maximum depths of 308.6, 302.4, 293.4, and 152.0 mbsf, respectively, with an average recovery of 103.5% (Expedition 306 Scientists, 2006). The Holocene to uppermost Miocene sedimentary succession at Site U1313 comprises nannofossil ooze with varying amounts of foraminifers and clay- to gravel-sized terrigenous components. Two major lithologic units were identified. Unit I consists of Holocene to Upper Pliocene alternating nannofossil ooze, silty clay nannofossil ooze, and nannofossil ooze with clay. Unit II

consists of Upper Pliocene to uppermost Miocene nannofossil ooze, characterized by high (~95%) and uniform carbonate concentrations. The shipboard magnetic stratigraphy at Site U1313 was constructed on the basis of continuous measurements of natural remanent magnetization (NRM) after AF demagnetization at peak fields of 20 mT. NRM intensities after 20 mT peak field demagnetization are in the  $10^{-3}$  to  $10^{-4}$  A/m range above 150 mbsf, and fall to the  $10^{-4}$  to  $10^{-5}$  A/m range in the lower part of the section (150-275 mbsf).

U-channel samples collected post-cruise have allowed refinement of the shipboard magnetic stratigraphy at Site U1313. The polarity stratigraphy can now be resolved for the Gauss and Gilbert Chrons, and for the latest Miocene, down to ~285 meters composite depth (mcd). The nannofossil oozes have a weak low-coercivity magnetization carried by magnetite. Although volume magnetic susceptibility is weak and partially negative, it is reproducible as demonstrated by replicate measurements on u-channel samples. Natural gamma radiation and reflectance data, collected shipboard on whole core sections, and magnetic susceptibility from u-channel samples can all be correlated to the benthic oxygen isotope stack of Lisiecki and Raymo (2004). The age model for Site U1313 is based on the correlation of the u-channel magnetic susceptibility record to a benthic oxygen isotope stack and, in part, to the astronomic solution for insolation. The resulting reversal ages are consistent (within one obliquity cycle) with established reversal ages in current polarity timescales. Three relative paleointensity proxies (slopes of NRM/ARM, NRM/IRM, and NRM/ARM-acquisition) are broadly consistent with each other, can be correlated to Pacific and Indian ocean records of the same age, and show little evidence for the “saw-tooth” pattern of paleointensity decrease, observed in other records of the same age.

## Methods

At Site U1313, u-channel samples (2x2 cm square cross-section and 150 cm in length) were collected from the center of the split face of core sections in the 120-285 meters composite depth (mcd) interval of the shipboard-derived composite section that corresponds to the 2.4-6.2 Ma interval. The natural remanent magnetization (NRM) of u-channel samples was measured each 1-cm down-section on a 2G-Enterprises pass-through cryogenic magnetometer at the University of Florida. From 120 mcd to 170 mcd, the NRM of u-channel samples was AF demagnetized in the 20-60 mT interval using 5 mT increments. Below 170 mcd, the weak magnetization intensities led to the NRM being demagnetized in 2.5 mT increments in the 20-40 mT peak field range. Volume susceptibility was then measured each 1-cm down-section using a susceptibility track specifically designed for u-channel samples that has a measurement resolution of a few centimeters (Thomas et al., 2003). The volume susceptibility values are very low, but repeatable, varying in the  $-10^{-2}$  to  $10^{-2}$  (SI) range. The mean of three replicate measurements, and the resulting standard deviation, constituted the susceptibility record.

Anhyseretic remanent magnetization (ARM) was applied using an AF field of 100 mT and a bias DC field of 50  $\mu$ T. Isothermal remanent magnetization (IRM) was imparted using a 0.5 T DC field. Both artificial remanences were demagnetized with the same AF steps used to demagnetize NRM. ARM acquisition was also measured for the 120-170 mcd interval using increasing AF peak fields in 5 mT increments in the 20-60 mT peak field range, and a bias DC field of 50  $\mu$ T.

In the 120-170 mcd interval, principal components were calculated from the NRM data using the method of Kirschvink (1980) applied to the 20-60 mT demagnetization interval. In the lower part of the section, below 170 mcd, a single demagnetization step (30 mT) was generally used to determine the characteristic magnetization due to the weak magnetization intensities that

precluded the definition of magnetization components. NRM data were normalized by ARM, ARM-acquisition, and IRM to generate relative paleointensity (RPI) proxies. For the 120-170 mcd interval, slopes of NRM/ARM and NRM/IRM were calculated for each measurement position (each 1-cm) in the 20-60 mT peak field range. The linear correlation coefficient (R) provided a measure of the uncertainty in the value of the slope. Similarly, for normalization by ARM-acquisition, the slope of the NRM-lost vs ARM-gained plot was calculated together with a linear correlation coefficient (R). The paleointensity proxy based on ARM-acquisition is analogous to the “pseudo-Thellier” method of Tauxe et al. (1995). From 170 to ~245 mcd, NRM/ARM and NRM/IRM values were calculated using the mean of 5 values of the ratio, calculated for 5 demagnetization steps in the 20-30 mT interval (2.5 mT increments).

## Results

The magnetic polarity stratigraphy at IODP Site U1313, that is reported here, covers the interval between the Miocene-Pliocene boundary and the onset of the Matuyama Chron. The polarity subchrons: Kaena, Mammoth, Cochiti, Nunivak, Sidujfall, and Thevra are all clearly defined (Figures 6-2 and 6-3, Table 6-1), however, below ~250 mcd, polarity zones are poorly defined. The age of the base of the u-channelled section is Late Miocene (~6.2 Ma).

NRM intensities (prior to demagnetization of u-channel samples) are weak, lying in the  $10^{-3}$ - $10^{-4}$  A/m range in the 120 mcd-170 mcd interval, and in the  $10^{-4}$ - $10^{-5}$  A/m range below 170 mcd (Figures 6-2 and 6-3). Magnetization components can be adequately defined down to 170 mcd, as indicated by orthogonal projections of demagnetization data (Figure 6-4), and maximum angular deviation (MAD) values that accompany component magnetizations (Figure 6-2). In the lower part of the section, magnetization components could not be adequately resolved from orthogonal projections because there is no systematic decrease in magnetization intensity to the

origin of the projection. The definition of the characteristic magnetization in this interval was based on a single demagnetization step (30 mT peak field). An initial age model was based on the location of polarity reversals, the polarity timescale of Cande and Kent (1995), and the assumption of constant sedimentation rates within polarity chrons, yielding interval mean sedimentation rates of 3-6 cm/kyr (Figure 6-5).

Normalized remanence values (RPI proxies) were calculated using three normalizers: demagnetized ARM, demagnetized IRM, and ARM-acquisition. At each 1-cm interval, in the 120-170 mcd interval, the normalized remanence values were calculated by determining the slopes of NRM versus the normalizer, in the 20-40 mT AF peak field range (Figure 6-6). The linear correlation coefficient ( $R$ ) of the slope yields a measure of the uncertainty in the definition of the slope. Although the three RPI proxies show similar variability, the NRM/ARM and NRM/ARM-acquisition records show anomalously high values, particularly in the 120-130 mcd interval and at about 153 mcd (Figure 6-6). The NRM/IRM record does not show these anomalous values, and was therefore used as the Site U1313 RPI proxy for comparison with other RPI records.

Anhyseretic susceptibility divided by susceptibility ( $k_{arm}/k$ ) is sensitive to magnetite grain size, with high values indicating finer grains. The magnetite grain size proxy was calculated for the 120-160 mcd interval where susceptibility values are positive. The  $k_{arm}/k$  values indicate that, in intervals where the NRM/ARM and NRM/ARM-acquisition RPI proxies are anomalously high, the magnetite grain size is apparently relatively coarse (shaded intervals in Figure 6-7). These intervals are coincident with the darker (glacial) intervals in the section, implying the presence of coarser magnetic material, possibly ice rafting debris (IRD), during the glacial intervals. This interpretation is supported by other magnetic properties: ARM is very



weak in the affected intervals, and the IRM intensities are also relatively low. Magnetic susceptibility values in these intervals are, however, consistent with the surrounding sediment, consistent with the magnetite in these intervals being anomalously coarse grained.

In the 170-220 mcd interval, NRM components could not be adequately defined because of the very weak NRM intensities (Figures 6-2 and 6-3). For this interval, we plot mean values for NRM/ARM and NRM/IRM for five demagnetization steps (2.5 mT increments) in the 20-30 mT peak field range (Figure 6-8). The standard deviation about the mean gives a measure of the variability in normalized remanence values in this demagnetization range.

The RPI record (NRM/IRM) from IODP Site U1313 can be correlated to the East Pacific paleointensity stack (EPAPIS) of Yamazaki and Oda (2005) back to 3 Ma, to the Valet and Meynadier (1993) record from the Pacific Ocean (ODP Leg 138) back to 4 Ma, and to the Indian Ocean record (Core MD90-0940) of Meynadier et al. (1994) beyond 5 Ma (Figure 6-9). The age model for the ODP Leg 138 record is from the astronomical tuning of the gamma ray attenuation (GRA) density record (Shackleton et al., 1995). The age model for the EPAPIS stack is based on the correlation of ARM intensity to the oxygen isotope record from ODP Site 1143 from the South China Sea (Tian et al., 2002). The age model for Core MD90-0940, from the Indian Ocean, was determined by correlation to ODP Sites 709 and 758 using nannofossil events and reversal boundaries.

Volume magnetic susceptibility records from the u-channel samples vary between low positive and low negative values (Figure 6-10). Triplicate measurements at 1-cm spacing for each u-channel sample yielded standard deviations that indicate that the low susceptibility values are reproducible. The reflectance ( $L^*$ ) and natural gamma radiation records, acquired shipboard each 5 cm (Expedition 306 Scientists, 2006), co-vary with the susceptibility record (Figure 6-11),

indicating that all three parameters are mainly controlled by biogenic (carbonate) dilution of terrigenous (detrital) input. The susceptibility record can be correlated to the benthic oxygen isotope stack of Lisiecki and Raymo (2004), and this correlation (Figure 6-12) is used to acquire the age model for the 2.4-5.3 Ma interval at Site U1313. The resulting age model yields a more detailed picture of sedimentation rates, relative to that acquired from reversal ages and the assumption of constant sedimentation rates in polarity chrons (Figure 6-5). The polarity reversal ages in the 2.4-5.3 Ma interval, based on correlations of susceptibility to the benthic isotope stack, are within one obliquity cycle of reversal ages in modern polarity timescales (Table 6-2), with the exception of the reversal boundaries of the Kaena and Mammoth subchrons (values in square brackets in Table 2) that are up to 155 kyrs younger than given in the Lourens et al., (2004) timescale. In this interval (2.8-3.4 Ma), a Gaussian-shaped filter centered at 41 kyr, applied to the magnetic susceptibility, can be compared to the astronomic solution for summer insolation at 65°N from Laskar et al. (2004) (Figure 6-13). The filtered susceptibility data shows a modulation that is consistent with the modulation of calculated summer insolation at 65° N. Minor adjustments of the filtered susceptibility record to fit the astronomic solution results in ages for the Kaena and Mammoth subchrons that are consistent with published astronomically-based timescales (Table 2).

## **Discussion**

The calibrated polarity reversal ages from Site U1313, based on a correlation of the susceptibility record to the isotope stack of Lisiecki and Raymo (2004) and to the insolation solution of Laskar et al. (2004), differ by less than an obliquity cycle (41 kyr) from reversal ages in modern polarity timescales (Table 2). The polarity timescales of Cande and Kent (1995) and Lourens et al. (2004) utilized the Gauss-Gilbert timescale of Hilgen (1991a,b) that was based on cyclostratigraphy in the Trubi Limestones in Sicily. Hilgen (1991a,b) correlated the  $\text{CaCO}_3$

cycles in the Trubi Limestones to the precession and eccentricity orbital solutions of Berger (1978). Very minor adjustments to these ages, to make them compatible with the new astronomic solutions of Laskar et al. (2004), were incorporated in the Lourens et al. (2004) timescale.

The relative paleointensity record from IODP Site U1313 can be correlated with the Pacific records of Valet and Meynadier (1993) and Yamazaki and Oda (2005), and to the Indian Ocean record of Meynadier et al. (1994) (Figure 6-9). The so-called “saw-tooth” pattern in relative paleointensity, whereby relative paleointensity declines within polarity chrons and abruptly recovers post-reversal, was first described from ODP Leg 138 sediments (Valet and Meynadier, 1993). This “saw-tooth” pattern received a great deal of attention as it may provide clues to mechanism of triggering of polarity reversals. The abrupt recovery in paleointensity post-reversal followed by a slow decrease in intensity leading to the next reversal was particularly clear in subchron C2An.1n (late Gauss) in the ODP Leg 138 sediments (Figure 6-9). This “saw-tooth” pattern has been identified in other equatorial Pacific records, as well as Indian Ocean records (Meynadier et al., 1994; Valet et al., 1994; Thibault et al., 1995) but is not seen in all RPI records from this interval (Tauxe and Shackleton, 1994; Kok and Tauxe, 1999). Kok and Tauxe (1996a, 1996b) used a cumulative viscous remanence (VRM) model to explain the “saw-tooth” pattern of paleointensity in the Gauss Chronozone. Individual polarity zones are not uniformly affected by VRM acquisition, and VRM acquired over millions of years can be resistant to the AF demagnetization techniques. Mazaud (1996) developed an alternative model whereby some but not all magnetic particles in the sediment acquire NRM at the time of deposition, while the remaining grains acquire magnetization after deposition in the subsequent polarity zone. This leads to a decrease in intensity of the magnetization leading up to a reversal

due to the competing effect of the magnetization acquired at the time of deposition and that acquired progressively in opposite polarity.

The RPI record from IODP Site U1313 is one of only a handful of high-sedimentation-rate RPI records for the interval from 2.5 Ma to 5.3 Ma, with sedimentation rates in the 3-6 cm/kyr range. From 2.5 Ma to 4 Ma, the RPI record can be correlated to records from the Pacific Ocean (Valet and Meynadier, 1993; Yamazaki and Oda, 2005). Between 4 Ma and 5.3 Ma, the Site U1313 RPI record is less robust than for the younger part of the record, however, the standard deviations associated with the mean normalized remanence values are low, indicating consistent normalized remanence values for different demagnetization steps. The older part of the RPI record can be adequately correlated to the only other RPI record available for this time interval, the record of Meynadier et al. (1994) from the Indian Ocean (Figure 6-9). The Site U1313 RPI record does not clearly show the “saw-tooth” pattern of RPI variations first recognized in the Gauss Chronozone of ODP Leg 138 sediments from the Pacific Ocean (Valet and Meynadier, 1993). This observation tends to indicate that the “saw-tooth” pattern of RPI may be an artifact of delayed remanence acquisition as suggested by Kok and Tauxe (1996a,b) and Mazaud (1996), rather than a feature of the geomagnetic field at this time.

The magnetic stratigraphy from Site U1313 covers the interval from 2.5 Ma to 6.2 Ma, and all known subchrons of the Gauss and Gilbert are recorded. Interestingly, there are no polarity excursions in the Site U1313 record, although the relatively high sedimentation rates at Site U1313 might be expected to reveal them, and no excursions have been unequivocally detected elsewhere in this time interval. Cycles in the magnetic susceptibility record at Site U1313 have allowed age-calibration by correlation to the benthic oxygen isotope stack of Lisiecki and Raymo (2004). The tuned ages of the reversal boundaries are consistent with current timescales (e.g.

Lourens et al., 2004) that all obtained their astronomically calibrated reversal ages for Gauss and Gilbert subchrons from the work of Hilgen (1991a,b) in the Trubi Limestones of southern Italy, which is therefore ratified by this present work.

Table 6-1. Depth of polarity chrons from IODP Site U1313 in meters composite depth (mcd). Estimated uncertainties in the depth of the reversal boundaries are given in parentheses.

Chron CK95	Depth (mcd)	Age (ka) CK95
top C2An.1n (base Matuyama)	123.17 ( $\pm 0.13$ )	2.5810
base C2An.1n (top Kaena)	142.83 ( $+0.21$ )	3.0400
top C2An.2n (base Kaena)	146.33 ( $\pm 0.10$ )	3.1100
base C2An.2n (top Mammoth)	150.67 ( $\pm 0.10$ )	3.2200
top C2An.3n (base Mammoth)	154.50 ( $\pm 0.10$ )	3.3300
base C2An.3n (base Gauss)	168.61 ( $\pm 0.15$ )	3.5800
top C3n.1n (top Cochiti)	195.28 ( $\pm 0.10$ )	4.1800
base C3n.1n (base Cochiti)	200.83 ( $\pm 0.10$ )	4.2900
top C3n.2n (top Nunivak)	209.50 ( $\pm 0.15$ )	4.4800
base C3n.2n (base Nunivak)	216.33 ( $\pm 0.15$ )	4.6200
top C3n.3n (top Sidufjall)	224.17 ( $\pm 0.10$ )	4.8000
base C3n.3n (base Sidufjall)	228.83 ( $\pm 0.15$ )	4.8900
top C3n.4n (top Thevra)	233.83 ( $\pm 0.10$ )	4.9800
base C3n.4n (base Thevra)	245.67 ( $\pm 0.05$ )	5.2300
top C3An.1n	267.22 ( $\pm 0.20$ )	5.8940
base C3An.1n	277.17 ( $\pm 0.05$ )	6.1370
top C3An.2n	280.67 ( $\pm 0.05$ )	6.2690

Table 6-2. Polarity reversal ages determined at Site U1313, compared with the polarity reversal ages in the polarity timescales of Cande and Kent (1995), Lourens et al., (2004) and Shackleton et al. (1995). Difference between the Site U1313 reversal ages and timescale ages are given in parentheses. Ages in square brackets indicate the ages of reversals in the Gauss Chron based on the fit of susceptibility to the benthic oxygen isotope stack (Figure 6-12), prior to final tuning to the astronomical solution for insolation (Figure 6-13).

Chron	U1313 Age (Ma)	CK95 Age (Ma)	ATNTS Age (Ma)	Leg 138 Age (Ma)
Base Matuyama	2.616	2.581 (-0.035)	2.581 (-0.035)	
Top Kaena	3.074 [2.998]	3.040 (-0.034)	3.032 (-0.042)	3.046 (-0.028)
Base Kaena	3.153 [3.052]	3.110 (-0.043)	3.116 (-0.037)	3.131 (-0.022)
Top Mammoth	3.268 [3.107]	3.220 (-0.048)	3.207 (-0.061)	3.233 (-0.035)
Base Mammoth	3.346 [3.176]	3.330 (-0.016)	3.330 (-0.016)	3.331 (-0.015)
Base Gauss	3.549	3.580 (+0.031)	3.596 (+0.047)	3.594 (+0.045)
Top Cochiti	4.144	4.180 (+0.036)	4.187 (+0.043)	4.199 (+0.055)
Base Cochiti	4.277	4.290 (+0.013)	4.300 (+0.023)	4.316 (+0.089)
Top Nunivak	4.500	4.480 (-0.02)	4.493 (-0.007)	4.479 (-0.021)
Base Nunivak	4.631	4.620 (-0.011)	4.631 (0)	4.623 (-0.008)
Top Sidufjall	4.760	4.800 (+0.04)	4.799 (-0.39)	4.781 (+0.021)
Base Sidufjall	4.889	4.890 (+0.001)	4.896 (+0.007)	4.878 (-0.011)
Top Thevra	5.009	4.980 (-0.029)	4.997 (-0.012)	4.977 (-0.032)
Base Thevra	5.273	5.230 (0.043)	5.235 (0.038)	5.232 (-0.041)

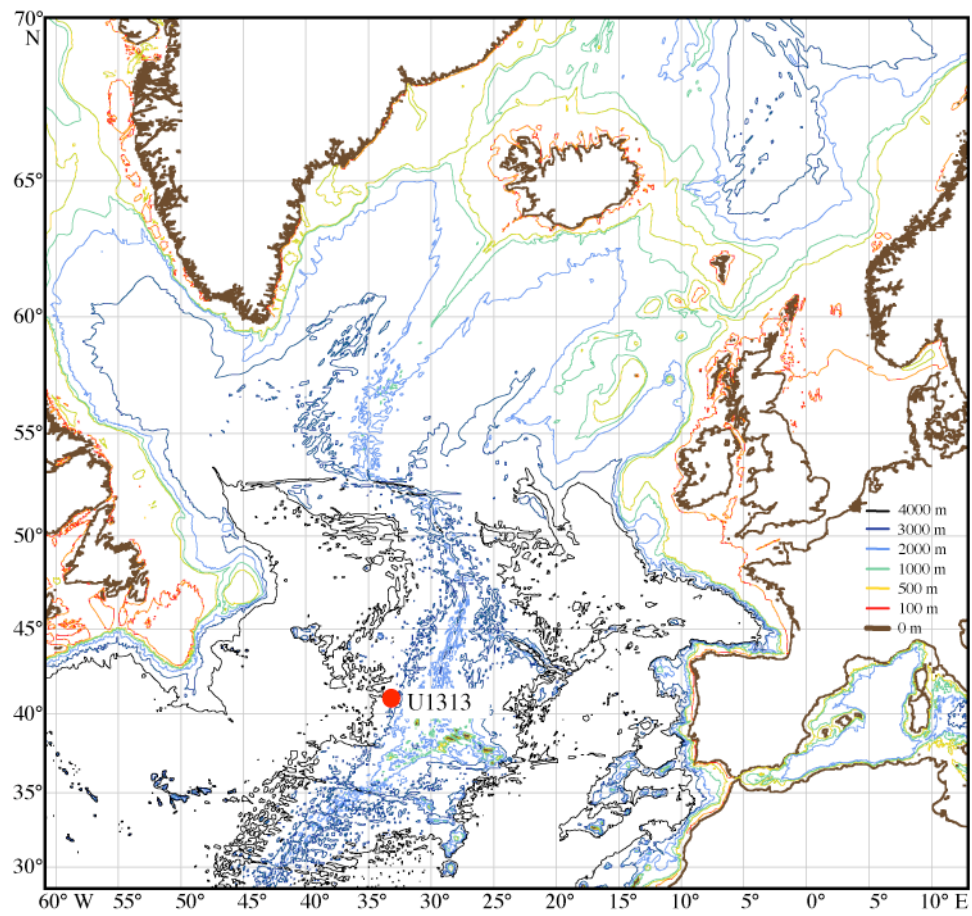


Figure 6-1. Location map for IODP Site U1313.



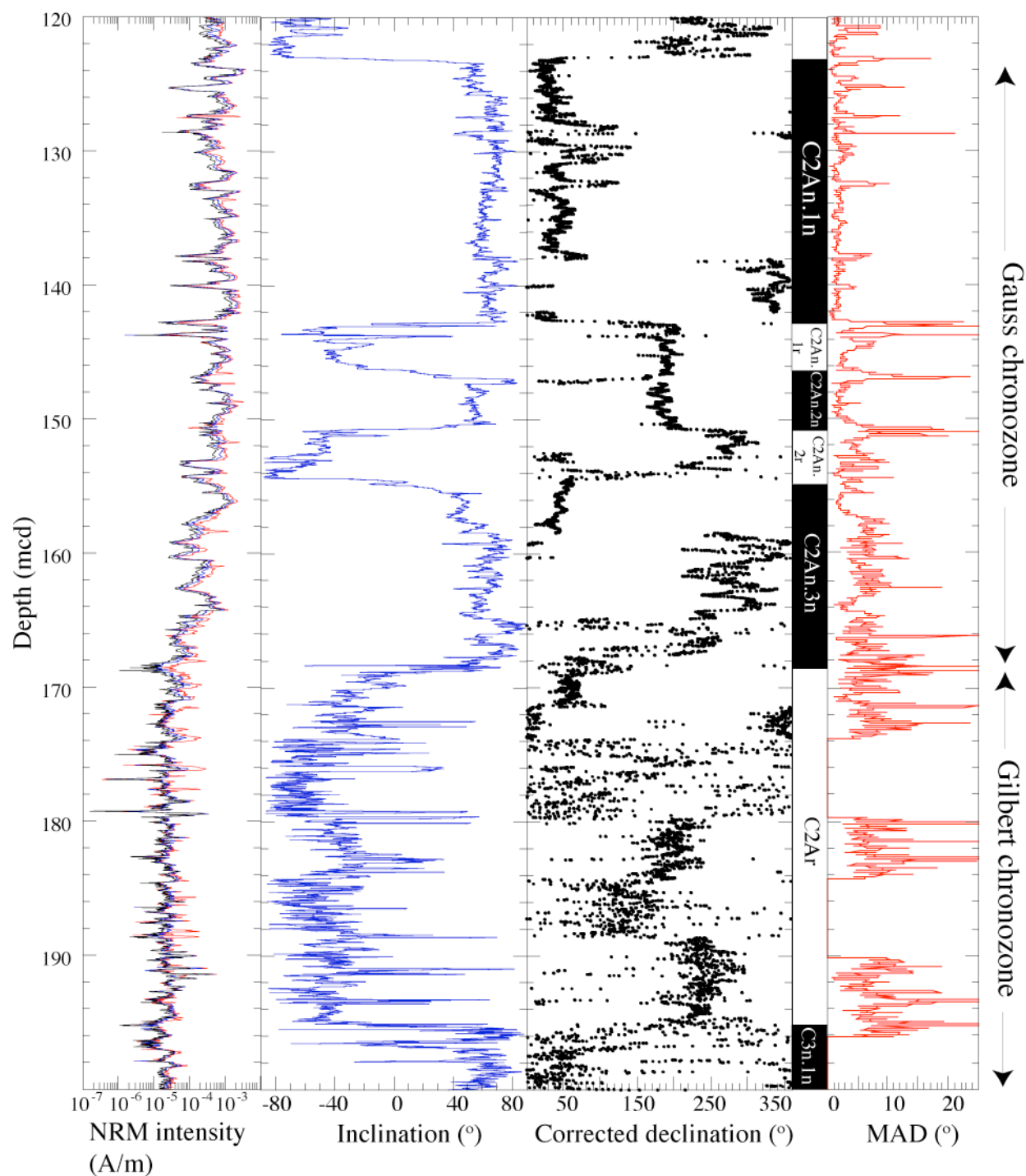


Figure 6-2. Magnetic polarity stratigraphy from IODP Site U1313 in the 120-200 mcd interval. Inclination data from u-channel samples are shown by the blue line. Declination data are shown by the dotted black line. MAD values are shown by the red line. Left plot shows NRM intensity data on a log scale at 0, 20 and 30 mT AF demagnetization steps. Black bars indicate normal polarity, white bars indicate reverse polarity. Chrons are labeled according the Cande and Kent (1992).

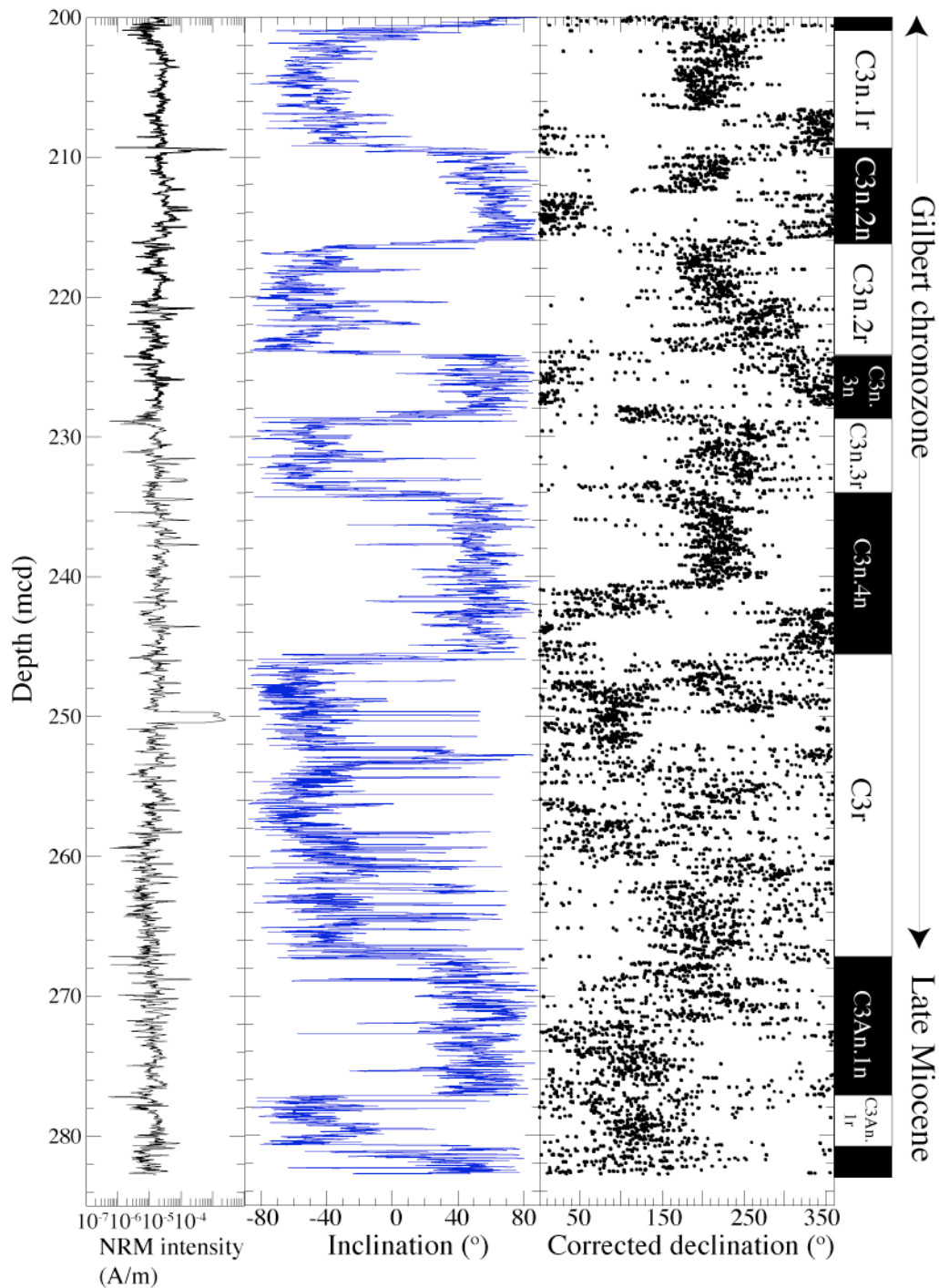


Figure 6-3. Magnetic polarity stratigraphy from IODP Site U1313 in the 200-280 mcd interval from u-channel samples using a single AF demagnetization peak field (30 mT). Inclination data (blue line), declination data (dotted black line). Left plot shows NRM intensity data on a log scale prior to AF demagnetization of u-channel samples. Black bars indicate normal polarity, white bars indicate reverse polarity. Chrons are labeled according the Cande and Kent (1992).

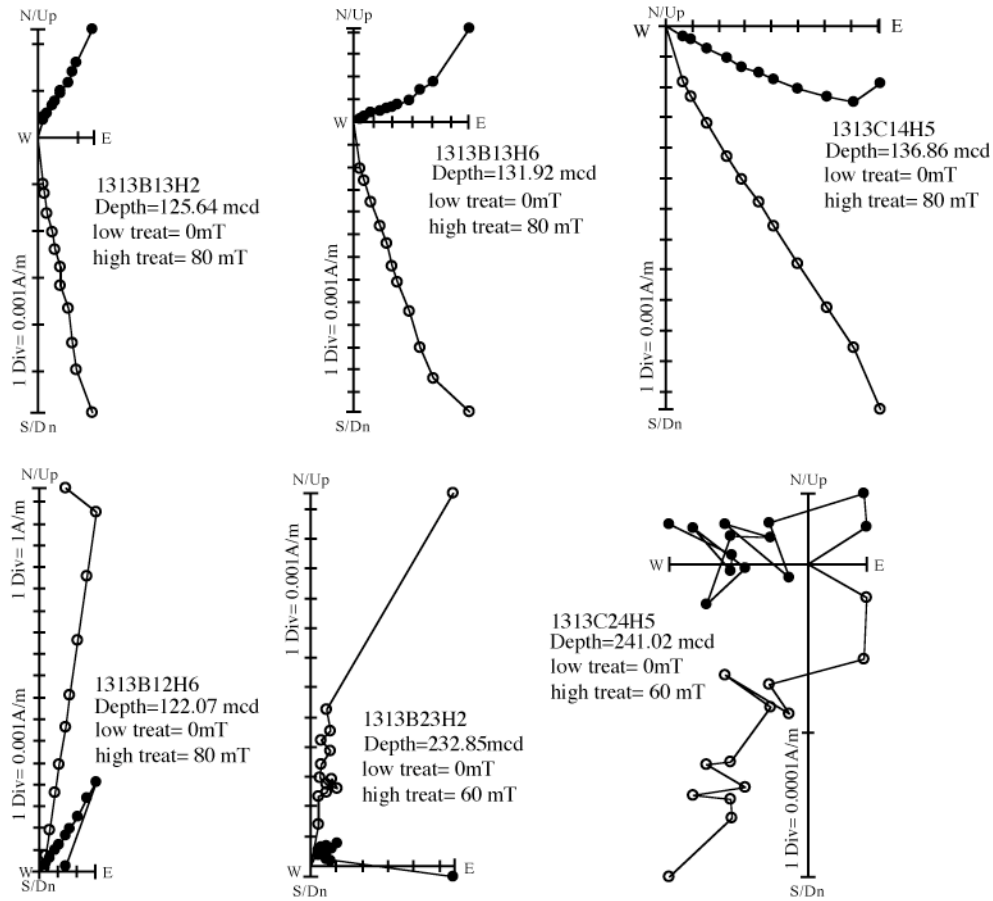


Figure 6-4. Vector end-point projections of AF demagnetization data for particular horizons from u-channel samples. Open circles indicate the vector end-point projection on the vertical plane while closed circles indicate the vector end-point projection on the horizontal plane.

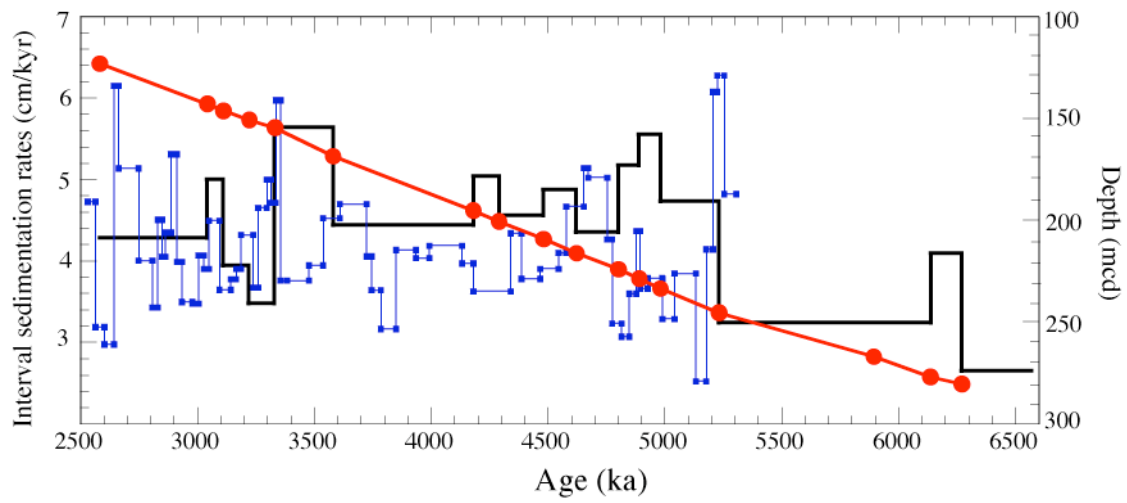


Figure 6-5. Interval sedimentation rates (black line), and age-depth plot (red line) calculated using the magnetic polarity stratigraphy only and interval sedimentation rates from the fit of susceptibility to the target benthic oxygen isotope curve (blue line).

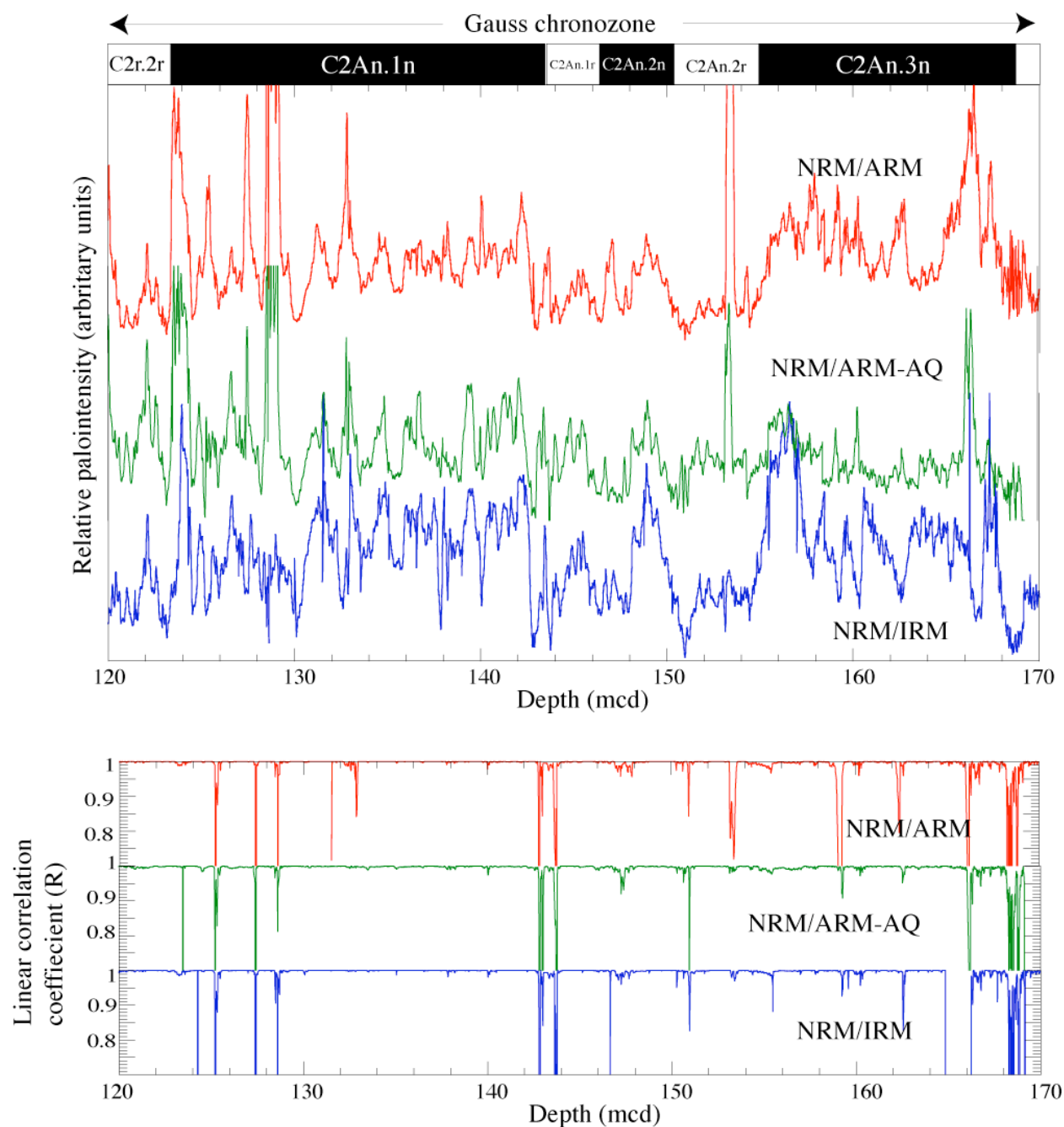


Figure 6-6. Gauss Chronozone at Site U1313: Three relative paleointensity proxies: slope of NRM/ARM (red line), slope of NRM/ARM-acquisition (blue line) and slope of NRM/IRM (green line) for the 120-170 mcd interval. All calculated in the 20-60 mT peak field demagnetization interval. Black bar indicates normal polarity, white bar reverse polarity. Chrons are labeled according the Cande and Kent (1992). Lower plot shows R-values for the slopes of NRM/ARM, NRM lost versus ARM gained and NRM/IRM.

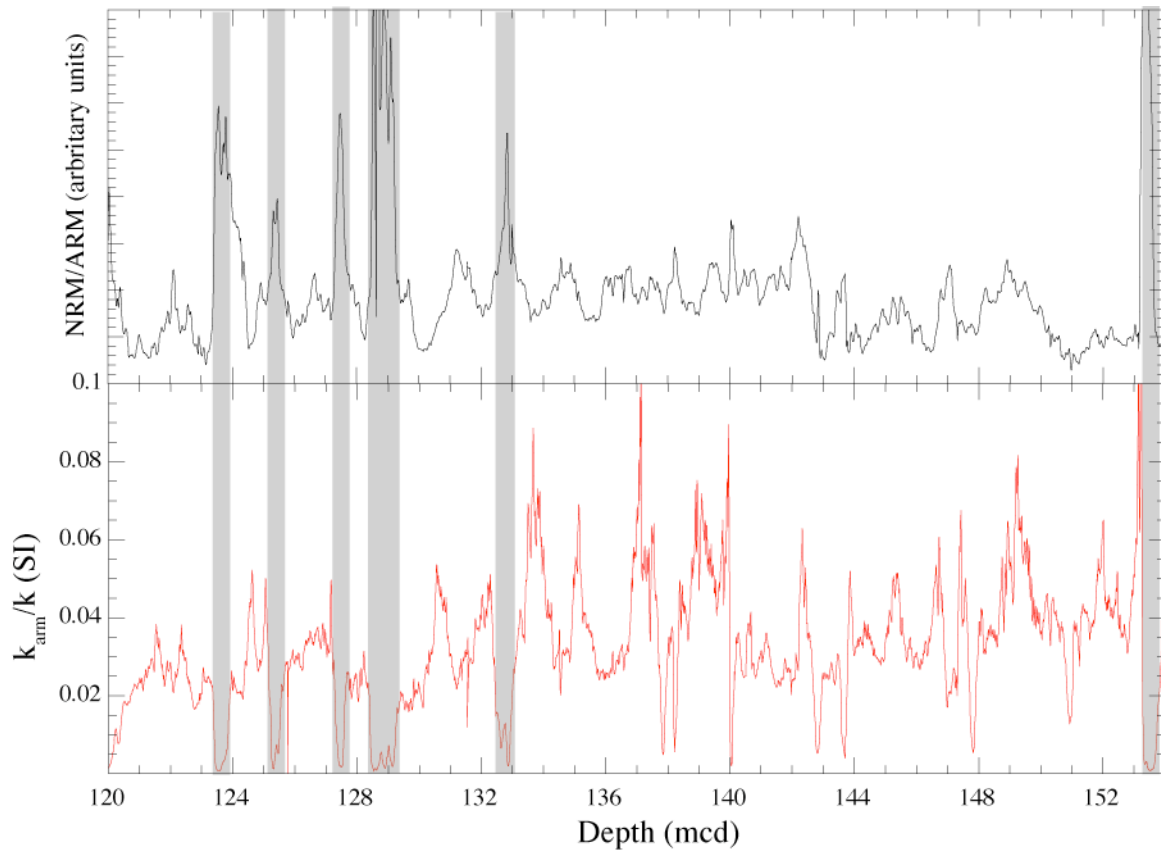


Figure 6-7. The magnetic grain size proxy, anhysteretic susceptibility divided by susceptibility ( $k_{arm}/k$ ), for the 2.5-3.3 Ma interval. Shading shows the darker (glacial) intervals characterized by coarser magnetite grain size.

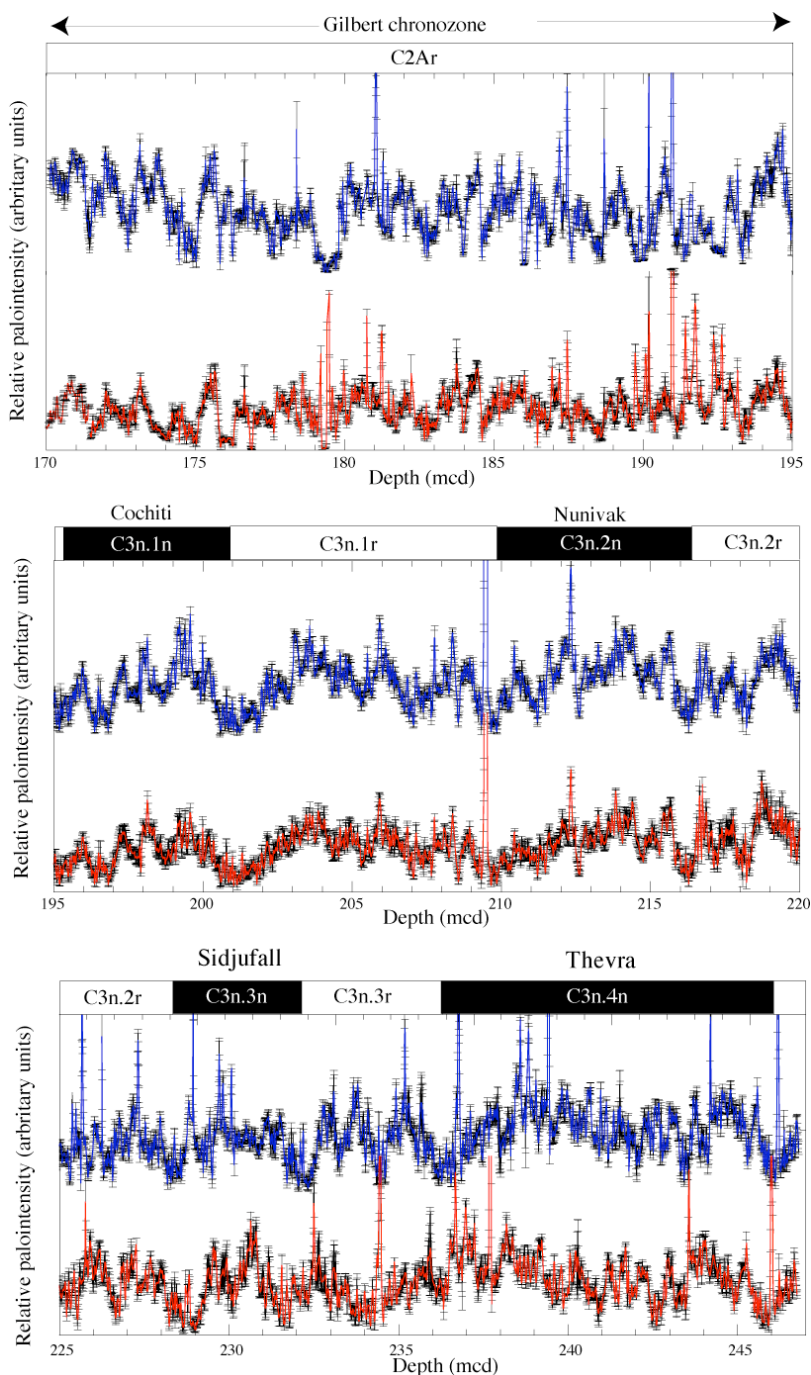


Figure 6-8. Later part of the Gilbert Chronozone at Site U1313: Two relative paleointensity proxies NRM/ARM (red line) and NRM/IRM (green line) with standard deviation shown by a black bar, for the 170-220 mcd interval, calculated over five AF demagnetization steps in the 20-30 mT peak field interval. Black indicates normal polarity, white reverse polarity. Chrons are labeled according the Cande and Kent (1992).

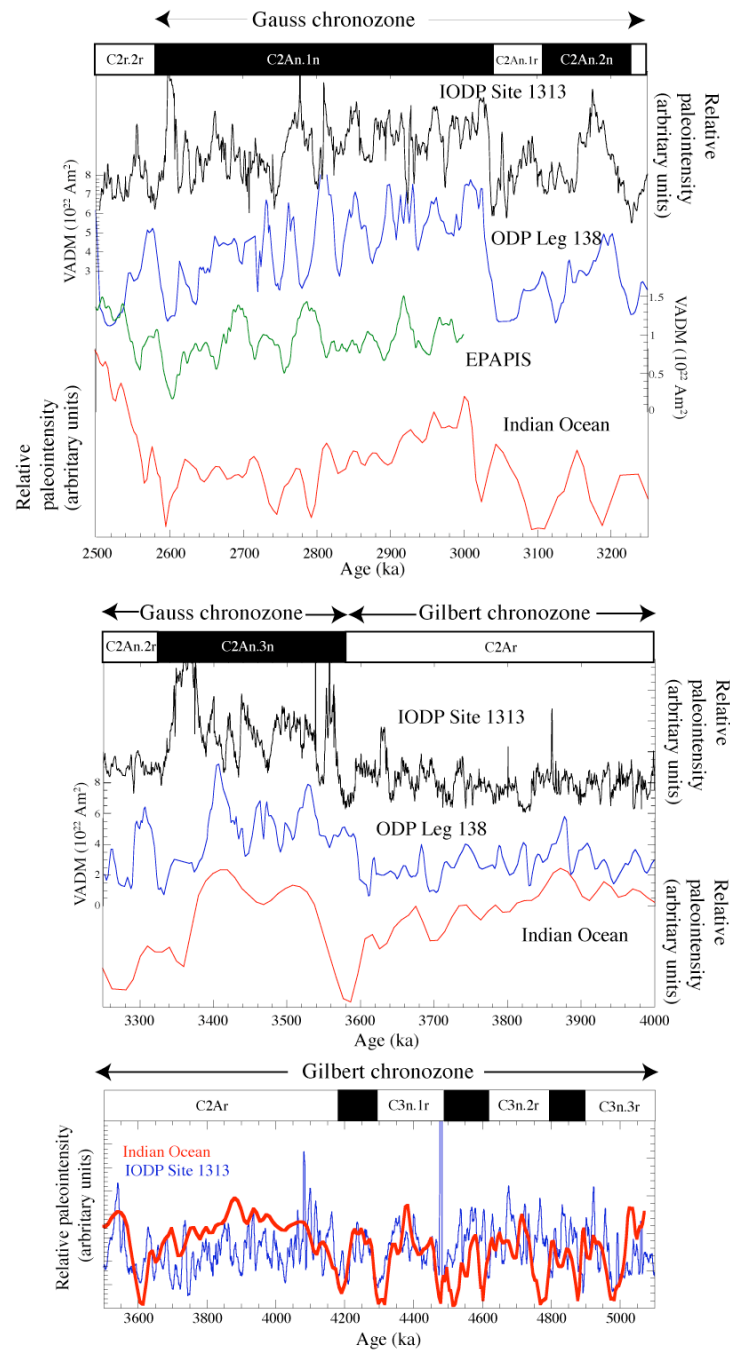


Figure 6-9. Relative paleointensity records from IODP Site U1313 (black line), the Pacific record of Valet and Meynadier (1993) (blue line), the Pacific EPAPIS stack (Yamazaki and Oda, 2005) (green line) and the Indian Ocean record (Meynadier et al., 1994) (red line) between 2.5-4 Ma. Black bar indicates normal polarity, white bar reverse polarity. Chrons are labeled according to the Cande and Kent (1992). Lower plot shows the IODP Site U1313 relative paleointensity record after a 9-point smooth (blue line) overlaid by the Indian Ocean paleointensity record (Meynadier et al., 1994) (red line) in the 3.5-5.2 Ma interval.



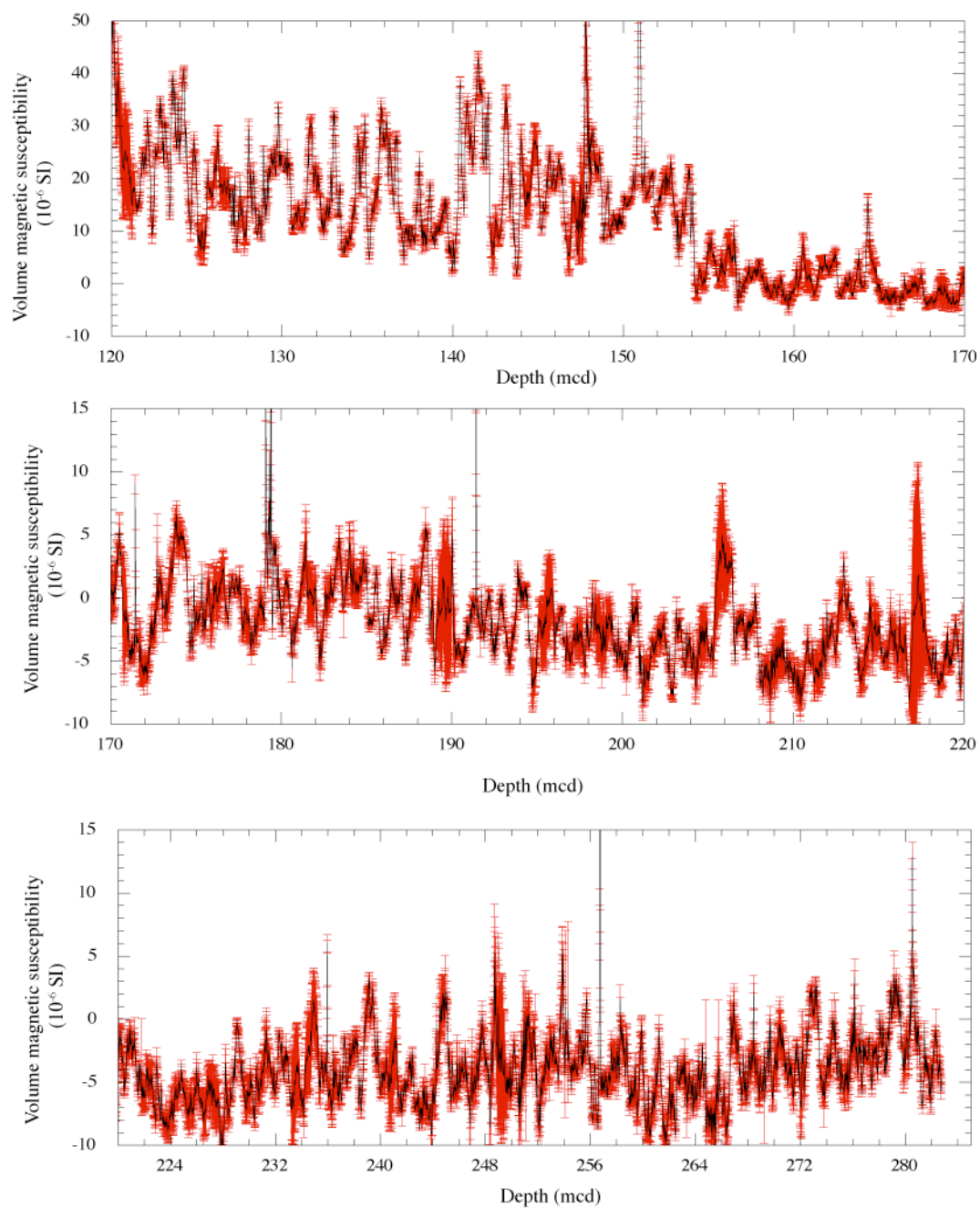


Figure 6-10. Volume magnetic susceptibility from u-channel samples. Black line is a mean of three measurements, red bars indicate the standard deviation from the mean.

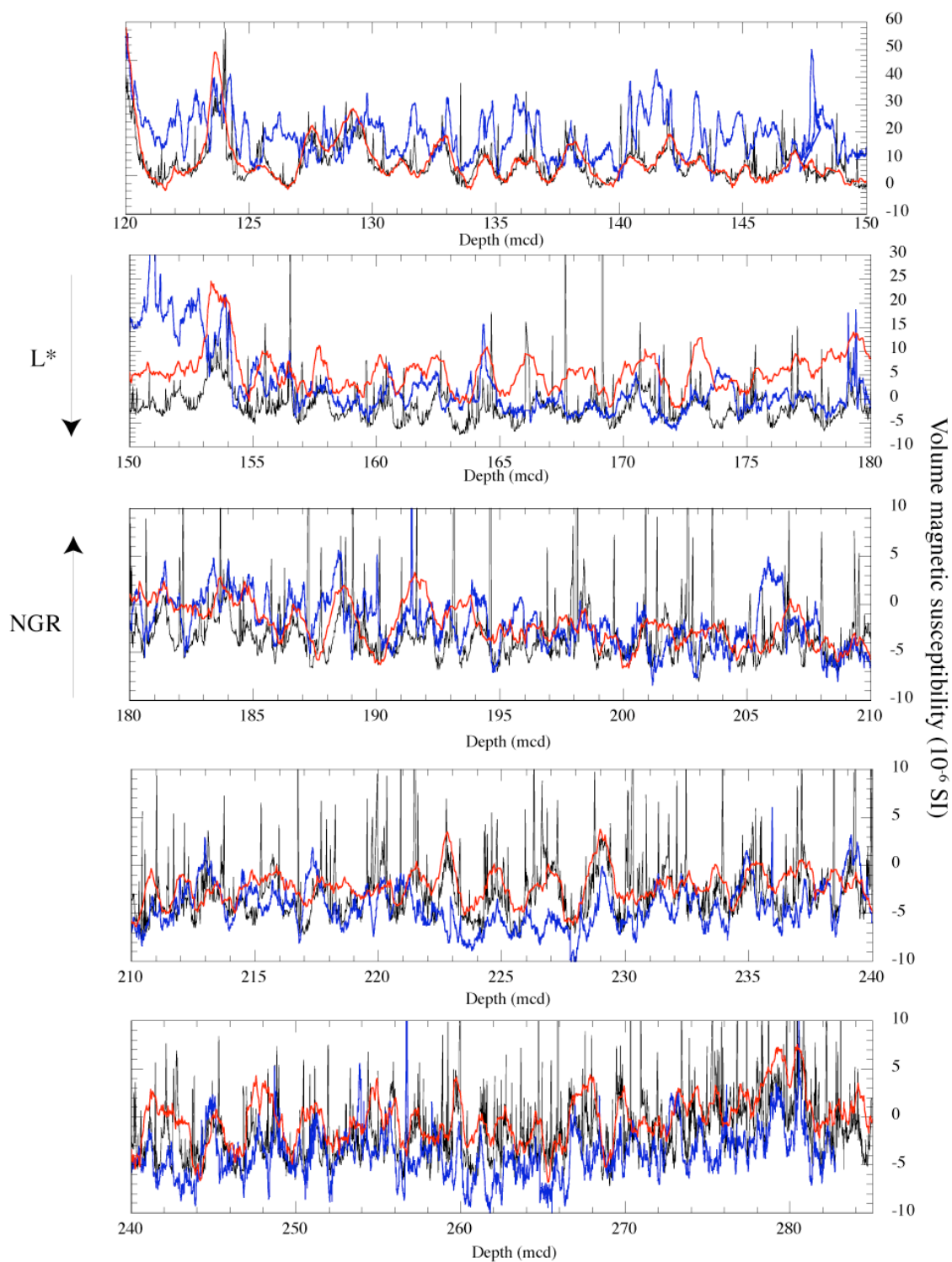


Figure 6-11. Volume magnetic susceptibility from u-channel samples (blue line) and  $L^*$  reflectance data measured shipboard (black line). Red line is smoothed natural gamma radiation (NGR) data.

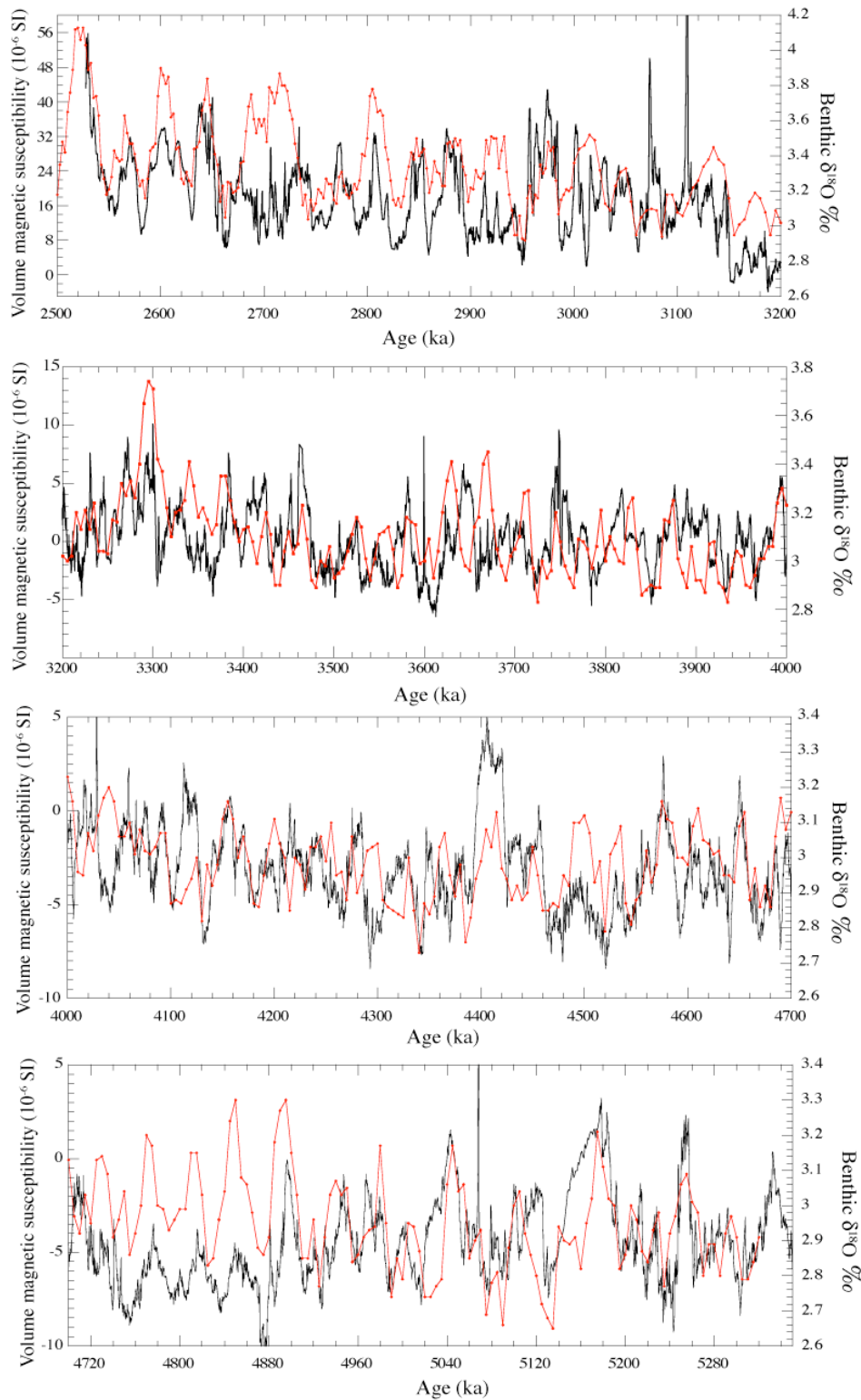


Figure 6-12. Mean volume magnetic susceptibility (black line) tuned to the benthic oxygen isotope stack of Lisiecki and Raymo (2004) (red line) for the 2.5-5.3 Ma interval.

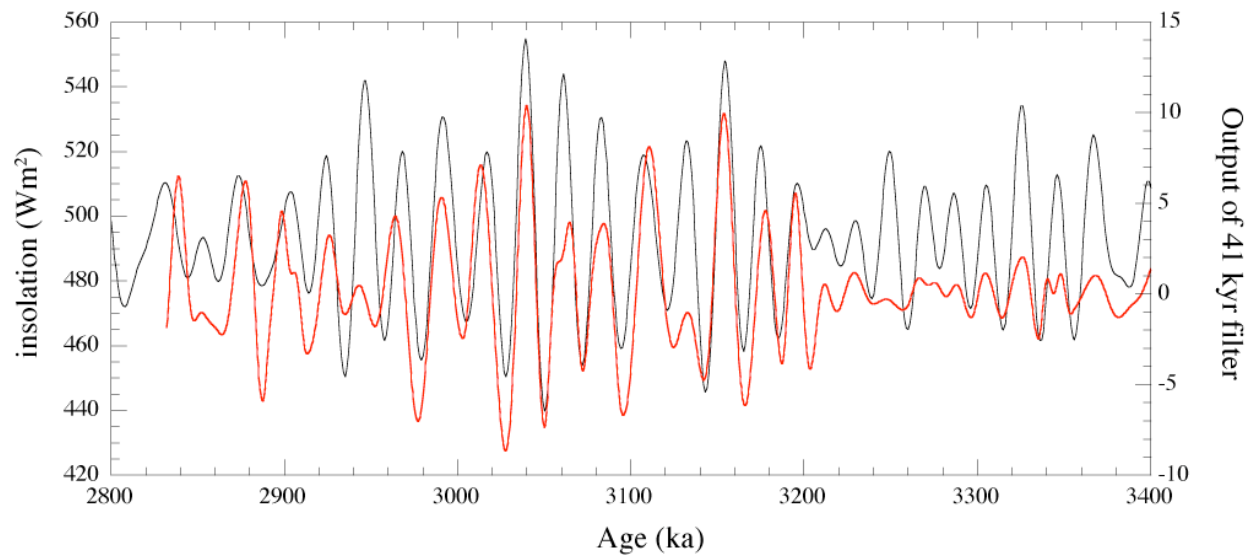


Figure 6-13. Output of a gaussian filter centered on a period of 41 kyr (bandpass=  $0.024 \text{ kyr}^{-1}$ ) applied to the u-channel volume susceptibility record (black line) and the astronomic solution for summer insolation at  $65^\circ\text{N}$  from Laskar et al. (2004).

## CHAPTER 7

### ODP SITE 1092 REVISED COMPOSITE DEPTH SECTION HAS IMPLICATIONS FOR UPPER MIOCENE "CRYPTOCHRONS"

#### **Introduction**

ODP Site 1092 is located in the sub-Antarctic South Atlantic (46°24.7'S, 7°4.8'E, water depth= 1974m). A magnetic polarity stratigraphy was presented for two time intervals (1.95 to ~3.6 Ma and ~5.9 to ~13.5 Ma) by Evans and Channell (2003). As is routine aboard the R/V *Joides Resolution*, composite stratigraphic depths (mcd) for site 1092 were constructed from multi-sensor track (MST) data. Magnetic susceptibility, gamma ray attenuation porosity (GRAPE) and light reflectance data, were used to correlate among holes at the site and to derive an optimal record (splice) of the sedimentary section (Shipboard Scientific Party, 1999). The composite depths for ODP site 1092 have now been revised using X-ray fluorescence (XRF) scans of half-cores. These new data have allowed improved correlation among the holes at the site. The revised meters composite depth (rmcd) scheme has resulted in significant changes in hole-to-hole correlation, particularly within the interval correlative to subchron C5n.2n.

Using the shipboard composite section, Evans and Channell (2003) identified four reverse polarity subzones within the polarity zone correlative to C5n.2n. The four polarity subzones were considered to be correlative to "cryptochrons" in the polarity timescale of Cande and Kent (1992) and were labeled as C5n.2n-1 to C5n.2n-4. The results imply that "cryptochrons" originally identified within marine magnetic anomaly 5 by Blakely (1974) signify polarity reversals rather than solely geomagnetic intensity minima. On the revised composite depth scale, the reverse polarity subchrons labeled as C5n.2n-2 and C5n.2n-3 by Evans and Channell (2003) become a single subchron recorded in two different holes. The result supports the revised composite depth scale and indicates three, not four, subchrons within C5n.2n.

### **Revised Composite Depths (rmcd)**

Shipboard MST data (magnetic susceptibility, GRAPE) and light reflectance data from site 1092 are often too uniform, particularly in the Upper Miocene section (120-185 mcd), for precise hole-to-hole correlation. As part of a project to assess carbonate sedimentation in the southern oceans, Westerhold and Bickert (in preparation) have measured most of the archive halves of cores from site 1092 using the XRF core scanner at the Universität Bremen (Röhl and Abrams, 2000). Fe and Ca intensity data, measured every 2 cm, are often more variable than shipboard MST data and generally provide an efficient means of hole-to-hole correlation.

Some core sections within the shipboard composite splice were not scanned for XRF because the working and archive halves had been too heavily sampled (partly for u-channels to generate the magnetic data). For core sections without XRF data, shipboard magnetic susceptibility could be adequately matched to core sections with Fe intensity data from XRF scans. Some cores from outside the splice had to be stretched or squeezed to conform with the overall depth scale of the shipboard composite section. Drilling related expansion and contraction in these poorly consolidated sediments contributes to the lack of precise correlation of depth scales between holes (Shipboard Scientific Party, 1999). The depth scale of the shipboard composite section (with no stretching or squeezing of cores within the splice) was adhered to in the construction of the revised composite section (rmcd).

Above core 1092A-12H, the shipboard composite section (mcd) is consistent with hole-to-hole correlations based on both MST and XRF data. In the shipboard splice, core 1092C-12H overlies 1092A-12H. core 1092C-12H can be well correlated to 1092B-12H using XRF and magnetic susceptibility, and this correlation is consistent with shipboard composite depths. Correlation from 1092C-12H to the underlying core in the splice (1092A-12H) is poor for both MST and XRF data. However, 1092B-12H can be well correlated to 1092C-13H, but only when

the latter is moved 90 cm up relative to 1092B-12H. This shift is the uppermost modification of the composite section depths. Below this, 1092A-13H can be well correlated to its neighboring cores in the splice (1092C-13H and 1092C-14H), however, the correlation to 1092C-14H requires that this core should be moved up 2.58 m into 1092A-13H. The rationale for this adjustment, based on Fe intensity (XRF) data, is illustrated in Figure 7-1.

### **Implications for Magnetic Stratigraphy**

Augmentation of the MST data by XRF data leads to offsets between the shipboard composite depths (mcd) and the revised composite depths (rmcd) that reach a maximum of 3.54 m in 1092C-14H (Table 5-1). The resulting modification of the composite section provides new composite depths for polarity zone boundaries at site 1092 (Table 7-2 and Figure 7-2), with new age estimates for subchrons not included in the standard geomagnetic polarity timescale (GPTS). The magnetostratigraphic interpretation (the correlation of polarity zones to polarity chronos) is the same as in Evans and Channell (2003) apart from the interval within C5n.2n. When utilizing the shipboard composite section, this normal polarity chronozone appeared to contain four thin polarity subzones that Evans and Channell (2003) associated with “cryptochrons” in marine oceanic magnetic anomaly data. The revision of the composite section indicates that there is duplication of polarity subzones that is an artifact of miscalculations in shipboard composite depths. Polarity subchrons, that were originally labeled C5n.2n-2 (recorded in core 1092A-13H) and C5n.2n-3 (recorded in core 1092C-14H), become a single subchron (relabelled as C5n.2n-2). The realignment of cores 1092A-13H and 1092C-14H within the composite section (Figure 7-1b) results in coincidence of the records of C5n.2n-2 and C5n.2n-3 (Figure 7-3a,b). This not only ratifies the adjustment of the composite section but also reduces the number of subchrons within C5n.2n from four to three (Figure 7-3), consistent with the number of “cryptochrons” in the GPTS of Cande and Kent (1992). Normalized remanence (mean NRM/IRM), used as a

proxy for geomagnetic paleointensity in Evans and Channell (2003), can also be well correlated between cores 1092A-13H and 1092C-14H after revision of the composite depths (Figure 7-3 c,d). The revised composite depths also alter the estimated duration of C5n.2n-2 and C5n.2n-3. C5n.2n-2 now has an estimated duration of 5 kyr, while the duration of C5n.2n-3 increases to 11 kyr, assuming a uniform sedimentation rate within C5n.2n.

In the Orera section (Spain), Abdul Aziz et al. (2003) found three normal polarity subzones within C5r (two within C5r.2r and one within C5r.3r) that are not represented in the GPTS of Cande and Kent (1992, 1995). This augmented C5r could be correlated with the polarity zones at site 1092 by moving the onset of C5r.3r to 179.41 rmcd (Krijgsman, pers comm., 2003). The polarity zones at site 1092 correlative to these three features have thicknesses of 1.75m (C5r.2r-1n), 0.23m (C5r.2r-2n) and 0.38m (C5r.3r-1n). This interpretation appears consistent with a hiatus at 180.48 rmcd advocated by Censarek and Gersonde (2002) from the diatom biostratigraphy. The hiatus was placed at 180.48 rmcd on the basis of the coincidence of the first occurrences of *Denticulopsis praedimorpha* and *Nitzschia denticuloides*, and the last occurrence of *Actinocyclus ingens* var. *nodus*, although the ages of these diatom events are poorly constrained.

In a recent study of chron C5 at ODP site 887, Bowles et al. (2003) found no evidence for reverse polarity subzones within C5n.2n and concluded that “cryptochrons” of this age recognized in marine magnetic anomaly data represent fluctuations in geomagnetic field intensity. The mean sedimentation rate in C5n.2n at site 887 is 1cm/kyr, or ~ 30% of that at site 1092, and it is therefore less likely that polarity intervals of the duration seen at ODP site 1092 would have been recorded at site 887.



The short duration of the reverse polarity intervals within C5n.2n at site 1092 may indicate that they are “excursions” rather than polarity subchrons. Various criteria have been suggested to distinguish “excursions” from polarity subchrons (Cande and Kent, 1992; Gubbins, 1999; Roberts and Lewin-Harris, 2000). Roberts and Lewin-Harris (2000) suggested that for a polarity excursion to qualify as a polarity subchron it should be bounded by two field reversals, and that decreases in paleointensity should be apparent at both bounding reversals. Of the three subchrons within C5n.2n at site 1092, only C5n.2n-3 exhibits a clear recovery in paleointensity between the reversals.

The fundamental conclusion of Evans and Channell (2003) that short duration (5-11 kyr) polarity subchrons exist within C5n.2n, that are probably correlative to “cryptochrons” interpreted from oceanic magnetic anomaly data, has not changed. However, the number of polarity subchrons within C5n.2n has been reduced from four to three by revision of composite depths at site 1092.

Table 7-1. Adjusted depths of core tops from ODP site 1092.

Core	mbsf	Ship mcd*	Offset mcd to mbsf (m)	Revised mcd (rmcd)	Offset mbsf to rmcd (m)	Offset mcd to rmcd (m)
177-1092A-						
12H	103	115.41	12.41	114.48	11.48	-0.93
13H	112.5	126.72	14.22	125.80	13.30	-0.92
14H	122	138.12	16.12	136.51	14.51	-1.61
15H	131.5	149.74	18.24	147.26	15.76	-2.48
16H	141	160.18	19.18	159.01	18.01	-1.17
17H	150.5	168.72	18.22	170.14	19.64	1.42
18H	160	179.85	19.85	181.57	21.57	1.72
19H	169.5	191.84	22.34	191.07	21.57	-0.77
20H	179	201.34	22.34	200.57	21.57	-0.77
177-1092B-						
13H	111.4	122.22	10.82	121.57	10.17	-0.65
14H	121.4	134.32	12.92	132.68	11.28	-1.64
15H	130.9	146.62	15.72	144.14	13.24	-2.48
16H	140.4	155.72	15.32	154.74	14.34	-0.98
17H	149.9	166.76	16.86	165.23	15.33	-1.53
18H	159.4	175.31	15.91	176.96	17.56	1.65
177-1092C-						
13H	108.5	119.93	11.43	119.01	10.51	-0.92
14H	118	132.82	14.82	129.28	11.28	-3.54
15H	127.5	142.70	15.20	140.22	12.72	-2.48
16H	137	155.70	18.70	151.72	14.72	-3.98
17H	146.5	166.38	19.88	162.34	15.84	-4.04
18H	156	175.79	19.79	173.91	17.91	-1.88

Table 7-2. Position of the polarity zone boundaries at site 1092 in shipboard mcd and rmcd. Ages of polarity chrons are from the geomagnetic polarity timescale (GPTS) of Cande and Kent (1992, 1995). Ages of polarity subchrons not featured in the GPTS are marked by an asterisk and estimated assuming constant sedimentation rates within polarity chrons.

Depth (mcd)	rmcd	Chron	Age (Ma) CK95
121.48	120.55	Base C5n.1n	9.880
122.40	121.47	Top C5n.2n	9.920
127.92	127.00	Top C5n.2n.1	10.098*
128.01	127.15	Base C5n.2n.1	10.103*
132.88	131.95	Top C5n.2n.2	10.258*
133.02	132.16	Base C5n.2n.2	10.263*
151.31	148.60	Top C5n.2n.3	10.803*
151.43	148.95	Base C5n.2n.3	10.814*
156.60	154.12	Base C5n.2n	10.949
158.80	157.82	Top C5r.1n	11.052
160.00	159.02	Base C5r.1n	11.099
163.10	161.91	Top C5r.2n	11.476
164.54	163.37	Base C5r.2n	11.531
170.60	169.07	Top C5r.3r.1n	11.866*
170.79	169.26	Base C5r.3r.1n	11.877*
171.75	173.24	Top C5An.1n	11.935
173.00	174.42	Base C5An.1n	12.078
174.20	175.67	Top C5An.2n	12.184
174.49	175.94	Base C5An.2n	12.401
177.70	179.35	Top C5Ar.1n	12.678
178.50	180.15	Base C5Ar.1n	12.708
179.00	180.65	Top C5Ar.2n	12.775
179.42	181.13	Base C5Ar.2n	12.819
180.29	181.94	Top C5AAn	12.991
181.55	183.20	Base C5AAn	13.139
181.95	183.60	Top C5AAr.1n	13.208*
182.02	183.67	Base C5AAr.1n	13.220*
182.50	184.15	Top C5ABn	13.302

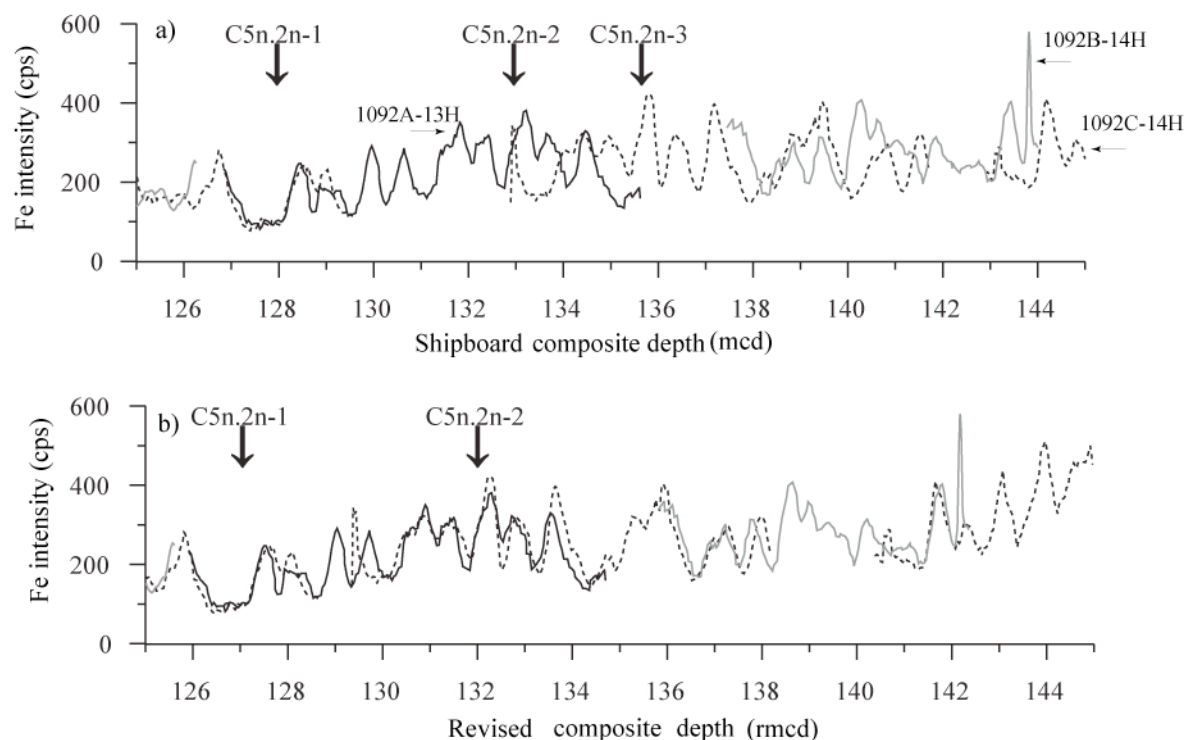


Figure 7-1. (a) Fe intensity (XRF) data plotted as a five-point moving average on the shipboard composite depth (mcd) scheme, with the position of the three subchrons identified in core sections 1092C-13H-6, 1092A-13H-4 and 1092C-14H-2 (C5n.2n-1 to 3) by Evans and Channell (2003). The thick line indicates data from hole 1092A, the thin line from hole 1092B and the dashed line from hole 1092C. (b) Fe intensity (XRF) data plotted as a five-point moving average on the revised composite depth (rmcd) scheme. Line notation as for Fig. 1a. On the revised composite depth (rmcd) scheme, C5n.2n-2 and C5n.2n-3 merge into a single subchron (C5n.2n-2).

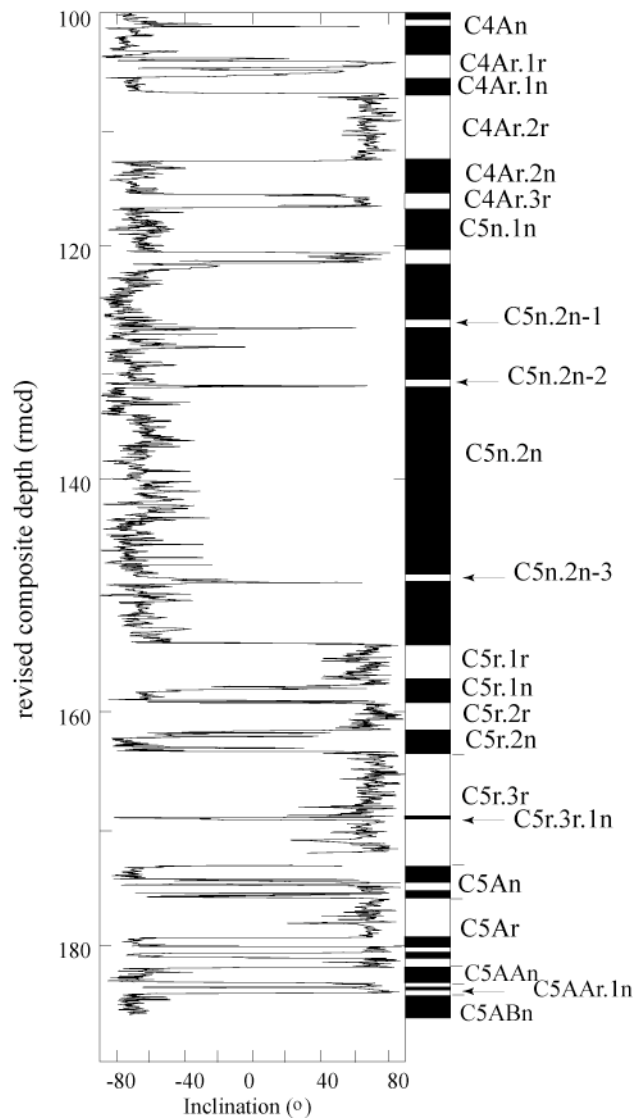


Figure 7-2. Inclination of the characteristic magnetization component plotted against revised composite depth (rmcd) for site 1092. Polarity chrons are labeled according to Cande and Kent (1992). Arrows indicate subchrons within C5n.2n, C5r.3r and C5AAn.1n. Polarity interpretation: black indicates normal polarity, white reverse polarity.

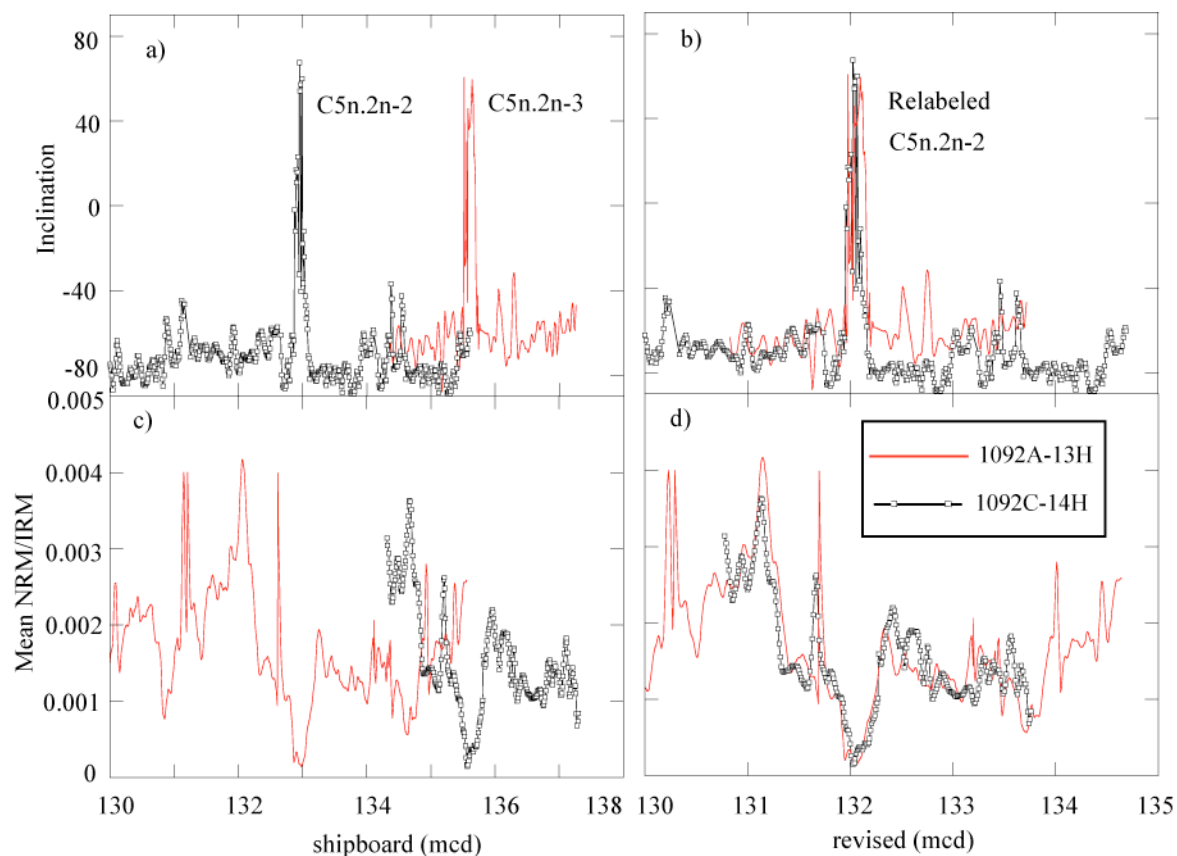


Figure 7-3. Site 1092: (a) Inclination of the characteristic magnetization component plotted against shipboard composite depth (mcd) showing C5n.2n-2 and C5n.2n-3 according to Evans and Channell (2003). (b) Inclination of the characteristic magnetization component plotted against revised composite depth (rmcd) showing that subchrons C5n.2n-2 and C5n.2n-3 of Evans and Channell (2003) become a single subchron (now labeled C5n.2n-2). (c) Mean of the ratio of natural remanent magnetization (NRM) to isothermal remanent magnetization (IRM), calculated for nine demagnetization steps in the 20-60 mT demagnetization range, plotted against shipboard composite depth (mcd), (d) Mean of the ratio of natural remanent magnetization (NRM) to isothermal remanent magnetization (IRM), calculated for nine demagnetization steps in the 20-60 mT demagnetization range, plotted against revised composite depth (rmcd).

## CHAPTER 8

### ASTRONOMICAL AGES FOR MIOCENE POLARITY CHRONS C4AR-C5R (9.3-11.2 MA), AND FOR THREE EXCURSION CHRONS WITHIN C5N.2N

#### **Introduction**

Site 1092 was drilled in January 1998 on Meteor Rise, close to DSDP Site 704, during ODP Leg 177 in the South Atlantic. The site produced a clear magnetic stratigraphy from 4-13 Ma including the interval between C4Ar.1n and C5r.1n when sedimentation rates were ~3 cm/kyr (Figure 8-1). Four short reverse polarity intervals (excursion chrons) were identified within subchron C5n.2n (Evans and Channell, 2003). This number was reduced to three due to recognition of an error in the Site 1092 composite splice, revealed by correlation of X-ray fluorescence (XRF) core scanning data, that resulted in duplication of one of the excursion zones (Evans et al., 2004).

The three "cryptochrons" in C5n.2n listed by Cande and Kent (1992, 1995), hereafter referred to as CK92/95, originate from the work of Blakely (1974) who identified three short-wavelength magnetic anomalies ("tiny wiggles" in the terminology of CK92/95) within "Anomaly 5" from a stack of marine magnetic anomaly (MMA) records from the NE Pacific Ocean. The term "cryptochron" expresses the uncertainty in origin of these "tiny wiggles" that may be attributed to polarity excursions/chrons or fluctuations in geomagnetic paleointensity. The resolution of Blakely's (1974) record did not allow precise estimation of the spacing of the short wavelength anomalies. They were placed at ~300 kyr intervals within C5n.2n, and Blakely (1974) attributed these short wavelength anomalies to full polarity reversals of the geomagnetic field. These polarity subchrons within C5n.2n were included in some subsequent timescales including those of Ness et al. (1980) and Harland et al. (1982, 1990), but were relegated to "cryptochrons" in CK92/95.

In the last decade, CK92/95 has been the standard polarity timescale used in the vast majority of studies that involve the integration of magnetic, bio- and chemo- stratigraphies. The timescale was constructed by deriving a composite geomagnetic polarity sequence from marine magnetic anomaly spacings. In the 0-5 Ma interval, CK95 used astrochronologically-derived numerical ages for polarity chrons available at the time (Shackleton et al., 1990; Hilgen et al., 1991). Beyond 5 Ma, using the assumption of smoothly varying spreading rates, a spline function was used to fit 8 radiometric age-calibration points, in the 14.8-84.0 Ma interval, to the Late Cretaceous-Cenozoic polarity record.

Since the publication of CK92/95, the astrochronological calibration of the polarity timescale has been extended beyond the last 5 Myrs. The majority of these developments have been incorporated into the recently published ATNTS2004 timescale of Lourens et al. (2004). For the Late Miocene, these authors used a blend of previously published astronomical timescales (Abdul Aziz et al., 2003; Hilgen et al., 1995; 2003). adjusted to the latest astronomical solutions (Laskar et al., 1993). This adjustment resulted in minor modification of the ages of the reversal boundaries from those given in the primary publications.

For the polarity chrons in the C4Ar.1r -C4Ar.3r interval, Lourens et al., (2004) utilized records from the Mediterranean (Hilgen et al., 1995), and from Monti dei Corvi (northern Italy) (Hilgen et al., 2003). At Monti dei Corvi, Hilgen et al. (2003) tuned a cyclic alternation of marls, marly limestones and organic-rich beds to the 65°N summer insolation time series (Laskar et al., 1993). This allowed astronomic calibration of the polarity chrons in the interval from C4An to the young end of C5n.2n. In the C5n.2n-C5Ar interval, Lourens et al. (2004) incorporated the work of Abdul Aziz et al. (2003) from the lacustrine Orera section in Spain. This section produced a reliable magnetic stratigraphy from the onset of C5n.2n to C5Ar.2n. The astronomic



calibration of the reversal boundaries was accomplished using the cyclic alternation of mudstones and dolomitic carbonates identified in the sequence.

In this study, we use new oxygen isotope records from ODP Site 1092 (Paulsen et al., in press) to astronomically calibrate polarity chrons C4Ar-C5r (9.3-11.2 Ma). Spectral analysis reveals a dominant obliquity (41-kyr) cycle in the oxygen isotope record and we use this to calibrate the Site 1092 record to the astronomical solution (Laskar et al., 2004). This study differs from previous astronomical timescales for this interval (Abdul Aziz et al., 2003; Hilgen et al., 2003) in that it uses oxygen isotope records rather than lithologic cycles as the means of astronomical calibration.

### **Methods and Results**

At ODP Site 1092, oxygen isotope data for the Middle to Late Miocene (7-15 Ma) were generated from three species of foraminifers (Figure 8-2) (see (Paulsen et al., in press). Benthic oxygen isotope data were generated from the benthic foraminifer *Cibicidoides kullenbergi*. Planktic oxygen isotope data were generated from two species: *Globigerina bulloides* and *Globorotalia scitula*. A power spectrum using the Blackman-Tuckey method with a Bartlett window, was generated in the depth domain from the stacked oxygen isotope record, using the Analyseries program of Paillard et al. (1996) (Figure 8-3a). This showed power at two frequencies:  $0.78 \text{ m}^{-1}$  and  $0.25 \text{ m}^{-1}$ . A gaussian filter centered at  $0.78 (\pm 0.234) \text{ m}^{-1}$  was then applied to the stacked oxygen isotope records to extract this dominant cycle. The record was then placed on an initial age model based on the magnetic stratigraphy (Evans and Channell, 2003) and the ATNTS2004 timescale (Lourens et al., 2004). The dominant cycle was identified as the 41-kyr obliquity cycle (Figure 8-3b) and individual (obliquity) cycles were numbered from youngest to oldest (1-45) (Figure 8-2). The second peak at a frequency of  $0.25 \text{ m}^{-1}$  was identified as close to the 100 kyr eccentricity period.

The oxygen isotope stack was tuned to an astronomical target curve, which was derived from the sum of normalized values (minus the mean and divided by the standard deviation) of eccentricity (E), obliquity (T) and negative precession (P) (E+T-P) (Laskar et al., 2004). Tuning of the isotope record was only possible in the 9.3-11.2 Ma interval due to lower sedimentation rates and condensed horizons outside this interval.

For Neogene sections, it is often assumed that the 41 kyr component of  $\delta^{18}\text{O}$  is globally correlative, and not likely to be variable in phase relative to orbital forcing (Clemens, 1999). Much of the power in the climate spectrum since the early Oligocene appears to be concentrated in the obliquity band (Zachos et al., 2001). At Site 1092, the final age model was obtained by tuning the initial age model (from ETP tuning) until the coherence calculated using cross-spectral analysis was maximized between the filtered  $\delta^{18}\text{O}$  record (filter centered at 41 kyr) and the orbital obliquity signal. Coherence between the oxygen isotope stack and ETP is close to one at the obliquity frequency (Figure 8-3c). The 1.2 Myr modulation of the obliquity cycle is clearly visible in the filtered isotope record (Figure 8-4) facilitating an unambiguous match to the orbital obliquity target. In this way, we produced an orbitally tuned age model for the 9.3-11.2 Ma interval at Site 1092.

The resulting astronomically tuned ages for C5n.2n are 44 kyrs younger at the onset, and 19 kyrs younger at the termination, than ages in ATNTS2004 (Lourens et al., 2004). The new ages are also significantly different from the CK92/95 ages, with the onset of C5n.2n being 47 kyrs older and the termination 62 kyrs older (Table 8-1). Although the difference is close to one obliquity cycle, an offset by one obliquity cycle would give an inappropriate match between the  $\delta^{18}\text{O}$  records and the ETP curve (Figure 8-4). For example, if we shift the oxygen isotope records one obliquity cycle younger then the light  $\delta^{18}\text{O}$  values of *G. bulloides* and *C. kullenbergi* in the

interval 10.78 to 10.72 Ma (Figure 8-4) would be located in the ETP minimum at ~10.7 Ma which can be considered unrealistic. Interval sedimentation rates at Site 1092, calculated for the C4Ar-C5r interval using the age-depth tie points from the tuning of the oxygen isotope records, vary from 1.7 cm/kyr to 3.7 cm/kyr for the entire interval and vary from 2.5 cm/kyr to 3.7 cm/kyr for C5n.2n (Figure 8-5).

### **Comparison with Other Timescales**

The greatest potential source of error in the age model is uncertainty in the orbital solution, which may be as high as 20 kyr at 10 Ma (Lourens et al., 2004; Laskar et al., 2004), whereas our tuning errors should be no more than a few thousand years. A component of the uncertainty in placement of the reversal boundaries can be estimated using the mean sedimentation rate (3 cm/kyr) and the response function width (at half-height) of ~4.5 cm for the 2G Enterprises u-channel magnetometer, giving a nominal error of ~2 kyrs for each reversal boundary. This error was mitigated by deconvolution (Guyodo et al., 2002) of the u-channel record across the excursions (Evans and Channell, 2003), resulting in a modified error estimate of ~1 kyr for the C5n.2n polarity excursions. These estimates do not include error in placement of polarity zone boundaries associated with delayed remanence acquisition, referred to as post-Depositional Remanent Magnetization (pDRM). Following Channell and Guyodo, (2004), the sediment lock-in beneath the bioturbated surface layer in pelagic sediments is abrupt, and can therefore the lock-in depth can be estimated from the mean sedimentation rate and the thickness of the surface bioturbated mixed layer (<10 cm in most pelagic environments (Trauth et al., 1997; Smith and Rabouille, 2002)). In the case of Site 1092, assuming a 10 cm bioturbated surface layer, the delay in remanence acquisition would be about 3 kyr.

A data gap occurs in the oxygen isotope records at 155.8-157.3 revised meters composite depth (rmcd). The gaussian filter identifies two obliquity cycles in this data gap (Figure 8-2). If

we assume that three cycles occurred in this gap, the sedimentation rates would be anomalously low (2.3 cm/kyr), while a single cycle causes an increase in sedimentation rates (5.1 cm/kyr). Two obliquity cycles yields sedimentation rates of 3.2 cm/kyr consistent with those adjacent to this interval. The revised composite section is well constrained in this interval (Evans et al., 2004), and there are no indications in physical properties of a likely change in sedimentation rate.

Comparison of the new astronomically-tuned ages for subchrons C4Ar.1n to C5r.1n (9.3-11.2 Ma) with ATNTS2004 (Lourens et al., 2004) reveal differences of 5-48 kyrs (Table 8-1). A large part of the age discrepancy is probably due to the low resolution of the paleomagnetic record in the Monti de Corvi section (Hilgen et al., 2003) that provides the basis for the ATNTS2004 timescale in this interval. In this section, the polarity reversals are poorly defined and the pattern fit of polarity zones to polarity chrons is ambiguous, due to weak and unstable magnetic remanence. Hilgen et al. (2003) gave errors of 25-77 kyrs for the astronomical ages for the reversal boundaries at Monti dei Corvi, due largely to poor definition of polarity zones (see Table 3 of Hilgen et al., 2003). For C4Ar.1n-C4Ar.2n, the differences between the astronomical ages obtained at Site 1092 and those obtained at Monti dei Corvi are within these error estimates, and the differences reach 71 kyrs for subchron C5n.1n where the error estimates at Monti dei Corvi are largest.

Site 1092 and CK92/95 ages differ by ~100 kyrs in the interval between C4Ar.1n and C4Ar.2n. Between the top of chron C5n.1n and the base of C5r.1n, the differences are 44-67 kyrs (Table 6-1). This narrow range indicates that the durations of subchrons in this interval are very consistent between the two timescales. CK92/95 relies on two calibration points for the middle to late Miocene interval. The first is placed at the older end of subchron C3n.4n with an age of 5.23

Ma from the astrochronological work of Hilgen (1991). The second age calibration point at 14.8 Ma at the young end of subchron C5Bn, was derived from radioisotopic age constraints on the correlative N9/N10 foraminifer zone boundary (see Cande and Kent, 1992).

Shackleton et al. (1995) constructed a timescale for the Late Neogene based on gamma ray attenuation (GRA) bulk density data from sediment cores obtained during ODP Leg 138. For the 0-6 Ma interval, cycles identified in the GRA bulk density data were tuned to the orbital insolation record of Berger and Loutre (1991). The Late Miocene (6-14.8 Ma) timescale was recalibrated using two tie-points at 5.875 Ma (termination of C3An) and 9.64 Ma (termination of C5n) and fitting a cubic-spline to estimate spreading rates in the manner adopted by CK92. The age control point at the termination of C5n (9.64 Ma) was generated by taking the radiometric age of 9.66  $\pm$  0.05 Ma from Baksi (1992) and adjusting it to the closest age that allowed the GRA bulk density to be matched directly to the insolation record. The ages obtained by Shackleton et al. (1995) are 153-225 kyrs younger than those obtained for Site 1092 (Table 8-1). There are several possible factors that could contribute to these differences. (1) The sediment record from the ODP Leg 138 sites may not be complete in the older part, possibly attributable to use of the XCB coring system. (2) The quality of the GRA bulk density data deteriorates, and the match to the insolation record becomes ambiguous, in the older part of the record. (3) Sedimentation rates are low ( $\sim$ 1-2 cm/kyr) in the Late Miocene at Leg 138 sites (Shackleton et al., 1995).

The Monti Gibliscemi section in Sicily (Italy) is a deep marine cyclically bedded hemipelagic succession of Miocene age (Hilgen et al., 2000). Due to weak magnetic intensities and overprinting, a magnetic stratigraphy was not obtained from the section. Hilgen et al. (2000)] indirectly estimated astronomical ages for polarity chron boundaries by transferring the

astronomical ages of calcareous nannofossil events at Monti Ghibliscemi to ODP Leg 138 sites in the equatorial Pacific that have reliable magnetic stratigraphies (Schneider, 1995). Linear interpolation of sedimentation rates between nannofossil datums yielded ages for polarity chron boundaries (Hilgen et al., 2000). In the interval from C5n.1n to the base of C5n.2n, the ages from Monti Ghibliscemi are consistently older than ages from Site 1092 with the mean difference being ~40 kyrs (Table 8-1). For subchron C5r.1n, the ages are younger than those obtained in this study by 37 and 38 kyrs at the young and old end of the subchron, respectively.

### **Excursion Chrons**

Previous estimates of the duration of the polarity excursion chron within C5n.2n from ODP Site 1092 have relied on the assumption of constant sedimentation rates within the chron (Evans and Channell, 2003). Based on a mean sedimentation rate within C5n.2n of ~3 cm/kyr, the excursion chrons were estimated to have a duration of 6-11 kyrs. The new astronomical calibration yields durations for these excursion chrons of 3-4 kyrs (Table 8-1).

DSDP Site 608 has recently yielded a revised magnetic stratigraphy for the Middle to Late Miocene (Krijgsman and Kent, 2004). Discrete samples collected every 2.5 cm at Site 608 indicate three excursions within C5n.2n, albeit represented by single samples, with estimated durations of 1-6 kyrs. Three reverse polarity intervals at ODP Site 884 on the Detroit Seamount in the NW Pacific Ocean were placed within C5n.2n (Roberts and Lewin-Harris, 2000), and were calculated by the authors to have durations of 6, 26 and 28 kyrs. Ambiguities in the interpretation of the magnetic stratigraphy at Site 884, and the apparent duration of these reverse polarity intervals, makes it unlikely that they correlate to the excursional directions identified at Site 1092 (see Evans and Channell, 2003).

Roperch et al. (1999) studied a 4.5 km thick middle Miocene continental red bed section in the Bolivian Altiplano. Magnetostratigraphic results indicate that the sequence was deposited

during the 14-9 Ma interval, and has a mean sedimentation rate of 97 cm/kyr in the 11.5-9.2 Ma interval. Roperch et al. (1999) identified one reverse polarity interval represented by five samples (at 3714-3719 m above base of section) within the normal polarity interval correlative to C5n.2n. Using an estimate for the mean sedimentation rate within C5n.2n (97 cm/kyr), this reverse interval has a duration of ~5 kyrs. The Ulloma tuff lies ~100 meters below the reverse polarity zone and has yielded an age of 10.35 +/-0.06 Ma from  $^{40}\text{Ar}/^{39}\text{Ar}$  dating of sanidine crystals (Marshall et al., 1992). Assuming a constant sedimentation rate from the top of the polarity zone correlative to C5n.2n to the Ulloma tuff the reverse polarity zone has an age of 10.21 Ma and a duration of ~8 kyrs.

Bowles et al. (2003) studied the sedimentary section at ODP Site 887 from the North Pacific that covers the C5n interval. The core was sampled using discrete samples at 2.5 cm spacing. The mean sedimentation rate within C5n.2n (1 cm/kyr) implies a sampling resolution of 2500 yrs, however no reverse polarity intervals were detected within C5n.2n. In view of the sedimentation rates at Site 887, it is possible that polarity intervals of the duration seen at ODP Site 1092 would not have been recorded using this sampling regime.

The Bowers et al. (2001) deep-tow marine magnetic anomaly (MMA) record from the southern East Pacific Rise (EPR) (Figure 8-7) is one of the most detailed MMA records for this time interval with an the average half-spreading rates of 42 mm/yr. In Figure 8-7, we correlate the Site 1092 paleointensity record from Evans and Channell (2003) to the deep-tow MMA record. The three brief excursion chrons observed in C5n.2n at Site 1092 can then be placed into the deep-tow MMA record (arrows from below in Figure 8-7). The preferred correlation between the relative paleointensity record from Site 1092 and the deep tow magnetic anomaly record yields a correlation of Site 1092 excursion chrons to the deep-tow record that differs from

the Bowers et al. (2001) correlation (arrows from top in Figure 8-7) of CK92/95 “tiny wiggles” (cryptochrons) from the North Pacific stack to the EPR deep-tow record.

Oxygen isotope records from ODP Site 1092 have allowed astronomic calibration of the ages of eight polarity chron boundaries (C4Ar.1n-C5r.1n), and of three excursion chrons within C5n.2n (Evans and Channell, 2003; Evans et al., 2004). This is the first time astronomically calibrated ages have been assigned to the excursion chrons within C5n.2n, and they indicate durations of 3-4 kyr. This duration estimate is consistent with the model of Gubbins (1999) that predicts that excursions should have durations less than the magnetic diffusion time (3 kyrs) for the inner core (Hollerbach and Jones, 1995). The duration of these excursions is less than the duration for reversal transitions such as the Matuyama-Brunhes boundary (5-10 kyrs, e.g. Channell and Kleiven, 2000) implying that the outer core must maintain the opposite or transitional polarity state for greater than ~3 kyrs to allow the outer core field to diffuse through the inner core and hence stabilize the outer core field (Gubbins, 1999). The duration for excursions, such as those within C5n.2n, which appear as abrupt swings to reverse polarity and return to normal polarity, was apparently insufficient for establishment of a prolonged reverse polarity interval.



Table 8-1. Astronomical ages from recent timescales compared with those inferred at ODP Site 1092. Numbers in parentheses indicate the difference between Site 1092 estimates (this paper) and other timescales. CK95- Cande and Kent (1995), ATNTS2004- Lourens et al., (2004), A2003- Abdul Aziz et al. (2003), S1995- Shackleton et al. (1995), H1995- Hilgen et al. (1995), H2000- Hilgen et al. (2000), H2003- Hilgen et al. (2003).

Subchron	Depth (mcd)	1092 age (ka) (errors) *	CK95 age (ka)	ATNTS2004 (ka)	A2003 (ka)	S1995 (ka)	H1995 (ka)	H2000 (ka)	H2003 (ka)
Top C4Ar.1n	105.13 ( $\pm 0.03$ )	9351 ( $\pm 2$ )	9230 (-121)	9312 (-39)		9142 (-209)			9364 (+13)
Base C4Ar.1n	106.96 ( $\pm 0.19$ )	9443 ( $\pm 10$ )	9308 (-135)	9409 (-34)		9218 (-225)			9364 (+13)
Top C4Ar.2n	112.60 ( $\pm 0.05$ )	9671 ( $\pm 3$ )	9580 (-91)	9656 (-15)		9482 (-189)	9629 (-42)	9652 (-19)	9687 (+16)
Base C4Ar.2n	115.60 ( $\pm 0.04$ )	9765 ( $\pm 2$ )	9642 (-123)	9717 (-48)		9543 (-222)	9740 (-25)	9762 (-3)	9729 (-36)
Top C5n.1n	116.80 ( $\pm 0.05$ )	9807 ( $\pm 2$ )	9740 (-67)	9779 (-28)		9639 (-168)		9841 (+34)	9770 (-37)
Base C5n.1n	120.79 ( $\pm 0.05$ )	9942 ( $\pm 2$ )	9880 (-62)	9934 (-8)		9775 (-167)		10000 (+58)	9871 (-71)
Top C5n.2n	121.61 ( $\pm 0.07$ )	9968 ( $\pm 2$ )	9920 (-62)	9987 (+19)		9815 (-153)		10037 (+66)	10004 (+36)
Top C5n.2n.1	127.00	10154 ( $\pm 1$ )	10091 (-63)						
Base C5n.2n.1	127.09	10157 ( $\pm 1$ )	10093 (-64)						
Top C5n.2n.2	131.96	10309 ( $\pm 1$ )	10248 (-61)						
Base C5n.2n.2	132.10	10313 ( $\pm 1$ )	10252 (-61)						
Top C5n.2n.3	148.83	10826 ( $\pm 1$ )	10782 (-44)						
Base C5n.2n.3	148.95	10829 ( $\pm 1$ )	10785 (-44)						
Base C5n.2n	154.12 ( $\pm 0.09$ )	10996 ( $\pm 2$ )	10949 (-47)	11040 (+44)	11043 (+47)	10839 (-157)		10998 (+2)	
Top C5r.1n	157.71 ( $\pm 0.12$ )	11108 ( $\pm 4$ )	11052 (-57)	11118 (+10)	11122 (+14)	10943 (-165)		11071 (-37)	
Base C5r.1n	159.03 ( $\pm 0.03$ )	11149 ( $\pm 1$ )	11099 (-50)	11154 (+5)	11158 (+9)	10991 (-158)		11111 (-38)	

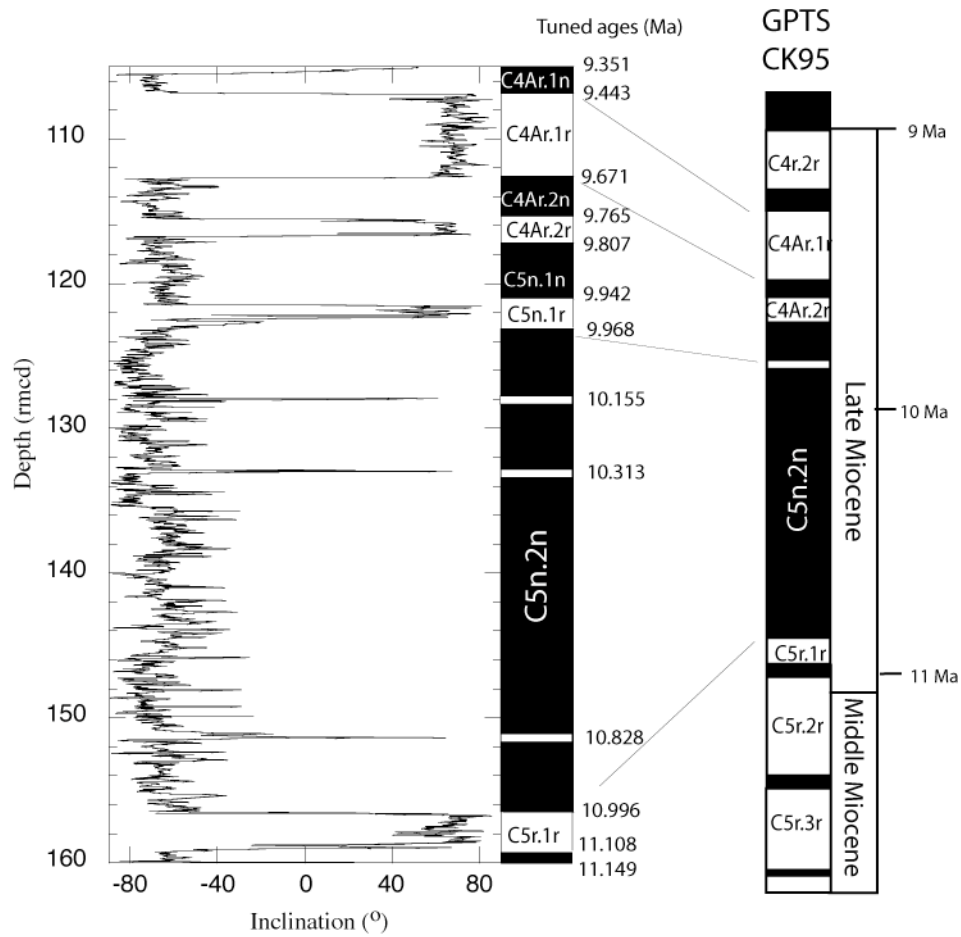


Figure 8-1. Magnetic component inclination for the C4Ar.1n-C5r.1n interval from ODP Site 1092 (Evans and Channell, 2003) compared to the geomagnetic polarity timescale of Cande and Kent (1992; 1995). rmcd= revised meters composite depth.

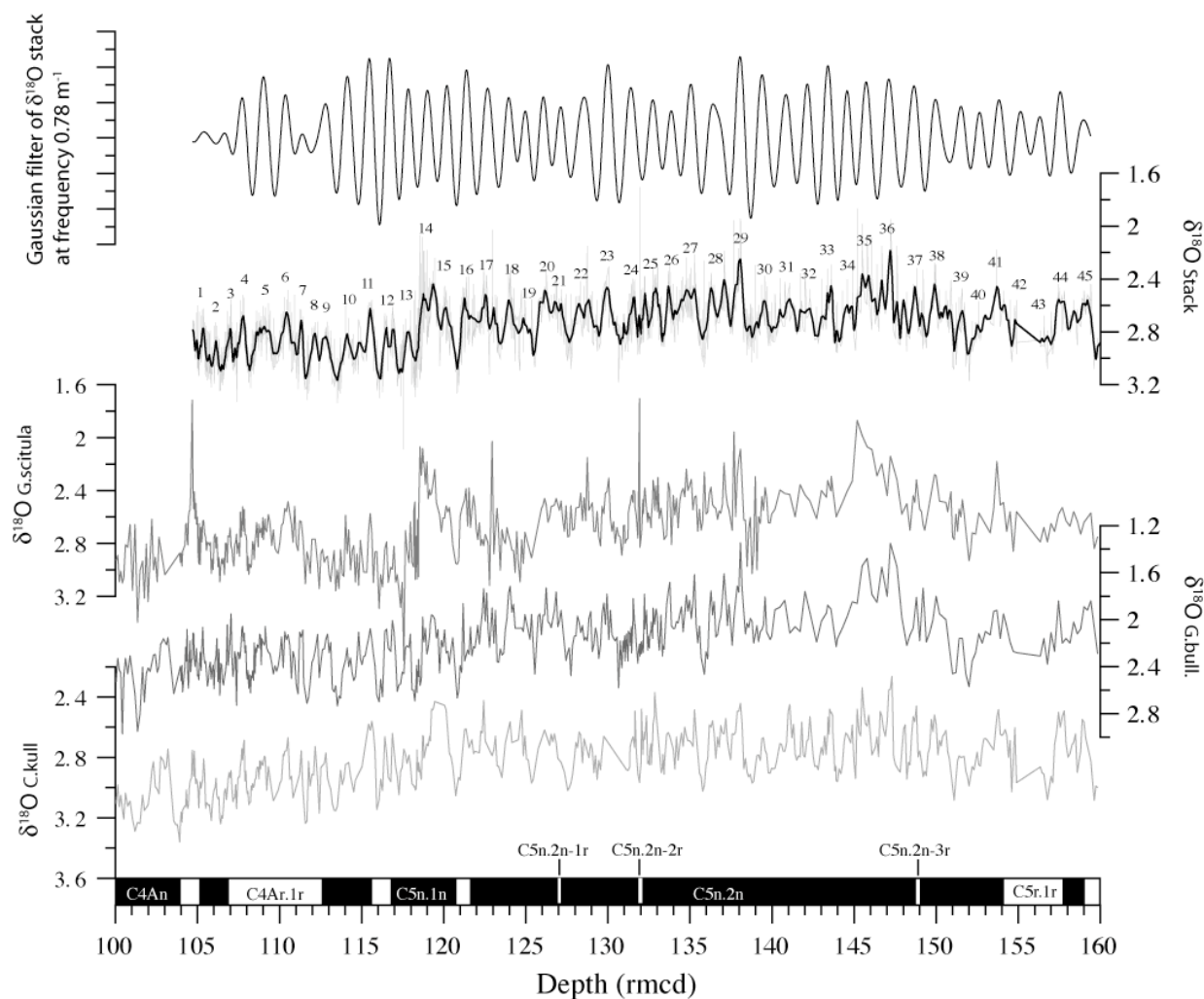


Figure 8-2. Oxygen isotope records from the C4An-C5r.1n interval at ODP Site 1092. The top frame shows the output of a gaussian filter centered at a frequency of  $0.78 \text{ m}^{-1}$  applied to the stacked  $\delta^{18}\text{O}$  record. The stacked  $\delta^{18}\text{O}$  record with numbered obliquity cycles is shown superimposed on the same record with a 5-point smoothing. The three  $\delta^{18}\text{O}$  records from different planktic and benthic foraminiferal species were used to generate the stack.

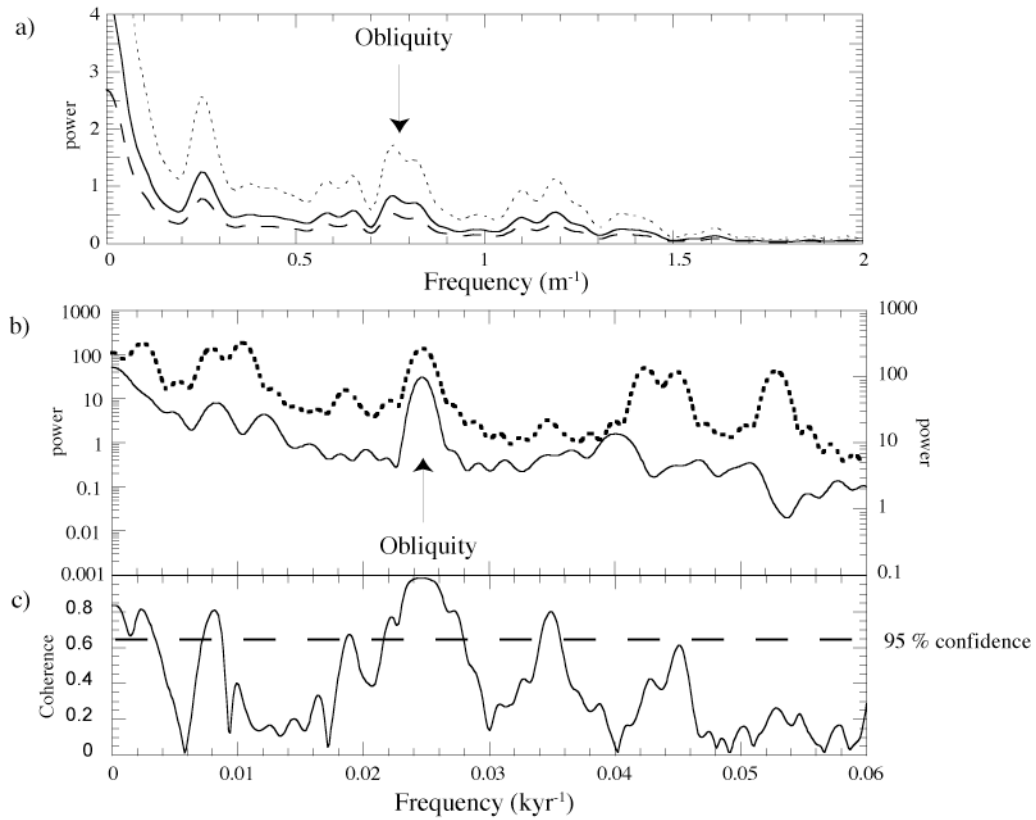


Figure 8-3. a) Power spectrum generated from the oxygen isotope stack in the depth domain (solid line). b) Dashed line is the power spectrum generated from the ETP target (Laskar et al., 2004) and the solid line is the power spectrum generated from the stacked oxygen isotope records after tuning. c) Coherence between the  $\delta^{18}\text{O}$  stack and the ETP target curve, line indicates 95% confidence limit for coherence peaks.

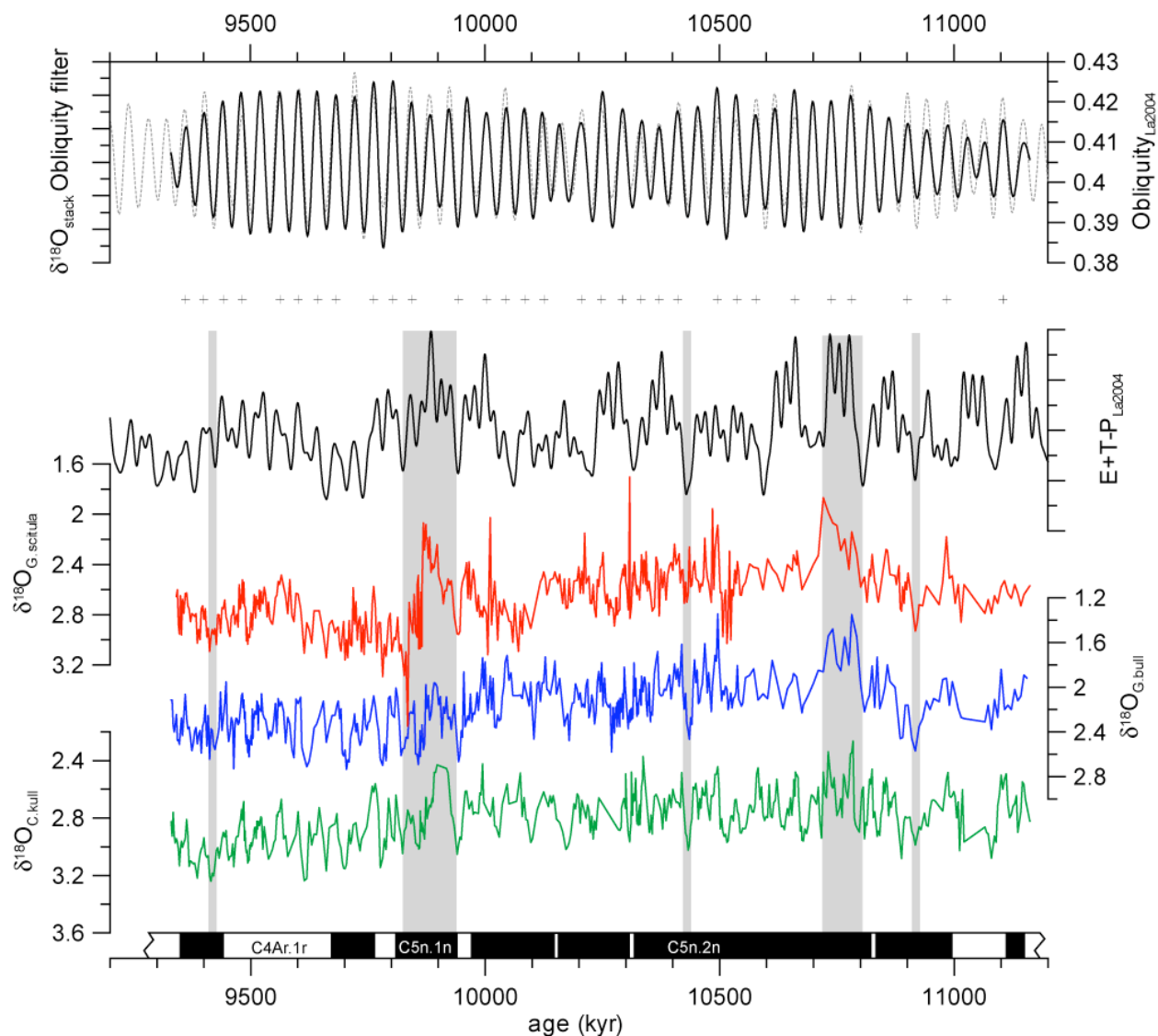


Figure 8-4. Upper plot shows the correlation of the filtered (filter centered at  $0.0244 \pm 0.0073$  kyr<sup>-1</sup>) oxygen isotope stack to the astronomical solution for obliquity (Laskar et al., 2004). Lower plot shows the correlation of the three oxygen isotope records from Site 1092 to the ETP solution (Laskar et al., 2004). Crosses mark the tie points between the oxygen isotope stack and the ETP curve. Shaded areas indicate critical intervals in the correlation between the records that facilitate an unambiguous match between the oxygen isotope record and the ETP astronomic solution.

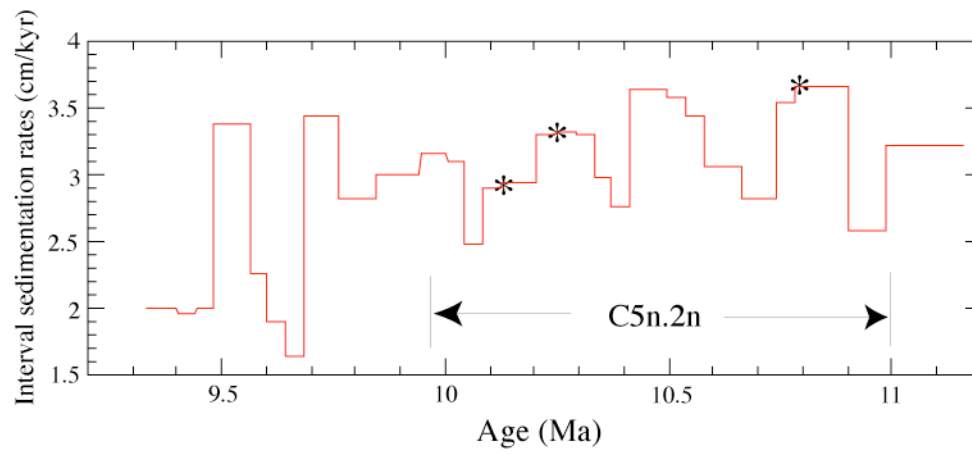


Figure 8-5. Interval sedimentation rates for the C4Ar.1n-C5r.1n interval calculated using the new astrochronology. Asterisks indicate the position of polarity excursions within C5n.2n.

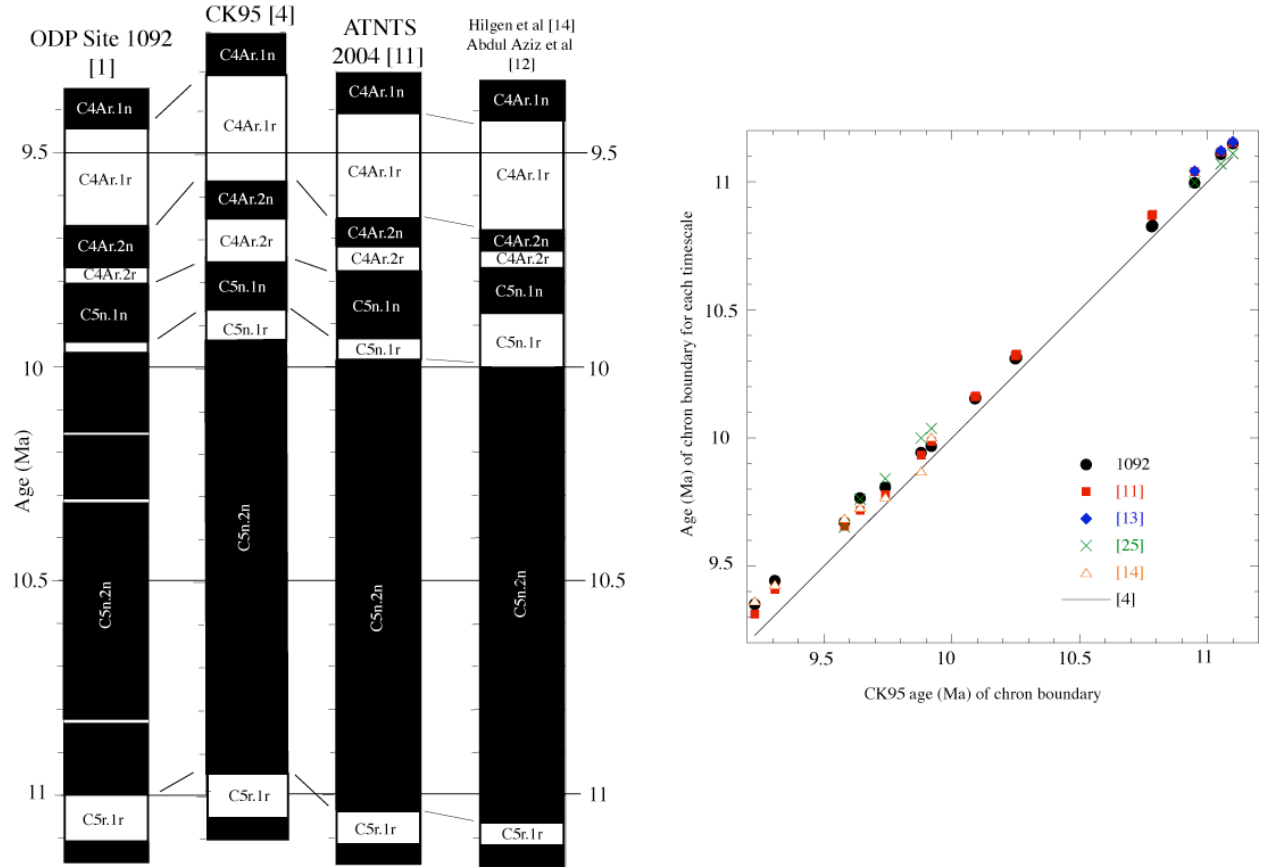


Figure 8-6. Comparison of the age estimates of polarity chrons at ODP Site 1092 (this paper) to the timescale of Cande and Kent (1992; 1995), to the ATNTS2004 timescale (Lourens et al., 2004), and to the timescales of Hilgen et al. (1995; 2000), and Abdul Aziz et al. (2003).

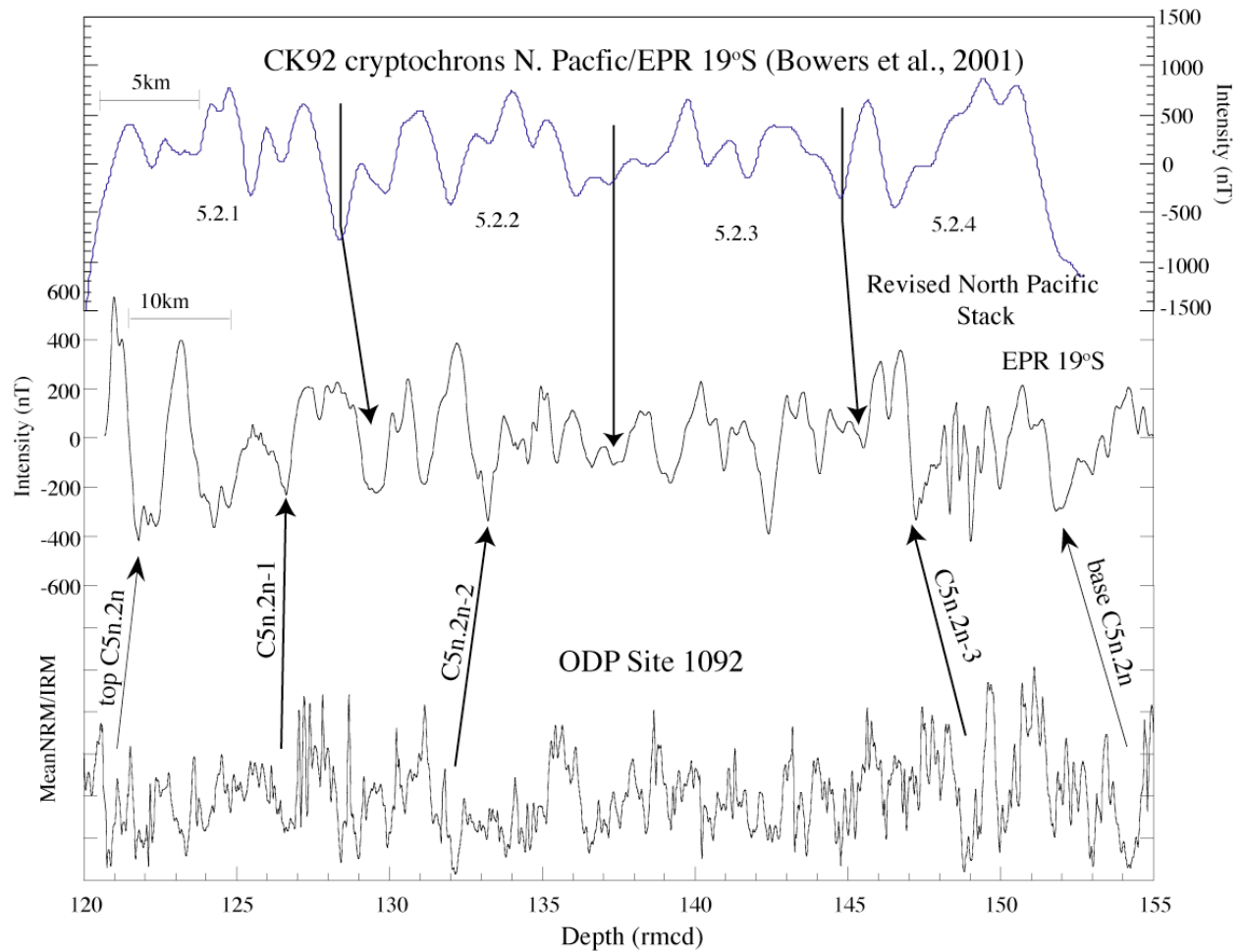


Figure 8-7. The Site 1092 relative paleointensity record for C5n.2n (base), the deep-tow magnetic anomaly record from the East Pacific Rise at 19°S (middle) and the revised North Pacific Stack (Bowers et al., 2001). Numbering on the revised North Pacific stack is after [35]. Arrows from above indicate the proposed correlation (Bowers et al., 2001) of CK92 cryptochrons to the revised N. Pacific Stack and the EPR 19S deep-tow record. Arrows from below indicate our preferred correlation of the polarity excursion chrons to the deep-tow record.



## CHAPTER 9

### CONCLUSIONS AND FUTURE WORK

The work presented in this dissertation illustrates the spectrum of timescales upon which the sedimentary record of the geomagnetic field can be used as a tool for stratigraphic correlation. The amount of information that can be gained from a particular sedimentary record depends on a number of factors: the type of sediment, the magnetic remanence carrier, the length of the record and the geographic location the core was collected. As such, this work has demonstrated the enormous possibilities that sedimentary records of the geomagnetic field have in terms of improving our understanding of changes in the geomagnetic field over time, their uses in stratigraphic correlation on varying timescales, and the importance of environmental magnetism to paleoclimatology. As more sedimentary cores are collected from the world's oceans, our understanding of the paleomagnetic field can only increase.

In Brunhes age sediments from the North Atlantic a combination of relative paleointensity and oxygen isotope records have been used to develop paleointensity-assisted chronostratigraphies. Detrital layers identified on the Eirik drift have been placed in a paleointensity-assisted chronostratigraphic framework, allowing improved correlation to other records of detrital layers from the North Atlantic. A new relative paleointensity stack for the 0-85 ka interval has been developed using three new paleointensity records and eight existing records. This stack has been placed on the Shackleton-revised GISP chronology by correlation of a benthic oxygen isotope record to Core MD95-2042 from the Portuguese Margin.

Miocene to Pleistocene age sediments from the Pacific and Atlantic Oceans have produced reliable magnetic stratigraphies back to 12 Ma. Integration of the magnetic stratigraphy with cycle stratigraphy has allowed astronomic calibration of the interval from 9.3-11.2 Ma at ODP Site 1092, in the 1-6 Ma interval at ODP Site 1208 and between 2.5 Ma and 6 Ma at IODP Site

U1313. Integration with biostratigraphic data has resulted in a new Late Miocene to Recent planktonic foraminifer biostratigraphic zonation for the northwest Pacific. In Pliocene age sediments from IODP Site U1313 (a re-occupation of DSDP Site 607) a record of relative paleointensity between 2.5 Ma and 6 Ma is one of only a handful of records for this interval.

Even though the geomagnetic polarity timescale has recently been revised with the entire Neogene section of the timescale being astronomically calibrated, much work is still required on older (Paleogene) parts of the timescale. I have been working on a collaborative project with Thomas Westerhold, Ursula Rohl and others to improve the Paleogene GPTS. This has resulted in the compilation of magnetostratigraphic results from two ODP Legs (198 and 208) along with XRF scanning data and other physical properties from the cores, resulting in the first astronomically calibrated timescale for the Paleocene (Westerhold et al., in preparation). By integrating published ODP data and land-based records with ODP Leg 198 and 208 sites, a Paleogene cyclostratigraphy has been accomplished (Westerhold et al., in preparation). The next phase of this work will be on Eocene age sediments from ODP Leg 198.

## LIST OF REFERENCES

- Abdul Aziz, H., Krijgsman, W., Hilgen, F.J., Wilson, D.S., Calvo, J.P., 2003. An astronomical polarity timescale for the late middle Miocene based on cyclic continental sequences. *J. Geophys. Res.* 108, 2159, doi:10.1029/2002JB001818.
- Arthur, M.A., Srivastava, S.P., Kaminski, M., Jarrad, R., Osler J, 1989. Seismic stratigraphy and history of deep circulation and sediment drift development in Baffin Bay and the Labrador Sea. In: Srivastava, S.P., Arthur, M.A., Clement, B., (Eds.), *Proceedings of the ODP, Sci. Results 105. Ocean Drilling Program. College Station, TX*, 957-975.
- Backman, J., Raffi, I., 1997. Calibration of Miocene nannofossil events to orbitally tuned cyclostratigraphies from Ceara Rise. In: Shackleton, N.J., Curry, W.B., Richter, C., Bralower, T.J. (Eds.). *Proceedings of the ODP, Sci. Results 154. Ocean Drilling Program. College Station, TX*, 83-99.
- Backman, J., Pestiaux, P., 1987. Pliocene *Discoaster* abundance variations, Deep Sea Drilling Project Site 606: Biochronology and paleoenvironmental implications. In: Ruddiman, W.F., Kidd R.B., Thomas, E., Shipboard Scientists. *Init. Repts. DSDP 94. Washington, D.C., US Government Printing Office*, 903-910.
- Baksi, A., 1992. A  $^{40}\text{Ar}/^{39}\text{Ar}$  age for the termination of Chron 5; a new calibration point for the Miocene section of the GPTS. *Trans. Am. Geophys. Union (EOS)* 73, 630.
- Ballini, M., Kissel, C., Colin, C., Richter, T., 2006. Deep-water mass source and dynamic associated with rapid climatic variations during the last glacial stage in the North Atlantic: A multiproxy investigation of the detrital fraction of deep-sea sediment. *Geochem. Geophys. Geosys.* 7, doi:10.1029/2005GC001070.
- Bassinot, F., Labeyrie, L., Shipboard Scientific Party, 1996. IMAGES MD101, a bord du Marion-Dufresne du 29 mai au 11 juillet 1995, 217 pp., *Inst. Francais pour la Rech. et la Technol. Polaires, Plouzane, France*.
- Baumgartner, S., Beer, J., Masarik, J., Wagner, G. Meynadier, L., Synal, H.-A., 1998. Geomagnetic modulation of the  $^{36}\text{Cl}$  flux in the GRIP ice core, Greenland. *Science* 279, 1330-1332.
- Berger, A., 1988. Milankovitch theory and climate. *Rev. Geophys.* 26, 624-657.
- Berger, A. 1978. Long-term variations of daily insolation and Quaternary climatic change. *J. Atmos. Sci.* 35, 2362-2367.
- Berger, A., Loutre, M.F., 1991. Insolation values for the climate of the last 10 million years. *Quat. Sci. Rev.* 10, 297-317.

- Berggren, W.A., Kent, D.V., Swisher, C.C., Aubry, M-P., 1995a. A revised Cenozoic geochronology and chronostratigraphy. In: Berggren, W.A., Kent, D.V., Aubry, M-P., Hardenbol, J., (Eds.). *Geochronology time scales and global stratigraphic correlation*. SEPM Special publication 54, pp. 129-206.
- Berggren, W.A., Hilgen F.J., Langereis, C.G., Kent, D.V., Obradovich, J.D., Raffi, I., Raymo, M.E., Shackleton, N.J., 1995b. Late Neogene chronology: New perspectives in high-resolution stratigraphy. *GSA Bulletin* 107, 1272-1287.
- Berggren, W.A., Kent, D.V., van Couvering J.A., 1985. Neogene geochronology and chronostratigraphy. In: Snelling, N.J. (Ed.). *The chronology of the geological record*. Geological Society of London Memoir 10, 211-250.
- Bianchi, G.G., McCave, I.N., 2000. Hydrography and sedimentation under the deep western boundary current on Bjorn and Gardar Drifts, Iceland Basin. *Marine Geology* 165, 137-169.
- Blakely, R.J., 1974. Geomagnetic reversals and crustal spreading rates during the Miocene. *J. Geophys. Res.* 79, 2979-2985.
- Bodén, P., Backman, J., 1996. A laminated sediment sequence from northern North Atlantic Ocean and its climatic record. *Geology* 24, 507-510.
- Bolli, H.M., Saunders, J.B., 1985a. Oligocene to Holocene low latitude planktonic foraminifera. In: Bolli, H.M., Saunders, J.B., Perch-Nielsen, K. (Eds.). *Plankton Stratigraphy*, Cambridge, Cambridge University Press, pp. 155-262.
- Bolli, H.M., Saunders, J.B., Perch-Nielsen, K., 1985b. Introduction to the foraminiferal chapters. In: Bolli, H.M., Saunders, J.B., Perch-Nielsen, K., (Eds.). *Plankton Stratigraphy*, Cambridge, Cambridge University Press, pp. 11-16.
- Bond, G.C., Showers, W., Elliot, M., Evans, M., Lotti, R., Hajdas, I., Bonani, G., Johnson, S., 1999. The North Atlantic's 1-2 kyr climate rhythm: relation to Heinrich Events, Dansgaard/Oeschger Cycles and the Little Ice Age. In: Clark, P.U., Webb R.S., Keigwin, L.D., (Eds.). *Mechanisms of global climate change at millennial time scales*. Geophysical Monograph 112, 35-58.
- Bowers, N.E., Cande, S.C., Gee, J., Hildebrand, J.A., Parker, R.L., 2001. Fluctuations of the paleomagnetic field during chron C5 as recorded in near bottom marine magnetic anomaly data. *J. Geophys. Res.* 106, 26,379-26,396.
- Bowles, J., Tauxe, L., Gee, J., McMillan, D., Cande S., 2003. Source of tiny wiggles in Chron C5: A comparison of sedimentary relative intensity and marine magnetic anomalies. *Geochem. Geophys. Geosyst.* 4, 1049, doi:10.1029/2002GC000489.
- Bown, P.R., 2005. Cenozoic calcareous nannofossil biostratigraphy, ODP Leg 198 Site 1208 (Shatsky Rise, northwest Pacific Ocean). In: Bralower, T.J., Premoli-Silva, I., Malone, M.J. (Eds.), *Proceedings of the ODP, Sci. Results* 198, 1-44 [Online].

- Bown, P.R., Young, J.R., 1998. Techniques. In Bown, P.R. (Ed.), *Calcareous nannofossil biostratigraphy*: Dordrecht, The Netherlands (Kluwer Academic Publ.), pp. 16–28.
- Bralower, T.J., Premoli Silva, I., Malone, M.J., The Shipboard Scientific Party, 2002. *Proceedings of the ODP, Init. Repts. 198 [CD-ROM]*. Ocean Drilling Program, Texas A&M University, College Station, TX.
- Broecker, W., Denton, G.H., 1989. The role of ocean-atmosphere reorganizations in glacial cycles. *Geochimica et Cosmochimica Acta* 53, 2465-2501.
- Bukry, D., 1973. Low-latitude coccolith biostratigraphic zonation. In: Edgar, N.T., Saunders, J.B., and Shipboard Scientists. *Init. Repts. DSDP, 15*, Washington (U.S. Govt. Printing Office), 685–703.
- Bukry, D., 1975. Coccolith and silicoflagellate stratigraphy, northwestern Pacific Ocean, Deep Sea Drilling Project Leg 32. In: Larson, R.L., Moberly, R., Shipboard Scientists. *Init. Repts. DSDP, 32*. Washington (U.S. Govt. Printing Office), 677–701.
- Cande, S.C., Kent, D.V., 1992. A new geomagnetic polarity timescale for the late Cretaceous and Cenozoic. *J. Geophys. Res.* 97, 13917-13951.
- Cande, S.C., Kent, D.V., 1995. Revised calibration of the geomagnetic polarity timescale for the late Cretaceous and Cenozoic. *J. Geophys. Res.* 100, 6093-6095.
- Censarek, B., Gersonde, R., 2002. Miocene diatom biostratigraphy at ODP sites 689, 690, 1088, 1092 (Atlantic sector of the Southern Ocean). *Marine Micropaleontology* 45, 309-356.
- Channell, J.E.T., 1999. Geomagnetic paleointensity and directional secular variation at Ocean Drilling Program (ODP) Site 984 (Bjorn Drift) since 500 ka: Comparisons with ODP Site 983 (Gardar Drift). *J. Geophys. Res.* 104, 22,937-22,951.
- Channell, J.E.T., D.A. Hodell, B. Lehman, 1997. Relative geomagnetic paleointensity and  $\delta^{18}\text{O}$  at ODP Site 983 (Gardar Drift, North Atlantic) since 350 ka. *Earth Planet. Sci. Lett.* 153, 103-118.
- Channell, J.E.T., Labs, J., Raymo, M.E., 2003. The Reunion subchronozone at ODP Site 981 (Feni Drift, North Atlantic). *Earth Planet. Sci. Lett.* 215, 1-12.
- Channell, J.E.T., Mazaud, A., Sullivan, P., Turner, S., Raymo, M.E., 2002. Geomagnetic excursions and paleointensities in the 0.9-2.15 Ma interval of the Matuyama Chron at ODP Sites 983 and 984 (Iceland Basin). *J. Geophys. Res.* 107, doi:10.1029/2001JB000491.
- Channell, J.E.T., Kanamatsu, T., Sato, T., Stein, R., Alvarez Zarikian, C.A., Malone, M.J., Expedition 303/306 Scientists, 2006. *Proceedings IODP, 303/306*. College Station TX (Integrated Ocean Drilling Program Management International, Inc.). doi:10.2204/iodp.proc.303306.104.

- Charles, C.D., Lynch-Stieglitz, J., Ninnemann, U.S., Fairbanks, R.G., 1996. Climate connections between the hemispheres revealed by deep sea sediment core/ice core correlations. *Earth Planet. Sci. Lett.* 142, 19-28.
- Chough, S.K., Hesse, R., 1985. Contourites from Eirik Ridge, south of Greenland. *Sedimentary Geology* 41, 185-199.
- Clemens, S.C., 1999. An astronomical tuning stratigraphy for Pliocene sections: implications for global-scale correlation and phase relationship. In: Shackleton, N.J., McCave, I.N., Weedon, G.P., (Eds.). *Phil. Trans. R. Soc. Lond. A*, 1949-1973.
- Clement, B. M., Robinson, F., 1986. The magnetostratigraphy of Leg 94 sediments, In: Ruddiman, W.F., Kidd, R. B., Thomas, E., Shipboard Scientists, Init. Repts. DSDP 94: Washington (U.S. Government Printing Office), 635-650
- Day, R., Fuller, M., Schmidt, V.A., 1977. Hysteresis properties of titanomagnetites: grain-size and compositional dependence. *Phys. Earth Planet. Int.* 13, 260-267.
- Evans, H.F., Channell, J.E.T., Sager, W.W., 2005. Late Miocene–Holocene magnetic polarity stratigraphy and astrochronology, ODP Leg 198, Shatsky Rise. In: Bralower, T.J., Premoli Silva, I., Malone, M.J. (Eds.), *Proceedings ODP, Sci. Results 198 [CD-ROM]*. Ocean Drilling Program. Texas A&M University College Station, TX, 1-39.
- Evans H.F., Westerhold, T., Channell, J.E.T., 2004. ODP Site 1092: revised composite depth section has implications for Upper Miocene "cryptochrons". *Geophys. J. Inter.* 156, 195-199.
- Evans H.F., Channell, J.E.T., 2003. Upper Miocene magnetic stratigraphy at ODP Site 1092 (sub-Antarctic South Atlantic): recognition of cryptochrons in C5n.2n. *Geophys. J. Inter.* 153, 483-496.
- Evans, H.F., Channell, J.E.T., Stoner, J.S., Hillaire-Marcel, C., Wright, J.D., Neitzke, L.C., Mountain G.S., submitted. Paleointensity-assisted chronostratigraphy of detrital layers on the Eirik Drift (North Atlantic) since marine isotope stage 11. *Geochem. Geophys. Geosyst.* Submitted.
- Expedition 303 Scientists, 2006. Site U1304. In: Channell, J.E.T., Kanamatsu, T., Sato, T., Stein, R., Alvarez Zarikian, C.A., Malone, M.J., Expedition 303/306 Scientists. *Proceedings IODP, 303/306: College Station TX (IODP Management International, Inc.)*. doi:10.2204/iodp.proc.303306.104.
- Expedition 306 Scientists, 2006. Expedition 306 summary. In: Channell, J.E.T., Kanamatsu, T., Sato, T., Stein, R., Alvarez Zarikian, C.A., Malone, M.J., Expedition 303/306 Scientists. *Proceedings IODP, 303/306: College Station TX (IODP Management International, Inc.)*. doi:10.2204/iodp.proc.303306.109.

- Funder, S., Hjory, C., Landvik, J. Y., Nam, S.-I., Reeh, N., Stein, R., 1998. History of a stable ice margin- East Greenland during the Middle and Upper Pleistocene. *Quat. Sci. Rev.* 17, 77-123.
- Gradstein, F., Ogg, J., Smith A., 2005. *A Geologic time scale 2004*. Cambridge, Cambridge University Press, pp. 589.
- Grootes, P.M., Stuvier, M., 1997. Oxygen 18/16 variability in Greenland snow and ice with 1033 to 105-year time resolution. *J. Geophys. Res.* 102, 26,455-26,470.
- Gubbins, D., 1999. The distinction between geomagnetic excursions and reversals. *Geophys. J. Inter.* 137, F1-F3.
- Guyodo, Y., Channell, J.E.T., Thomas, R.G., 2003. Deconvolution of u-channel paleomagnetic data near geomagnetic reversals and short events. *Geophys. Res. Letters* 29, 1845, doi:10.1029/2002GL014963.
- Hagelberg, T.K., Pisias, N.G., Shackleton N.J., Mix, A.C., Harris S., 1995. Refinement of a high-resolution, continuous sedimentary section for studying equatorial Pacific Ocean paleoceanography, Leg 138. In: Pisias, N.G., Mayer, L.A., Janecek, T.R. Palmer-Julson, A., van Andel, T.H., (Eds.). *Proceedings ODP Sci., Res. 138. Ocean Drilling Program*, College Station, TX, 31-46.
- Harland, W.B., Cox, A.V. Llewellyn, P.G., Pickton, C.A.G., Smith, A.G., Walters, R., 1982. *A Geologic Time Scale*. Cambridge Univ. Press, Cambridge.
- Harland, W.B., Armstrong, R., Cox, A.V., Craig, L., Smith, A., Smith, D., 1990. *A Geologic Time Scale 1989*. Cambridge Univ. Press, Cambridge.
- Hemming, S., 2004. Heinrich Events: Massive Late Pleistocene detritus layers of the North Atlantic and their global imprint. *Rev. Geophys.* 42, RG1005, doi:10.1029/2003RG000128.
- Heirtzler, J.R., Dickson, G.O., Herron, E.M., Pittman, W.C., III, LePichon, X., 1968. Marine magnetic anomalies, geomagnetic field reversal and motions of the ocean floor and continents. *J. Geophys. Res.* 73, 2119-2136.
- Hilgen, F.J., 1991a. Astronomical calibration of Gauss to Matuyama sapropels in the Mediterranean and implication for the Geomagnetic Polarity Time Scale. *Earth Planet. Sci. Lett.* 104, 226-244.
- Hilgen, F.J., 1991b. Extension of the astronomically calibrated (polarity) time scale to Miocene/Pliocene boundary. *Earth Planet. Sci. Lett.* 107, 349-368.
- Hilgen, F.J., Krijgsman, W., Langereis, C.G., Lourens, L.J., Santarelli, A., Zachariasse, W.J., 1995. Extending the astronomical (polarity) time scale into the Miocene. *Earth Planet. Sci. Lett.* 136, 495-510.

- Hilgen, F.J., Krijgsman, W., Raffi, I., Turco, E., Zachariasse, W.J., 2000. Integrated stratigraphy and astronomical calibration of the Serravallian/Tortonian boundary section at Monte Gibliscemi (Sicily, Italy). *Marine Micropaleontology* 38, 181-211.
- Hilgen, F.J., Abdul Aziz, H., Krijgsman, W., Raffi, I., Turco, E., 2003. Integrated stratigraphy and astronomical tuning of the Serravallian and lower Tortonian at Monti dei Corvi (Middle-Upper Miocene, northern Italy). *Palaeogeography, Palaeoclimatology, Palaeoecology* 199, 229-264.
- Hillaire-Marcel, C., Bilodeau, G., 2000. Instabilities in the Labrador Sea water mass structure during the last climatic cycle. *Can. J. Earth Sci.* 37, 795-809.
- Hillaire-Marcel, C., De Vernal, A., Bilodeau, G., Wu, G., 1994. Isotope stratigraphy, sedimentation rates, deep circulation, and carbonate events in the Labrador Sea during the last ~200 ka. *Can. J. Earth Sci.* 31, 63-89.
- Hiscott, R.N., Aksu, A.E., Mudie, P.J., Parsons, D.F., 2001. A 340,000 year record of ice rafting, paleoclimatic fluctuations, and shelf crossing glacial advances in the southwestern Labrador Sea. *Global and Planetary Change* 28, 227-240.
- Hodell, D.A., Charles, C.D., Sierro, F.J., 2001. Late Pleistocene evolution of the ocean's carbonate system. *Earth Planet. Sci. Lett.* 192, 109-124.
- Hodell, D.A., Kennett, J.P., 1986. Late Miocene-early Pliocene stratigraphy and paleoceanography of the South Atlantic and southwest Pacific Oceans: A synthesis. *Paleoceanography* 1, 285-311.
- Hollerbach, R., Jones, C.A., 1995. On the magnetically stabilizing role of the Earth's inner core, *Phys. Earth Planet. Inter.* 87, 171-181.
- Iaccarino, S., 1985. Mediterranean Miocene and Pliocene planktic foraminifera. In: Bolli, H.M., Saunders, J.B., Perch-Nielsen, K. (Eds.). *Plankton Stratigraphy*, Cambridge, Cambridge University Press, pp. 283-314.
- Jenkins, D.G., 1985. Southern and mid-latitude Paleocene to Holocene planktic foraminifera. In: Bolli, H.M., Saunders, J.B., Perch-Nielsen, K. (Eds.). *Plankton Stratigraphy*, Cambridge, Cambridge University Press, pp. 263-282.
- Jouzel, J., Lorius, C., Petit, J.R., Genthon, C., Barkov, N.I., Kotlyakov, V.M., Petrov, V.M., 1987. Vostok ice core: a continuous isotope temperature record over the last climatic cycle (160 000 years). *Nature* 329, 402-408.
- Kawase, M., Sarmiento, J.L., 1986. Circulation and nutrients in middepth Atlantic waters, J., *Geophys. Res.* 91, 9748-9770.
- Keller, G., 1979a, Late Neogene planktonic foraminiferal biostratigraphy and paleoceanography of the northwest Pacific DSDP Site 296. *Palaeogeography Palaeoclimatology, Palaeoecology* 27, 129-154.



- Keller, G., 1979b. Late Neogene paleoceanography of the North Pacific DSDP Sites 173, 310 and 296. *Marine Micropaleontology* 4, 159-172.
- Keller, G., 1979c. Early Pliocene to Pleistocene planktonic foraminiferal datum levels in the North Pacific: DSDP Sites 173, 310, 296. *Marine Micropaleontology* 4, 281-294.
- Kennett, J.P., Srinivasan, M., 1983. *Neogene Planktonic Foraminifera: A phylogenetic atlas*: Stroudsberg, Hutchinson Ross Publishing Co. pp. 265.
- King, J.W., Banerjee, S.K., Marvin, J., 1983. A new rock-magnetic approach to selecting sediments for geomagnetic paleointensity studies: application to paleointensity for the last 4000 years. *J. Geophys. Res.* 88, 5911-5921.
- Kirschvink, J.L., 1980. The least squares lines and plane analysis of palaeomagnetic data. *Geophys. J. R. Astr. Soc.* 62, 699-718.
- Kissel, C., Laj, C., Labeyrie, L., Dokken, T., Voelker, A., Blamart, D., 1999. Rapid climatic variations during marine isotope stage 3: magnetic analysis of sediments from the Nordic Seas and North Atlantic. *Earth Planet. Sci. Lett.* 171, 489-502.
- Kok, Y.S., Tauxe, L., 1996a. Saw-toothed pattern of relative paleointensity records and cumulative viscous remanence. *Earth Planet. Sci. Lett.* 137, 95-99.
- Kok, Y.S., Tauxe, L., 1996b. Saw-toothed pattern of sedimentary paleointensity records explained by cumulative viscous remanence. *Earth Planet. Sci. Lett.* 144, 9-14.
- Krijgsman W., Kent, D.V. 2004. Non-uniform occurrences of short-term polarity fluctuations in the geomagnetic field? New results from Middle to Late Miocene sediments from the North Atlantic. In: *Timescales of the paleomagnetic field*. Channell, J.E.T., Kent, D.V., Lowrie, W., Meert, J. G. (Eds.). AGU Geophysical Monograph 145, 161-174.
- Laj, C., Kissel, C., Beer, J., 2004. High resolution global paleointensity stack since 75 kyr (GLOPIS-75) Calibrated to absolute values. In: *Timescales of the paleomagnetic field*. Channell, J.E.T., Kent, D.V., Lowrie, W., Meert, J. G. (Eds.). AGU Geophysical Monograph 145, 255-265.
- Laj, C., Kissel, C., Mazaud, A., Channell, J.E.T., Beer, J., 2000. North Atlantic paleointensity stack since 75 ka (NAPIS-75) and the duration of the Laschamp event. *Phil. Trans. Roy. Soc.* 358, 1009-1025.
- Laskar, J., Joutel, H., Boudin, F., 1993. Orbital, precessional and insolation quantities for the Earth from -20 Myr to +10 Myr. *Astron. Astrophys.* 270, 522-533.
- Laskar, J., Robutel, P., Joutel, F., Gastineau, M., Correia, A.C.M., Levrard, B., 2004. A long term numerical solution for the insolation quantities of the Earth. *Astron. Astrophys.* 428, 261-285.

- Lisiecki L., Raymo, M., 2005. A Pliocene-Pleistocene stack of 57 globally distributed benthic  $\delta^{18}\text{O}$  records. *Paleoceanography* 20, doi:10.1029/2004PA001071.
- Lourens, L.J., Hilgen, F.J., Laskar, J., Shackleton, N.J., Wilson D., 2004. The Neogene Period. In: Gradstein, F.M., J.G. Ogg, A.G. Smith, (Eds.). *Geologic Time Scale 2004*. Cambridge Univ. Press, pp. 409-440.
- Lucotte, M., Hillaire-Marcel, C., 1994. Identification et distribution des grandes masses d'eau dans les mers du Labrador et d'Irminger. *Can. J. Earth Sci.* 31, 5-13.
- Lund, S.P., Acton, G., Clement, B., Hastedt, M., Okada, M., Williams, T., Shipboard Scientific Party, 1998. Geomagnetic field excursions occurred often during the last million years. *Trans. Am. Geophys. Union (EOS)* 79, 178-179.
- Maenaka, K., 1983. Magnetostratigraphic study of the Osaka Group, with special reference to the existence of pre and post-Jaramillo episodes in the Late Matuyama polarity epoch. *Mem. Hanazono Univ.* 14, 1-65.
- Martinson, D.G., Pisias, N. G., Hays, J.D., Imbrie, J., Moore, T.C., Shackleton, N.J., 1987. Age dating and the orbital theory of the Ice Ages: development of a high-resolution 0 to 300,000-year chronostratigraphy. *Quat. Res.* 27, 1-29.
- Mazaud, A., 1996. 'Sawtooth' variation in magnetic intensity profiles and delayed acquisition of magnetization in deep sea cores. *Earth Planet. Sci. Lett.* 139, 379-386.
- McCartney, M.S., 1992. Recirculating components to the deep boundary current of the northern North Atlantic. *Prog. Oceanog.* 29, 283-383.
- McCave, I.N., Tucholke, B.E., 1986. Deep current-controlled sedimentation in the western North Atlantic. In: *The geology of North America: The Western Atlantic region*. Vogt, P.R., Tucholke, B.E., (Eds.). *Geol. Soc. Am., DNAG Ser., Boulder, CO., Vol., M Spec. Publ.*, pp. 451-468.
- McCave, I. N., Manighetti, B., Robinson, S.G., 1995. Sortable silt and fine sediment slicing: Parameters for paleocurrent speed and paleoceanography. *Paleoceanography* 10, 593-610.
- Meese, D.A., Gow, A. J., Alley, R.B., Zielinski, G.A., Grootes, P.M., Ram, M., Taylor, K.C., Mayewski, P.A., Bolzan, J.F., 1997. The Greenland Ice Sheet Project 2 depth-age scale: Methods and results. *J. Geophys. Res.* 102, 26,411-26,423.
- Meynadier, L., Valet, J-P., Bassinot, F., Shackleton, N.J., Guyodo, Y., 1994. Asymmetrical sawtooth pattern of the geomagnetic field intensity from equatorial sediments in the Pacific and Indian Oceans. *Earth Planet. Sci. Lett.* 126, 109-127.
- Miller, K.G., Tucholke, B.E., 1983. Development of Cenozoic abyssal circulation south of the Greenland-Scotland Ridge. In: Bott, M.H.P. (Ed.), *Structure and Development of the Greenland-Scotland Ridge: New Methods and Concepts*. Plenum Press, New York, pp. 549-589.

- Moreno, E., Thouveny, N., Delanghe, D., McCave, I.N., Shackleton, N.J., 2002. Climatic and oceanographic changes in the Northeast Atlantic reflected by magnetic properties of sediments deposited on the Portuguese Margin during the last 340 ka. *Earth Planet. Sci. Lett.* 202, 465-480.
- Muscheler, R., Beer, J., Kubik, P.W., Synal, H.-A., 2005. Geomagnetic field intensity during the last 60,000 years based on  $^{10}\text{Be}$  and  $^{36}\text{Cl}$  from the Summit ice cores and  $^{14}\text{C}$ . *Quat. Sci. Reviews* 24, 1849-1860.
- Ness, G., Levi, S., Couch, R., 1980. Marine magnetic anomaly timescales for the Cenozoic and Late Cretaceous: A precis, critique and synthesis. *Reviews of Geophysics and Space Physics* 18, 4, 753-770.
- Okada, H., Bukry, D., 1980. Supplementary modification and introduction of code numbers to the low-latitude coccolith biostratigraphic zonation (Bukry, 1973; 1975). *Marine Micropaleontology* 5, 321-325.
- Opdyke, N.D., Glass, B., Hays, J.P., Foster, J., 1966. Paleomagnetic study of Antarctica deep-sea cores. *Science* 154, 349-357.
- Opdyke, N.D., Channell, J.E.T., 1996. *Magnetic stratigraphy*. Academic Press, San Diego, Calif., 346 pp.
- Paillard, D., Labeyrie, L., Yiou, P., 1996. Macintosh program performs time-series analysis, *Trans. Am. Geophys. Union*, EOS 77, 379.
- Paulsen, H., Westerhold, T., Bickert, T., in press. Middle to Late Miocene oxygen isotope stratigraphy of the Southern Ocean. *Geology*, in press.
- Raffi, I., Flores, J.-A., 1995. Pleistocene through Miocene calcareous nannofossils from eastern equatorial Pacific Ocean (ODP Leg 138). In: Pisias, N.G., Mayer, L.A., Janecek, T.R., Palmer-Julson, A., van Andel, T.H., (Eds.). *Proceedings ODP, Sci., Res. 138*. Ocean Drilling Program, College Station, TX, 59-72.
- Raymo, M.E., Ruddiman, W.F., Backman, J., Clement, B.M., Martinson, D.G., 1989. Late Pliocene variation in Northern Hemisphere ice sheets and North Atlantic Deep Water circulation. *Paleoceanography* 4, 413-446.
- Rea, D.K., Basov, I.A., Janecek, T.R., Palmer-Julson, A., Shipboard Scientific Party 1993. *Proceedings ODP, Init. Repts.*, 145, College Station, TX, ODP.
- Rio, D., Raffi, I., Villa, G., 1990. Pliocene-Pleistocene calcareous nannofossil distribution patterns in the western Mediterranean. In: Kastens, K.A., Mascle, J. *Proceedings of the ODP, Sci. Res., Leg 107*. Ocean Drilling Program, College Station, TX, ODP, 513-533.
- Roberts, A.P., Lewin-Harris, J.C., 2000. Marine magnetic anomalies: evidence that 'tiny wiggles' represent short-period geomagnetic polarity intervals. *Earth Planet. Sci. Lett.* 183, 375-388.

- Röhl, U., Abrams, L.J., 2000. High-resolution, downhole, and non-destructive core measurements from Sites 999 and 1001 in the Caribbean Sea: application to the Late Paleocene Thermal Maximum. In: Leckie, R.M., Sigurdsson, H., Acton, G.D., Draper G. (Eds.). Proceedings ODP, Sci. Res. 165. Ocean Drilling Program, College Station, TX, 191-203.
- Ruddiman, W.F., Raymo, M., McIntyre, A., 1986. Matuyama 41,000-year cycles: North Atlantic Ocean and northern hemisphere ice sheets. *Earth Planet. Sci. Lett.* 80:117–129.
- Ruddiman, W.F., Kidd, R.B., Thomas, E., Shipboard Scientific Party 1987. Init. Repts. DSDP, 94 (Pts. 1 and 2), Washington (U.S. Govt. Printing Office).
- Schneider, D.A., 1995. Paleomagnetism of some Leg 138 sediments: detailing Miocene magnetostratigraphy, In: Pisias, N.G., Mayer, L.A., Janecek, T.R. Palmer-Julson, A., van Andel, T.H., (Eds.). Proceedings ODP Sci., Res. 138. Ocean Drilling Program, College Station, TX, 59-72.
- Shackleton, N.J., Fairbanks, R.G., Chiu, T.-C., Parrenin, F., 2004. Absolute calibration of the Greenland time scale: implications for Antarctic time scales and for  $\Delta^{14}\text{C}$ . *Quat. Sci. Reviews* 23, 1513-1522.
- Shackleton, N.J., Crowhurst, S., 1997. Sediment fluxes based on an orbitally tuned time scale 5 Ma to 14 Ma, Site 926. In: Shackleton, N.J., Curry, W.B., Richter, C., Bralower, T.J. (Eds.). Proceedings ODP Sci., Res. 154. Ocean Drilling Program. College Station, TX 69-82.
- Shackleton, N.J., Crowhurst, S., Hagelberg, T., Pisias, N.G., Schneider, D.A., 1995. A new Late Neogene time scale: application to Leg 138 sediments. In: Pisias, N.G., Mayer, L.A., Janecek, T.R. Palmer-Julson, A., van Andel, T.H., (Eds.). Proceedings ODP Sci., Res. 138. Ocean Drilling Program, College Station, TX, 73-101.
- Shackleton, N.J., Baldauf, J.G., Flores, J-A., Iwai, M., Moore, T.C., Raffi, I., Vincent, E., 1995a. Biostratigraphic summary for Leg 138. In: Pisias, N.G., Mayer, L.A., Janecek, T.R. Palmer-Julson, A., van Andel, T.H., (Eds.). Proceedings ODP Sci., Res. 138. Ocean Drilling Program, College Station, TX, 73-101.
- Shackleton, N.J., Berger, A., Peltier, W.R., 1990. An alternative astronomical calibration of the lower Pleistocene timescale based on ODP site 677. *Trans. R. Soc. Edinburgh* 81, 251-261.
- Shackleton, N. J., Hall, M. A., Boersma, A., 1984. Oxygen and carbon isotope data from Leg 74 foraminifers, Init. Rep. DSDP 74, Washington (U.S. Govt. Printing Office), 599–612.
- Shipboard Scientific Party, 1999. Site 1092. In: Gersonde, R., Hodell, D.A., Blum, P., Shipboard Scientific Party. Proceedings ODP Init. Repts. 177, Ocean Drilling Program, College Station, TX, 1-82.

- Shipboard Scientific Party, 2002a. Leg 198 Summary. In: Bralower, T.J. Premoli-Silva I., Malone M., Shipboard Scientific Party. Proceedings ODP, Init. Repts. 198 [CD-ROM], College Station, TX (Ocean Drilling Program) 1-148.
- Shipboard Scientific Party, 2002b. Site 1208. In Bralower, T.J., Premoli Silva, I., Malone, M.J., Shipboard Scientific Party. Proc. ODP, Init. Repts., 198: College Station, TX (Ocean Drilling Program), 1–93. doi:10.2973/odp.proc.ir.198.104.2002.
- Singer, B.S., Hoffman, K.A., Chauvin, A., Coe, R.S., Pringle, M.S., 1999. Dating transitionally magnetized lavas of the late Matuyama chron: Toward a new  $^{40}\text{Ar}/^{39}\text{Ar}$  timescale of reversals and events. *J. Geophys. Res.* 104, 679-693.
- Snowball, I., Sandgren, P., 2004. Geomagnetic field intensity changes in Sweden between 9000 and 450 cal BP: extending the record of archaeomagnetic jerks by means of lake sediments and the pseudo-Thellier technique. *Earth Planet. Sci. Lett.* 227, 361-376.
- Snowball, I., Moros, M., 2003. Saw-tooth pattern of North Atlantic current speed during Dansgaard-Oeschger cycles revealed by the magnetic grain size of Reykjanes Ridge sediments at 59 N. *Paleoceanography* 18, doi:10.1029/2001PA000732.
- Srinivasan, M.S., Sinha, D.K., 1993. Late Neogene planktonic foraminiferal events of the southwest Pacific and Indian Ocean: A comparison. In: Tsuchi, R., Ingle, J.C., Eds. *Pacific Neogene environment, evolution and events*: Tokyo, University of Tokyo Press, pp. 203-220.
- Srivastava, S.P., Tapscott, C.R., 1986. Plate kinematics of the North Atlantic. In: *The Geology of North America: The Western Atlantic Region*. Vogt, P.R., Tucholke, B.E., (Eds.), *Geol. Soc. Am., DNAG Ser., Boulder, CO., Vol., M, Spec. Publ., p. 589-604.*
- Stoner, J.S., Channell, J.E.T., Hodell, D.A., Charles, C., 2003. A 580 kyr paleomagnetic record from the sub-Antarctic South Atlantic (ODP Site 1089). *J. Geophys. Res.* 108, doi:10.1029/2001JB001390.
- Stoner, J.S., Laj, C., Channell, J.E.T., Kissel, C., 2000. South Atlantic (SAPIS) and North Atlantic (NAPIS) geomagnetic paleointensity stacks (0-80 ka): implications for inter-hemispheric correlation. *Quat. Sci. Reviews* 21, 1141-1151.
- Stoner, J.S., Channell, J.E.T., Hillaire-Marcel, C., 1996. The magnetic signature of rapidly deposited detrital layers from the deep Labrador Sea: Relationship to North Atlantic Heinrich layers. *Paleoceanography* 11, 309-325.
- Stoner, J.S., Channell, J.E.T., Hillaire-Marcel, C., 1995a. Late Pleistocene relative geomagnetic paleointensity from the deep Labrador Sea: Regional and global correlations. *Earth Planet. Sci. Lett.* 134, 237-252.
- Stoner, J.S., Channell, J.E.T., Hillaire-Marcel, C., 1995b. Magnetic properties of deep-sea sediments off southwest Greenland: Evidence for major differences between the last two deglaciations. *Geology* 23, 241-244.

- Tauxe, L., 1993. Sedimentary records of relative paleointensity of the geomagnetic field: Theory and practice. *Rev. Geophys.* 31, 319-354.
- Tauxe, L., Hartl, P., 1997. 11 million years of Oligocene geomagnetic field behaviour. *Geophys. J. Int.* 128, 217-229.
- Tauxe, L., Pick, T., Kok, Y.S., 1995. Relative paleointensity in sediments: a pseudo-Thellier approach. *Geophys. Res. Lett.* 22, 2885-2888.
- Tauxe, L., Shackleton, N.J., 1994. Relative paleointensity records from the Ontong-Java Plateau. *Geophys. J. Int.* 117, 769-782.
- Thibault, J., J. P. Pozzi, V. Barthe's, Dubuisson, G., 1995. Continuous record of geomagnetic field intensity between 4.7 and 2.7 Ma from downhole measurements. *Earth. Planet. Sci. Lett.* 136, 541-550.
- Thomas, R., Guyodo, Y., Channell, J.E.T., 2004. U-channel track for susceptibility measurements. *Geochem. Geophys. Geosyst.* 1050, doi: 10.1029/2002GC000454
- Tian, J., Wang, P., Cheng, X., Li, Q., 2002. Astronomically tuned Plio-Pleistocene benthic  $\delta^{18}\text{O}$  record from South China Sea and Atlantic-Pacific comparison. *Earth Planet. Sci. Lett.* 203, 1015-1029.
- Turon, J.-L., Hillaire-Marcel, C., Shipboard Participants, 1999. IMAGES V mission of the Marion Dufresne. Leg 2, 30 June to 24 July 1999. *Geol. Surv. Canada, Open File* 3782.
- Valet, J-P. Time variations in geomagnetic intensity, 2003. *Rev. Geophys.* 41, doi:10.1029/2001RG000104.
- Valet, J-P., Meynadier, L., 1993. Geomagnetic field intensity and reversals during the past four million years. *Nature* 366, 234-238.
- Van Kreveld, S.A., Knappertsbusch, M., Ottens, J., Ganssen, G., van Hinte, J., 1996. Biogenic carbonate and ice-rafted debris (Heinrich layer) accumulation in deep-sea sediments from a Northeast Atlantic piston core. *Mar. Geol.* 131, 21-46.
- Venti, N.J., 2006. Revised Late Neogene mid-latitude planktic foraminiferal biostratigraphy for the Northwest Pacific (Shatsky Rise), ODP Leg 198. MS Thesis, University of Massachusetts.
- Venz, K.A., Hodell, D.A., Stanton, C., Warnke, D.A., 1999. A 1.0 Myr record of Glacial North Atlantic Intermediate Water Variability from ODP Site 982 in the northeast Atlantic. *Paleoceanography* 14, 42-52.
- Voelker, A., Sarnthein, M., Grootes, P. M., Erlenkeuser, H., Laj, C., Mazaud, A., Nadeau, M.J., Schleicher, M., 1998. Correlation of marine  $^{14}\text{C}$  ages from the Nordic sea with GISP2 isotope record: implication for  $^{14}\text{C}$  calibration beyond 25 ka BP. *Radiocarbon* 40, 517-534.

- Westerhold T., Roehl, U., Raffi, I., Bowles, J., Evans, H.F., in preparation. The first complete orbital chronology for the Paleocene: Implications for the Geomagnetic Polarity Time Scale and the age of the K-T boundary.
- Yamazaki, T., Oda, H., 2005. A geomagnetic paleointensity stack between 0.8 and 3.0 Ma from equatorial Pacific sediment cores. *Geochem. Geophys. Geosys.* 11, doi:10.1029/2005GC001001.
- Yang, S., Oda, H., Shaw, J., 2000. Variations in the geomagnetic dipole moment over the last 12,000 years. *Geophys. J. Int.* 140, 158-162.
- Young, J.R., 1998. Neogene. In Bown, P.R. (Ed.). *Calcareous Nannofossil Biostratigraphy*. Dordrecht, The Netherlands (Kluwer Academic Publ.), pp. 225–265.

## BIOGRAPHICAL SKETCH

Helen F. Evans was born in Swansea, South Wales, in 1977 to Terry and Eryl Evans. Growing up in an area of outstanding natural beauty she gained an interest at a young age in geology and natural sciences. She earned three A-levels in geology, chemistry and biology from Gowerton Comprehensive School in 1995. The same year she began an undergraduate career at Imperial College of Science, Technology and Medicine, in London. She graduated with honors in 1998 with a BSc. in geology with paleontology and Associateship of the Royal School of Mines (ARSM). After taking a year out she moved to the University of Florida to continue her education in geology. She gained a MS in Geology from the University of Florida in 2001 with a thesis entitled "Late Miocene to Pleistocene Magnetic Stratigraphy at ODP Site 1092 (subantarctic South Atlantic)". During her stay at the University of Florida, Helen was awarded a McLaughlin Dissertation Fellowship, the University Women's Club Graduate Student Scholarship and an outstanding academic achievement award from the College of Liberal Arts and Sciences. She also spent seven weeks at sea aboard the JOIDES Resolution during a research cruise to the North Atlantic. Helen is a member of the American Geophysical Union and the Geological Society of America. She has been an author on sixteen abstracts presented at international meetings and six peer-reviewed journal articles.